

**Sub-10 nm  
focused electron beam  
induced deposition**

Proefschrift  
ter verkrijging van de graad van doctor  
aan de Technische Universiteit Delft,  
op gezag van de Rector Magnificus prof. dr. ir. J.T. Fokkema,  
voorzitter van het College voor Promoties,  
in het openbaar te verdedigen op 22 februari 2008 om 12.30 uur  
door Willem Frederik VAN DORP  
materiaalkundig ingenieur, chemisch technisch ingenieur,  
geboren te Opperdoes

Dit proefschrift is goedgekeurd door de promotor:

Prof. dr. ir. P. Kruit

Samenstelling promotiecommissie:

Rector Magnificus	Voorzitter
Prof. dr. ir. P. Kruit	Technische Universiteit Delft, promotor
Prof. dr. H.W. Zandbergen	Technische Universiteit Delft
Prof. dr. ir. H.S.J. van der Zant	Technische Universiteit Delft
Prof. dr. J.R. Long	Technische Universiteit Delft
Dr. ir. A.J. Koster	Universiteit Leiden
Dr. P.A. Crozier	Arizona State University
Dr. C.W. Hagen	Technische Universiteit Delft

Het onderzoek beschreven in dit proefschrift is financieel ondersteund door NanoNed.

Niets uit dit werk mag worden gekopieerd, gereproduceerd of elektronisch worden opgeslagen zonder de uitdrukkelijke toestemming van de auteur.

“Hardly anyone ever produces a new idea. It is always some combination of old ideas that leads to reward. Revolutions are few and far between. It is steady progress that counts.”

L. Solymar & D. Walsh

Voor mijn ouders,  
voor hun geduld.

## **Abstract “Sub-10 nm focused electron beam induced deposition”**

Electron beam induced deposition (EBID) is a process in which precursor molecules are adsorbed on a substrate and are dissociated under the influence of a focused electron beam. Nonvolatile fragments of the molecules stick to the substrate and form a deposit, while the volatile fragments are pumped away by the vacuum system.

In the project preceding the presently described work, EBID was studied to find out what was required to write features smaller than 10-15 nm (which was the limit at that time). A strategy was found and demonstrated with the writing of 2 nm wide contamination lines. The aim for the work described here was to reach the next limit and using an organometallic precursor.

Work started with a critical review of literature from the past 70-odd years. The review shows that the physical processes occurring in EBID are generally well understood. By combining models for electron scattering in a solid and electron beam induced heating and knowledge of growth regimes, the majority of the experimental results was explained qualitatively. The review makes clear that several major issues remain. The fact that cross sections for electron scattering in a solid and electron-induced precursor dissociation are not well known, makes it difficult to interpret experiments where the acceleration voltage is varied. Related to this is the limited understanding of electron-induced precursor dissociation. The dissociation mechanism is one of the key factors determining the purity of the deposits and a better understanding of this process will help to develop EBID to its full potential.

The growth behavior at the sub-10 nm regime was explored by writing lines and arrays of dots from  $W(CO)_6$ . The smallest average values that have been found for the full width at half maximum, are 1.9 nm for lines and 0.72 nm for dots. These are world records for EBID and for the first time, it is shown that growth on this scale is determined by random processes. The deposits consist of so few molecules, that the counting statistics become visible. The result is that, despite identical conditions, deposits are not identical. The final deposited mass varies from dot to dot and dots do not nucleate exactly on the irradiated position, but randomly around it. This results in nonsymmetrical dots in the early stage of growth.

More insight into the deposition process is obtained by monitoring the annular dark field signal during the growth. This revealed that the growth rate during the deposition is not constant. The method also allowed control over the growth, for instance to prevent the occurrence of a proximity effect.

Atomic force microscopy measurements allowed quantification of the deposited volume. The distributions of the deposited volume as a function of dwell time bear a close similarity to Poisson distributions, which suggests that the deposited dots consist of a number of discrete units. From a fit of Poisson distributions to the volume distributions, it was concluded that the volume per unit is as small as  $0.4 \text{ nm}^3$ . This volume is almost just as small as a single  $W(CO)_6$  molecule in the solid phase.

The work described in this thesis opens up a whole new decade of feature sizes from 20 to sub-1 nm and brings the ultimate resolution of single molecules within reach.

## Samenvatting “Sub-10 nm gefocuseerde elektronenbundelgeïnduceerde depositie”

Bij elektronengeïnduceerde depositie (EBID) worden precursormoleculen die op een oppervlak zijn geadsorbeerd, ontleed onder invloed van een gefocuseerde elektronenbundel. De niet-vluchtige delen hechten aan het substraat en vormen het depositiet. De vluchtige delen worden weggepompt door het vacuumsysteem.

In het project dat aan het hier beschreven werk voorafging, werd onderzocht wat er voor nodig was om met EBID kleiner te kunnen schrijven dan 10-15 nm (de toenmalige grens). Een strategie werd gevonden en gedemonstreerd met het schrijven van 2 nm brede contaminatie lijnen. Het hier beschreven werk heeft als doel het bereiken van de volgende grens gebruikmakend van een organometallische precursor.

Allereerst is de literatuur van de afgelopen 70 jaar kritisch bekeken. Deze studie wijst uit dat de fysische processen die bij EBID een rol spelen, over het algemeen goed zijn begrepen. Met modellen voor verstrooiing van elektronen in een vaste stof en elektronengeïnduceerde opwarming en kennis van groeiregimes kunnen de meeste resultaten verklaard worden. Het overzicht brengt ook onduidelijkheden naar voren. Dat de doorsnedes voor verstrooiing van elektronen in vaste stof en voor het ontleden van precursormoleculen niet goed bekend zijn, bemoeilijkt de interpretatie resultaten van experimenten waar de energie van de elektronen gevarieerd is. Dit vindt zijn oorzaak in het beperkte begrip van de manier waarop elektronen precursormoleculen ontleden. Dit mechanisme is (onder andere) bepalend voor de zuiverheid van het depositiet en meer begrip is nodig om de voordelen van EBID ten volste te benutten.

Het groeiedrag in het sub-10 nm regime is bestudeerd door lijnen en arrays van puntjes te schrijven met  $W(CO)_6$ . De kleinste gemiddelde waarden die gevonden zijn voor de breedte bij halve hoogte, zijn 1.9 nm voor lijnen 0.72 nm voor puntjes. Dit zijn wereldrecords en voor het eerst is laten zien dat groei op deze schaal bepaald wordt door willekeurige processen. De depositieten bevatten zo weinig moleculen, dat de telstatistiek zichtbaar wordt. Het gevolg is dat, ondanks identieke omstandigheden, de depositieten niet identiek zijn. De neergelegde massa varieert van puntje tot puntje en nucleatie gebeurt niet precies op de belichte plek, maar willekeurig daar omheen. Het gevolg is dat puntjes in het begin van het groeiproces asymmetrisch zijn.

Het volgen van het *annular dark field* signaal tijdens de groei biedt meer inzicht in het groeiproces. Het blijkt dat de groeisnelheid tijdens het schrijven niet constant is. Het groeiproces kan met deze methode ook worden beheerst, bijvoorbeeld om te voorkomen dat de groei beïnvloed wordt door de nabijheid van andere depositieten.

De hoeveelheid neergelegd materiaal is gekwantificeerd met metingen met een atomaire krachtmicroscopie. De verdelingen van het neergelegde volume als functie van de schrijftijd lijken sterk op Poisson verdelingen. Dat impliceert dat de puntjes bestaan uit een discreet aantal eenheden. Door Poisson verdelingen met de volume verdelingen te vergelijken, is bepaald dat het volume van zo'n eenheid  $0.4 \text{ nm}^3$  is. Dit is bijna net zo klein als een enkel  $W(CO)_6$  molecuul in de vaste fase.

Het hier beschreven werk opent een geheel nieuw gebied voor patronen van 20 tot minder dan 1 nm en brengt de ultieme resolutie van enkele moleculen binnen bereik.



## Contents

	Abstract	iv
	Samenvatting	v
1.	Introduction	1
2.	Critical literature review	5
3.	Experimental details	73
4.	Approaching the resolution limit of nanometer-scale electron beam-induced deposition	79
5.	Statistical variation analysis of sub-5-nm-sized electron-beam-induced deposits	87
6.	Solutions to a proximity effect in high resolution electron beam induced deposition	95
7.	<i>In situ</i> monitoring and control of material growth for high resolution electron beam induced deposition	105
8.	Growth behavior near the ultimate resolution of nanometer-scale focused electron beam-induced deposits	113
9.	Remaining issues	129
10.	Conclusions	137
11.	References	141
	Appendices	155
	Curriculum Vitae	160
	Bibliography	161
	Acknowledgements	162
	Dankwoord	163



## 1. Introduction

### Contents

I. What is EBID? .....	2
II. Why study sub-10 nm EBID?.....	2
III. Contents of this thesis .....	3

## I. What is EBID?

Focused electron beam induced processing (FEBIP) is a direct-write lithography technique. An electron beam is focused onto a substrate in the presence of a precursor gas. Locally, under the influence of the electron beam, the precursor molecules are dissociated into volatile and nonvolatile fragments (see Fig. 1). Depending on the type of precursor, the nonvolatile components stick to the substrate and form a deposit (in the case of electron beam induced deposition, EBID) or react with the substrate and form volatile species (in the case of electron beam induced etching, EBIE). Since it is possible to focus electron beams down to sizes smaller than a tenth of a nanometer, this technique is very well suited for the definition of micro- to nanometer-sized structures. By controlling the scan pattern, two and three-dimensional structures can be created. Since EBID is usually performed in scanning electron microscopes, positioning and imaging of the desired structure can be done very quickly and accurately.

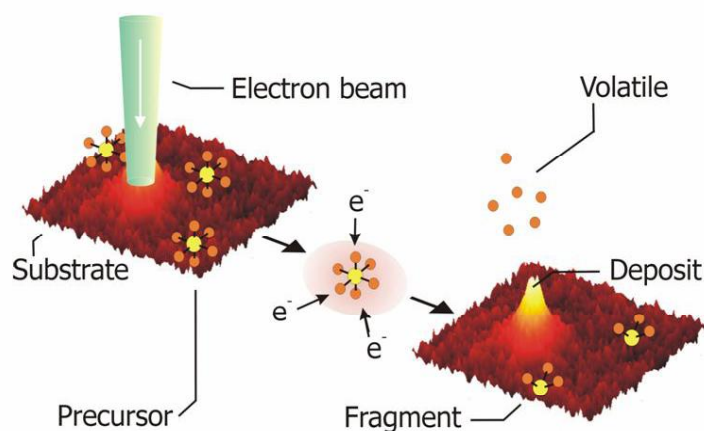


*Fig. 1. A schematic representation of focused electron beam induced deposition. Locally, under the influence of the electron beam, precursor molecules are dissociated. The nonvolatile fragments form a deposit.*

## II. Why study sub-10 nm EBID?

The resolution of patterning techniques is ever increasing. The dominant method for the patterning for integrated circuits (IC's) is light lithography. EBID is very unlikely to become such a high throughput technique in the foreseeable future, but IC's give a practical reference frame as they are a well known application. IC's available in the shops today are fabricated using ultraviolet light and masks and have features that are 45 nm wide and spaced 130 nm apart. The state of the art for extreme ultraviolet light is around 30 nm [1].

A maskless technique that is capable of higher resolution than the techniques using light is electron beam lithography (EBL). The best result (using an organic resist) at the time of writing is lines of 5-6 nm wide, spaced at 20 nm [2]. A disadvantage of this technique is that it is slower than light lithography. Flood exposures (such as in light lithography) are not possible and every part of the pattern has to be defined by an electron beam individually. There are developments to increase the throughput for EBL (by using multiple beams instead

of just one), but currently the main applications are dedicated circuits or devices for science and industry.

The smallest building blocks available to us are atoms, so a single atom is the ultimate lithographic resolution. This ultimate limit has been reached with the positioning of Xe atoms in a pattern on a Cu surface with a scanning tip microscope (STM) [3]. However, this technique is a lot slower than EBL, because the atoms need to be moved around one by one. This is very time consuming and at the moment not at all a likely candidate for any serious application as a lithography tool.

EBID is a technique that is situated somewhere between EBL and STM, both in resolution and in speed. At present, it is capable of achieving a higher resolution than EBL, but is also slower. It is much faster than STM, but it cannot (yet) reach the ultimate resolution of a single atom. A significant advantage of EBID is that the pattern is written directly, without the use of resists. This means flat substrates are not required and less process steps are involved in the fabrication. Another advantage is that the definition is not limited to 2D patterns, but that 3D fabrication is possible. At present, a serious disadvantage is the low metal content and low conductivity of wires fabricated by EBID.

It is the capability of obtaining the high resolution that makes this technique very interesting. At the start of the research for this thesis, a resolution of 2 nm was demonstrated [4]. If the problem of the low conductivity can be solved, it has the potential of becoming an important tool for rapid prototyping. If the disadvantage of the low speed can be compensated with the use of multiple beams, it may also become suitable for larger-scale applications. In this thesis, the growth behavior at the sub-10 nm regime was explored. One reason to do this, is to see how far the resolution of this technique can be pushed. Can EBID match STM in achieving the ultimate resolution of a single atom? Another reason is to learn about the relevant physics and the requirements for fabrication on this scale. This knowledge can be used to develop EBID into a unique additive technique, capable of locally modifying products with the ultimate resolution and a high flexibility.

EBID is already being used as a mask repair technique and to functionalize tips for scanning probe microscopy. It is a good candidate to add ultra-high resolution details to imprint masks. If the current limitations are solved, future applications can be more diverse. For instance, EBID can be used to create quantum dots in IC's. One can also envision the deposition of single molecules or nanometer-sized dots in microreactors to act as a binding site for bioactive complexes or as catalyst particles to locally enhance reactions. In the far future, it might even be possible to create new phases of material by combining atoms of different elements.

### **III. Contents of this thesis**

Chapter 2 is a critical review of the available literature on the subject of EBID. There are many parameters involved in EBID and the process has been studied by many in many different ways and under many different conditions. Not surprisingly, this has resulted in a large amount and a large variety of results. The intent of this literature review is to make clear to what extent these results lead to a comprehensive understanding of all mechanisms

involved. What is the consistency of the results? And can everything be explained with the models that are available now? How far are we from fabricating the products that we want to make? The critical review leads to a number of conclusions; amongst others that the physical processes are generally speaking well understood and modeled.

Before starting with the experimental results, information regarding the experiments is given in Chapter 3. Essential experimental details are described together with the results in the corresponding Chapters 4-8, so Chapter 3 only contains background information.

As mentioned, Chapters 4-8 contain the experimental results. In Chapter 4, it is demonstrated that a resolution of 1.0 nm can be obtained for dots and 1.9 nm for lines. Also, two nonlinearities are observed. (1) Dots fabricated under identical conditions do not have the same mass and size, but a variation in mass is observed. (2) A proximity effect is observed, where the height of parallel lines is dependent on the spacing between the lines.

The first nonlinear effect, the variation in dot mass, is studied in more detail in Chapter 5. The variation is studied for 2 average deposit masses and an estimation of the number of molecules per deposit is made. Based on this estimation, the nonlinear effect is attributed to the number of molecules involved in the deposition process rather than the number of electrons.

The second nonlinear effect, the proximity effect, is studied in more detail in Chapter 6. An explanation for the underlying mechanism is given and strategies for avoiding the proximity effect are presented.

It was found that more control over and insight into the deposition process was desirable. In Chapter 7, experiments are described where the ADF signal was monitored and used to control the growth *in situ*. The control over the ADF signal appeared to be insufficient to reduce the variation in dot mass, but it was effective in avoiding the proximity effect. Comparison of the signal to noise ratio of the ADF signal indicated a potential sensitivity of a single molecule.

Chapter 8 describes how the techniques used are pushed further towards their limit. The spatial resolution of EBID was increased to 0.8 nm for dots. The randomness of the deposition process, already apparent from the variation in deposit mass, is also made visible in the nonsymmetrical deposit shapes. To obtain more insight in the number of molecules per deposit, ADF imaging was combined with atomic force microscopy. A detailed comparison was made between the observed mass distributions and Poisson distributions. A new scan strategy was developed to get an improved sampling of the deposits. This allowed the observation that the growth rate of dots is not constant during the deposition. Discrete steps of a constant height, indicative of the deposition of single molecules, were not detected.

Remaining issues that did not lead to definite conclusions are discussed in Chapter 9. Finally, in Chapter 10, conclusions are drawn and an outlook for further research is presented. An explanatory list of the precursor names, symbols used in Chapter 2 and abbreviations is given in the appendix.

Because many of the chapters in this thesis are intended for publication or have already been published, it is possible that the same information appears more than once.

## 2. A critical literature review of focused electron beam induced deposition

*W.F. van Dorp, C.W. Hagen*

Delft University of Technology, Faculty of Applied Sciences, Lorentzweg 1, 2628 CJ Delft, the Netherlands

### **Abstract**

An extensive review is given of the results from literature. Focused electron beam induced deposition (EBID) is a complex process, where many and often mutually dependent factors are involved. The process has been studied by many over many years in many different experimental setups, so it is not surprising that there is a great variety of experimental results. To come to a better understanding of the process, it is important to see to which extent the experimental results are consistent with each other and with the existing model. To do this, it is necessary to categorize and interpret all these results. In this review, this has been done by sorting all data from literature by the specific parameter that was varied (current density, acceleration voltage, scan patterns, etc.). Each of these parameters can have an effect on the final deposit properties, such as the physical dimensions, the composition, the morphology or the conductivity. For each parameter-property combination, the available data is discussed and (as far as possible) interpreted.

**Contents**

I. Introduction.....	8
II. Focused electron beam induced processes in general.....	10
II.A. Substrate – precursor molecule interaction.....	11
II.B. Electron– substrate interaction.....	11
II.C. Electron– precursor molecule interaction.....	13
II.D. Interplay between factors.....	14
III. Theoretical model.....	15
III.A. Basic model.....	15
III.B. Electron- and precursor-limited regimes.....	16
III.C. Temperature.....	17
IV. Beam parameters.....	18
IV.A. Current density.....	18
IV.A.1. Height.....	18
IV.B.2. Width.....	22
IV.C.3. Composition and morphology.....	25
III.D.3. Density.....	28
III.E.4. Conductivity.....	29
IV.B. Electron Energy.....	31
IV.B.1. Height and width.....	32
IV.B.2. Composition and morphology.....	34
IV.B.3. Conductivity.....	35
IV.C. Conclusions.....	36
V. Scan pattern and scan strategy.....	36
V.A. Scan pattern.....	37
V.A.1. Height and width.....	37
V.A.2. Composition and morphology.....	39
V.B. Scan strategy.....	40
V.B.1. Height and width.....	40
V.B.2. Conductivity.....	42
V.C. Scan speed.....	43
V.D. Writing direction.....	44
V.D.1. Height.....	44
V.D.2. Composition and morphology.....	45
V.E. Proximity effects.....	46
V.E.1. Deposit location.....	46
V.E.2. Composition and resistivity.....	50
V.F. Conclusions.....	51
VI. Additional circumstances.....	52
VI.A. During experiments.....	52
VI.A.1. Substrate heating.....	52

---

VI.A.1.a. Height and width .....	52
VI.A.1.b. Composition and morphology.....	54
VI.A.1.c. Conductivity.....	55
VI.A.2. Tilting during deposition.....	55
VI.A.3. Biasing sample during deposition.....	56
VI.B. Post-deposition treatment .....	56
VI.B.1. Extra irradiation .....	56
VI.B.2. Annealing.....	57
VI.B.2.a. Composition .....	57
VI.B.2.b. Conductivity.....	58
VI.C. Conclusions .....	59
VII. Substrate .....	60
VIII. Precursor .....	63
VIII.A. Introduction.....	63
VIII.B. Precursor gas only .....	64
VIII.C. Reactive gases .....	67
VIII.D. Precursor pressure .....	67
VIII.E. Conclusions .....	69
IX. Conclusions.....	70

## I. Introduction

Focused electron beam induced deposition (EBID) is a lithography technique that allows the definition of patterns on a substrate using electron beams. By scanning a focused electron beam over the sample in the presence of a precursor gas, the pattern is defined directly and (in principle) no pre- or postprocessing is required. EBID is mostly performed in electron microscopes, so direct *in situ* inspection of the fabricated structure is very easy. Since electron beams can be focused into spots with diameters varying from micrometers down to sub-Ångstrom level, this direct-write process is suitable for the micro- and nanometer regime. EBID is a technique that is part of the larger family of focused electron beam processes (FEBIP). Apart from EBID, this family also includes, for instance, focused electron beam induced etching (EBIE) and focused electron beam induced heating.

EBID and EBIE are lithography techniques that have been around for many decades now, the first reports on the topic coming from Steward in 1934 [5]. He found contamination growth in his electron optical system. While he considered the deposits as a “very insidious and prevalent source of errors”, something that clearly needed to be avoided, Christy [6] and Baker *et al.* [7] were among the first to see a potentially useful side of the technique and deposited conducting films. In recent years, EBID is a field of growing interest (see Fig. 1).

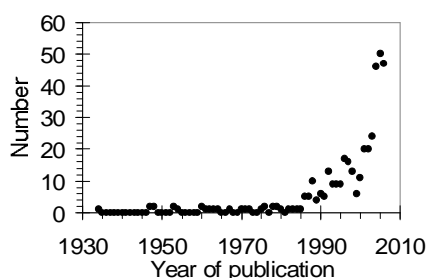


Fig. 1. Number of publications as function of the year of publication. Since the first mention of contamination growth in 1934, FEBIP gained increasing interest since the end of the 1980's.

The precursors used in EBID are contamination (carbon species from the residual gas in the electron optical system), metalorganic precursors (for instance  $W(CO)_6$  or  $Me_3PtCp$ ) or inorganic precursors (for instance  $WF_6$ ). Typical examples of deposits are shown in Fig. 2. One of the major advantages of EBID is that the deposition can be performed on flat (Fig. 2a) as well as topographical surfaces (Fig. 2b). As long as it is possible to focus the electron beam properly on the sample, deposition can be performed. Another advantage is that the fabrication of 3-dimensional structures is possible. Disadvantages are the low growth rates compared to other lithography techniques such as electron beam lithography (EBL), and the deposit composition. The typical deposit created from metalorganic precursors consists of a nanocomposite material: metal crystals of a few nanometers in size embedded in a matrix of amorphous carbon (a-C). See also Fig. 2c. Such deposits contain around 10% metal and the other 90% is carbon and other elements originally contained in the precursor molecule. Inorganic precursors, especially the fluorine-based precursors, tend to yield deposits with higher metal concentrations.

In the course of time, many applications have been developed. A nonexhaustive list is presented in Table I.

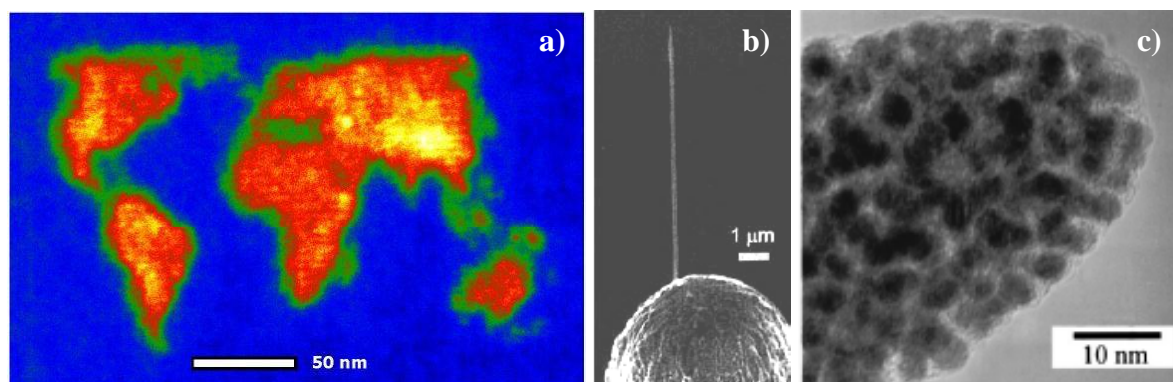


Fig. 2. Typical examples of EBID deposits. (a) A topographical map of the world on a flat substrate. Note the presence of the Himalayas, the Rocky Mountains and the Andes. (b) A tip grown on an STM probe [8]. (c) High resolution TEM image of a typical EBID deposit, showing nanocomposite material (nanometer sized metal crystals in an amorphous carbon matrix) [9].

Table I. Applications that have been developed based on EBID.

Application	References
Probes (functionalized tips for scanning probe microscopy or for local conductivity measurements)	[10], [11], [12], [13], [14], [15], [16], [17], [18]
Conducting or nonconducting joining technique	[19], [20], [21], [22], [23], [24]
Conducting wires	[25], [26], [27], [28]
Mask repair	[29], [30], [31]
Electron sources	[32], [33], [34]
Micro-Hall and micro-SQUID devices	[35], [36]
Nanotweezers and gripping devices	[37], [38]
Nano-optic patterns or photonic crystals	[39], [40]
Entire miniature electron optical systems	[41]
Diodes	[42]
Seeds for nanotube growth	[43]

Despite its long history, detailed knowledge of the process is still very much dispersed. Not only “a plethora of materials” has been studied, as Randolph *et al.* [44] have put it, but the entire collection of publications on FEBIP can be described as a plethora of results. The fact that the process is known under many names, is perfectly illustrating for this unhelpful situation: EBID (electron beam induced deposition), EBIR (electron beam induced resist), EBIM (electron beam induced metal formation), EBAD (electron beam assisted deposition), EBISED (electron beam induced selective etching and deposition), EB-CVD (electron beam

induced chemical vapor deposition), electron beam stimulated deposition, electron beam induced surface reaction, electron beam or e-beam writing, environmental electron beam deposition, electron beam assisted direct-write nanolithography, contamination lithography, additive lithography or 3D deposition lithography.

Since EBID is a very complex phenomenon (as will become clear in the next chapter), it is important to have an overview of all available useful results that is as complete as possible. This is not the first review on EBID: reviews by Silvis-Cividjian *et al.* [45] and Randolph *et al.* [46] have appeared earlier and summarize published results and achievements. It is felt that there is a need for a more critical review, in which it is determined to which extent the available models for the EBID process are valid and complete. To do this, it is important to compare as many results as possible and try to recognize the major trends. This overview is an attempt at such a study. Out of the approximately 400 articles that have appeared on FEBIP, we have selected nearly 200 articles. The results from these articles have been sorted and interpreted as far as possible using a model that is presented. We do not claim to be fully complete, but we have tried to make this overview extensive. Since EBID is the most studied member of the FEBIP family, we restrict ourselves to EBID. For a good review on EBIE, we refer the reader to [46].

This review serves three purposes. (1) To collect and summarize relevant information from available literature. (2) To interpret this information and, where possible, compare to available (qualitative) models. (3) To suggest strategies for further research into EBID.

The setup of the review is as follows. After giving a short introduction in chapter II on the various parameters that are important for the process, we discuss the effect of each of the parameters that can be varied in the EBID process: the electron beam (chapter III), the scan pattern and the scan strategy (chapter IV), additional circumstances, such as heating the substrate during or after deposition (chapter V), the substrate (chapter VI) and finally the precursor (chapter VII). We discuss the reported influence of these parameters on relevant properties of the deposition process and, if possible, we suggest a qualitative model. Conclusions from all described results and an outlook for further work are presented in chapter IX.

## **II. Focused electron beam induced processes in general**

The basic principle of FEBIP is quite simple. Gas molecules (most commonly metalorganic molecules) are adsorbed on a substrate. Under the influence of the electron beam, the precursor molecules are dissociated into volatile and nonvolatile components. Depending on the type of precursor, the nonvolatile components adhere to the substrate and form a deposit (in the case of EBID) or react with the substrate and form volatile species (in the case of EBIE). Hence, a structure is grown (Fig. 3a) or the substrate is etched (Fig. 3b). This beam induced reaction occurs only locally, at or around the irradiated area. We now will go into more detail by describing the most important interactions playing a role in FEBIP.

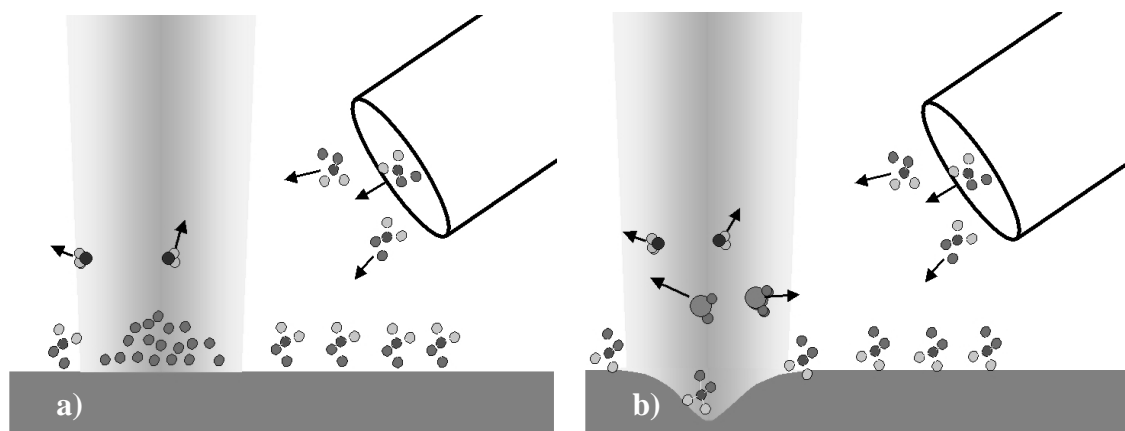


Fig. 3. A schematic drawing of EBID (a) and EBIE (b). Courtesy of I. Utke.

### II.A. Substrate – precursor molecule interaction

The many different interactions complicate matters quite severely. To begin with, there are the interactions between substrate and precursor molecules, such as diffusion, adsorption and desorption. Adsorption of the precursor molecule may occur as chemisorption or physisorption, depending on the combination of precursor, substrate and temperature. The residence time  $\tau$  of the precursor molecule on the substrate also can affect beam induced processes. A longer  $\tau$  gives a higher probability of dissociation by the incoming or emitted electrons. Taking into account that the majority of the FEBIP experiments are done under non-UHV conditions, the precise condition of the vacuum and the substrate surface is generally unknown. Furthermore, as soon as the deposition process starts in the case of EBID, the interface of interest changes from substrate surface to deposit surface. This transition stage is specifically important for the fabrication of the high resolution structures, where the growth is stopped in or soon after the nucleation stage of the deposit.

### II.B. Electron– substrate interaction

Then there are the interactions between electron beam and substrate. At the start of the FEBIP experiment, a beam of electrons (primary electrons, PE's) is focused onto a clean substrate. In a simplified picture, the PE's collide with the solid and are deflected from their original trajectory. If an inelastic collision occurs, part of the initial energy can be transferred from the PE to other electrons in the solid. These electrons will in turn interact with the solid and scatter. The newly generated electrons are called secondary electrons (SE's) if their energy upon leaving the substrate is smaller than 50 eV and backscattered electrons (BSE's) if their energy is larger than 50 eV. The average length these electrons travel between two collisions (the mean free path) is dependent on their energy. As a result of all these collisions, there is a (sort of onion shaped) volume of scattering events in the solid below the irradiated spot (Fig. 4a). The shape and the size of this volume depend on the PE energy and the substrate. From this volume, SE's and BSE's can escape from the substrate and enter into the vacuum. So on the substrate surface, around the irradiated spot, an energy spectrum (Fig. 4b) and a spatial distribution (Fig. 4c) exists of electrons being emitted. Monte Carlo simulations

have been developed to model this process [47, 48, 49, 50]. Precursor molecule dissociation can occur every time an electron crosses the interface between substrate and vacuum.

Matters become more complicated by the fact that the shape and often the composition of the target change during the FEBIP experiment. In the case of EBID for instance, a pillar can grow and the electron scattering volume will become more confined to the pillar as it becomes longer. Electrons (for instance forward scattered electrons, FSE's) can also cross the target-vacuum interface several times (Fig. 4d). As a result of the electron scattering, there is a constant energy transfer from the PE's to the substrate and/or the growing structure, which may lead to electron beam induced heating (EBIH). Furthermore, if the target is electrically nonconducting, a difference between the flux of inbound PE's and outbound SE's and BSE's can lead to charging of the sample. Finally, when the PE energy is around 50 keV or larger, physical sputtering of the target material by the high energy PE's can occur [51]. This is especially relevant for FEBIP experiments in (scanning) transmission electron microscopes ((S)TEMs), where the acceleration voltage is usually 200-300 keV.

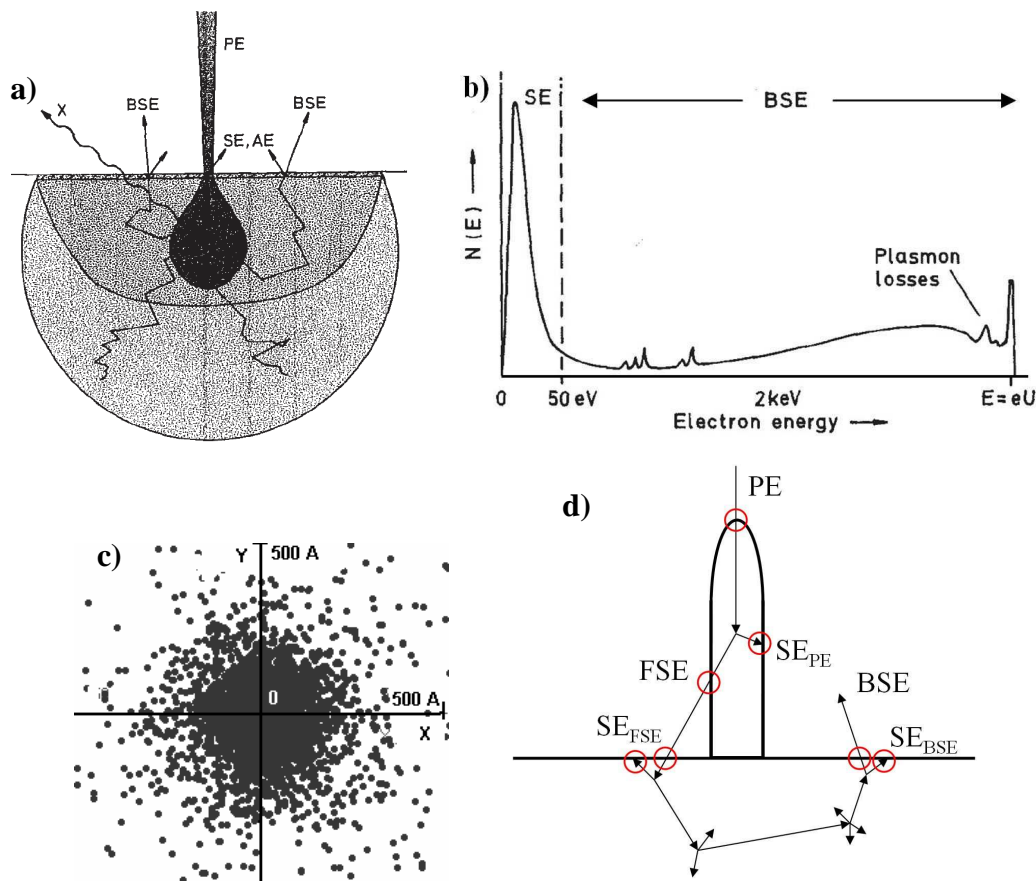


Fig. 4.(a) A schematic drawing of the electron scattering volume in a flat substrate [52]. (b) A typical energy spectrum of electrons emitted from the substrate [52]. The PE energy is equal to  $eU$ . (c) Top view of (simulated) SE emission sites on a flat substrate, showing the spatial distribution [53]. (d) In the case of a growing 3-dimensional deposit, electrons can cross the target-vacuum interface in many different ways. For tips longer than the BSE range, the electron scattering volume will be more confined to the tip.

### II.C. Electron– precursor molecule interaction

Finally, there is the interaction between the electrons and the precursor molecules. Dissociation is the most important one for this review, but electron beam stimulated desorption also can occur. The probability that an electron induces the scission of a bond in a precursor molecule depends on the electron energy and is generally expressed as a cross section  $\sigma_{(E)}$  [ $\text{cm}^2$ ]. The larger the cross section, the larger the probability that a bond in the molecule is broken. The cross section for dissociation of adsorbed molecules is a difficult issue, since it depends on many parameters. It depends for instance on the energy of the bonds within the molecule and is strongly influenced by the environment, the available reaction paths for the dissociation event or even the specific geometry in which the molecule is adsorbed. Studies on the interaction between adsorbed molecules and low energy electrons show that dissociative electron attachment (DEA) and dipolar dissociation (DD) are important processes [54]. Energies as low as a few eV can be sufficient to induce the scission of bonds in precursor molecules, such as for hydrocarbons present on a contaminated sample [55] and hfac-Cu-VTMS [56]. George and Beauchamp [57] used broad area UV irradiation to induce precursor decomposition and found that the yield was primarily dependent on the photoelectron yield of the substrate. There was no deposition when the photon energy was below the photoelectron emission threshold. In Fig. 5a, three cross sections for low-energy electron induced dissociation are plotted for  $\text{Fe}(\text{CO})_5$ . Rowntree reports  $\sigma_{AB}$  and  $\sigma_{BC}$ , cross sections for a two-step dissociation; from the original  $\text{Fe}(\text{CO})_5$  molecule (A) into an intermediate species (B) and from B into the final material that remains after prolonged irradiation (C) [58]. Henderson *et al.* measured  $\sigma_{\text{total}}$ , the total cross section for the dissociation of a monolayer of adsorbed  $\text{Fe}(\text{CO})_5$  [59].

These studies clearly indicate that low-energy electrons (i.e. SE's) are relevant for the deposition process. However, they do not exclude the possibility that electrons with a higher energy can also contribute to EBID growth. This can be for instance by dissociative ionization (DI), which typically has a cross section (measured for molecules in the gas phase) with a peak at around 100 eV and decreases with increasing electron energy [60].

The mentioned dissociation mechanisms (DEA, DD and DI) have cross sections that have their maximum well below 1 keV. One may be tempted to conclude from this that the deposit growth is determined by electrons with energies  $<1$  keV, but that could be premature. In the typical EBID experiment, the current density of  $>1$  keV electrons in the area directly under the PE beam is very high, compared to the current density of low-energy electrons. That means that, although the absolute cross sections for high-energy electrons may be small, the absolute number may be high enough to make their contribution to deposit growth significant (see Fig. 5b). Definite conclusions cannot be drawn, since there is little information on the balance between the contributions of low- and high-energy electrons to the dissociation of adsorbed molecules.

As a result, there is no consensus yet on this particular topic in the field of FEBIP research. The lack of information becomes most evident in the different Monte Carlo simulations that have been developed to model EBID growth. In these simulations, a dissociation cross section has to be assumed. Silvis-Cividjian *et al.* [61] concentrate on the effect of electrons with

energies  $<1$  keV, while Fowlkes *et al.* [62] have taken a more even balance between low- and high-energy electrons. Mitsuishi *et al.* [63] on the other hand used a cross section where the low-energy cut-off was set at 35.5 eV. The three cross sections are plotted in Fig. 5a.

Apart from influencing the growth rates, it is also conceivable that the different dissociation processes (DEA, DD and DI) influence the composition of the deposit. It is possible that the dissociation mechanism determines which fragment of the molecule desorbs after electron impact. Ideally, all carrier groups desorb and only the target material (for instance Fe in the case of  $\text{Fe}(\text{CO})_5$ ) remains in the deposit. In any case, to advance the understanding and modelling of FEBIP, the progress of the study of dissociation processes such as DEA, DD and DI is very important.

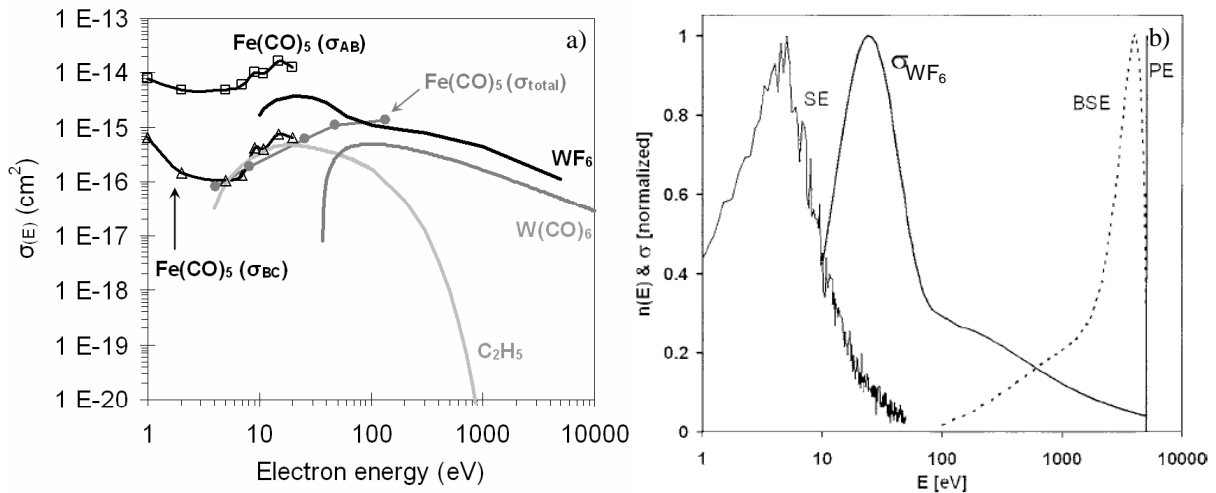


Fig. 5. (a) Measured and estimated cross sections for the dissociation of precursors often used in EBID. Cross sections for  $\text{Fe}(\text{CO})_5$  are reported by Rowntree ( $\sigma_{AB}$  and  $\sigma_{BC}$ ) [58] and Henderson *et al.* ( $\sigma_{total}$ ) [59]. In Monte Carlo simulations, cross section for  $\text{C}_2\text{H}_5$  (Silvis-Cividjian *et al.* [61]),  $\text{WF}_6$  (Fowlkes *et al.* [62]) and  $\text{W}(\text{CO})_6$  (Mitsuishi *et al.* [63]) were used. (b) The simulated energy distribution of SE's and BSE's emitted from a Ge substrate and the estimated cross section for the dissociation of  $\text{WF}_6$  as function of electron energy. All distributions are normalized. From [62].

#### II.D. Interplay between factors

Looking at the 3 types of interactions discussed in the previous paragraphs, it appears that there are a lot of factors involved in the deposition process. One can think of the electron flux, the energy spectrum of the electrons that cross the substrate-vacuum interface, the spatial distribution of electron scattering in the irradiated target, the cross section of the precursor as function of electron energy, precursor adsorption behavior (physisorption, chemisorption), precursor residence time on the substrate, precursor diffusion, (electron stimulated) desorption, electron beam induced heating, the gas flux, the orientation of the precursor source with respect to the deposition location, the deposit or surface geometry, chemical reaction paths that are available, background gas pressure and composition or the thermal and electrical conductance of substrate and deposit. All of these factors act simultaneously and many of them only locally, in or around the irradiated area. The factors are not independent of

each other and, since the shape of the irradiated target evolves during the process, the dependence is not constant. And, as if matters were not complex enough, most of the FEBIP experiments are performed under non-UHV conditions, so often quite a number of factors during the experiment are unknown and/or uncontrolled. The interplay between all these factors can lead to an immense variety of possible phenomena, of which perhaps only a small part has yet been observed and is reported in this overview.

### III. Theoretical model

#### III.A. Basic model

Before discussing experimental results, it is helpful to see what we can expect on the basis of the description of the process given in the previous chapter. A lot of parameters were mentioned and not all of these parameters can be put into a theoretical model straight away. So to study the effect of some of the parameters, we start with a rather simple model similar to that suggested by Scheuer *et al.* [64]. Starting with the precursor molecule coverage  $N$  [ $\text{cm}^{-2}$ ], it will depend on the number of molecules that adsorb from the gas phase, the number of molecules that are decomposed by the electron beam and the number of molecules that desorb to the gas phase. This gives:

$$\frac{dN}{dt} = gF \left( 1 - \frac{N}{N_0} \right) - \sigma_{(E)}NJ - \frac{N}{\tau} \quad (1)$$

with  $g$  the sticking factor,  $F$  [ $\text{cm}^{-2} \text{s}^{-1}$ ] the gas flux arriving at the substrate,  $N_0$  [ $\text{cm}^{-2}$ ] the available adsorption site density in a monolayer,  $J$  [electrons  $\text{s}^{-1} \text{cm}^{-2}$ ] the current density and  $\tau$  the residence time [s] of precursor molecules on the surface. Usually, two simplifications are made. As explained in paragraph II.C, the cross section for dissociation  $\sigma_{(E)}$  is dependent on the electron energy. Since  $\sigma_{(E)}$  is unknown,  $\sigma$  (the integral value of  $\sigma_{(E)}$ ) is used. Furthermore, in reality  $J = J_{PE} + J_{BSE} + J_{SE}$ , where  $J_{PE}$ ,  $J_{BSE}$  and  $J_{SE}$  are the PE, BSE and SE current densities, respectively. Since  $J_{BSE}$  and  $J_{SE}$  are usually not measured during experiments, it is assumed that  $J = J_{PE}$ . A steady state situation for the coverage  $N$  is reached when  $dN/dt = 0$ , which means:

$$N = N_0 \left( \frac{\frac{gF}{N_0}}{\frac{gF}{N_0} + \sigma J + \frac{1}{\tau}} \right) \quad (2)$$

If the growth rate  $R$  [cm/s] is defined as:

$$R = V_{molecule} N \sigma J \quad (3)$$

with  $V_{molecule}$  [ $\text{cm}^3$ ] the volume of a deposited molecule, the combination of equation (2) and (3) gives:

$$R = V_{molecule} N_0 \frac{\left( \frac{gF}{N_0} \right) \sigma J}{\left( \frac{gF}{N_0} + \sigma J + \frac{1}{\tau} \right)} \quad (4)$$

### III.B. Electron- and precursor-limited regimes

We will now look at two simplified cases that give us insight in the deposition process. For simplicity, desorption is ignored. Two distinguishing regimes can be defined,  $(gF/N_0) \gg \sigma J$  and  $(gF/N_0) \ll \sigma J$ . This reduces equation (4) to:

$$(gF/N_0) \gg \sigma J : \quad R = V_{molecule} N_0 \sigma J \quad (5)$$

$$(gF/N_0) \ll \sigma J : \quad R = V_{molecule} gF \quad (6)$$

In the first regime, the growth is limited by the current density and has become independent of the gas flux. This is defined as the electron-limited regime. In the second regime, the growth is limited by the number of molecules arriving at the irradiated area and has become independent of the current density. This is defined as the precursor-limited regime. The effect of the two different regimes can be large. For a constant area, a change in  $J$  is a change in the time-scale at which a specific number of electrons is supplied. This affects not only  $R$ , but it can also affect other deposit properties. The ratio of electrons per deposited molecule can change dramatically, which can give different degrees of fragmentation.

Practical reasons for measuring the growth rate are for instance to determine the rate of contamination growth in an electron optical system, to find suitable growth conditions for the fabrication of applications or to study fundamental aspects of the deposition process. We will see in the next chapter that measurements of the growth rate are presented in different ways in literature. Different units are used: some authors report  $V_{deposit}$  [ $\text{nm}^3$ ], some report  $R$  [ $\text{nm/s}$ ] and some report the deposit height  $h$  [ $\text{nm}$ ]. This is measured as function of  $J$ , beam current  $I$  [electrons  $\text{s}^{-1}$ ] or the accumulated charge  $Q$  [C]. The relations are:

$$V_{deposit} = R t_{dwell} A_{deposit} \quad (7)$$

$$h = R t_{dwell} \quad (8)$$

$$I = J A_{beam} \quad (9)$$

$$Q = I t_{dwell} \quad (10)$$

with  $t_{dwell}$  [s] the dwell time,  $A_{deposit}$  [ $\text{cm}^2$ ] the area of the deposit and  $A_{beam}$  [ $\text{cm}^2$ ] the area of the electron beam.

The various ways results are presented, complicate the comparison of results from the different sources. Another complicating matter is that in (nearly) every electron optical system, the beam diameter ( $d_{beam}$ ) changes when  $I$  is changed. A change in  $d_{beam}$  will affect  $R$  (if deposition is done in spot-mode), because  $d_{deposit}$  will change accordingly. If  $V_{deposit}$  is kept constant and  $d_{deposit}$  decreases,  $R$  becomes higher. In many cases,  $d_{beam}$  or  $d_{deposit}$  are not measured or reported, in which case it is not clear how  $R$  or  $h$  should be interpreted precisely. To avoid this complication for cases where only  $I$  is reported, we restrict ourselves to measurements of  $V_{deposit}$  as function of  $I$ . This complication is absent for measurements where  $h$  was reported as function of  $J$ , because both parameters are expressed per area ( $h = V_{deposit}/A_{deposit}$  and  $J = I/A_{beam}$ ).

It was mentioned in the previous paragraph that the growth regimes can be of significant influence. It is interesting to see how the two regimes can be recognized in the various representations we have just discussed. The electron-limited (e.l.) and precursor-limited (p.l.) regimes are indicated in Fig. 6. At low current densities,  $(gF/N_0) \gg \sigma J$  and  $h$  is linearly dependent on  $J$  (according to equation 5). At high current densities,  $(gF/N_0) \ll \sigma J$  and  $h$

becomes independent of  $J$  (according to equation 6). The same behavior is observed when  $V_{deposit}$  is used instead of  $h$ , except for the scaling with  $d_{deposit}$ .

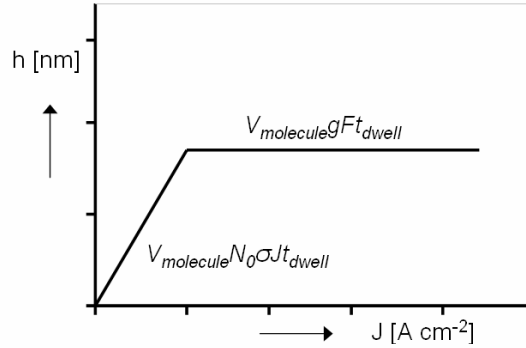


Fig. 6. Schematic drawing of the deposit height  $h$  as function of the  $J$ .

Alternatively,  $h$  can be plotted as function of  $Q$ . According to equation 9, there are 2 ways to do this: either vary  $J$  (or  $I$ ) and keep  $t_{dwell}$  constant, or vary  $t_{dwell}$  and keep  $J$  (or  $I$ ) constant. Both cases are shown in Fig. 7. The first case, where  $J$  (or  $I$ ) is varied (Fig. 7a), is the same situation as in Fig. 6. The second case, where  $t_{dwell}$  is varied, the electron and precursor-limited regimes are characterized merely by a different slope (Fig. 7b).

Yet another representation of the deposit growth behavior is a plot of  $h$  as function of  $t_{dwell}$ , for a constant  $I$  (see Fig. 7c). This is basically the same data as shown in Fig. 7b, and both plots can be made for the same experiment. The difference is that in Fig. 7c the time scale is made visible. Similarly, the growth regime cannot be easily distinguished in the plot of  $h$  versus  $Q$ , since the regimes are again characterized merely by a different slope.

The measurements of the deposited amount of material as function of the growth conditions allow for a determination of the growth efficiency. This can be defined as the increase in  $h$  per PE [nm/electron]. From the definition of the 2 regimes, it becomes clear that the growth efficiency is highest in the electron-limited regime and lowest in the precursor-limited regime.

### III.C. Temperature

The simplifications made in the previous paragraph are not allowed when the effect of desorption cannot be ignored. This is for instance the case when the temperature is varied to study the effect on the growth rate, composition or conductivity, or where the temperature is not constant during the deposition process. In these cases, the temperature will influence the residence time of molecules on the substrate. The relation between  $\tau$  and temperature can be expressed by:

$$\tau = (1/\nu) \exp(E_{des}/kT) \quad (11)$$

where  $\nu$  is the vibrational frequency of an adsorbed molecule [s<sup>-1</sup>],  $E_{des}$  is the desorption energy [J],  $k$  is the Boltzmann constant [m<sup>2</sup> kg s<sup>-2</sup> K<sup>-1</sup>] and  $T$  is the temperature [K]. Qualitatively speaking, equation (11) shows that as the temperature increases,  $\tau$  will decrease. In equation (4), a decrease in  $\tau$  will lead to a decrease of  $R$ . So as the temperature increases, the growth rate will decrease.

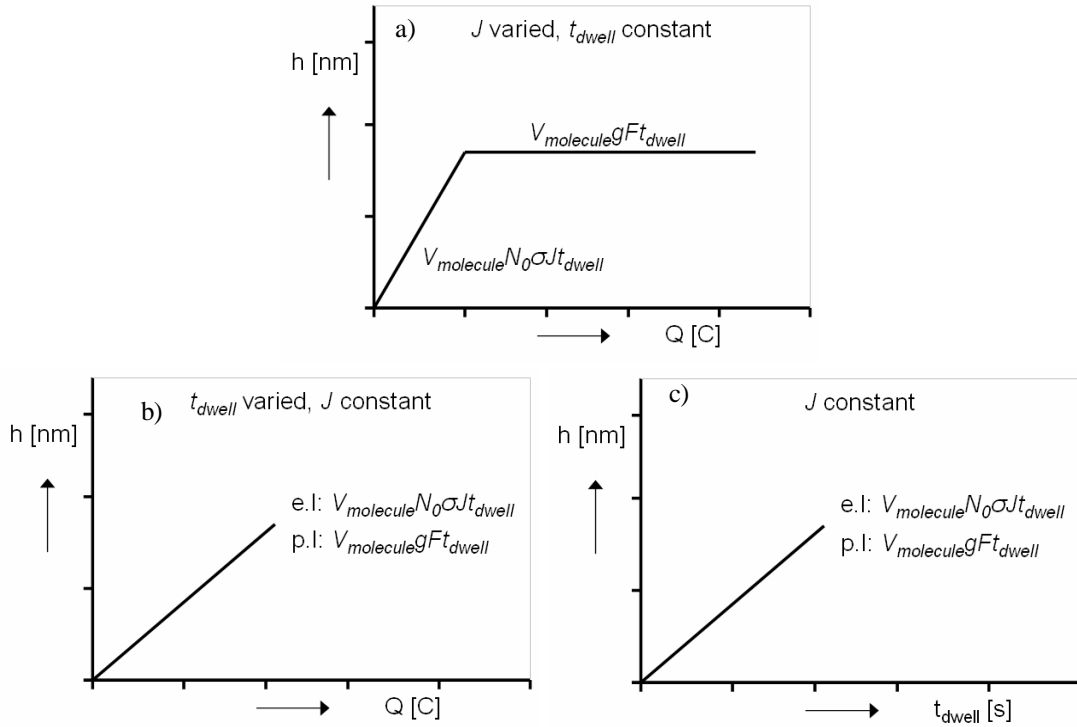


Fig. 7. Schematic drawing of the deposit height  $h$  as function of  $Q$ . The electron-limited (e.l.) and precursor-limited (p.l.) regimes are indicated. (a) Behavior where  $J$  (or  $I$ ) is varied and  $t_{dwell}$  is kept constant. (b) Behavior where  $t_{dwell}$  is varied and  $J$  (or  $I$ ) is kept constant. (c) Same as (b), but now as function of  $t_{dwell}$ .

How the temperature affects the growth rate quantitatively cannot be established that easily. A situation where the growth is either electron- or precursor-limited can still be obtained, but the conditions under which this occurs are less straightforward to estimate.

## IV. Beam parameters

### IV.A. Current density

#### IV.A.1. Height

Now that we have a (simple) growth model and know how to interpret it, we can discuss results from literature. In Fig. 8a, b and c  $h$  as function of  $J$  is plotted for 5 different experiments. The data is shown in 3 different graphs to present the different orders of magnitude and yet still use linear scales. Linear behavior is found for deposition with  $\text{Pt}(\text{PF}_3)_4$  and  $\text{Os}_3(\text{CO})_{12}$ , while for  $\text{Ru}_3(\text{CO})_{12}$ , diffusion pump oil and  $\text{SiH}_2\text{Cl}_2$  the  $h$  saturates with increasing  $J$ . Based on the model discussed in the previous chapter, this means an electron-limited regime was found for  $\text{Pt}(\text{PF}_3)_4$  and  $\text{Os}_3(\text{CO})_{12}$ , and a precursor-limited regime was found for  $\text{Ru}_3(\text{CO})_{12}$ , diffusion pump oil and  $\text{SiH}_2\text{Cl}_2$ . The different results can be explained quantitatively to a (relatively) large extent. For instance, based on the results for  $\text{Ru}_3(\text{CO})_{12}$  where growth was precursor-limited, one would expect that growth was precursor-limited for  $\text{Pt}(\text{PF}_3)_4$  too, because  $J$  was largest in the latter case. However, the opposite is true. This can be explained by differences in  $\sigma_{(E)}$  and  $F$ . The amount of electrons needed for the dissociation of 1  $\text{Pt}(\text{PF}_3)_4$  molecule is estimated at  $1.8 \times 10^3$  [65] and for  $\text{Ru}_3(\text{CO})_{12}$  this was about 280

of 1  $\text{Pt}(\text{PF}_3)_4$  molecule is estimated at  $1.8 \times 10^3$  [65] and for  $\text{Ru}_3(\text{CO})_{12}$  this was about 280 [64]. The gas flux in the experiment with  $\text{Pt}(\text{PF}_3)_4$  was larger than in the experiment with  $\text{Ru}_3(\text{CO})_{12}$  ( $1 \times 10^{16}$  vs.  $3 \times 10^{14}$  molecules  $\text{cm}^{-2} \text{s}^{-1}$ ). These two differences explain the two growth regimes. For the experiment with diffusion pump oil, the precursor-limited regime can be explained by the limited  $F$  (about  $5 \times 10^{11}$  molecules  $\text{cm}^{-2} \text{s}^{-1}$ ). In the experiment with  $\text{SiH}_2\text{Cl}_2$  a significantly larger precursor flux was used (in the order of  $10^{16}$  molecules  $\text{cm}^{-2} \text{s}^{-1}$ ) [66], but due to the fact that  $J$  was a factor of  $10^5$  times larger than for the other experiments, growth was still precursor-limited. The only case for which a quantitative explanation is difficult to give, is  $\text{Os}_3(\text{CO})_{12}$ . For  $\text{Os}_3(\text{CO})_{12}$ ,  $h$  was higher (see Fig. 8c) and  $F$  was lower than for  $\text{Ru}_3(\text{CO})_{12}$  [64], but the growth was still in the electron-limited regime. The higher  $h$  indicates that either  $\sigma_{(E)}$  or  $N$  was larger. If  $F$  was lower,  $N$  can only be larger if the sticking coefficient was higher. One would expect that both a higher  $\sigma_{(E)}$  and a higher sticking coefficient would lead to a precursor-limited regime, but the linear dependency on current density indicates that the growth is electron-limited. An explanation is not given by the authors.

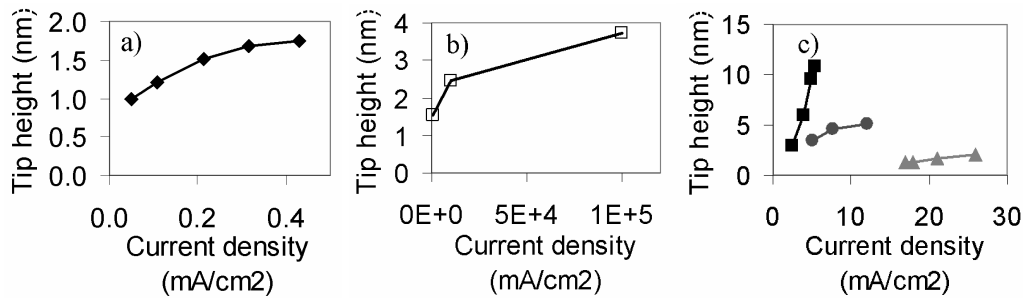


Fig. 8. Tip height as function of the current density. Data is plotted in 3 graphs to present the different orders of magnitude and yet still use linear scales.

◆	Diffusion pump oil	Christy	[6]
□	$\text{SiH}_2\text{Cl}_2$	Ichihashi et al.	[66]
■	$\text{Os}_3(\text{CO})_{12}$	Scheuer et al.	[64]
●	$\text{Ru}_3(\text{CO})_{12}$	Scheuer et al.	[64]
▲	$\text{Pt}(\text{PF}_3)_4$	Wang et al.	[65]

Measurements of  $V_{\text{deposit}}$  as function of  $I$  are shown in Fig. 9a and b. For all data points  $t_{\text{dwell}}$  was 120 s. For the experiment with TEOS (■) [39] two things can be noticed for the change from 20 to 100 pA: (1)  $V_{\text{deposit}}$  is larger at 100 pA than at 20 pA and (2)  $V_{\text{deposit}}$  saturates. This indicates that the growth regime changes from electron-limited to precursor-limited between 20 and 100 pA. The same behavior, except now in a more extreme form, is observed for the deposition with  $\text{Me}_2\text{-Au-acac}$  (●) [19]. The increase in  $V_{\text{deposit}}$  is roughly linear for beam currents of about 2 pA to 200 pA, which indicates the electron-limited regime. When a significantly larger amount of electrons (beam current of 6 nA instead of 200 pA) is supplied in the same time span,  $V_{\text{deposit}}$  saturates. This indicates the precursor-limited regime.

Entirely different behavior is observed for the experiment with contamination (▲) [13]. For low beam currents (between 3 and 30 pA)  $V_{\text{deposit}}$  increases roughly linear with increasing  $I$ . But when  $I$  is increased above 30 pA (up to 200 pA),  $V_{\text{deposit}}$  decreases. Similar behavior was

found for contamination growth for beam currents  $>25$  pA by Miura *et al.* [42] (not shown because the dwell times used were not reported). A decrease in  $V_{deposit}$  does not mean that material was removed from a deposit, but that less material was deposited in the same dwell time.  $F$  was constant during the entire experiment, so the number of molecules arriving at the irradiated area was also constant. The decrease in  $V_{deposit}$  could be the result of a decrease in  $V_{molecule}$  at higher beam currents. Extrapolating  $R$  from low  $I$  (i.e. from the electron-limited regime) to 200 pA, this would be a decrease in  $V_{molecule}$  in the order of  $10^3$ . Such a strong decrease is not very likely. So this decrease cannot be explained anymore with the simplified model we used to describe the electron- and precursor-limited regime and we must turn to the more complicated model that includes the residence time  $\tau$ . As mentioned in paragraph III.C, a decrease in  $\tau$  will lead to a decrease in  $R$  and therefore in  $V_{deposit}$ .

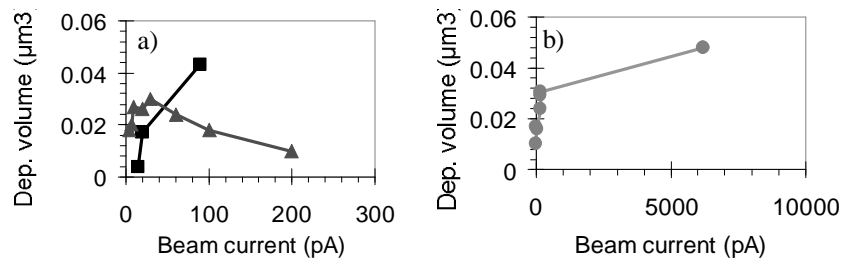


Fig. 9. Deposited volume as function of beam current. The dwell time was 120 s in all cases.

- |   |                          |                        |      |
|---|--------------------------|------------------------|------|
| ▲ | Contamination            | Schiffmann             | [13] |
| ■ | TEOS                     | Perentes <i>et al.</i> | [39] |
| ● | Me <sub>2</sub> -Au-acac | Molhave <i>et al.</i>  | [19] |

If all other conditions are kept constant during the experiment, a decrease in  $\tau$  can only be the result of an increase in temperature. This can be caused by electron beam induced heating (EBIH). EBIH is the result of energy transfer from the PE's to phonons in the substrate. The theoretical power  $P$  that is supplied by the electron beam to an irradiated target is:

$$P = V_{PE} \times I \quad (2)$$

with  $V_{PE}$  the acceleration voltage and  $I$  the beam current. In practice, the effect of this power input on the target temperature will depend on the amount of energy that is actually transferred (for instance BSE's or SE's emitted from the target do not transfer their energy) and on the heat dissipation from irradiated area to bulk. If the heat dissipation is larger than the power input, the temperature will not be affected. But if the heat dissipation is less, the temperature will rise. There is some disagreement on the question whether EBIH plays a significant role in EBID. Based on calculations, Li *et al.* [67] assume that EBIH has a negligible effect. Folch *et al.* [68] come to the same conclusion based on experimental data. However, Bret *et al.* [69], Randolph *et al.* [44] and Utke *et al.* [70] assume that the increase in temperature can be as much as 60 - 80 °C for tip depositions. And the sharp decrease in growth efficiency for contamination in Fig. 9a (▲) is certainly consistent with the behavior that is expected when there is significant EBIH.

Until now we have discussed measurements of  $h$  as function of  $J$  (Fig. 8) and  $V_{deposit}$  as function of  $I$  (Fig. 9). The growth of deposits is often characterized by measuring  $h$  as function of  $Q$  or  $t_{dwell}$ . In practice, this is the same measurement. As mentioned in paragraph III.B, the 2 plots give a different picture. Results from literature for the growth of tips are shown in Fig. 10 on a log-log scale ( $h$  versus  $Q$  in Fig. 10a,  $h$  versus  $t_{dwell}$  in Fig. 10b). There is not sufficient information available to explain the trends in Fig. 10 completely. It is also difficult to compare results obtained with different precursors. With information that is available, we will try to explain 2 trends. First of all, Fig. 10a shows that tips fabricated from  $\text{Me}_2\text{-Au-acac}$  ( $\blacktriangle$ ) and  $\text{Me}_2\text{-Au-tfac}$  ( $\bullet$ ) were grown to the same height, but the  $Q$  required to obtain that height differs by 2 orders of magnitude. On the other hand, Fig. 10b shows that the same height was obtained in practically the same time span. Considering the chemical similarity of the precursors, it is expected that  $\sigma_{(E)}$  and  $V_{molecule}$  are similar. The gas flux was reported in different units ( $\text{Pa l s}^{-1}$  versus  $\text{Pa}$ ), so  $F$  cannot be compared. However,  $I$  is known for both experiments. In the experiment with  $\text{Me}_2\text{-Au-acac}$  a beam current of 60 pA was used, versus a beam current of 10 nA for the experiment with  $\text{Me}_2\text{-Au-tfac}$ . Since the same  $h$  was obtained in the same  $t_{dwell}$ , this must mean that  $I$  was not the determining factor for the tip grown from  $\text{Me}_2\text{-Au-tfac}$ . In other words, the experiment with  $\text{Me}_2\text{-Au-tfac}$  was precursor-limited and a large part of the electrons was simply wasted, speaking from the point of view of growth efficiency.

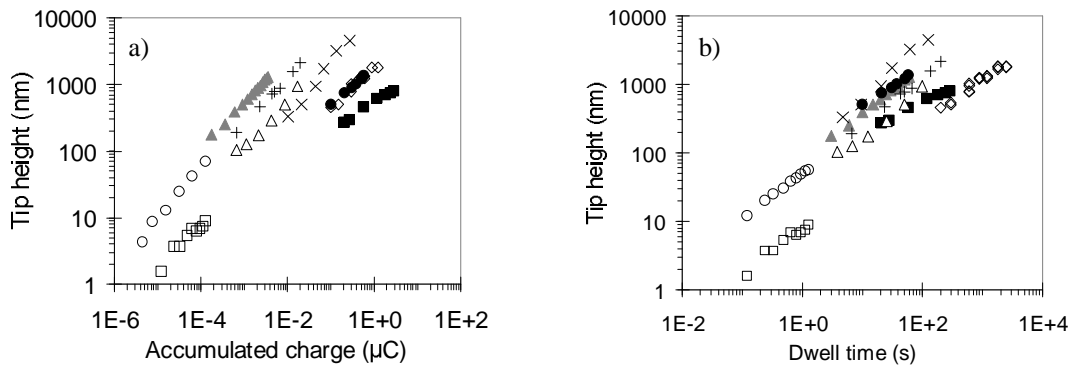


Fig. 10. (a) Deposit height as function of accumulated charge. (b) Same data, now as function of dwell time.

$\blacktriangle$	$\text{Me}_2\text{-Au-acac}$	<i>Koops et al.</i>	[71]
$\bullet$	$\text{Me}_2\text{-Au-tfac}$	<i>Koops et al.</i>	[29]
$\blacksquare$	$\text{W}(\text{CO})_6$	<i>Koops et al.</i>	[29]
+	$\text{W}(\text{CO})_6$	<i>Kohlmann et al.</i>	[72]
$\diamond$	$\text{W}(\text{CO})_6$	<i>Liu et al.</i>	[73]
$\triangle$	$\text{CpPt Me}_3$	<i>Hübner et al.</i>	[74]
x	$\text{Co}_2\text{CO}_8$	<i>Lau et al.</i>	[12]
$\circ$	$\text{WF}_6$	<i>Hiroshima and Komuro</i>	[75]
$\square$	Contamination	<i>Hiroshima and Komuro</i>	[75]

Something similar can be said for the deposition with  $W(CO)_6$ . PE energies used for the deposition were 20 keV (Kohlmann *et al.* (+)), 25 keV (Koops *et al.* (■)) and 200 keV (Liu *et al.* (◇)). The gas flux can again not be compared (no numbers are given or different units are used). The only information available is the beam current. Kohlmann *et al.* have used the lowest  $I$ , 100 pA, and have the highest growth efficiency [nm/C]. The beam current in the experiment by Koops *et al.* was 10 nA. Compared to Kohlmann *et al.*, this resulted in a growth efficiency of about 500 times smaller (Fig. 10a), while the  $t_{dwell}$  to reach the same  $h$  was only about 5 times longer (Fig. 10b). The difference of a factor of 100 is a strong indication that the experiment by Koops *et al.* was precursor-limited. Liu *et al.* (◇) used a beam current of 0.5 nA. Compared to the experiment by Kohlmann *et al.*, the growth efficiency is a factor of 50 times smaller and it took about 10 times longer to reach the same  $h$ . This leaves a factor of 5 to be explained. Possibly, the difference is due to the higher PE energy, growth was precursor-limited or  $V_{molecule}$  decreased during the deposition. Data from different diagrams can be combined. Enough information is available from the articles to compare results from Fig. 9 and Fig. 10a. This is done in Fig. 11. A comparison with Fig. 10b is not possible, because the data in Fig. 9 was obtained by keeping  $t_{dwell}$  constant. When trying to compare the data in Fig. 11, we have to keep in mind that the time-dependence is different for both types of data. The measurements from Fig. 9 (shown in black in Fig. 11) were obtained by varying the  $I$  for a constant  $t_{dwell}$ , while the measurements from Fig. 10 (shown in grey in Fig. 11) were obtained by varying  $t_{dwell}$  for a constant  $I$ . So when a black curve has a negative slope (such as for instance for contamination (▲) or for  $Me_2$ -Au-acac (●)), it does not mean that material was removed, but it means that  $h$  decreased when  $I$  was increased for a constant  $t_{dwell}$ . From the negative slopes, it is observed that the growth regimes in the experiments where  $I$  was varied (black curves), were all precursor-limited at the highest beam currents.

#### IV.B.2. Width

Concerning the lateral growth, it is consistently reported that increasing  $I$  leads to an increase in  $d_{deposit}$  [19, 42, 72, 78], with  $d_{deposit}$  increasing proportional to  $\sqrt{I}$  [19, 72]. However, as mentioned in paragraph III.B,  $d_{beam}$  also increases with  $I$ , also proportional to  $\sqrt{I}$  (to a first approximation). This implies that  $d_{deposit}$  depends on  $d_{beam}$  rather than on  $I$ . This is confirmed by Beaulieu *et al.* [78], who report that the lateral growth rate is independent of  $I$ .

Not only is  $d_{deposit}$  dependent on  $d_{beam}$ , there is also a distinct dependence on  $Q$ . To keep matters simple, we consider the growth of tips (by keeping the beam in a stationary position on the sample). It is consistently measured that (1) the  $d_{deposit}$  increases with increasing  $d_{beam}$  and (2) the development of  $d_{deposit}$  as function of  $t_{dwell}$  consists of a fast increase, followed by saturation [72, 10, 76, 13, 77, 78]. Experimental results are shown in Fig. 12a, the inset shows a blow-up of the very early growth stage. A similar trend was found by Mitsuishi *et al.* [79] and Liu *et al.* [73] (not shown). The deposit diameter is always larger than the primary electron beam diameter.

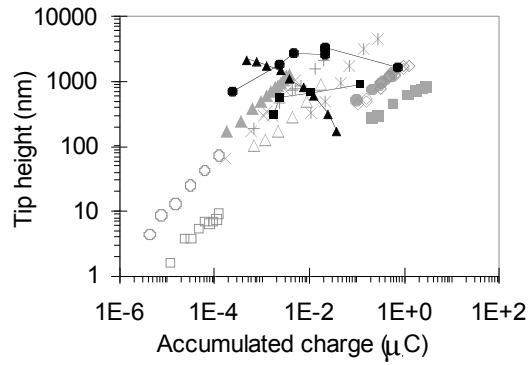


Fig. 11. Data from Fig. 9 and b superimposed on Fig. 10a to compare the effect of beam current and dwell time.

▲	$Me_2-Au-acac$	Koops <i>et al.</i>	[71]
●	$Me_2-Au-tfac$	Koops <i>et al.</i>	[29]
■	$W(CO)_6$	Koops <i>et al.</i>	[29]
+	$W(CO)_6$ (20kV)	Kohlmann <i>et al.</i>	[72]
◇	$W(CO)_6$	Liu <i>et al.</i>	[73]
△	$CpPtMe_3$	Hübner <i>et al.</i>	[74]
×	$Co_2CO_8$	Lau <i>et al.</i>	[12]
○	$WF_6$	Hiroshima and Komuro	[75]
□	Contamination	Hiroshima and Komuro	[75]
▲	Contamination	Schiffmann	[13]
■	TEOS	Perentes <i>et al.</i>	[39]
●	$Me_2-Au-acac$	Mølhav <i>et al.</i>	[19]

A model for this lateral broadening of tips was suggested by Silvis-Cividjian *et al.* [61]. At the start of the deposition process, the electron beam is focused on a fixed spot on a flat surface. SE's are being emitted from the substrate around the irradiated point and dissociate adsorbed precursor molecules. As the deposit starts to grow, SE's continue to be emitted from the substrate, but emission from the deposit itself will also occur. The electrons exit from all sides of the deposit and cause deposition on all sides of it. Since the SE's have a certain escape length, deposition can occur outside the trajectories of the PE's. This is the initial growth stage where  $d_{deposit}$  increases rapidly. Once  $d_{deposit}$  is about equal to the  $d_{beam}$  plus twice the SE escape length, the lateral growth stops. Fig. 12b shows a typical result from a Monte Carlo simulation. The lines indicate the time evolution of the cross-sectional tip profiles.

In paragraph II.C., we have seen that it is not clear what the relative contribution of the PE's, BSE's and SE's is to the growth. The results of the model by Silvis-Cividjian, which takes into account only dissociation by SE's, are qualitatively consistent with the experimentally observed lateral growth behavior. In the Monte Carlo simulation by Fowlkes *et al.* [62], a dissociation cross section was used that also takes into account the contribution of PE's and BSE's. Analysis of tip growth behavior showed that the vertical growth is due mostly to direct dissociation by PE's and the lateral growth is due mostly to SE's. As the tip grows longer, its sidewall surface area becomes larger and the amount of SE's that cross the

substrate-vacuum interface (and contribute to the lateral growth) increases. So although the real cross section for dissociation is unknown, it seems reasonable to assume that the lateral broadening is due mostly to dissociation by SE's.

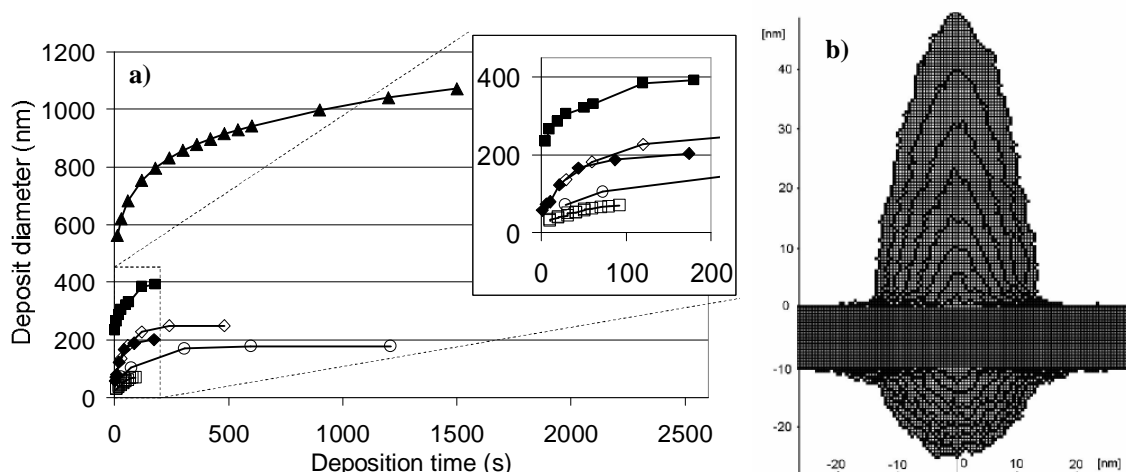


Fig. 12. The development of the width of an EBID structure. (a) Experimental results. Inset shows the width development for short times. (b) Result from a Monte Carlo simulation. The lines indicate the time evolution of the cross-sectional profiles [61].

▲	MeCpPtMe <sub>3</sub>	Beaulieu et al.	[78]
○	TEOS	Perentes et al.	[39]
■	W(CO) <sub>6</sub>	Kohlmann et al.	[72]
□	Fe(CO) <sub>5</sub>	Shimojo et al.	[77]
◆	CpPtMe <sub>3</sub>	Hübner et al.	[74]
◇	Contamination	Schiffmann	[13]

Deposits with a small width can be fabricated by using a small beam and stopping the deposition process before lateral widening occurs. In that case, a dot is deposited instead of a high aspect ratio tip. Stopping the growth process in its initial stage influences also the height of the deposits, so in this regime it is not possible to control the aspect ratio independently of the width of the deposit merely with the accumulated charge. Sub-10 nm structures have been fabricated with widths of 8 nm [80, 81], 5 nm [82], 4 nm [83], 3.5 nm [84], 1.5 nm [85] and even 1.0 nm [86]. While for large deposits the deposited mass is identical every time the experiment is repeated, a significant variation in mass is found for the very smallest deposits. Van Dorp *et al.* [87] have deposited arrays of sub-5 nm dots on an a-C substrate with a constant dwell time per array. A typical array is shown in Fig. 13a (an annular dark field image obtained in a STEM). It is observed that the intensity of the dots (= proportional to the deposited mass) is not constant over the array; some of the dots are very bright while other dots are barely visible. When the average deposit mass is determined for each array, a linear dependency on the dwell time is found (Fig. 13b). In Fig. 13c, the distribution of deposited masses is shown for these arrays. The scaling of the arbitrary units for the deposited mass is identical for Fig. 13b and c. Negative values are the result of background subtractions used to determine the deposited mass from the STEM images. As the dwell time decreases, the width

of the distribution of masses increases (relative to the average deposited mass) and the distributions become skewed. This is behavior that is consistent with Poisson statistics. Poisson theory describes the probability that an event occurs during a particular interval, given an expected number of discrete occurrences. In other words, these experiments suggest that the deposition process consists of discrete dissociation events and this becomes visible during the nucleation stage of a deposit.

The difficulty with these high resolution experiments is that the precise experimental conditions are not well known, especially since deposition is done under non-UHV conditions ( $10^{-3}$  mbar). For the micrometer-sized tips we discussed earlier this is less relevant, since for nearly the entire growth process the deposit surface is the determining factor, not the substrate surface. For the high resolution experiments, the growth is terminated in the nucleation stage and the substrate surface and its chemical condition play a major role.

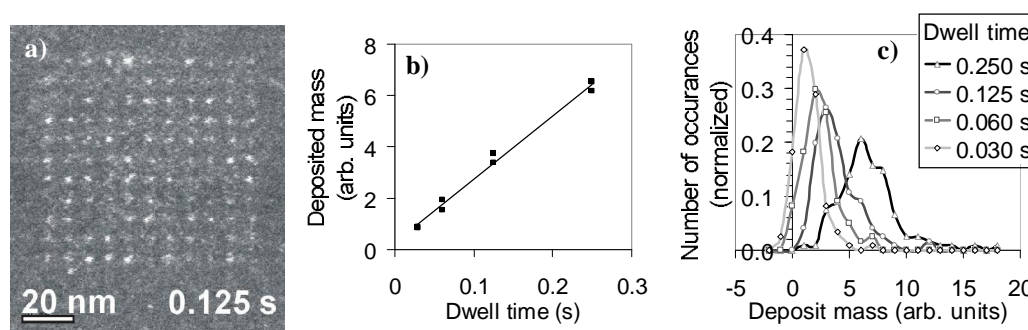


Fig. 13. (a) ADF image of an array of sub-5 nm dots. Although the dwell time was constant (0.125 s) for all the dots in the array, it is observed that the dot intensity (= proportional to the deposited mass) is not constant. (b) The average mass per array as function of dwell time. (c) The distribution of masses for the different dwell times. The scaling of the arbitrary units for the deposited mass is identical for (b) and (c).

#### IV.C.3. Composition and morphology

For nearly all experiments with metal containing precursors, the metal content increases with increasing beam current. Results for  $\text{Mo}(\text{CO})_6$ ,  $\text{CpPtMe}_3$  and  $\text{Me}_2\text{-Au-tfac}$  [88, 89, 90, 33] and  $\text{Co}_2\text{CO}_8$  [11] are shown in Fig. 14. The metal content for deposits of  $\text{Me}_2\text{-Au-acac}$  and  $\text{Me}_2\text{-Au-hfac}$  show a similar dependency on beam current as  $\text{Me}_2\text{-Au-tfac}$  [33]. An increase of the Co content with beam current was also reported by [12].

The increase of the metal content with beam current that is observed in Fig. 14 can be due to two parallel processes. First of all, with an increase in beam current, the time frame in which the deposit is exposed to a specific amount of accumulated charge decreases. As we have seen earlier, this can lead to a shift from electron-limited to precursor-limited regime. Related to this, the increase in beam current can induce an increase in the desorption of fragments of (initially only partially dissociated) precursor molecules. This can lead to higher concentrations of nonvolatile (amongst others metal) components in the final deposit. Another mechanism is EBIIH. As we have seen in the previous paragraph, there are indications that EBIIH can lead to a significant rise in temperature for tip depositions. A raise in temperature

may for instance facilitate the desorption of volatile species, as well as change the dissociation mechanism. We will discuss this in more detail below, where we present the dependence of the deposit morphology on the beam current.

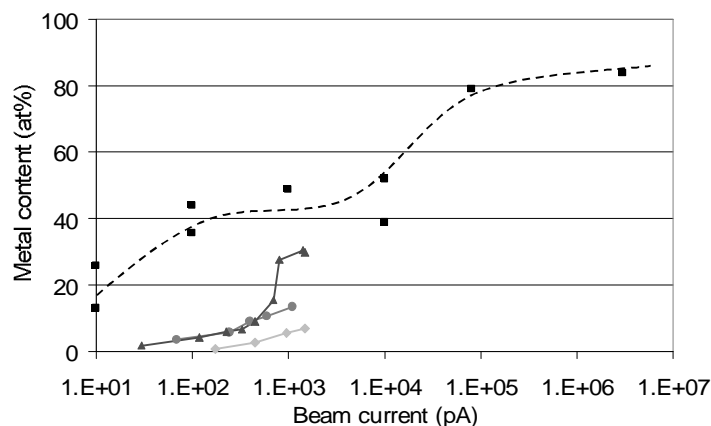


Fig. 14. The metal content as function of the beam current. Lines are drawn to guide the eye.

■	$\text{Co}_2(\text{CO})_8$	Utke et al.	[11]
▲	$\text{Me}_2\text{-Au-tcac}$	Weber et al.	[33]
●	$\text{CpPtMe}_3$	Weber et al.	[90]
◆	$\text{Mo}(\text{CO})_6$	Weber et al.	[90]

The morphology of tips can clearly be affected by the beam current. It is reported for tips deposited from  $\text{Me}_2\text{-Au-acac}$ ,  $\text{Me}_2\text{-Au-tfac}$ ,  $\text{Me}_2\text{-Au-hfac}$ ,  $\text{Cu}(\text{hfac})_2$ ,  $\text{Mo}(\text{CO})_6$  and  $\text{CpPtMe}_3$  that at low beam currents, the tips have a smooth shank and are completely amorphous. In contrast, tips deposited with high beam currents have an irregular shape and are polycrystalline, the crystallites being between 2 and 8 nm in size [90]. The transition between the two regimes was for instance for  $\text{Au}(\text{CH}_3)_2\text{-tfac}$  around 60 pA. An example of the roughening of the Mo tip surface is shown in Fig. 15a. Similar surface roughening was also observed for  $\text{hfac-Cu-VMTS}$  [91] (Fig. 15b) and in a more extreme form for  $[\text{Co}(\text{CO}_3)\text{NO}]$ , (Fig. 15c, [12]) and  $\text{Co}_2\text{CO}_8$  (Fig. 15d, [11]). Please note that all deposits in Fig. 15 were created with the beam in spot-mode.

In an elaborate study, the development of the morphology during the growth of tips deposited from  $\text{Co}_2(\text{CO})_8$  was determined and was found to be quite complex [92]. At low beam currents (20 and 112 pA) the surface of the tips is smooth surface and the material consists of nano-composite material (1-2 nm Co crystals embedded in an amorphous C and O rich matrix). The surface of the longer tips (dwell times of 300 to 600 s) is still smooth, but on the inside a crust and core forms at the bottom of the tips. This sub-structure of crust and core becomes more apparent for deposits from higher beam currents (1.1 and 10 nA), where it extends along the entire length of the tip (see Fig. 16). The crust, consisting of Co crystals, surrounds the nano-composite core. When the beam current is increased further to 82 nA, the core/crust structure is absent and only Co rich crystalline material is found. When the beam current is finally increased to 3  $\mu\text{A}$ , the surface becomes rough and the deposit consists of crystals of micrometer length growing in a whisker-like shape towards the precursor source (see Fig. 15d).

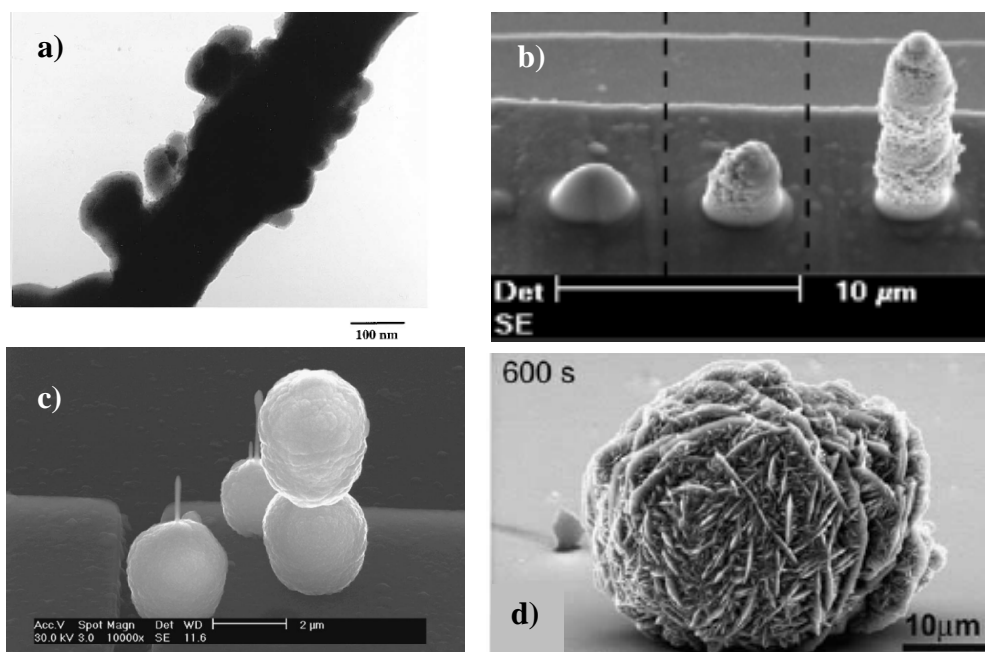


Fig. 15. Surface morphologies for high current deposits created with the beam in spot mode. Deposits from (a)  $\text{Mo}(\text{CO})_6$  [90], (b) HFA-Cu-VMTS [91], (c)  $[\text{Co}(\text{CO}_3)\text{NO}]$  [12] and (d)  $\text{Co}_2\text{CO}_8$  [11].

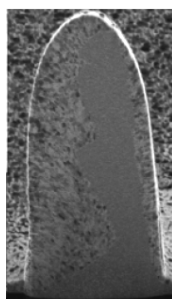


Fig. 16. Core-crust structure in a tip grown from  $\text{Co}_2(\text{CO})_8$ . [92].

The authors explain these results to a significant extent by EBIF. Taking into account the limited thermal conductivity of the deposit material, the heat dissipation from tip to substrate will be a determining factor for the temperature of the tip. At low beam currents and when the tip is still short, the heat dissipation will be sufficient to keep the tip at room temperature. But when the tip length or the beam current increases, the temperature of the tip will be raised above room temperature. At 82 nA, the estimated temperature rise is nearly one degree, which increases to more than 30 degrees at 3  $\mu\text{A}$  for the described experimental conditions. The desorption of volatile species can be facilitated by the higher temperature, leading to a higher metal content. Apart from this, the dissociation mechanism can change at higher temperatures.  $\text{Co}_2(\text{CO})_8$  normally has an endothermal decomposition reaction occurring around 100  $^\circ\text{C}$ , which is above the estimated temperature reached in tips at the highest beam current. But this thermal decomposition temperature can be significantly lowered if the activation energy for decomposition is lowered by autocatalytic effects. In this example, deposited Co would act as catalyst for the decomposition of  $\text{Co}_2(\text{CO})_8$ . Similar behavior has been observed for  $\text{Fe}(\text{CO})_5$  and  $\text{Cr}(\text{CO})_6$  [93]. These autocatalytic effects can bring the thermal decomposition

temperature to within the temperature range reached during the described experiments. A similar combination of temperature rise and autocatalytic effect is expected to be the cause for the development of the deposit from  $[\text{Co}(\text{CO}_3)\text{NO}]$ .

The roughening that was observed at the highest beam currents for  $\text{Me}_2\text{-Au-acac}$ ,  $\text{Me}_2\text{-Au-tfac}$ ,  $\text{Me}_2\text{-Au-hfac}$ ,  $\text{Cu(hfac)}_2$ ,  $\text{Mo}(\text{CO})_6$ ,  $\text{CpPtMe}_3$  and  $\text{hfac-Cu-VMTS}$  may be due to crystallization. As a result of the increase in temperature, volatile fragments desorb more easily and the (increased amount of) metal rearranges into small crystals. The fact that the roughening was observed for quite different precursors indicates again that EBID can play a significant role in EBID.

There are also examples where the effect of the beam current is not fundamentally different from the effect of the accumulated charge. For instance, the deposition of Ni-containing squares on a carbon substrate (kept at  $-85\text{ }^\circ\text{C}$ ) from  $\text{Ni}(\text{C}_5\text{H}_5)_2$  [81]. At a low accumulated charge, the squares were open, porous structures and the deposited material formed a network with (relatively) large openings (Fig. 17a). Upon continued irradiation, the porous structures closed to form (nearly) solid films (Fig. 17b). Structures created with different beam currents but with a similar accumulated charge were in a similar state of transition from open structure to closed film. The fact that accumulated charge and beam current were interchangeable indicates that the accumulated charge is the only parameter relevant for the deposition behavior under these specific conditions. An explanation for the formation of the open structures was not given.

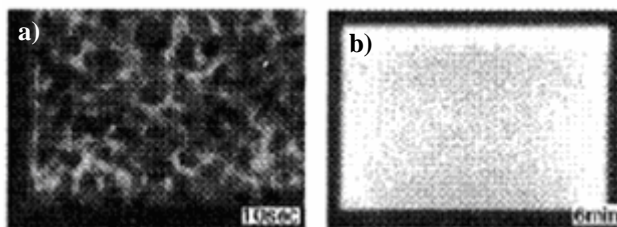


Fig. 17. The effect of accumulated charge on the morphology of squares deposited from  $\text{Ni}(\text{C}_5\text{H}_5)_2$  at  $-85\text{ }^\circ\text{C}$ . (a) At a low accumulated charge, a porous, open structure is formed. (b) At higher accumulated charges, a closed, solid film is formed [81].

### III.D.3. Density

Another property that can be measured as function of the beam current is the deposit density. The density of tips deposited from TMOS, HFA-Cu-VMTS and  $\text{Co}_2\text{CO}_8$  has been measured for beam currents of 0.1, 1 and 100 nA [70]. It was found that the density of the deposit from TMOS is independent of the beam current used. For deposits from HFA-Cu-VMTS both the density and the metal content increased with increasing beam current. Tips created with 1 nA had a rough surface. For  $\text{Co}_2\text{CO}_8$ , similar behavior was observed. See Table II for a summary of the results. The bulk density is  $8.96\text{ g/cm}^3$  for Cu and  $8.90\text{ g/cm}^3$  for Co.

The independence of the density and composition of deposits from TEOS led the authors to the conclusion that the decomposition is fully due to dissociation by electrons and that thermal effects are absent. The TEOS precursor molecule dissociates thermally at about 580

°C, which is much higher than the calculated temperature rise for a beam current of 1 nA (about 87 °C). The rough surface in the case of the Cu deposits and the large increase in metal content for the Co deposits indicate thermally assisted deposition (see also the previous paragraph).

*Table II. The effect of increasing beam current on the density and metal content of deposits from HFA-Cu-VMTS and  $\text{Co}_2(\text{CO})_8$  [70]. Higher beam currents lead to a higher density and metal content for both precursors. Bulk density are  $8.96 \text{ g/cm}^3$  (Cu) and  $8.90 \text{ g/cm}^3$  (Co).*

Beam current (nA)	Metal content (at%)		Total deposit density ( $\text{g/cm}^3$ )	
	Cu	Co	Cu	Co
0.1	14	31	2.05	4.2
1	30	-	4.3	-
100	-	73	-	7.2

#### III.E.4. Conductivity

Consistent with the increase in metal content, the resistivity of EBID wires decreases with increasing beam current. The relevant data is summarized in Table III and a typical example of the dependency is shown in Fig. 18a. Koops *et al.* and Weber *et al.* [33, 88, 89, 90] only give specific details for experiments with  $\text{Me}_2\text{-Au-tfac}$ , but mention a similar behavior for the other two gold precursors. A wide spread in resistivities for constant beam currents was found for  $\text{Co}_2(\text{CO})_8$  deposits and this was attributed to the scan method used to fabricate the Co containing wires. More details on this aspect can be found in paragraph V.E.2.

For nearly all precursors in Table III, the resistivity behavior as function of the beam current is related to the metal content. As shown in Fig. 14, the metal content consistently increases with increasing beam current. This is also consistent with the I-V characteristics, which were determined after deposition at different temperatures for the platinum and the gold wires. The gold wires deposited with the high beam current show ohmic behavior, which is probably caused by tunneling of current between the gold crystals which are spaced about 1-2 nm apart. At lower beam currents, the gold wires contain less metal and show nonlinear characteristics, probably Poole-Frenkel conduction or activated tunneling. The platinum wires have a lower metal content than the gold wires (see Fig. 14), and show only the nonlinear behavior. An exception to this rule is the experiment with  $\text{AuCl}(\text{PF}_3)_3$  [94]. This precursor yielded pure gold crystals, even at the lowest beam current. The resistivity of wires decreased with increasing beam current, which is the result of better grain percolation (see Fig. 18), so this is effectively not so much the result of the beam current, but rather the result of more accumulated charge.

When the conductivity of deposits is measured as function of accumulated charge, the general trend is that the resistance decreases with increasing accumulated charge. This is for instance the case in measurements by Bruk *et al.* [95]. They have found that the resistance of wires deposited from  $\text{Fe}_3(\text{CO})_{12}$  decreases with increasing accumulated charge. However, since the dimensions of the deposits were not reported, it is not possible to elucidate the

mechanism by which the resistance decreased. This can be the result of merely a larger wire cross section (a thicker wire can carry more current) or also of a change in resistivity. The latter case would imply an accumulated charge-dependent change in material properties.

Table III. Results from measurements of the resistivity of EBID wires as function of the beam current.

Material	Author(s)	Ref.	Highest resistivity (beam current)	Lowest resistivity (beam current)
CpPtMe <sub>3</sub>	Koops <i>et al.</i> ,	[33]	5.5 Ωcm (200 pA)	1 Ωcm (660 pA)
Me <sub>2</sub> -Au-acac,	Weber <i>et al.</i> ,	[88]	400 Ωcm (100 pA)	2 × 10 <sup>-2</sup> Ωcm (900 pA)
Me <sub>2</sub> -Au-tfac,	Schlößler <i>et al.</i>	[89]		
Me <sub>2</sub> -Au-hfac		[90]		
Mo(CO) <sub>6</sub>		[96]		
Co <sub>2</sub> (CO) <sub>8</sub>	Lau <i>et al.</i>	[12]	5 Ωcm (183 pA)	1.6 × 10 <sup>-4</sup> Ωcm (10.7 nA)
W(CO) <sub>6</sub>	Kohlmann <i>et al.</i>	[113]		2 × 10 <sup>-2</sup> Ωcm (1000 pA)
Fe <sub>3</sub> (CO) <sub>12</sub>	Brük <i>et al.</i>	[95]	10 <sup>3</sup> Ωcm (11 pA)	4 × 10 <sup>-2</sup> Ωcm (232 nA)

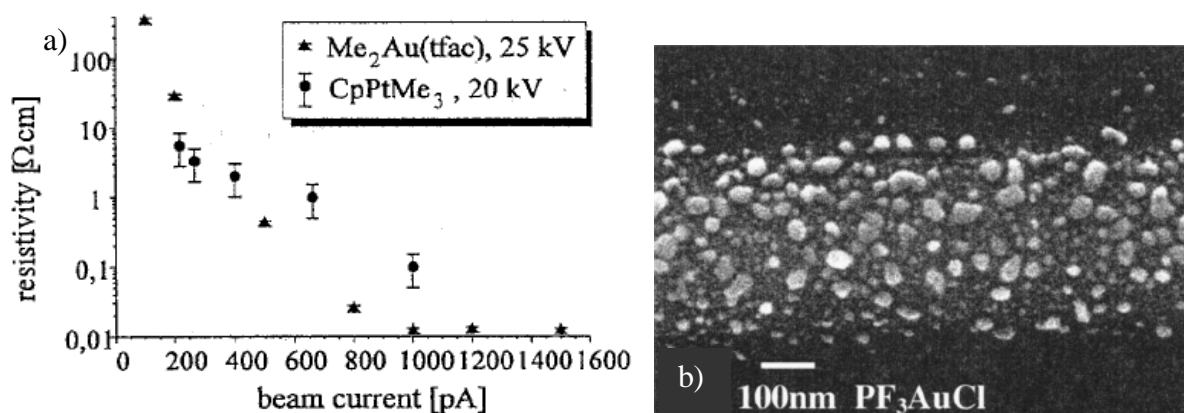


Fig. 18. (a) A typical example of the dependence of the resistivity of EBID wires on the beam current [96]. (b) Grains of gold deposited from Au(PF<sub>3</sub>)<sub>3</sub>. The grains were found for all beam currents, so changes in resistivity as function of beam current are the result of grain percolation [94].

A more complete experiment was performed with W(CO)<sub>6</sub> [76]. The electrical properties of EBID wires were measured *in situ*, for electron doses varying from  $0.1 \times 10^5 - 5 \times 10^5$  C/m<sup>2</sup>. A fixed potential was applied over the wire at regular intervals during the deposition. This gives the development of the current passed through the wire as function of the total accumulated charge. For the various beam energies used, a constant trend was observed. Initially, the current increment per charge increment increased rapidly, after which the current increment stabilized to a constant value. In other words, the conductivity increases nonlinearly in the initial stage and shows a linear increase later on. The authors explain the initial nonlinear stage by a change in the structure of the wire. The wire starts as a discontinuous line of nuclei and evolves into a continuous wire. In the later stage, when the

wire has become continuous, the increase in conductivity is merely the result of an increase in wire cross section. This implies that the deposition mechanism remains unchanged during the growth and that it is independent of the accumulated charge.

An anomalously high decrease in resistivity is reported for squares deposited from  $WF_6$  [97]. The accumulated charge was varied by varying the pitch between the pixels. With a variation in accumulated charge of a factor of 16, the amount of deposited material increased by a factor of about 10 and the resistivity decreased from  $1.3 \times 10^3$  to  $8.4 \times 10^{-2}$  Ohm cm (a factor of  $10^5$ ). An explanation for this behavior is not given.

#### IV.B. Electron Energy

As was discussed in paragraph II.C, experiments have shown that electrons with energies of about 5 to a few hundred eV contribute significantly to the growth of deposits. The relative contribution of high-energy electrons to the growth is less clear. It is tempting to think that  $\sigma(E)$  can be determined for a specific precursor by measuring the deposition yield as function of the PE energy. This is, however, not as straightforward as it seems.

Relevant for the deposition yield is the amount, the energy and the location of the electrons that cross the target-vacuum interface. For flat surfaces, the energy spectrum of emitted electrons (BSE's, SE's) remains almost unaffected by the PE energy [98], except for PE energies close to the SE peak (see Fig. 19a). The most significant change is in the total yield of emitted electrons, which increases sharply to a maximum with increasing PE energy, after which it slowly decreases (see Fig. 19b). This increase is mostly due to an increase in the amount of SE's. For PE energies close to the SE peak, the energy spectrum becomes dominated by the PE's.

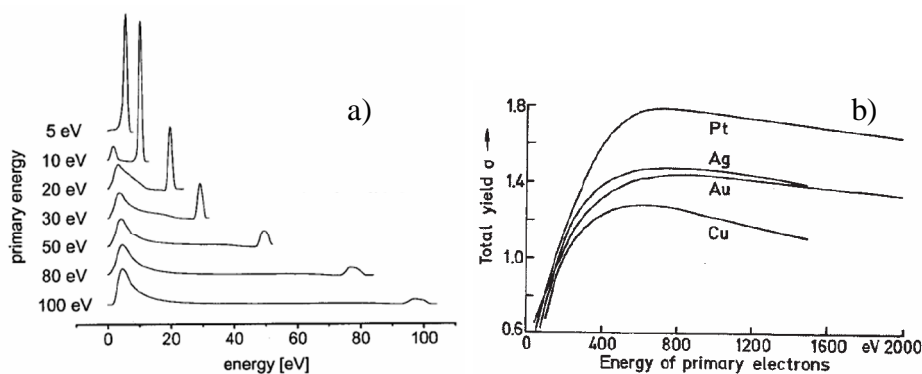


Fig. 19. (a) Energy spectrum of emitted electrons for various PE energies ranging from 5 – 100 eV [99]. (b) Total yield of emitted electrons (BSE's and SE's) as function of PE energy [52].

The total flux of electrons is the sum of the PE's and the total yield of emitted electrons. When the deposition yield changes with changing PE energy, this can be the result of two parallel effects: (1) a change in cross section for dissociation by the PE's and (2) a change in the amount of emitted electrons. Since we want to determine the first effect, we need to have a measure or a model for the second effect. And the model needs to be very accurate, because

most of the emitted electrons are SE's and the effect of the change in cross section may be relatively small. Building such an accurate model is not easy and it is made more difficult by the fact that the spatial distribution of PE's and emitted SE's varies strongly as function of location on the substrate. For deposition with a focused beam, the incident PE's are concentrated in a small area, while the SE's are distributed over a much larger region. This becomes even more complex when tips are deposited. The balance between SE's, BSE's and PE's can shift during the evolution of the tip. And on top of this, there is the difficulty that in the typical experiment, the PE energy is not the only parameter that is varied. Usually in SEMs, the beam size and/or the beam current changes together with the acceleration voltage [100].

In EBID experiments, occasionally the electron currents are measured *in situ* [101, 102], but in general the yield of emitted electrons is not measured. Elaborate models are being developed [62], which can give valuable insight in how balances shift during EBID growth. However, it is still not straightforward to distinguish between the different mechanisms influencing the deposition process and to point out the prevailing one.

#### IV.B.1. Height and width

Having put things in perspective, we will discuss results from experiments. Two types of behavior are observed when varying the PE energy. A decrease of deposit height with increasing PE energy is shown in Fig. 20a [103, 104, 105, 106] and Fig. 20b [107]. Data presented in some reports does not allow sufficient quantification to distinguish precisely this behaviour, but is consistent in the trend that the growth rate is higher at low voltages than at high voltages [108, 109, 78, 20, 26].

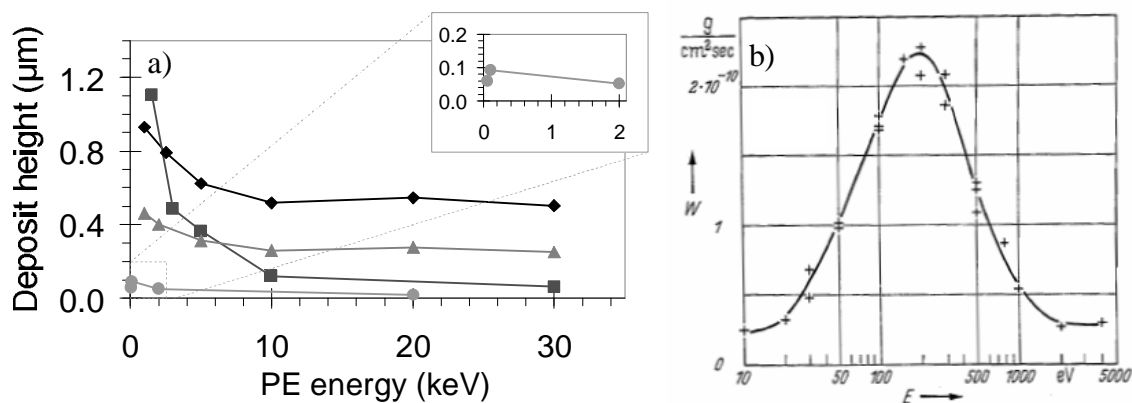


Fig. 20. (a) Deposit heights as function of the PE energy shows a similar dependence as the generation behavior of secondary electrons. Inset shows the experiment by Hoyle *et al.* between 0.06 and 2 kV. (b) The deposit yield in  $\text{g cm}^{-2} \text{s}$  for diffusion pump oil as function of PE energy [107].

◆	$\text{Me}_3\text{PtCp}$	Takai <i>et al.</i>	[105]
■	$\text{W}(\text{CO})_6$	Bauerdick <i>et al.</i>	[104]
▲	$\text{Me}_3\text{PtCp}$	Lipp <i>et al.</i>	[103]
●	$\text{W}(\text{CO})_6$	Hoyle <i>et al.</i>	[106]

A different type of behavior is shown in Fig. 21: an increase of the deposit height with increasing energy between 2 and 20 kV, after which the deposit height stays constant or shows a slight decrease [110, 44, 13, 72]. In some cases [13, 72], this behavior is very consistent for different dwell times (seconds and minutes, resp.).

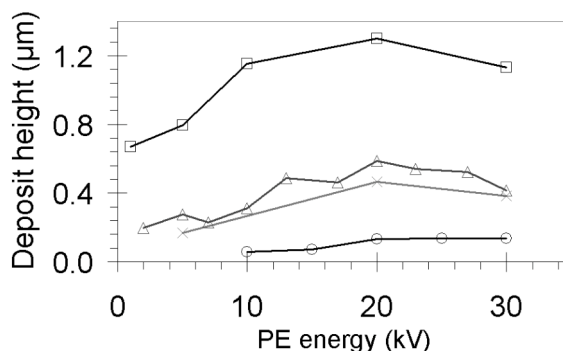


Fig. 21. Deposit heights as function of primary electron energy.

- Contamination Schiffmann [13]
- ×  $W(CO)_6$  Kohlmann et al. [72]
- △ TEOS Randolph et al. [44]
- Contamination Miura et al. [110]

The dependency of deposit height on PE energy in Fig. 20 seems to be consistent with the dependency of the yield of emitted electrons (BSE's and SE's) on PE energy in Fig. 19b. Starting at PE energies of a few hundred eV, the deposition yield decreases strongly and becomes nearly constant for PE energies of 10-30 keV. This implies that in these experiments the deposit height was mainly dependent on the number of emitted SE's.

The results in Fig. 21 seem to be conflicting with this trend. An increase of the deposit height for higher PE energies is found, not a decrease. This can possibly be explained by the size of the interaction volume of scattered electrons in the target. As Weber *et al.* [33] point out, “the major difference when dealing with tips instead of flat substrates is the reduced scattering volume.” At high energies, the probability for a primary electron to exit the tip after a scattering event is significant, because the tip is a high and narrow structure. At low energies, scattering occurs mostly within the tip, which can have EBIH as result. Depending on the PE energy, the temperature rise can be as much as 50 °C, as becomes clear from a model by Randolph *et al.* [44] based on the effect suggested by Weber *et al.* (see Fig. 22). Due to the temperature rise at lower PE energies, the residence time  $\tau$  of adsorbed precursor molecules decreases, which in turn leads to a lower vertical growth rate. This trend is consistent with the trend found in the experiments by Randolph *et al.* (△, Fig. 21). The effect of EBIH would also explain the other results in Fig. 21. Kohlmann *et al.* (×, Fig. 21) deposited tips. And for the experiments by Schiffmann (□) and by Miura *et al.* (○) we have already seen that EBIH most likely played a significant role during variations of the beam current (see paragraph IV.A.1).

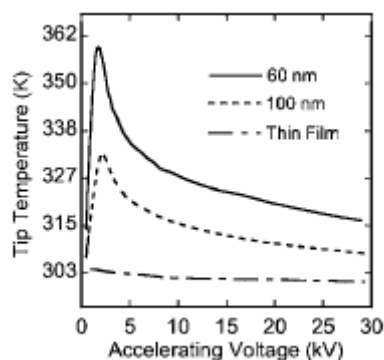


Fig. 22. Calculated temperature in tips (60 nm and 100 nm length) compared to a thin film. [44]

The trends in Fig. 21 may be explained with EBIH, but this explanation raises some questions for the trends observed in Fig. 20. Bauerdick *et al.* (■, Fig. 20) and Beaulieu *et al.* [78], Ding *et al.* [20] and Croitoru *et al.* [26] (not shown) have also deposited tips or dots and they measure a decrease in growth rate with increasing PE energy. This is in contradiction with the trend we would expect if the effect of EBIH was significant. For Bauerdick *et al.* (■, Fig. 20), this inconsistency can be explained by a different scan strategy. The tips were not grown by keeping the e-beam in a stationary position on the sample, but by giving a series of short exposures. Between the exposures, there is time for the thermal energy to dissipate to the underlying substrate, so the effect of EBIH is expected to be much less. It is not possible to use this explanation for the results by Beaulieu *et al.* [78], Ding *et al.* [20] and Croitoru *et al.* [26], because they grew tips with the beam in spot mode. Due to the lack of detailed information (local precursor pressure, beam currents used, etc.) this inconsistency remains unexplained. In conclusion, the combined model of (1) the correlation between deposition yield and SE yield and (2) EBIH seems to be valid for most experiments. However, it leaves some experimental results unexplained and the measurements are not sufficiently accurate to exclude the contribution from PE's to the growth.

As for the lateral dimensions, all measurements are influenced by the fact that the diameter of the primary electron beam changes with changing the electron energy. For the case where the beam diameter was measured, it was reported that there is little dependence of lateral dimension on electron beam energy [72].

#### IV.B.2. Composition and morphology

The results from articles reporting on the influence of the PE energy on the composition of deposits vary quite significantly. Details about the experiments are often not given, so the interpretation of the results is difficult. A clear influence of the PE energy was reported by Weber *et al.* for a number of precursors ( $\text{Me}_2\text{-Au-tfac}$ ,  $\text{Me}_2\text{-Au-hfac}$ ,  $\text{Me}_2\text{-Au-acac}$ ,  $\text{Mo}(\text{CO})_6$ ) [33]. The metal content of tips increased with decreasing the PE energy. Numbers (compositions or PE energies) are not given. When irradiating condensed  $\text{WF}_6$  layers in an Auger SEM, the dissociation rate was found to decrease with increasing beam energy [111].

The behavior observed for the Au and Mo precursors was explained by the authors as resulting from “the cross section for inelastic scattering, which is increasing with decreasing electron energy” [33]. Most likely, they refer to the cross section for scattering of PE’s, which is larger at lower PE energies. By this, they imply that the higher metal content of the tips at lower PE energies is the result of the larger abundance of SE’s. In this picture, a decrease in PE energy is equivalent to increasing the accumulated charge per unit time. This mechanism would be consistent with the behavior observed for  $WF_6$ .

In several other studies, no influence of the PE energy was found. Folch *et al.* report that the composition of deposits from  $Me_2$ -Au-hfac was constant for PE energies between 10 and 40 keV [68]. For contamination deposits, the ratio between  $sp^2$ - and  $sp^3$ -bonded C was measured for PE energies between 3 keV and 20 keV [20]. Variations were not above the uncertainty level of about 10% of the measurement technique (EELS). The diffraction patterns of 50 nm thick films deposited from  $W(CO)_6$  obtained in the TEM showed no visible difference when fabricated with different beam energies [76]. And the composition of rectangles deposited from  $[RhCl(PF_3)_2]_2$  was found to be independent of the PE energy [112].

The independence of the composition from PE energy for deposits  $Me_2$ -Au-hfac found by Folch *et al.* [68] is surprising, since Weber *et al.* did find a dependence for the same precursor [33]. According to Folch *et al.*, the observed lack of dependence “rules out the possibility that substrate heating by the impinging electrons plays a significant role in the EBID mechanism, as the heating effect increases with increasing energy.” It is not straightforward to see why this is so, because it is not mentioned whether tips or squares are deposited. This would imply that in the results by Weber *et al.* EBID *did* play a significant role. Keeping in mind the discussion in the previous paragraph and the fact that Weber *et al.* deposited tips, this sounds plausible. However, lack of information prevents more definite conclusions.

#### IV.B.3. Conductivity

The inconsistency in the effect of the PE energy on the composition of deposits is also found for measurements of the conductivity. It was found for  $W(CO)_6$  by Hoyle *et al.* that the conductivity increases with decreasing energy (varied between 500 eV and 20 keV) [106]. This trend was confirmed for  $W(CO)_6$  lines deposited with energies between 20 keV and 30 keV by Kohlmann *et al.* [113]. In contradiction with these results, the conductivity of lines deposited from  $MeCpPtMe_3$  decreased by a factor of 3 when the PE energy increased from 5 to 20 keV [114].

These inconsistent results are difficult to explain. In all 3 cases, the deposits were created by scanning the pattern (lines or squares) a large number of times to obtain sufficient height. This, and the fact that low aspect ratio structures were used (instead of tips for instance), makes the occurrence of EBID in any of the experiments not very likely. Hoyle *et al.* explain their results by assuming that SE’s play a major role in the deposition process. At lower PE energies, precursor molecules undergo more collisions with electrons, increasing the desorption of volatile species and increasing the metal content. The same mechanism would have occurred for the Pt-precursor, so that does not explain the difference. The contrasting

results may be due to difference in precursor chemistry, but again, a mechanism is not easy to see.

#### *IV.C. Conclusions*

Regarding the vertical growth of deposits, measurements of the effect of the current density are mostly consistent with each other and with the existing growth model. The plot that gives most insight into the growth process is a measurement of  $h$  as function of  $J$  (or  $V_{deposit}$  as function of  $I$ ). The electron-limited and precursor-limited regimes can be identified and explained quantitatively (to some extent) for experimental results. An experiment with contamination indicates that a high  $J$  (or  $I$ ) can lead to EBIH, which significantly affects the vertical growth rate. Often, the vertical growth is reported in terms of  $h$  as function of  $Q$  or  $t_{dwell}$ . For most of these cases, too much information is missing (such as the local precursor flux) to explain the observed behavior quantitatively, and sometimes even qualitatively. Contradictory results were found for experiments where the influence of the PE energy on the vertical growth was studied. These contradictions could be explained to a large extent with a combination of the growth model and EBIH, but this approach leaves some results unexplained. Unfortunately, there is not enough information available to find out why.

Concerning the lateral growth, this is consistently found to be independent of  $J$  and the PE energy. Instead,  $d_{deposit}$  depends on  $d_{beam}$  and on  $Q$  (for growth in the electron-limited regime) and shows a fast initial increase followed by saturation. This behavior can be explained by dissociation by SE's emitted from the growing deposit itself. Deposits with a  $d_{deposit}$  as small as 1.0 nm have been created by stopping the growth in the fast increase stage. At these dimensions, the number of molecules per deposit is so small that the effect of the counting statistics becomes visible.

For metal-organic precursors, an increasing  $J$  generally leads to an increase in metal content, conductivity and density. Additionally, the deposit surface changes from smooth to rough. This is partially due to an increased degree of electron-induced dissociation and partially due to a change in dissociation mechanism. At a high  $J$ , EBIH can occur. If the precursor has a thermal decomposition temperature within the range of temperatures that can be reached by EBIH, the dissociation mechanism may not be merely electron-induced, but can also be thermally-induced. For precursors with a thermal decomposition temperature well above temperatures reached with EBIH (such as TEOS), no effect of  $J$  is observed. Inconsistent results were found for the effect of the PE energy on the composition, morphology and conductivity. It is suggested that EBIH or the amount of emitted SE's played a significant role during these experiments, but the lack of information prevents definite conclusions.

#### **V. Scan pattern and scan strategy**

One of the advantages of EBID is that 2-dimensional as well as 3-dimensional patterns can be defined. Apart from the properties of the beam (size, current, energy), the scan pattern as well as the scan strategy can have a significant influence on the deposit. A number of parameters are defined in the scan strategy. In the case of lines, for instance, the line length

and the scan speed are most apparent parameters. Related to this is the period between subsequent visits of the same point on the substrate. This is known under several names; “repeat times”, “loop times”, “refresh times”, “line times” or “delay times”. We will use the term “loop time”. Apart from these variables, the dose per scan can also be varied. For digital deflection systems, this is the number of pixels per line. These parameters can be interconnected (for instance the scan speed and the loop time), so it requires some care to perform and describe experiments in such a manner that conclusions can be drawn from the results.

### V.A. Scan pattern

#### V.A.1. Height and width

Until now we have mainly discussed the deposition of tips by spot irradiation. Although this is perhaps conceptually the simplest EBID experiment, we have already seen that this can lead to quite complex behavior. The fact whether the process is electron- or precursor-limited can significantly influence the growth rate, the composition and the morphology. Here we will see that it can also affect the height distribution of the deposit. In the extreme case, growth is precursor-limited almost directly from the start. An example is the use of residual gas as a (carbon) precursor. If a large beam is used, nonuniform height distributions are found, as for instance reported by Fourie [115] and Reimer *et al.* [116]. They studied contamination growth in early electron optical systems. When irradiating a substrate with a beam with a diameter of some  $\mu\text{m}$ 's, deposition of carbon occurred only along the edge of the beam and not in the centre. Typical deposit height profiles are shown in Fig. 23a, b and c.

The explanation for this behavior is the following [116]. If  $\sigma J \gg (gF/N_0)$ , the area under the beam will quickly become depleted of mobile precursor molecules. The supply of new molecules will have to come from outside the irradiated area. If direct adsorption from the gas phase is the prevalent supply mechanism, all locations under the e-beam have an equal probability for adsorption (and dissociation). If surface diffusion is the prevalent supply mechanism, molecules will diffuse from the outside inwards and will be pinned down before they reach the centre of the irradiated area. The fact that a ring structure is found, indicates that (for these particular experimental conditions) surface diffusion was the prevalent supply mechanism.

The effect of the 2 growth regimes can be reproduced well with theoretical models. Results from a continuum model developed by Utke *et al.* [117] and a Monte Carlo simulation developed by Smith *et al.* [118] are shown in Fig. 23d and e, respectively. The precursor-limited regime is called diffusion-limited in Fig. 23d. That the ring shape is not visible in Fig. 23e is probably due to the fact that a very small beam diameter was used.

Similar results were later found experimentally in similar conditions for lines and squares. The middle sections of lines (deposited from contamination, several  $\mu\text{m}$ 's wide) showed a different height profile than the end sections [119]. Fig. 24a shows an AFM image, Fig. 24b shows the height profiles. This indicates that the precursor supply is mainly by surface diffusion. The end sections have a larger area to draw hydrocarbons from than the middle section and therefore the end sections become higher than the middle section. The theory of

supply by diffusion was tested with a dedicated experiment. Around a spot on the substrate, 4 lines were scanned that connected to make a square. The spot and the surrounding lines were irradiated in alternating sequence. While keeping the scan strategy (total accumulated charge, dwell times, loop times) constant for the dot in the middle, the influence of the presence and the length of the 4 lines was studied (see Fig. 24c for a schematic representation). The height of an isolated dot was 209 nm, and this decreased to 139, 133 and 111 nm for squares of  $80 \times 80 \mu\text{m}^2$ ,  $60 \times 60 \mu\text{m}^2$  and  $40 \times 40 \mu\text{m}^2$ , respectively. This result is consistent with the theory that the primary supply mechanism is diffusion over the surface.

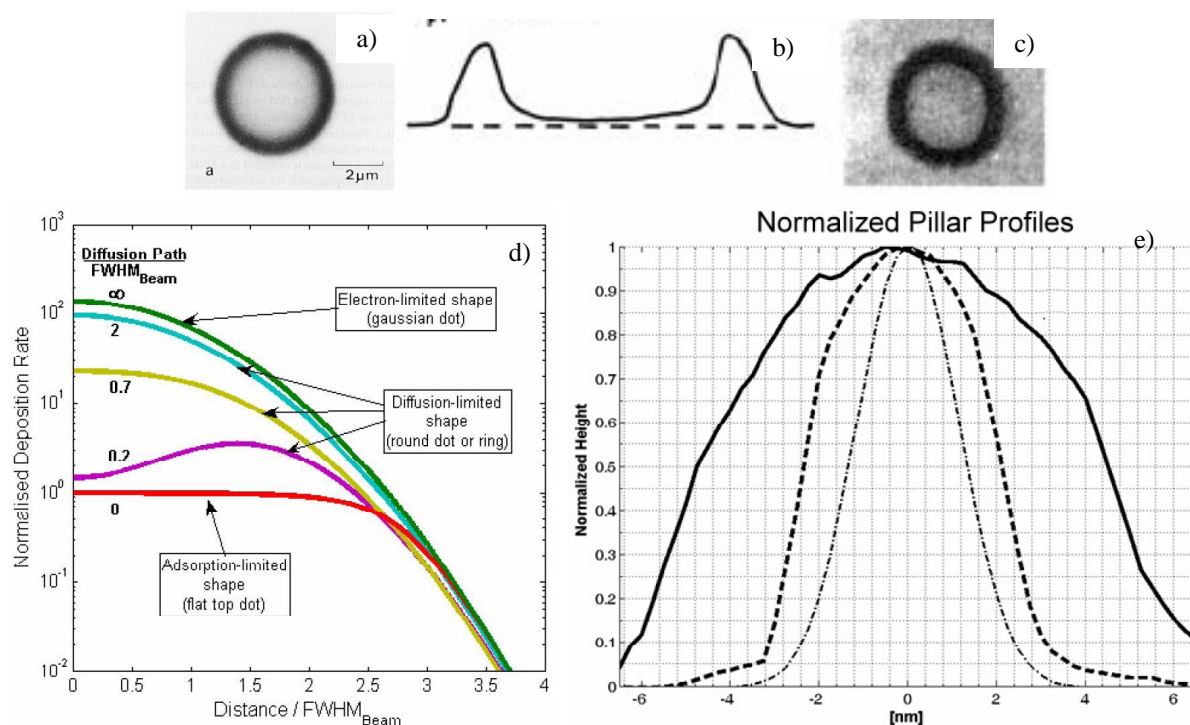


Fig. 23. (a) Contamination ring as result of broadbeam illumination [116]. (b) Height profile and (c) contamination ring [115]. (d) The growth rate as function of the normalized distance with the beam in spot-mode for different growth regimes, calculated from a continuum model [117]. The precursor-limited regime is called diffusion-limited. (e) Same as in (d), but now calculated from a Monte Carlo simulation [118]. The deposit profiles for the precursor-limited regime (—) and electron-limited regime (— —) are shown, together with the electron beam profile (— ■ —).

The same conclusion was drawn by Ding *et al.* [20] when depositing squares, using paraffin as a precursor. A small amount of paraffin was placed on a cleaned Si substrate and about  $35 \mu\text{m}$  away a square of several micrometers length and width was defined. The height profile of the resulting structure is shown in Fig. 24d. The edges are thicker than the middle, and the four corners are again higher than the edges. This is consistent with the diffusion picture sketched above, where the supply of molecules is largest for the corners and smallest for the middle of the square.

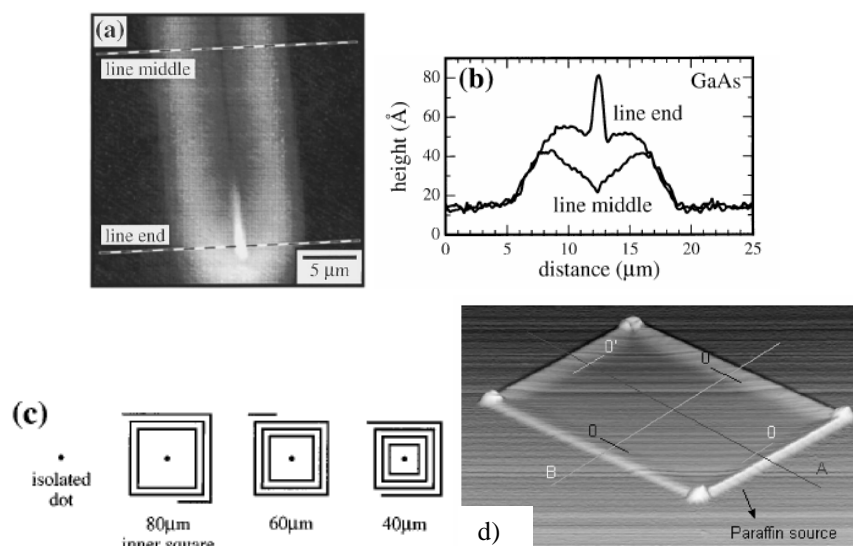


Fig. 24. Height profiles of deposits indicating that surface diffusion is the prevalent precursor supply mechanism. (a) AFM image of a line several  $\mu\text{m}$  wide. The line end has a different height profile than the line middle. (b) The absolute height profiles. (c) Test pattern to study the effect of surface diffusion. (d) Scanned square, where paraffin was used as precursor. (a, b, c) from [119], (d) from [20].

#### V.A.2. Composition and morphology

We have seen strong indications in paragraph IV.A.1 that EBIH can play a significant role in the deposition process. This happens when the energy input by the electron beam is larger than the energy dissipation from the deposit, as we have seen for deposits created with the beam in spot mode. Further evidence for EBIH in other instances comes from an experiment by Utke *et al.* [120]. Using HFA-Cu-VMTS as precursor, they created self-standing horizontal rods by scanning the beam (500 pA, 132 nm diameter) into vacuum from a copper substrate. The rods had a smooth surface, consisted of an amorphous C-rich matrix with dispersed 2-5 nm Cu nanocrystals and all precursor ligand elements (F, Si, O and C) were present. The next step was to deposit a vertical tip at the end of the self-standing rod. Close to where the vertical tip was grown, the rod was fully transformed into  $>100$  nm faceted Cu nanocrystals (Fig. 25a). F, O and Si had disappeared and the amount of C was greatly reduced. The explanation that the authors offer, is that during the growth of the vertical tip, the amount of inelastic scattering becomes much higher than during the growth of the (relatively thin) self-standing rod, simply because there is a larger volume of material under the beam. There will be a larger energy transfer from beam to target and due to the poor thermal conductivity, there will be a temperature gradient over the rod. Near the vertical tip, the decomposition temperature of the precursor can be approached and faceted Cu crystals are the result.

Liu *et al.* [121] did a similar experiment, also with a 500 pA beam current, but now with  $\text{W}(\text{CO})_6$ , a PE energy of 200 keV and a beam size of approximately 0.8 nm. They deposited self-standing sheets at the end of a pillar at the end of a self-standing rod (see Fig. 25c). The entire deposit remains amorphous. Probably, the amount of energy transferred to the entire

structure is much smaller than in the experiment by Utke *et al.*, because the high energy PE's have a much larger inelastic mean free path and scatter much less.

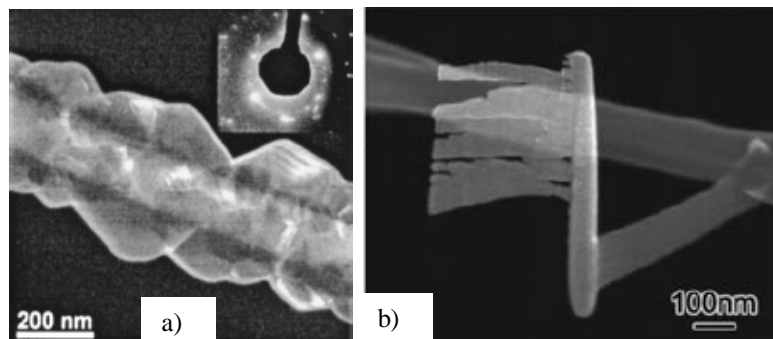


Fig. 25 (a) A self-standing rod after a point exposure at the end of the rod (not shown in the image). Initially, the rod consisted of an amorphous C-rich matrix with dispersed 2-5 nm Cu nanocrystals. As a result of the point the rod now consists of Cu crystals [120]. (b) Structure deposited from  $W(CO)_6$  by Liu *et al.* [121].

The composition of deposits from  $[RhCl(PF_3)_2]_2$  and  $[RhCl(CO)_2]_2$  appears to be unaffected by the scan pattern. Cicoira *et al.* [112] measured the composition for these precursors with AES. Deposits were created with the beam (2 and 10 nA) in area mode and in point mode and analysis showed a homogeneous distribution of the elements, with a Rh content of around 60 at.%, indifferent of the scan pattern (or other parameters such as beam current or PE energy). Analysis of  $[RhCl(PF_3)_2]_2$  deposits by TEM and EELS confirmed this [122].

## V.B. Scan strategy

### V.B.1. Height and width

The scan strategy concerns parameters such as the dose per scan, dwell times and loop times. Kohlmann *et al.* [113] have studied the effect of the dwell time and the loop time independently for depositions with the electron beam in spot mode. The precursor was  $W(CO)_6$  and the total accumulated charge per spot was kept constant. The deposit heights presented in Fig. 26a and Fig. 26b are normalized to a deposit height obtained with a continuous exposure (at the same accumulated charge). For a constant loop time, a decrease in dwell time from 150  $\mu$ s to 20  $\mu$ s leads to an increased normalized yield from 1 to 2 - 2.5 (see Fig. 26a). The decreasing yields at the longer dwell times is the result of “the progressing consumption of the adsorbate layer. ... The amount of decomposed precursor molecules per time unit is larger in the beginning than in later intervals of the dwell time.” In other words, the dissociation rate during an exposure period is not constant, but decreases because the surface coverage  $N$  decreases. At a constant dwell time, an increase in loop time from 0 to 150  $\mu$ s leads to an increase in normalized height from 1 to around 2 respectively (Fig. 26b). The higher yields at the longer loop times are due to the longer precursor replenishing times. The appearance of a saturation level for the yield indicates that  $n$  becomes constant at the higher loop times. At those loop times, the yield becomes independent of the dwell time.

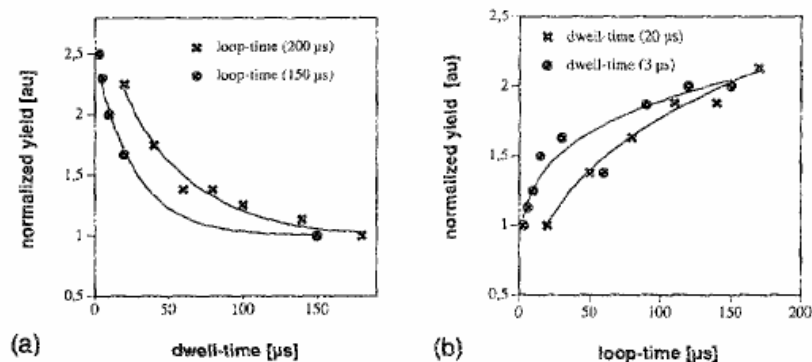


Fig. 26. The results from independent variations of the dwell times (a) and loop times (b) for tip deposits from  $W(CO)_6$ . The accumulated charge was kept constant. Yields were normalized to the yield of a tip deposited with a continuous exposure (at the same accumulated charge) [113].

Other studies where the loop time was varied confirm this proposed model. Similar behavior was found for squares deposited from TEOS (Lipp *et al.*, [123]) and lines and dots deposited from contamination (Amman *et al.*, [119]). Beaulieu *et al.* [78] do not give exact numbers, but do report that an increase in loop time by a factor of 4 gives an increase in vertical growth rate of a factor of 4. It is interesting that, for the different experiments, saturation of the deposition yield for the longer loop times occurs at different time scales. While saturation occurs in the order of 100-200  $\mu\text{s}$  in the experiments by Kohlmann *et al.*, Lipp *et al.* find time scales of 10-20 ms and Amman *et al.* find time scales in the order of 20 s. This must be due to differences in  $F$ . Amman *et al.* used contamination as a precursor and are therefore dependent on surface diffusion as supply mechanism (see also paragraph IV.A.1). Kohlmann *et al.* and Lipp *et al.* both report an  $F$  of  $10^{17}$  molecules  $\text{cm}^{-2} \text{s}^{-1}$ . The difference between the results by Kohlmann *et al.* and Lipp *et al.* are possibly due to the sticking coefficients of the precursors ( $W(CO)_6$  and TEOS, respectively).

Results are less consistent when the dwell time is varied. Sanchez *et al.* [124] mention (without giving absolute numbers) that short dwell times are beneficial for a high growth rate when scanning squares, similar to what Kohlmann *et al.* found. On the other hand, Lipp *et al.* [123] found that the effect on the deposition yield was less pronounced than in the experiments by Kohlmann *et al.* This may be due to the fact that the dwell times may have been too short. The current density Lipp *et al.* used was smaller than what Kohlmann *et al.* used ( $10 \text{ A cm}^{-2}$  instead of  $75 \text{ A cm}^{-2}$ ), which means one would expect that depletion occurs at longer dwell times (i.e. the curve in Fig. 26a shifts to the right). However, Lipp *et al.* used shorter dwell times (0.5-2  $\mu\text{s}$ ), where depletion may not have occurred at all. Beaulieu *et al.* [78] report that the dwell time did not appear to be significant at all. This can perhaps be explained by the fact that Beaulieu *et al.* used dwell times in the range of 5-500 ms; much longer than in the experiments by Kohlmann *et al.* or Lipp *et al.* It is possible that the deposition area was depleted from precursor molecules even at the smallest dwell times.

In some cases, the way the experiment is performed does not allow a full interpretation of the influence of dwell and loop times. For instance, when scanning a line of constant length

and with constant total accumulated charge, the dose per scan (in  $\text{C}/\text{m}^2$ ) was varied [125]. Effectively, this results in the simultaneous variation of both the dwell time per point and the loop time. Another example is a variation of the “linedose” (in  $\mu\text{C}/\text{cm}$ ) without keeping the total accumulated charge constant [75]. The simultaneous variation of several parameters prevents the determination of the influence of individual parameters such as dwell and loop times.

There are two reports of a dependency of the line width on the dwell and loop times. For contamination lines, a decrease in the loop time leads to a different height profile [119]. Fig. 27a shows profiles of lines written with loop times of 100.2, 30.6, 20.2 and 5.2 s (constant dwell time), a schematic drawing is shown in Fig. 27b. At the shorter loop times, the surface diffusion length is not sufficient to supply the central part of the line with contamination molecules and deposition only occurs at the edge of the structure. Beaulieu *et al.* [78] mention that a combined increase of dwell time and loop time gave a definite decrease in linewidth. However, since further details are not mentioned, it remains unclear why this is so.

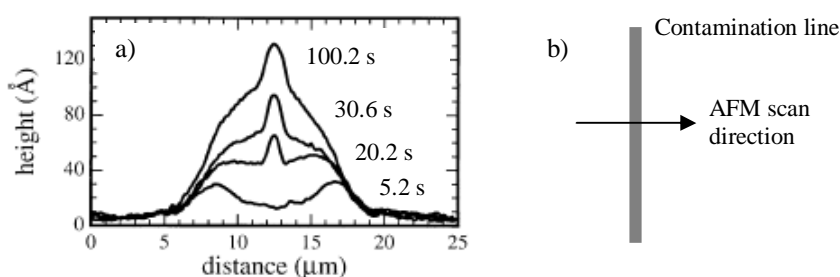


Fig. 27. (a) The height profiles of contamination lines deposited with different loop times (constant dwell time) [119]. The loop times are indicated in the figure. (b) Schematic drawing of the setup.

### V.B.2. Conductivity

Hoyle *et al.* [125] have written  $30\ \mu\text{m}$  lines with  $\text{W}(\text{CO})_6$  with a total dose of  $5 \times 10^5\ \text{C}/\text{m}^2$ , while the scan speed and corresponding number of scans were varied. Effectively, this results in a corresponding simultaneous variation of both the dwell time per point and the loop time. Measurements of the resistivity show two regimes. For fast scans (doses less than about  $500\ \text{C}/\text{m}^2$ , relatively short dwell and loop times), a high resistivity deposit is found, while for slow scans (doses larger than about  $5000\ \text{C}/\text{m}^2$ , relatively long dwell and loop times) a low resistivity is found. The authors describe these two regimes as “electron-flux limited” and “gas-flux limited”. In the gas-flux limited regime, “each deposited molecule undergoes a larger number of electron collisions while at the surface, and this may result in additional desorption of CO” and therefore contribute to a lower resistivity.

This model is confirmed by experiments by Hiroshima *et al.* [75] for  $\text{WF}_6$  and Utke *et al.* [126] for  $\text{Me}_2\text{-Au-tfa}$ . Hiroshima *et al.* report that a single slow scan yielded a line with lower resistivity than 200 fast scans. Similarly, Utke *et al.* have kept the total line dose constant and have tried a single slow pass ( $9\ \text{nm}/\text{s}$ ) versus  $6 \times 10^5$  fast passes ( $500\ \mu\text{m}/\text{s}$ ) per line. The resistivity is about 60 times higher for the fast scan (with relatively short dwell and loop times) than for the single slow scan (with relatively long dwell and loop times).

In conclusion, the trend seems to be that the effect of the scan strategy on the conductivity is dependent on the ratio between electrons and deposited molecules. If this ratio increases (more electrons per deposited molecule), the dissociation of molecules will be more complete and the conductivity increases.

### V.C. Scan speed

If a line is scanned by the electron beam in a single pass and the scan speed is increased from 0 nm/s onwards, a transition will be observed from pillar-growth to line-deposition. First studied by [71] and [127], the evolution of the growth behavior is well presented in Fig. 28a and b [128]. As the scan speed is increased (increasing from a to l), the structures become more and more inclined. At the same time, a second deposit starts to grow on the substrate, which becomes visible from pillar d or e onwards in Fig. 28a. As the pillar becomes more and more inclined, the second deposit can also “take off” from the substrate (illustrated by k and l in Fig. 28a). If the scan speeds are increased even further, periodic fence-like structures and finally solid lines (see Fig. 28c) are deposited [129, 130]. Based on an extensive study, it was found that the growth of these secondary structures and the periodic growth is caused by the decreasing precursor supply efficiency to the end of the inclined pillar. As a result of the increased diffusion path, the flux of precursor molecules reaching the end of the pillar decreases and the tip becomes thinner and narrower. From a certain scan speed onwards, the electron beam can penetrate the inclined pillar and create a second deposit on the substrate. As the primary pillar becomes thinner and thinner, more electrons penetrate and the vertical growth rate of the secondary structure increases. Finally, the primary and the secondary structure meet. The process then repeats itself. If the scan speed is increased, the thinning of the primary pillar and the growth of the secondary structure start earlier and the periodicity becomes smaller. Finally, a flat line is scanned.

A few other cases are known of secondary structures growing parallel to free-standing primary structures [127, 131]. It is likely that this is caused by the primary electrons getting through to the underlying substrate.

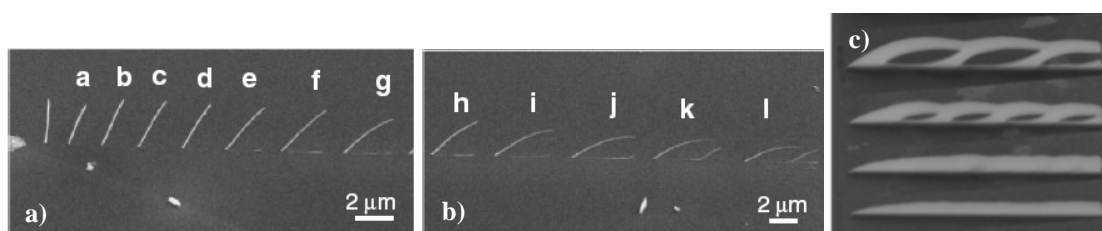


Fig. 28. (a, b) The inclination of tips as function of the scan speed [128]. At sufficiently large scan speeds, secondary deposits start to grow (starting from pillar e and f onwards) (c) At increased scan speeds, fence-like structures and finally solid lines are deposited [130].

The influence of the scan speed has also been studied for very high resolution (<10 nm width) self-standing structures. When the electron beam is scanned over a hole, a self-standing rod will grow. It is consistently reported that the width of the rods (dimension perpendicular to the e-beam and the scan direction) decreases with increasing speed of the electron beam [132, 133]. See also Fig. 29a. The width at scan speeds above  $\sim 10 \text{ nm s}^{-1}$

saturates at 7-10 nm. The width evolution of the rods is roughly similar to the evolution of dots as proposed by Silvis-Cividjian [61]. If the electron beam irradiates each position on the rod for a longer time, more SE's are emitted at the side of the rod and it becomes wider. The 1/scan speed relationship seems to indicate that the amount of material that is deposited per unit time remains constant for scan speeds up to  $10 \text{ nm s}^{-1}$ .

Apart from the width of the rods, the angle of inclination of the rods also appears to be dependent on the scan speed [132]. The angle between substrate and rod decreases with increasing scan speed. For scan speeds of 0.8, 4 and  $24 \text{ nm s}^{-1}$ , the angle of inclination was  $+55^\circ$ ,  $0^\circ$  and  $-15^\circ$ , respectively. The authors explain this with the (digitized) step sizes of the e-beam, which are made smaller when the scan speed is decreased. It is assumed that Gaussian shaped e-beam (0.8 nm diameter) creates Gaussian shaped deposits at each step of the e-beam. In Fig. 29c, a schematic drawing is depicted for three scan speeds: 0.8, 4 and  $24 \text{ nm s}^{-1}$ . At every new step, the beam is positioned somewhere on the slope of the already existing deposit. For a low, intermediate or high scan speed, this position is above (position A), around (position B) or below (position C) the initial height of the substrate. Hence, the inclination of the rods is dependent on the scan speed. Similar results were found by [127] for depositions in an ESEM.

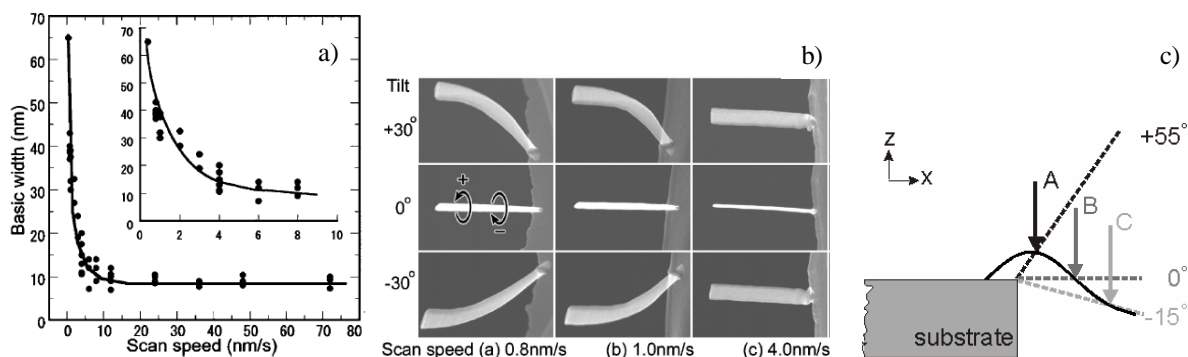


Fig. 29. (a) Width dependence of self-standing rods as function of the scan speed. (b) The dependence of the angle of inclination on the scan speed. (c) Schematic drawing of the effect of changing the scan speed [132].

## V.D. Writing direction

### V.D.1. Height

It has been observed that the writing direction with respect to the precursor source can be of influence on the vertical growth rate. The effect of the position of the gas nozzle was tested by depositing lines at a constant speed [134]. At the starting position of the line, a tip of constant height was deposited. The line was written from this tip towards the nozzle, or from this tip away from the nozzle (see Fig. 30). Considerably more material was deposited when the beam was scanned towards the gas nozzle than when it was scanned away from the gas nozzle, although the final line height remains constant. This dependency of the vertical growth rate on the orientation with respect to the nozzle was also found for other patterns. The proposed explanation is that the coverage of precursor molecules is not constant over the surface of the

tip. The side of the tip facing the gas nozzle has a higher coverage of precursor molecules than the side of the tip away from the gas nozzle. This shadowing effect causes the lower growth rate for the line that was written away from the gas nozzle. Estimations of the precursor coverage  $N$  in the shadowed areas based on the kinetic theory of gas quantitatively agree with the experimental results.

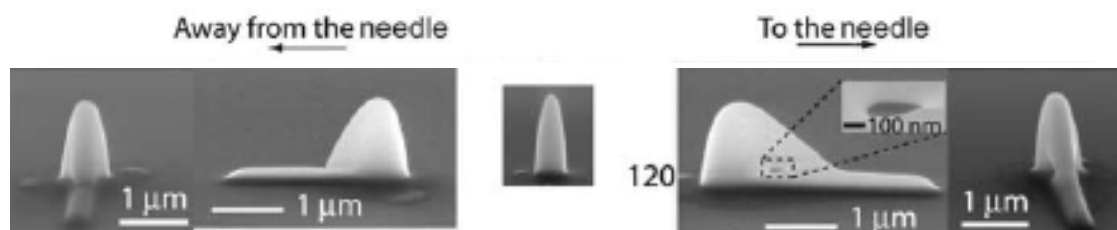


Fig. 30. The effect of the writing direction with respect to gas nozzle. A tip was deposited, followed by a line deposition. When the line was written away from the nozzle, significantly less material was deposited than when the line was written towards the nozzle [134].

A similar dependency was observed in an experiment where the precursor supply was mainly by diffusion over the surface instead of through the gas phase [20]. A small amount of paraffin was placed on a Si wafer and used as a precursor for the deposition a square about 35  $\mu\text{m}$  away. An complete AFM image of this square is shown in Fig. 24d and the height profile over line A in that figure is shown in Fig. 31. It shows that the side closest to the paraffin source (O) is higher than the side furthest away from the paraffin source (O').

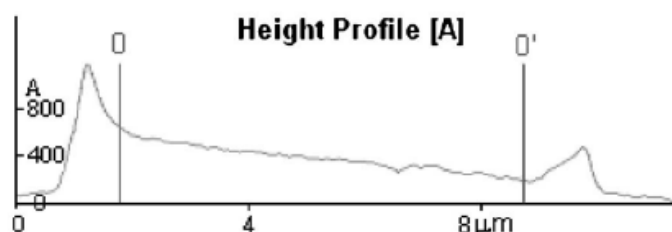


Fig. 31. Height profile of a square, demonstrating the influence of the direction of the precursor supply. The precursor source was located about 35  $\mu\text{m}$  away, on the left side of O.

#### V.D.2. Composition and morphology

The position of the gas nozzle with respect to the deposit can influence the deposit morphology, as can be seen in lateral cross sections taken from tips deposited from  $\text{Co}_2(\text{CO})_8$  [92]. For the image in Fig. 32, the gas nozzle was positioned on the right side. A cobalt-poor region is found in the area towards the gas nozzle, consisting of Co nanocrystals embedded in a matrix of a-C. This cobalt-poor region is asymmetrically surrounded by a crust with larger Co-grains (see also Fig. 16). In paragraph III.B.2, it was explained that the core/crust effect was probably due to EBIIH. The authors suggest that the Co-poor region is directed towards the gas nozzle as a consequence of a cooling effect of the arriving precursor molecules. The cooling effect is absent on the side of the tip that is shadowed from the gas nozzle and there EBIIH leads to the larger Co-grains in the surrounding crust. The shadowing effects can also lead to void formation in tips deposited with a high beam current (82 nA) [92].

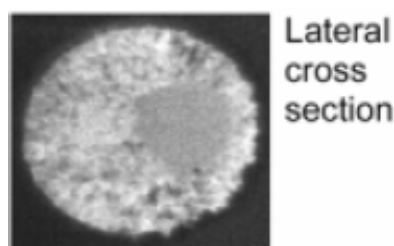


Fig. 32. Cross section demonstrating the influence of the direction of the gas nozzle. A Co-poor region is found off-center, on the side facing the precursor supply [92].

### V.E. Proximity effects

#### V.E.1. Deposit location

A proximity effect is strictly speaking not really a parameter that can be varied, such as for instance the beam current or the PE energy. However, a significant number of proximity effects has been reported until now for EBID, arising from different causes. Since these effects can significantly influence the final deposit shape or deposit distribution over the surface, we feel that a dedicated paragraph is justified. Proximity effects are well known in resist based electron beam lithography (EBL). It is usually caused by BSE's and presents itself as an extra and unintentional exposure of the resist layer surrounding the irradiated areas. Several types of proximity effects have already been reported for EBID, where matters are more complicated due to the fact that the irradiated targets are growing and therefore change in shape.

An effect similar to that in EBL, here called the "BSE proximity effect", was reported by for instance Lau *et al.* [12], Boero *et al.* [35] and Edinger *et al.* [30]. Extra deposition can be observed as a halo around the base of tips (Fig. 33a) or around lines (Fig. 33b). In Fig. 33b, the width of the halo was much larger on the SiO<sub>2</sub> than on the (pre-fabricated) pure Au pads. This is consistent with the larger backscatter range of the incident PE's for SiO<sub>2</sub> than for Au. Since the backscatter range is (amongst others) dependent on the energy of the incident PE's, working at low acceleration voltages is beneficial in reducing this proximity effect.

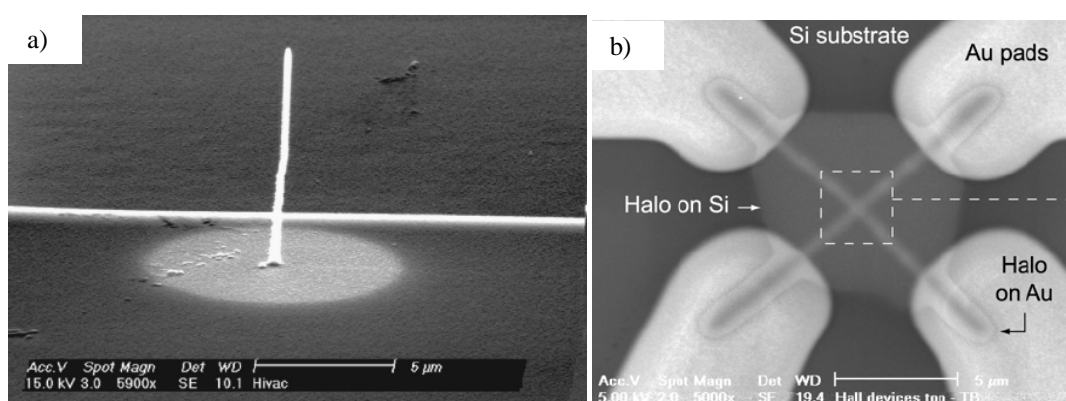


Fig. 33. Examples of a proximity effect as it is known in EBL. (a) A halo around a deposited tip [12]. In the article, no comment is given on the presence of the white line in the image. (b) A halo round deposited lines [91]. The width of the halo is larger on the Si than on the Au.

There is a proximity effect that is similar to the BSE proximity effect, except for the fact that it causes parasitic deposition on larger length scales. It was observed when a tall tip was grown on a substrate on which small Si particles were scattered [69]. Parasitic deposition was observed in the entire area surrounding the tip, but not in locations directly behind the Si particles (see Fig. 34). This excludes the BSE proximity effect, since that causes radially decreasing yet uniform parasitic deposition. Here, the parasitic deposition is caused by the spraying of high energy electrons that are scattered in the growing tip. These electrons have a much larger range than BSE's and will be blocked by obstacles in their path (such as Si particles). Although strictly speaking any electron that has undergone a scattering event and has an energy  $>50$  eV is defined as a BSE, this effect is here called the "FSE proximity effect". A few articles report parasitic deposition that can probably be attributed to this proximity effect. Zhang *et al.* [135] have observed parasitic deposition on very thin electron transparent membranes, where the substrate is too thin for BSE's to play a significant role (see Fig. 34b). Secondary ion mass spectroscopy (SIMS) performed by Gopal *et al.* [114, 136] has shown that Pt was distributed around a tall tip in an area many tens of micrometer wide (see Fig. 34c and d). They explained this by thermally assisted diffusion of dissociated species over the surface. Under influence of EBIIH of the grown tip, the life time of dissociated precursor molecules would then be sufficient to diffuse over large distances. We think, in the light of the above described experiments, it is more likely that the parasitic deposition is the result of the FSE proximity effect.

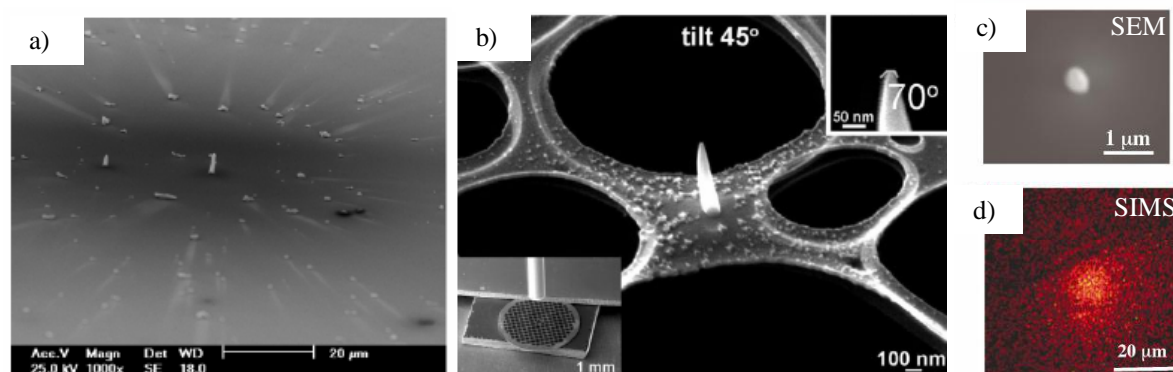


Fig. 34 (a) The shadowing effect of PE scattering from a growing tip ( $[\text{IrCl}(\text{PF}_3)_2]_2$ ) can be observed behind the surrounding Si particles [69]. (b) Growth of Fe crystals around a growing tip, deposited from  $\text{Fe}(\text{CO})_5$  [135]. (c) SEM image of a tip deposited from a Pt-precursor. (d) The SIMS map shows a wide spread of Pt deposition in the area surrounding the dot [114].

Several authors reported a type of proximity effect where parasitic deposition occurred on already existing structures when new deposits were created in the close vicinity. This was found for self-standing rods (Martin *et al.* [137], Aristov *et al.* [138]), dots (Lau *et al.* [12]) and tips (Mølhave *et al.* [127]). Aristov *et al.* have observed that the upper rod in Fig. 35a thickened as result of the fabrication of the lower rod, even though the deposition parameters were identical. Lau *et al.* deposited an array of dots with constant dwell time and observed

that the dots written earlier in the array were considerably thicker (Fig. 35b, array written from top to bottom, left to right). Aristov *et al.* suggest that the extra deposition is caused by SE spraying from the structure that is being fabricated. This effect is here called the “SE proximity effect”. In reality, the energy of the electrons is not measured and in principle, this unintentional growth can in principle also be caused by  $>50$  eV electrons which are scattered or generated in the newly grown structure. It is therefore possible that there is no fundamental difference between the FSE and the SE proximity effect.

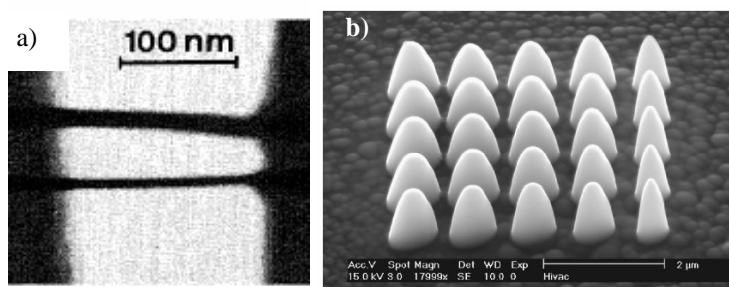


Fig. 35. Examples of the SE proximity effect. (a) During the writing of the second (lower) rod, the first (upper) rod became thicker [138]. (b) An array of dots, written from top to bottom, left to right. With the deposition of every new dot, previously written dots have become thicker [12].

Hiroshima and Komuro [75] and Van Dorp *et al.* [139] have reported studies on a proximity effect that is different from the proximity effects discussed until now in the sense that it affects the structures that are being written instead of the structures that are already present at the time of writing. The amount of material that is deposited under the electron beam (excluding parasitic deposition as result of the proximity effects described above) appears to be larger when the e-beam irradiates the side of an already existing structure than when it irradiates a flat area on the substrate. Hiroshima and Komuro observed a surprisingly high vertical growth rate when depositing lines in a single slow line scan, while Van Dorp *et al.* observed an increase in amount of deposited material when writing parallel lines with constant dwell time at a spacing of roughly the same magnitude as the width of the lines. The amount of deposited material is found to be proportional to  $1/\sin(\alpha)$ , where  $\alpha$  is the angle between the substrate and the e-beam. The effect is called here the “slope dependent proximity effect”. Van Dorp *et al.* found a good (qualitative) correlation between the SE emission from the irradiated structure and the extra amount of growth due to the proximity effect. However, this does not necessarily imply that the extra deposition is caused by enhanced SE emission from the sidewall of the irradiated structure. When one pictures the adsorbed precursor molecules as a uniform adsorbant layer, the probability for dissociation by PE’s increases with decreasing  $\alpha$  due to the enhanced path length through that adsorbant layer.

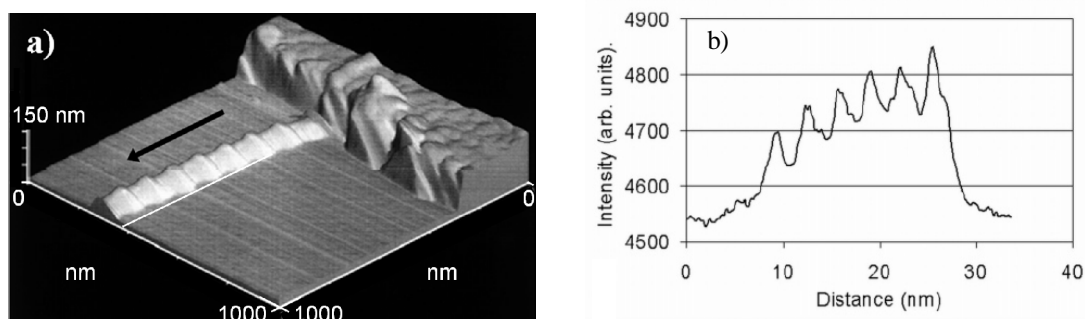


Fig. 36. (a) AFM image of a wire composed of stitched 80 nm long segments. At each start of each new stitch, extra material was deposited even though the accumulated charge was constant over the entire segments. [75] (b) Proximity effect as observed by Van Dorp *et al.* Lines were written from left to right [139].

In general, the deposition is assumed to be primarily the cause of dissociation by electrons. Experiments by Aristov *et al.* [138, 140] have indicated that surface plasmons can also contribute to the growth of EBID deposits. When positioning a stationary  $\sim 1$  nm beam about 35 nm away from the edge of a Fe film (circle in Fig. 37a), a protrusion grew away from the edge into the electron beam after an irradiation time of 160 s (Fig. 37b). EELS measurements suggested that the protrusion consisted of carbon (solid spectrum in Fig. 37c). When the EELS spectrum was recorded while the electron beam was positioned about 10 nm away from the protrusion, a peak of energy losses around 18 eV was observed (dotted spectrum in Fig. 37c). This value is clearly different from the plasmon loss energy for the carbon (25 eV) and indicates that surface plasmons (whose maximum energy for a-C is 17.7 eV) are responsible for the growth of the protrusion.

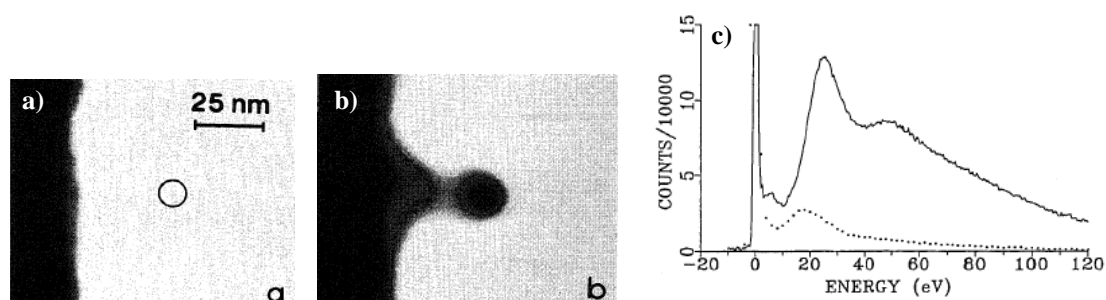


Fig. 37. An example of a proximity effect caused by surface plasmons. (a) Situation before and (b) after the electron beam was positioned in the circle. (c) The EELS spectrum when the e-beam is positioned on the protrusion (solid line) and 10 nm away from the protrusion (dotted line). The peak just below 20 eV is indicative of surface plasmons.

A proximity effect that is fundamentally different from all other types of proximity effect discussed until now, was observed by several authors [140, 127, 141]. It was observed that (initially straight) tips can bend when a new deposit is fabricated in the direct vicinity. This deformation can also occur during irradiation without precursor gas present and the bending of the pillar is generally in the direction towards the irradiated neighboring area. Fig. 38a shows 2 pillars which are bent plastically as result of post-deposition irradiation. Mitsubishi *et*

*al.* [141] came to the conclusion that the deformation was the result of charging. During the deposition of the second (lower) rod in Fig. 38b, electrons are emitted from the second rod itself. This leads to positive charging of the second rod, while the first rod is negatively charged. The opposite charges lead to deformation. Repeating the writing of the same pattern on a conducting Au-coated carbon substrate showed that this deformation proximity effect did not appear (Fig. 38c). This indicates that the bending and plastic deformation is caused by charging. Another strategy of avoiding the charging proximity effect is to use an alternating scan sequence, where the desired structures are grown simultaneously by scanning alternately.

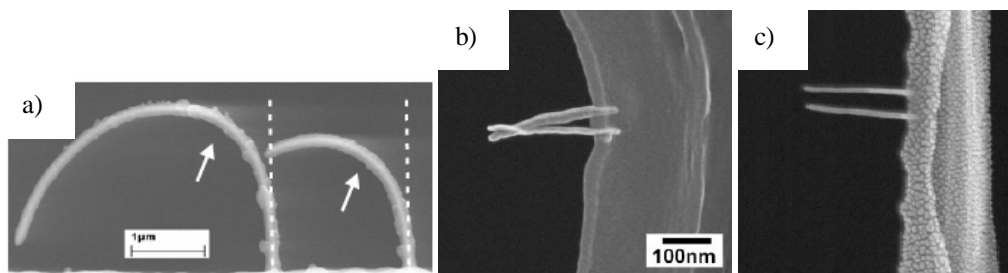


Fig. 38. (a) Deformation by post deposition imaging [127]. (b) Deformation of the upper rod as result of the fabrication of the lower rod. (c) The deformation in (b) can be prevented by writing the pillars in an alternating pattern or by using a conductive substrate. (b, c) from [141].

#### V.E.2. Composition and resistivity

It is interesting to note that the composition of the parasitic deposits resulting from the different types of proximity effects can be quite different from the intended, primary deposit. Lau *et al.* [12] have found a lower Co concentration in the parasitic deposits that were the result of the BSE and/or the SE proximity effect. The parasitic deposits typically have about 8 at% Co, whereas the primary deposit contains 35-45 at% Co. The lower metal content in the parasitic deposits drastically influenced the measured resistivity of EBID fabricated arches over 2 electrodes (Fig. 39a). The arches were written by alternately irradiating the two legs with decreasing spacing. While irradiating one leg, parasitic material was deposited on the other. The measured resistivity decreased significantly when tips were deposited, from which the authors conclude that the parasitic deposit has caused the high resistivity of the arches. Consistent with these observations, Molhave *et al.* [19] found a lower metal content in the parasitic deposits of the SE proximity effect. A layer with very low gold content formed on already deposited tips at the side that faced the irradiated spot nearby. In contrast to these findings, Zhang *et al.* [135, 142] and Shimojo *et al.* [77] have found the parasitic growth of bcc  $\alpha$ -Fe crystals when irradiating a small area on a-C membranes for prolonged dwell times (40-60 minutes) in the presence of  $\text{Fe}(\text{CO})_5$  (Fig. 39b). The presence of deposits outside the irradiated primary area can be explained with the FSE proximity effect.

It is surprising that the metal content is lower in the parasitic deposit (compared to the primary deposit) when using  $\text{Co}_2(\text{CO})_8$  or  $\text{Me}_2\text{-Au-acac}$  and higher when using  $\text{Fe}(\text{CO})_5$ . For  $\text{Fe}(\text{CO})_5$ , Zhang *et al.* [135] explain this by the time dissociated molecules have to re-arrange into a more energetically favourable position. Precursor molecules that are dissociated in the

primary irradiation area (the growing tip) do not get enough time to re-arrange because of the large number of PE's that impinge on a small area, and therefore the tip becomes amorphous. In the surrounding area, the current density on the substrate as result of the FSE proximity effect is much less and dissociated precursor molecules get more time to re-arrange.

There is some evidence to support this mechanism.  $\text{Fe}(\text{CO})_5$  is known to thermally decompose at temperatures as low as room temperature [143] or autocatalytically in the presence of Fe [144]. And an indication of the mobility of dissociated precursor molecules comes from an experiment by Ketheranathan *et al.* [145] with  $\text{Me}_2\text{-Au-acac}$  in a TEM. While irradiating the sample with a broad beam, cluster growth was observed in the bright field transmission images (Fig. 39c). The clusters nucleated, increased in size and sintered during the deposition process. This behavior suggests that dissociated precursor molecules diffuse over the surface to more energetically favourable positions. Similar mechanisms may have occurred during the parasitic depositions with  $\text{Fe}(\text{CO})_5$ .

For the Co and Au precursors, the mechanism might have been different. The thermal decomposition temperatures are well above room temperature and although autocatalytic decomposition has been reported for  $\text{Co}_2(\text{CO})_8$  (see also paragraph III.B.2), this still requires a temperature of about 60 °C [146]. This temperature was not reached for the parasitic deposits, nor for the primary deposits (judging from the absence of anomalously high growth rates such as in Fig. 15). So the Co or Au content of the parasitic deposits is perhaps a base value, which can become higher in the primary deposit due to the higher current density (more electrons to induce the desorption of fragments) or due to modest EBIH.

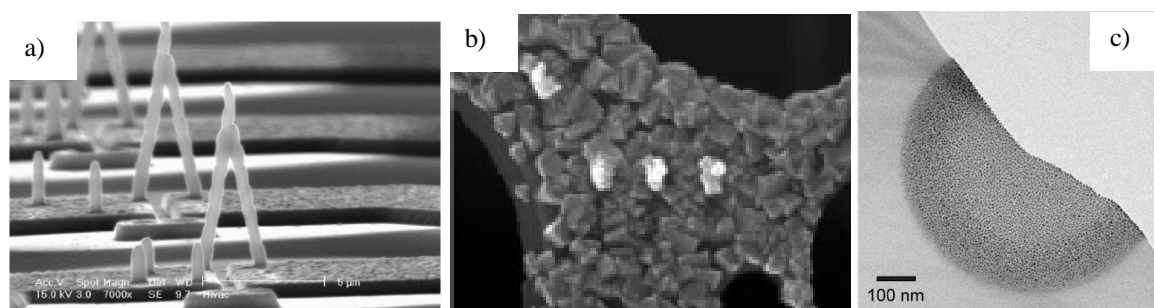


Fig. 39 (a) The measurement of the conductivity of deposits from  $\text{Co}_2(\text{CO})_8$  [12]. (b) Around 3 intentionally deposited tips, the parasitic deposition of Fe crystals was found [135]. The precursor was  $\text{Fe}(\text{CO})_5$ . (c) Cluster formation for broad beam deposition from  $\text{Me}_2\text{-Au-acac}$  [145].

#### V.F. Conclusions

In experiments where the main precursor supply mechanism is diffusion, the central part of a pattern can become depleted of molecules and fresh precursor molecules diffusing inwards are dissociated on the edge of the pattern. These effects are well reproduced by a continuum model and a Monte Carlo simulation reported in literature. The deposit composition and morphology will only be affected by the scan pattern if EBIH occurs. Beneficial for a high vertical growth rate is a scan strategy where dwell times are short and loop times are long. Beneficial for a high conductivity is a scan strategy where dwell times are long and loop times

are short. The two competing processes are on the one hand a high probability for an electron to dissociate a precursor molecule and on the other hand a large number of electrons per precursor molecule to achieve a high degree of fragmentation. The deposit height profile will be affected if loop times are so short that the surface is not replenished and growth is precursor-limited. This will result in deposition on the edge of the pattern, not in the central part.

If a line is scanned in a single pass and the scan speed is increased from 0 nm/s onwards, a transition will be observed from pillar-growth to line-deposition. This transition involves the growth of periodic, fence-like structures. This behavior is explained by variations in the balance between the vertical growth rate and the length of the precursor diffusion path. For high resolution self-standing deposits, the width and the inclination of the lines depend on the scan speed.

The writing direction with respect to the precursor source can affect the vertical growth rate for  $\mu\text{m}$ -sized deposits. The side of the structure facing the precursor source has the highest vertical growth rate. During deposition where EBID occurs and the precursor is supplied by a gas nozzle, the arriving precursor molecules can have a cooling effect. This is shown to have an effect on the deposit morphology.

Six types of proximity effects are identified and explained. These effects cause parasitic deposition (on ranges varying from nm's to tens of  $\mu\text{m}$ 's), affect the deposition rate of the primary deposit or cause deformation of neighboring deposits. It is observed that the composition, morphology and conductivity of parasitic deposits can be dramatically different from the primary deposit. There are indications that mechanisms such as EBID and autocatalytic decomposition were involved, but conclusive evidence is missing.

## **VI. Additional circumstances**

### *VI.A. During experiments*

#### *VI.A.1. Substrate heating*

##### *VI.A.1.a. Height and width*

Substrate heating has been shown as early as 1960 to have a large influence on the vertical deposition rate. The deposit heights as function of the temperature (at constant accumulated charge) are shown in Fig. 40. The overall trend is that the deposit height decreases with an increasing substrate temperature.

As discussed in paragraph III.C, a higher  $T$  will lead to a smaller residence time  $\tau$  hence a smaller probability that a precursor molecule is dissociated. Hence, the deposit height decreases. This trend is consistent with nearly all reported results in Fig. 40 and qualitatively confirmed by some authors [29, 15, 147]. Li *et al.* [67] show that this model is valid only for a specific regime: the electron-limited regime. For low beam currents (51 pA in this experiment) the deposition yield was only a function of  $\tau$ . At high beam currents (403 pA and higher) a precursor-limited regime was reached. The dissociation rate on the top of the tip was now not only a function of  $\tau$ , but also of the diffusion length of precursor molecules and the spatial distribution of the electron emission sites on the tip sidewall.

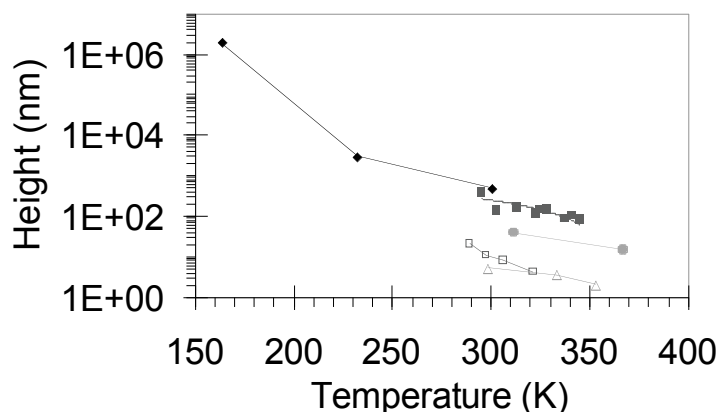


Fig. 40. Deposit height as function of temperature.

- |   |                   |                  |       |
|---|-------------------|------------------|-------|
| ◆ | WF <sub>6</sub>   | Matsui et al.    | [148] |
| ■ | WF <sub>6</sub>   | Randolph et al.  | [44]  |
| ● | TMA               | Ishibashi et al. | [149] |
| □ | Alkyl naphthalene | Ishibashi et al. | [149] |
| △ | Contamination     | Christy          | [6]   |

Another factor that can complicate the deposition behavior at nonambient temperatures is the precursor chemistry. This is what Matsui *et al.* (◆, Fig. 40) [148] observed when they deposited W from WF<sub>6</sub> on SiO<sub>2</sub> in a temperature range of -110 to 160 °C. For temperatures below 50 °C, the relatively simple relationship described above (a decrease of growth rate with an increase in temperature as result of shorter residence times) was valid. But at temperatures above 50 °C etching of the substrate occurred instead of deposition. The authors explained their results by assuming that the induced process involved both deposition and etching at all temperatures, and that the etching became the most influential process above 50 °C. The sensitivity of the precursor chemistry to the combination of substrate and precursor becomes clear from the fact that Li *et al.* [67] did not observe any etching of the Si substrate by WF<sub>6</sub> at temperatures above 50 °C.

If the substrate temperature is high enough, thermal decomposition can occur parallel to electron induced decomposition. For instance, for Fe(CO)<sub>5</sub> only electron induced decomposition is found at room temperature, while at 250 °C pure thermal decomposition is found. At an intermediate temperature (125 °C) a combination of electron induced and thermal decomposition was found [144] and the deposition efficiency was anomalously high (40 molecules per PE). This appeared to be due to catalytic effects, since small deposits continued to grow after the electron flux had stopped. Similar combinations of electron and thermally induced decomposition can also lead to the oriented growth of small crystals. When irradiating a Si(111) substrate, kept at temperatures between 400 °C and 600 °C, in the presence of Fe(CO)<sub>5</sub>, small iron silicide rods (length 10-80 nm, width 5-10 nm) developed along step edges [150, 151]. While the width of the rods stayed constant, the length of the rods increased with increasing dwell time.

Finally, at low temperatures condensation effects can occur. Ochiai *et al.* [152] observed that at a temperature of -12 °C so much material (other than the intended film) was deposited

that the pattern written with the electron beam could not be seen anymore. The authors mention that the condensation seems to be “enhanced by the electron beam irradiation”, but give no further details.

A direct influence of the temperature on the width of deposited pillars is not observed. Kohlmann *et al.* [72] have measured the dependence of the deposit width on substrate temperature, but have found no significant effect. Li *et al.* [67] did observe an effect, but that was indirectly the result of the growth regime. At high beam currents, the top of the pillar becomes depleted of precursor molecules and diffusion over the side walls of the pillar becomes the main source of precursor supply to the top. At lower temperatures, many of the molecules diffuse onto the pillar but are dissociated before they reach the top. At higher temperatures, the diffusion speed increases and less molecules are dissociated on the side walls. As a result, the pillar width increases with decreasing temperature (see Fig. 41).

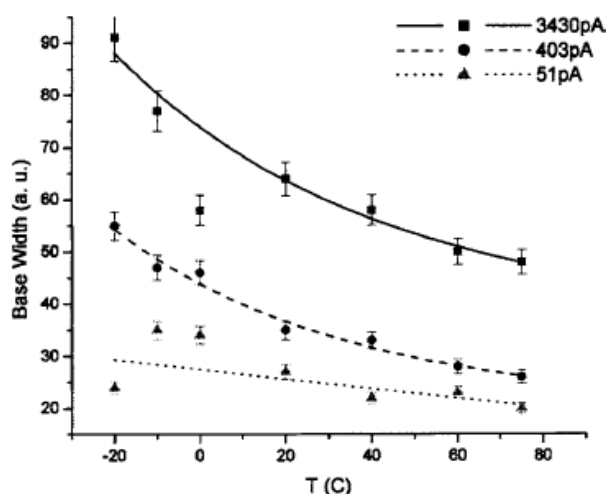


Fig. 41. Relative width of a tip as function of temperature, for different beam currents [67].

#### VI.A.1.b. Composition and morphology

Nearly all experiments where the metal content of the deposit was studied as function of the substrate temperature show a consistent trend: a higher temperature leads to a higher metal content. Fig. 42 shows the results for  $\text{WF}_6$  [148],  $\text{Me}_2\text{-Au-tfac}$  [153, 90],  $\text{Pt}(\text{PF}_3)_4$  [65] and trimethyl-gallium (TMG) in combination with cracked  $\text{AsH}_3$  [147].

This trend will be caused partially by the fact that the amount of adsorbed contamination (from the residual gas) decreases with temperature. But there are also precursor specific differences. The effect of substrate heating is very strong for the Au and Pt precursor. Wang *et al.* [65] suggest that the higher metal content at higher temperatures in their experiments is the result of the increased desorption of volatile groups. While electrons usually only affect the P-F bond (see also paragraph VIII.B), the raised temperature could increase the probability that the complete  $\text{PF}_3$  ligand is removed after electron impact. Another (possibly parallel) mechanism is that atoms or fragments that are separated after electron impact desorb more easily at higher temperature and are not trapped in the deposit. A similar mechanism could perhaps also explain the strong increase in metal content as function of temperature for

the Au precursor and the somewhat smaller increase of metal content in the deposits from TMG and cracked AsH<sub>3</sub>.

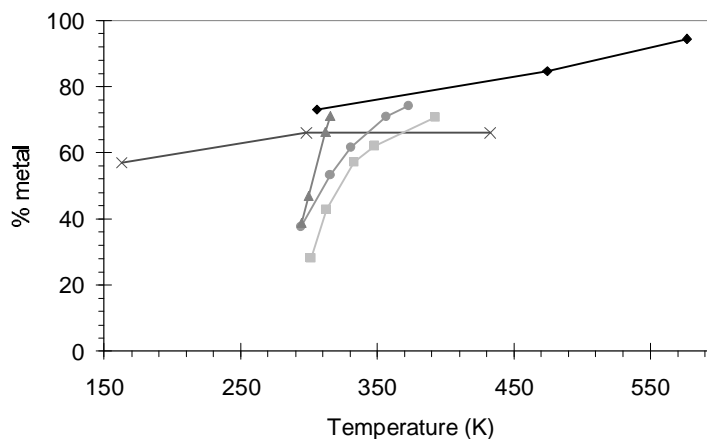


Fig. 42. The temperature dependence of the metal content.

- ◆ TMG and AsH<sub>3</sub> Takahashi *et al.* [147]
- × WF<sub>6</sub> Matsui *et al.* [148]
- Me<sub>2</sub>-Au-tfac Koops *et al.* [153]
- ▲ Me<sub>2</sub>-Au-tfac Weber *et al.* [90]
- Pt(PF<sub>3</sub>)<sub>4</sub> Wang *et al.* [65]

The effect of the temperature is rather weak for depositions with WF<sub>6</sub>. F is hardly detected (2% or less) for the temperature range used in the experiment [148]. Apparently, F is volatile enough to desorb completely even at low temperatures, in contrast to fragments of precursors described above. The other components in the deposit are C and O, most likely originating from the residual gas.

#### VI.A.1.c. Conductivity

If the general trend is that the metal content increases with increasing substrate temperature, then one would expect that the conductivity of deposits also increases. There are not many articles reporting measurements of the resistivity of the deposit as function of the temperature during deposition, but the available reports are consistent with this hypothesis. A resistivity of 10<sup>-4</sup> Ωcm was measured for deposits from Me<sub>2</sub>-Au-tfac at 80 °C [153], while this was 10<sup>-2</sup> Ωcm at room temperature [33]. In another report, a decrease in resistivity of a factor of 2 was reported for the same precursor when the substrate temperature was increased from room temperature to 60 °C [126].

#### VI.A.2. Tilting during deposition

In general, nearly all of the depositions are done with the sample surface perpendicular to the focused electron beam. There are two reports where the effect of tilting of the sample on the deposition rate has been measured. Using Fe(CO)<sub>5</sub> as a precursor, the deposition rate on a Au substrate was studied for two angles: 90° and 30° (angle between beam and substrate). The

deposition rate increased from  $8.5 \times 10^{-4}$  atoms/e<sup>-</sup> to  $1.2 \times 10^{-3}$  atoms/e<sup>-</sup>, respectively, a factor of around 1.4 [144]. Under the same conditions, the SE emission increased by a factor of 2. In another study specific numbers were not mentioned, but the deposition yield and the SE yield showed a similar dependence on the angle between beam and specimen [103].

These results are an indication that there is a correlation between the SE yield and the deposition yield. We have seen more indications of this in paragraph IV.B.1 and V.E.1, for instance. However, it needs to be remarked that, although there is a correlation, these experiments do not give a direct evidence that the deposition is caused merely by the SE's. Similar to the argument used for the slope dependent proximity effect (discussed in paragraph V.D.1), one can argue that the adsorbed precursor molecules form a layer covering the substrate. The length of the trajectory that the incident PE's travel through that layer increases with  $1/\sin(\alpha)$ , which is roughly similar to the angular dependence of the SE yield.

### *VI.A.3. Biasing sample during deposition*

In an attempt to fabricate narrower structures, Yavas *et al.* [154] have positively biased the sample to suppress the emission of SE's (no numbers given). The authors report that the pillar width was not affected by the bias.

That the expected result was not obtained by biasing the sample, is not surprising. The experiment was performed assuming that the SE's play a significant role in the deposition process. Supposing this assumption is correct, it is not straightforward to see how the bias would exactly influence the deposition process. In the first place, the emission of SE's may not have been suppressed. There is no electric field inside a conductor, so SE's will only be influenced by the electric field once they exit the sample. The bias affects the electron trajectories (redirecting them towards the sample), but does not suppress the emission of SE's. In practice, the deposit is not a perfect conductor, so the electric field will penetrate the deposit. But it is not clear to what extent this will influence the emission of the SE's. In the second place, SE's may not even need to exit the substrate in order to dissociate an adsorbed precursor molecule. It is conceivable that DEA or DD is possible when SE's approach the adsorbed molecule from the bulk of the substrate, without actually exiting the material. So without a better understanding of the influence of a bias on the SE behavior, this experiment is not very useful.

## *VI.B. Post-deposition treatment*

### *VI.B.1. Extra irradiation*

Post-deposition treatments are usually applied to improve the properties of the deposit and to remove unwanted fragments. One way to do this, is to expose the deposit to a high current beam after the precursor supply has been stopped. This extra exposure can have various effects, such as for instance graphitization. When exposing a-C deposits from contamination in the SEM to an 80 keV beam in a TEM for several minutes, a significant part of the a-C was transformed into graphite [24]. Other types of morphological change are also possible: the surface of a tip (~8 um high, deposited from hfac-Cu-VTMS) changed from smooth to rough when the apex of the tip was observed with a high current beam [91]. Interestingly, this

change occurred over the entire surface of the tip even though only the top part was irradiated (the tip was viewed under a tilt angle of  $70^\circ$ ). Apart from affecting the morphology, post-deposition irradiation can also affect the conductivity. For deposits from  $\text{Fe}_3(\text{CO})_{12}$ , it was reported that “additional irradiation of high-resistance lines (preliminarily deposited at low beam current values) at high  $I$  values leads to a considerable increase in the conductivity of lines” [95]. Similar results were found for deposits from  $\text{W}(\text{CO})_6$ , where the resistivity decreased with a factor of 20 [76]. And finally, post-deposition irradiation can be used to sculpt a deposit. A freestanding wire of about 10 nm width was grown in the SEM (from TEOS), after which the wire was exposed to a 200 keV high current electron beam in a TEM. The irradiation caused a relative increase of the Si content and a decrease in the width of the wire down to 1 nm before finally breaking [155].

The effect of the extra exposure can be the result of several (parallel) mechanisms. It can be the completion of the (initially) partial decomposition of the precursors, or the formation of volatile components with the help of residual background gases. The change in morphology of the copper tip seems to indicate that the influence of EBIH can be significant, because the bottom of the tip was affected without having been exposed (after deposition) to the e-beam. For the experiments in the TEM, knock-on damage by high energy ( $>50$  keV) electrons is a likely mechanism behind the changes in properties, especially since it strongly affects light elements in the target.

### VI.B.2. Annealing

#### VI.B.2.a. Composition

Apart from an extra post-deposition exposure, the deposit properties can also be improved with annealing. Free-standing, amorphous rods (deposited from  $\text{Fe}(\text{CO})_5$  on Si) changed into single-crystal  $\alpha$ -Fe when annealed under UHV-conditions at a temperature of  $600^\circ\text{C}$  [156, 157, 158]. Carbon and oxygen were hardly detected in the annealed rods and the shape remained almost unchanged. When repeating this procedure for deposits grown on a carbon grid, the deposits contained iron carbide or polycrystalline  $\alpha$ -Fe. Apparently, material from the substrate moves into the final deposit during annealing. The incorporation of elements from the substrate was also found for thin a-C films deposited on Si(100) from ethylene. At temperatures above 1170 K, the a-C film turned into SiC [159].

In other cases, crystals in an amorphous matrix are formed. After *in situ* annealing of selfstanding deposits created from  $\text{Cr}(\text{CO})_6$ ,  $\text{W}(\text{CO})_6$  and  $\text{Re}_2(\text{CO})_{10}$  nanocrystals ( $\sim 20$  nm in size) formed [160]. Electron diffraction of the crystals showed that the rhenium deposits contained pure Re crystals. For the other two materials, various phases were present, amongst others carbides. The growth of crystals was also found after the annealing of a rod deposit from hfac-Cu-VTMS [91]. Initially, the tip was smooth and showed uniform contrast, with the diffraction pattern showing mainly randomly oriented small Cu crystallites. Above temperatures of  $140^\circ\text{C}$ , larger Cu crystals formed. The tip morphology is shown in Fig. 43.

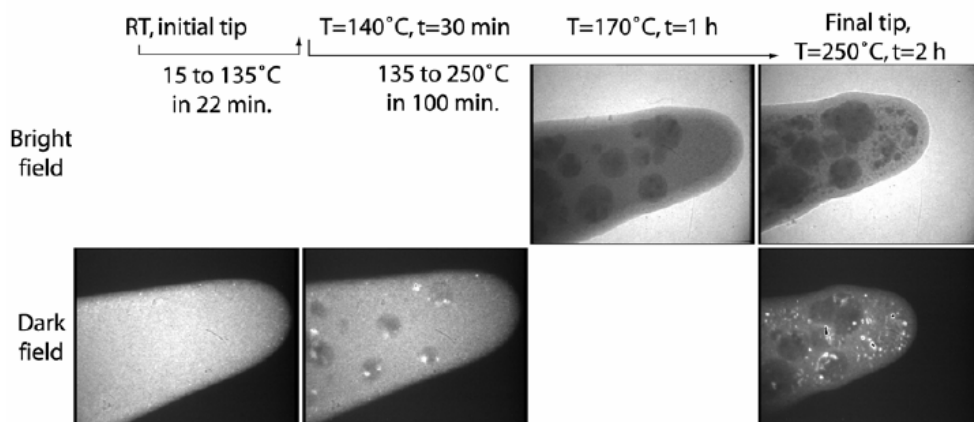


Fig. 43. Annealing of a rod deposited from *hfac*-Cu-VTMS [91].

Crystallization is found not only for metals, but also for carbon. When freestanding a-C rods are annealed in the presence of iron nanoparticles, the a-C can be converted into graphite [161, 162, 82]. An example is shown in the TEM micrographs in Fig. 44. At a temperature of 650 °C, iron particles migrated into the nanorod and graphitized the carbon as they did so.

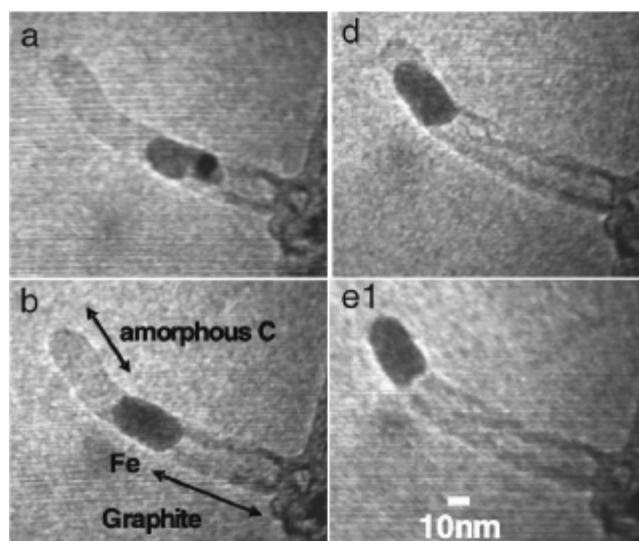


Fig. 44. Graphitization of carbon nanowire by an iron particle [161]. The annealing temperature was 650 °C.

Finally, when nanoscale deposits are annealed, annealing can entirely destroy the structure. While this did not occur for the Fe-deposit described above, it clearly occurred for a pattern consisting of Pt-containing dots. The dots were a few nanometers in size and when heated to a temperature of 800 °C, it was found that the pattern was completely deformed [163].

#### VI.B.2.b. Conductivity

For carbon structures that are graphitized during annealing, the conductivity clearly increases. Already in 1934, Steward studied films deposited from contamination [164]. When testing the conductivity with a telephone receiver, he found that the initially isolating film had

become conducting after heating the platinum substrate “bright red *in vacuo*”. The amorphous carbon had most likely turned into graphite. Similar results were found for graphitized nanorods, for which the resistivity decreased from  $68.9 \text{ } \Omega\text{cm}$  to  $5.2 \times 10^{-4} \text{ } \Omega\text{cm}$  [82].

Positive results have also been found for metal containing deposits. Deposits from  $\text{WF}_6$  showed an improvement of a factor of 10 when annealed at  $500 \text{ }^\circ\text{C}$  in a  $\text{H}_2$  atmosphere [165]. An improvement in conductivity of as much as 3 orders of magnitude was observed for deposits that were created with a low beam current. This is probably due to the fact that in those particular deposits, the dissociation of the precursor molecules was less complete and relatively more precursor fragments desorbed. See also Fig. 45. Annealing was also beneficial for the conductivity of deposits from  $\text{CpPtMe}_3$ . For wires, annealing for 2 hours at  $180 \text{ }^\circ\text{C}$  led to a drop by a factor of 3 in the resistance [96]. For tips used as emitters, the field emission current and the reliability of the emitters increased when annealing between  $400$  and  $750 \text{ }^\circ\text{C}$  [166].

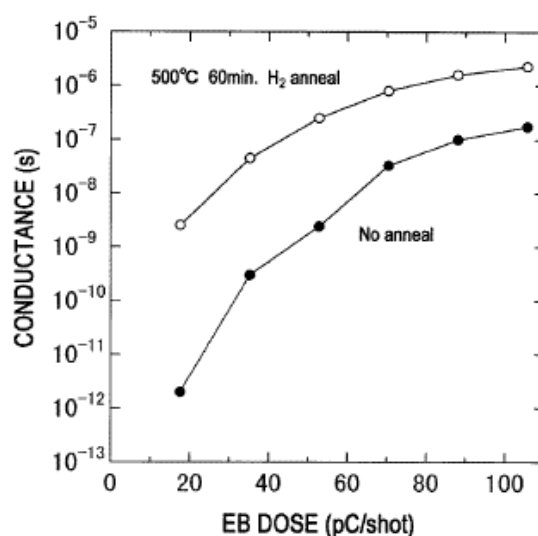


Fig. 45. The effect of annealing of wires deposited from  $\text{WF}_6$ . For wires deposited with a low beam current, the annealing has a stronger effect, up to as much as 3 orders of magnitude [165].

Annealing does not always improve the conductivity. For instance, annealing at  $170 \text{ }^\circ\text{C}$  for 10 minutes had no effect on wires deposited from  $\text{Fe}_3(\text{CO})_{12}$  [95]. The temperature may not have been high enough, since annealing at  $600 \text{ }^\circ\text{C}$  did give an effect for similar Fe containing deposits [156, 157, 158]. But even at high temperatures, annealing does not necessarily lead to improved conductivity. Annealing of lines deposited from  $\text{Me}_2\text{-Au-tfac}$  or  $\text{Co}_2(\text{CO})_8$  at temperatures around  $300 \text{ }^\circ\text{C}$  gave de-wetting instead of wetting: the lines separated into solidified droplets [126, 108, 167]. Apparently, the amorphous carbon matrix had oxidized and disappeared, leaving the (oxidized) metal grains.

### VI.C. Conclusions

It is consistently reported that a higher substrate temperature during deposition leads to lower vertical growth rates. This is caused by shorter residence times of adsorbed precursor

molecules. The lateral growth rate is only affected if the temperature leads to a change in the growth regime. If the substrate temperature is in the order of the precursor thermal decomposition temperature, dissociation can be thermally-induced parallel to electron-induced. This has been observed for a number of metal-organic precursors. The result is a higher metal content and a higher conductivity.

Experiments where the substrate is tilted during deposition indicate that there is a correlation between the deposition yield and the SE yield.

Post-deposition irradiation induces graphitization of a-C deposits, it can induce EBIH (thereby changing the deposit morphology from smooth to rough), the deposit conductivity can increase and deposits can be sculpted.

Post-deposition annealing can graphitize a-C deposits and can improve the metal content for metal containing deposits. Having said this, carbon appears to be an element that is difficult to remove by annealing. In most reported cases, carbon was generally still present in the deposit after annealing, often in the form of carbides. The formation of carbides is unfavourable, because it is a thermodynamically very stable compound. Another issue is the diffusion of substrate material into the deposit (observed for C, Si and Fe) and the deformation of the structure. The conductivity generally improves, provided the deposit stays intact and de-wetting does not occur.

## VII. Substrate

Important for the understanding of the physics of the deposition process is whether the substrate is of any influence. An influence can either be expected for substrate-precursor interactions (e.g. adsorption) or for electron-substrate interactions (e.g. SE yields). The first type of interaction was suggested to explain experiments where thin films (tens of Ångstroms thick at most) were deposited from  $WF_6$ . It was found that the growth rate on Si is higher than on Au (at the same pressure) [168]. According to the authors, the difference in growth rate is the result of a smaller adsorption coefficient of  $WF_6$  on Au than on Si. This seems likely, since the SE yield is in general larger for Au than for Si [169].

However, in most other studies, deposits are thicker and the relevant surface is the deposit surface, not the substrate surface. So in most cases, the electron-substrate interactions are dominant instead of the substrate-precursor interactions. The former become visible as differences in BSE and SE yields and in the spatial extent of the electron scattering in the substrate. Indications of the influence of BSE and SE yields come from experiments and simulations on, again, deposition on Au and Si. A Si sample was partially coated with a 500 nm layer of Au and deposition was performed over the edge of the Au layer with hfac-Cu-VTMS. The vertical growth rate was a factor of about 1.5 larger on the Au than on the Si [91]. This ratio compared well to calculated BSE yields for the two situations. Unfortunately, the deposition yields for a carbon precursor (acrylic acid) on the same substrate agree less well with the simulated BSE and SE yields. The author tentatively suggests a slightly different dissociation process (radical or ion assisted) but still assumes that the model is correct.

As far as the vertical growth rate is concerned, one would expect that the influence of the substrate is negligible when depositing tips. For most of the time, the interactions take place

in the tip and not in the underlying substrate. This theory is confirmed by experiments where tips were deposited on Al, Ti, Cu, W, Mo and Pb. There was no significant effect of the substrate on the vertical growth rate, composition or morphology [91]. Contradicting results were found for the deposition of selfstanding contamination rods. Different growth rates were observed for various substrates (amongst others Al, Ti, Cu, W) [170]. But since the residual gas was used as precursor and cleaning procedures of the substrates were not described, the concentration of residual gas molecules on the samples may not have been constant. Furthermore, one would expect substrate effects to be very small, because the majority of the relevant interactions occur on the growing selfstanding rod, nearly completely away from the substrate.

More clear examples of the influence of the substrate-electron interactions come from experiments where the deposit width is studied. For instance, when depositing contamination lines on GaAs and Si, significant shoulders on the lines were observed [119]. The width of the shoulders appears to be dependent on the substrate. Region 1 in Fig. 46a is the area where the PE's impinge on the GaAs substrate, region 2 indicates the range over which BSE's and SE's "interact with the substrate surface". They calculated the spatial extent of BSE scattering in the substrate for GaAs and Si and indicated this with the dashed lines in Fig. 46a and Fig. 46b, respectively. The calculated range is larger in Si than in GaAs, which is the result of the smaller density of Si. This coincides "fairly well" with the extent of region 2 for both samples. Furthermore, the measured height in region 2 is also less for Si than for GaAs, which is "consistent with the energy of the electron beam being scattered over a larger volume in the Si". This is a similar effect to the BSE proximity effect described in paragraph IV.E.1 (see also Fig. 33b). A similar dependency on the spatial distribution of electron scattering in the substrate was found for the diameter of tips. The diameter of tips deposited from CpPtMe<sub>3</sub> on Si, Cu and SiO<sub>x</sub> substrates were 199, 146 and 49 nm respectively, at identical accumulated charges [74]. These diameters "correspond with the main path length of those materials and the related proximity-function".

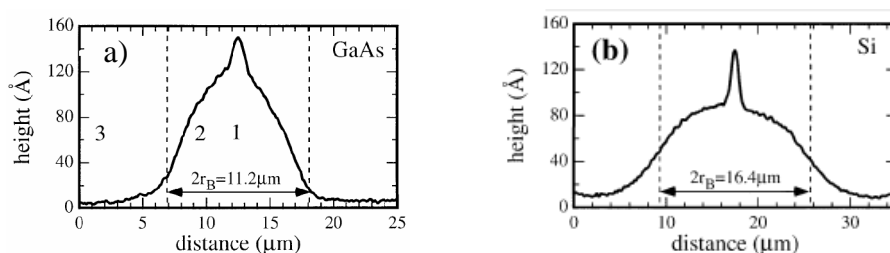


Fig. 46. Height profiles for line depositions on (a) GaAs and (b) Si [119].

Regarding the influence of the thickness of the substrate, there seems to be no effect on the width of deposits. Dots were deposited from W(CO)<sub>6</sub> on areas that were transparent (thin) and nontransparent (thick) to 200 keV electrons of a Si(110) sample. The width of the dots was not significantly influenced by substrate thickness [171]. This was confirmed by Monte Carlo simulations [172, 173].

Apart from adsorption behavior or the spatial extent of electron scattering, the conductivity of the substrate is also found to be of influence on the deposition process. An example of this, the deformation proximity effect, was already discussed in paragraph V.E.1. Depending on the conductivity of the substrate, already deposited structures were found to deform when new structures were grown in the neighborhood (see Fig. 38b and c). Another example is the growth of dendritic structures on insulating substrates such as  $\text{Al}_2\text{O}_3$  [174, 175, 176, 177], BN [178] and tetragonal zirconia crystals [179]. The dimensions of the structures can vary by orders of magnitude (see Fig. 47a and b) and the formation was observed for metalorganic precursors (e.g.  $\text{W}(\text{CO})_6$ ) and contamination. It is assumed that the dendritic growth is caused by charging of the sample. As a result of the charging, a local electric field is formed, which concentrates at convex areas. If the electric field is strong enough, (estimated field strengths in the order of  $10^6$ - $10^7$  V/m) precursor molecules in the gas phase are polarized and/or ionized and will follow deterministic instead of ballistic trajectories [178]. Similar growth was also observed for  $\text{W}(\text{CO})_6$  on 10 nm thick  $\text{Si}_3\text{N}_4$  membranes [180]. Arrays of dots were deposited in the STEM (Fig. 47c). When the sample was tilted, it became apparent that some of the dots were considerably higher than the average dots (Fig. 47d). These outliers also showed branching in some cases. This, and the fact that the irregular growth was not observed close to conducting areas on the substrate, is a strong indication that charging played a significant role.

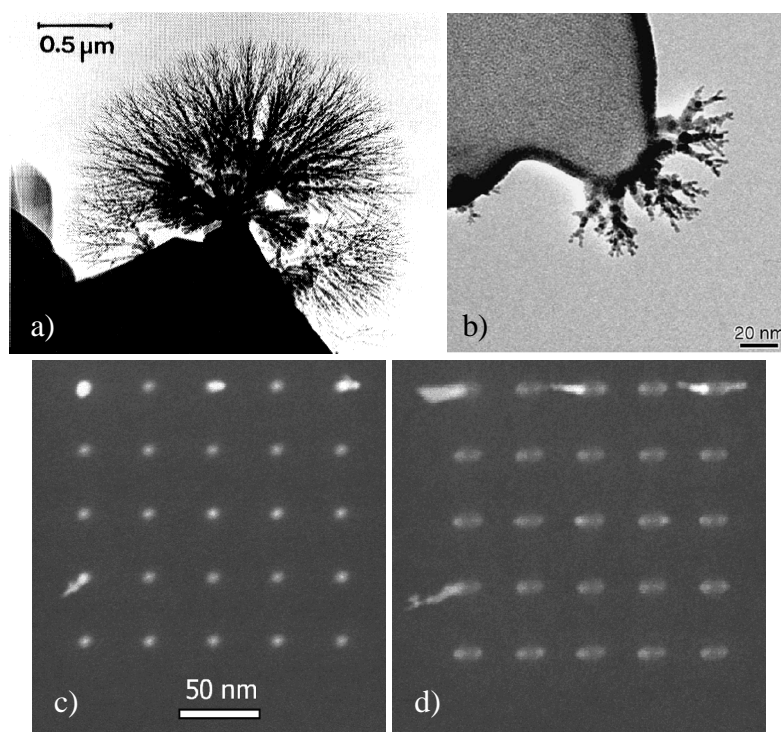


Fig. 47. Examples of the effect of an insulating substrate. (a) Dendritic growth from hydrocarbons on a BN crystal as result of broad beam illumination [178]. (b) Dendritic growth from  $\text{W}(\text{CO})_6$  on  $\text{Al}_2\text{O}_3$  as a result of broad beam illumination [174]. (c) An array of dots deposited from  $\text{W}(\text{CO})_6$  on  $\text{Si}_3\text{N}_4$ . (d) Same array as in (c), but now viewed under a tilt angle of  $20^\circ$ . The outliers are clearly higher than the average deposit and also show branching [180].

In conclusion, the substrate can affect the vertical growth rate. This can be due to changes in the adsorption behavior (for deposits several Å thick) and/or changes in the BSE and SE yields. The width of the deposits is found to be dependent on the spatial extent of the electron scattering in the substrate. The thickness of the substrate does not seem to affect the width of deposits. On insulating substrates, dendritic and irregular growth was observed, behavior that is most likely due to charging effects.

## VIII. Precursor

### VIII.A. Introduction

The precursor molecules contain the material to be deposited and as such, it is a crucial factor in the deposition process. Many different precursors have been tried for EBID. Fig. 48 shows that carbon precursors (residual gas, contamination in the electron optical system or carbon precursors) are most widely studied.  $W(CO)_6$ ,  $Fe(CO)_5$  and  $PtCpMe_3$  are the most popular metalorganic precursors and  $WF_6$  is the most frequently used anorganic precursor. Silvis-Cividjian and Hagen [45] present a fairly complete list of the precursors used, together with references.

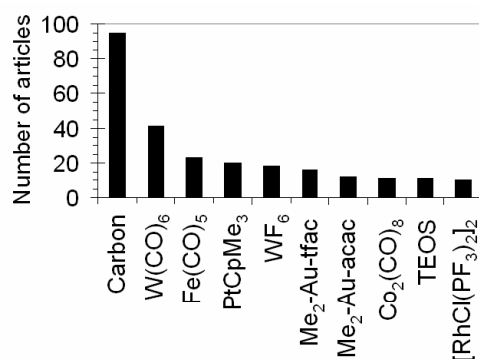


Fig. 48. Histogram of the number of articles that report on work on specific precursors. The 10 most popular precursors are shown.

According to Hoffmann [181], a suitable and useful precursor has a number of requirements: it needs to be a volatile compound at room temperature (either a gas, liquid or solid), it needs to decompose to the desired “product” in a fast, clean and highly selective way (ideally without additional reactant gas), vacuum contamination (corrosion) should not occur, it needs to evaporate completely, fast and without residue, it needs to be stable during storage and supply and it is preferably nontoxic and not expensive. On top of these requirements, we have to keep in mind that EBID experiments usually take place in high vacuum conditions and not in ultrahigh vacuum conditions. This means that there is a background pressure of water or air in the order of  $10^{-6}$  mbar. And still we want to have pure deposits.

At the moment, none of the precursors used for EBID reach the desired level of performance. Frequently used stable compounds such as  $W(CO)_6$  or  $PtCpMe_3$  yield deposits that contain typically about 10% metal.  $WF_6$ , a stable compound that yields a higher concentration of metal (80 – 100%) is an aggressive precursor that can damage electron optical equipment [182].  $AuCl(PF_3)_3$  or  $D_2GaN_3$ , precursors that are known to yield pure

deposits and are not aggressive, are very unstable and can be difficult or even dangerous to work with [183]. And a precursor such as  $\text{AuCl}_3$  does, in certain conditions, not yield any Au at all [184]. It can be safely stated that at the moment, the main factor limiting the application of EBID in devices is the lack of control over the composition of the deposits. Despite the importance of a good understanding of the dissociation mechanism for the progress in EBID research, the subject receives a relatively small amount attention compared to the other parameters described in this review. Improvement is mainly tried through tweaking of the beam parameters (beam current, acceleration voltage) or post-processing. The choice of precursor is mostly determined by the fact whether it is used often and whether it is readily available. Nearly all of the precursors used for EBID stem from the CVD world and there has been hardly any search for precursors dedicated to EBID.

### *VIII.B. Precursor gas only*

In order to make a start with the understanding of the dissociation mechanisms of precursors, systematic studies are required. There are a few such studies.

A study was made of the composition of deposits from purely organic precursors (styrene, acrylic acid, propionic acid, acetic acid and formic acid) and precursors containing fluorine, nitrogen and chlorine (trifluoroacetic acid, acetonitrile and  $\text{CCl}_4$ ). Analysis techniques used were EDX, micro elastic recoil detection analysis ( $\mu\text{ERDA}$ ), micro-Fourier transform infrared spectroscopy ( $\mu\text{FTIR}$ ) and micro-Raman. Surprisingly, the EDX,  $\mu\text{ERDA}$  and  $\mu\text{FTIR}$  measurements show that the deposits from the purely organic precursors are all chemically very similar [185, 91]. The composition is  $\text{C}_9\text{H}_2\text{O}_1$  (regardless of the stoichiometric composition of the precursor), 90-95% of the carbon is  $\text{sp}^2$  bonded (carbon - carbon), 5-10% is  $\text{sp}^3$  bonded (carbon - H) and the micro-Raman measurements indicate that the carbon deposits consist of nanocrystalline graphite with cluster sizes around 2 nm. Similar results are found for the precursors containing the components F, N and Cl. It was found that 90% of these specific components are lost during the deposition, either during precursor fixation or by continued irradiation of already deposited material during the deposition process. Analysis of deposits from two paraffins ( $\text{C}_{22}\text{H}_{46}$  and  $\text{C}_{24}\text{H}_{50}$ ) with EELS and Raman confirm these results [20]. Again, 80-90% of the carbon atoms was  $\text{sp}^2$  bonded and Raman studies showed a similar amount of disorder in the carbon.

Regarding the growth rate and the growth behavior, significant differences were found between acrylic acid and styrene. With a similar precursor flux reaching the irradiated area, acrylic acid has a 5 times higher growth rate than styrene [185]. This is most likely due to longer residence times of the acrylic acid molecules on the adsorption sites, which means its sticking coefficient is higher. This is caused by the fact that acrylic acid is a polar molecule and can form H-bonds, interactions which are much stronger than the Van der Waals forces for styrene.

Another difference is the deposit smoothness. While most of the precursors yield a smooth deposit, the deposits from formic acid are sometimes (and not reproducibly) rough and have a hollow structure (see Fig. 49) [185]. Apparently, electron-induced desorption of volatile

elements occurs inside the deposits after precursor fixation because these volatile elements are present in the precursor in a high ratio compared to the carbon ( $C/(O+H) = 1/4$ ).

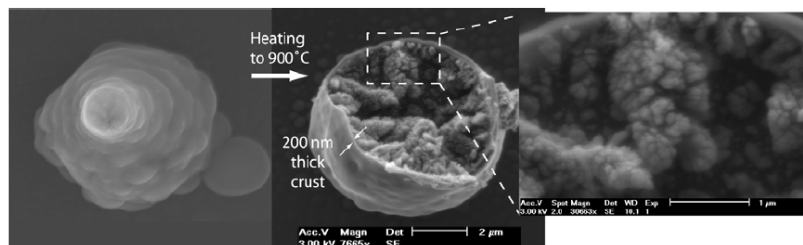


Fig. 49. Hollow pear shaped deposits from formic acid [91].

In another comparative study, the composition of deposits from 4 Cu-precursors was determined:  $Cu(hfac)_2$ ,  $hfac-Cu-MHY$ ,  $hfac-Cu-VTMS$ ,  $hfac-Cu-DMB$ . For  $Cu(hfac)_2$  and  $hfac-Cu-MHY$  stable compositions of 13-14% Cu and 75-80% C were found during sputtering cycles [129]. The Cu content for  $hfac-Cu-VTMS$  and  $hfac-Cu-DMB$  was estimated to be 15-20% and 60-70% C. The fluorine signal was not above the noise level. The authors conclude that the Cu content is not determined by the stoichiometric composition of the precursors, but more by the thermodynamic precursor stability and the electron/precursor flux ratio. These results are mostly consistent with experiments where the composition of physisorbed multilayers and deposits from  $hfac-Cu-VTMS$  was studied. It was found that the electron bombardment mostly affects the fluorine and oxygen containing groups in the  $hfac$  ligands, while the  $CH_x$  groups from the  $VTMS$  and  $hfac$  ligands remain mostly unaffected [56].

Two Rh precursors,  $[RhCl(PF_3)_2]_2$  and  $[RhCl(CO_2)]_2$ , appear to have very similar decomposition paths [112]. The composition for both precursors was independent on the accumulated charge, which indicates that the deposit is chemically quite stable. The Rh content was 60% and 56%, resp. and the Cl content was 7% and 5%, resp. The elements that are at the core of the precursor molecules are present in relatively high concentrations (19% P for the carbon-free precursor, 34% C for the carbon-containing precursor) and fluorine was not detected in either of the deposits. These experimental results are in contradiction with a theoretical model made for  $[RhCl(PF_3)_2]_2$ . Calculations based on density functional theory on the lowest energy pathways for decomposition indicate that the loss of the  $PF_3$  ligands is most favourably [186]. However, the electron beam induced deposits contain P and no F. Similar results were obtained for  $Pt(PF_3)_4$ . It was found that electrons mainly induce scissions of the P-F bond [65] and not the removal of complete PF ligands as in the case for thermal decomposition in CVD. The discrepancy between results from EBID on the one hand and results from calculations and CVD on the other, suggests that the electron induced dissociation is more complex than just a simple single-step process.

Few differences were observed between deposits from three Au precursors:  $Me_2-Au-acac$ ,  $Me_2-Au-tfac$  and  $Me_2-Au-hfac$ . For all precursors, the deposit composition is 10% Au, 20% O and 70% C for beam currents  $>900$  pA [33]. Again, fluorine is not detected. This indicates that the decomposition mechanism is similar.

For the cases described above, the dissociation was electron induced. In some of the preceding chapters and paragraphs, it has become clear that the contribution of thermal decomposition to the growth can be significant. In general, this is beneficial for the purity of the deposits, but in some cases the size and/or precise location of the deposit is more difficult to control. This was for instance observed when creating deposits with a large accumulated charge ( $\text{Co}_2\text{CO}_8$  [92]), with high beam currents ( $\text{Me}_2\text{-Au-acac}$ ,  $\text{Me}_2\text{-Au-tfac}$ ,  $\text{Me}_2\text{-Au-hfac}$ ,  $\text{Cu(hfac)}_2$ ,  $\text{Mo(CO)}_6$ ,  $\text{Me}_3\text{PtCp}$  [90],  $\text{Co}_2\text{CO}_8$  [92],  $\text{Co(CO)}_3\text{NO}$  [12],  $\text{hfac-Cu-VTMS}$  [91]) or in situations where the thermal conductivity of the deposit was low ( $\text{hfac-Cu-VTMS}$  [120]). And indications of autocatalytic effects were found for  $\text{Fe(CO)}_5$  [142]. These thermal effects are clearly precursor dependent. As an example, no thermal effects have been observed for  $[\text{RhCl(PF}_3)_2]_2$ , even though different scan patterns and deposition conditions have been tried [186].

Despite the indications that thermal effects are involved, it is not so easy to link the above mentioned effects to the thermal decomposition temperature. The precursors  $\text{Co}_2(\text{CO})_8$  and  $\text{hfac-Cu-VTMS}$  showed thermally enhanced decomposition and have a low thermal decomposition temperature: 60 °C [146] and 63 °C [129], respectively.  $\text{Fe(CO)}_5$  has demonstrated steady-state thermal decomposition even at -20 °C [143]. For these precursors thermally assisted decomposition has been observed during EBID. As mentioned, thermally assisted decomposition was not observed for  $[\text{RhCl(PF}_3)_2]_2$ , which also has a much higher thermal decomposition temperature (160 °C [187]). So far the trend is consistent, but this trend is contradicted by the thermal decomposition temperature of  $\text{Co(CO)}_3\text{NO}$  and  $\text{Me}_2\text{-Au-hfac}$ : 162 °C [188] and 160 °C [189], respectively.

Further evidence of the complexity of the dissociation process comes from studies on the proximity effects and the deposition on insulators. From the discussion of the various proximity effects in paragraph V.E.2 it became apparent that the composition of parasitic deposits can be very different from the primary deposits. And the composition of dendritic structures created on insulating substrates (discussed in paragraph VII) can also be very different from the usual, nondendritic deposits. For instance, deposits created from  $\text{W(CO)}_6$  are usually are nano-composites [133], with small W crystals in an a-C matrix. But the dendritic structures obtained on insulating surfaces were pure bcc tungsten crystals [174]. In contrast, dendritic structures created on insulators from the Pt precursor were not pure Pt, but nanocomposites [176].

Such contradictions, together with the observations that (1) in some cases the stoichiometric composition of a precursor seems to be irrelevant for the deposit composition (for the mentioned C, Cu and Au precursors) and (2) that EBID does not necessarily follow either the theoretically calculated lowest energy pathway or the thermal decomposition path, shows that the dissociation mechanism is not so simple as one may initially expect. The results also show that further detailed studies into the precursor chemistry and dissociation mechanisms are required to be able to improve the deposit composition.

### VIII.C. Reactive gases

Although the precursor chemistry is complex enough when the precursor gas is the only gas, as became clear in the preceding paragraph, it is possible to influence the decomposition mechanism by mixing in additional gases, so called reactive gases. The idea is that the reactive gas forms volatile components with unwanted fragments that otherwise remain on the sample after the dissociation of the precursor molecules. This prevents these fragments from polluting the deposit. Strictly speaking, nearly all experiments described in this review are done in the presence of a reactive gas. After all, the typical EBID system has a background vacuum of no better than  $10^{-6}$  or  $10^{-7}$  mbar, which is mostly due to the presence of water and air. Depending on the cleanliness of the system, carbon contamination will also be present. So during a typical EBID experiment, precursor molecules will be competing with for instance water molecules for surface adsorption sites and there will always be oxidizing components available to react with dissociation fragments.

However, there is a number of reports where the pressure of reactive gases was raised significantly above the background level. In a relatively simple example of precursor chemistry, the effect of mixing  $H_2$  with  $WCl_6$  during deposition was tested [148]. This made the W content increase from 95% to 100%, probably by the formation of HCl. Using a more complicated combination, Folch *et al.* [190] mixed 130 mTorr of  $Me_2-Au-hfac$  with 3 Torr of  $H_2O$  and with a mixture of 2 Torr of  $O_2$  and 8 Torr of Ar. While the Au content of squares deposited without reactive gas was 2-3% at most, this increased to 20% when  $H_2O$  was added and increased to about 50% when the Ar/ $O_2$  mixture was added. According to the authors,  $H_2O$  or  $O_2$  are ionized by the electron beam, react with the C from the deposits and form  $CO_2$  or CO. This would explain that the Ar/ $O_2$  mixture has more effect than the  $H_2O$ , because there is more O present. Molhave *et al.* [19] performed a similar experiment. They used a similar precursor ( $Me_2-Au-acac$ , partial pressure not reported), mixed in 0.4-0.9 Torr  $H_2O$  and instead of depositing squares, they deposited tips and wires. The results are quite different. The Au content increased, but not homogeneously distributed over the deposits. The gold was concentrated mostly in the core of the tips and wire, surrounded by a shell of amorphous carbonaceous material. This particular core-shell structure could only be fabricated in the presence of water; mixtures of  $H_2$  and  $O_2$  with the same amount of H and O as 0.8 Torr of  $H_2O$  did not have such an effect. That the effect of  $H_2O$  on the deposit composition is far from consistent, becomes evident from experiments by Crozier and Hagen [191].  $Me_3PtCp$  was mixed with  $H_2O$  and no influence was found on the deposit composition.

Wang *et al.* [65] have introduced  $O_2$  during deposition from  $Pt(PF_3)_4$ , but the Pt content increased only by a small amount, from around 17% to around 22 at%. Better results were obtained by Fischer *et al.* [109], who added oxygen during the deposition of  $SiO_2$  (precursor not mentioned) and were able to create carbon-free deposits.

### VIII.D. Precursor pressure

It is consistently reported that higher gas pressures lead to higher growth rates [29, 64, 149, 192]. In Fig. 51 the growth rate is plotted as function of the current density for 3 different  $Ru_3(CO)_{12}$  fluxes: (1) =  $3 \text{ cm}^{-2} \text{ s}^{-1}$ , (2) =  $1.5 \text{ cm}^{-2} \text{ s}^{-1}$ , (3) =  $0.9 \text{ cm}^{-2} \text{ s}^{-1}$ . As the precursor flux

increases, so does the growth rate. In the initial stages, the growth is electron-limited. In the final stages, the growth is precursor-limited.

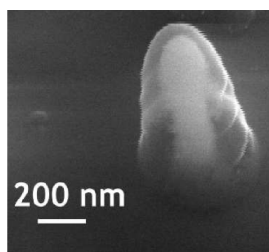


Fig. 50. Core-shell structure for a tip deposited from  $Me_2\text{-Au-acac}$  in the presence of  $H_2O$  [19].

A simulation has been developed to determine the local distribution of precursor molecules on the substrate for the supply from a gas nozzle typically used in EBID experiments. In the Monte Carlo simulation, molecular flow conditions are assumed. The distribution from the model is compared to the height distribution of impinging precursor molecules that are thermally dissociated on a heated substrate. A good quantitative agreement is found (see Fig. 51b) [193].

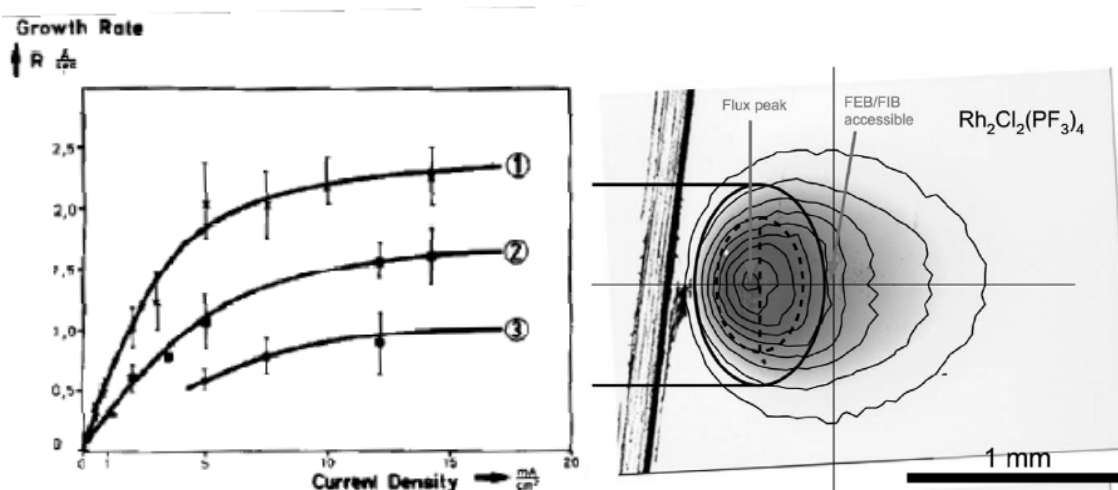


Fig. 51 (a) Growth rate as function of the current density for 3 different  $Ru_3(CO)_{12}$  fluxes. Precursor flux 1 =  $3 \text{ cm}^{-2} \text{ s}^{-1}$ , 2 =  $1.5 \text{ cm}^{-2} \text{ s}^{-1}$ , 3 =  $0.9 \text{ cm}^{-2} \text{ s}^{-1}$  [64]. (b) Comparison of the impinging precursor distribution between experiment (grey scale height map) and simulation (isodensity contours) [193].

Some reports mention the existence of a minimum gas pressure required for deposition. A pressure threshold of  $8.6 \times 10^{-4} \text{ Pa}$  was also found for deposition from  $CrO_2Cl_2$  [102]. Below this pressure, no Cr deposition was observed. It was found that etching of the (Cl-deficient)  $CrO_xCl_y$  film occurred during post-deposition irradiating in the presence of  $Cl_2$ . The authors suggest that there are 2 competing processes during growth from  $CrO_2Cl_2$ : dissociation of  $CrO_2Cl_2$  and recombination of  $CrO_xCl_y$  with Cl. But how the presence of these 2 competing processes would lead to the observed pressure threshold does not become quite clear. Pressure

thresholds were also found for  $W(CO)_6$  ( $1 \times 10^{-6}$  Pa) and  $Me_2-Au-acac$  ( $5 \times 10^{-7}$  Pa) [85]. Growth was not observed below these thresholds regardless of the beam current. The authors suggest that the a requirement for deposit growth is the presence of stable nuclei on the substrate. Below the mentioned precursor pressures, “the nuclei will not grow”. This would indicate a nonlinearity of a type that has not yet been reported elsewhere. Another explanation for the pressure threshold could be again 2 competing processes: this time dissociation of precursor molecules and knock-on damage by the PE’s. The PE energy was 200 keV and sputtering of the deposit nuclei by the PE’s is conceivable [51].

Morphological changes were observed for deposits from  $Ni(C_5H_5)_2$  as function of the gas pressure (range  $10^{-6} - 10^{-8}$  mbar) and substrate temperature (range  $-103 - 25$  °C). Depending on the precise conditions, uniform (Fig. 52a and b) or open structures (Fig. 52c and d) were found [81]. It appeared that the formation of uniform or open structures was determined by the ratio between the precursor partial pressure  $P_{\text{partial}}$  and the precursor equilibrium pressure  $P_{\text{equilibrium}}$  at the corresponding substrate temperature. Uniform deposits were formed for ratio’s  $P_{\text{partial}}/P_{\text{equilibrium}} < 1$ , open deposits were formed for  $P_{\text{partial}}/P_{\text{equilibrium}} > 1$ . How these conditions lead to the observed morphologies was not explained.

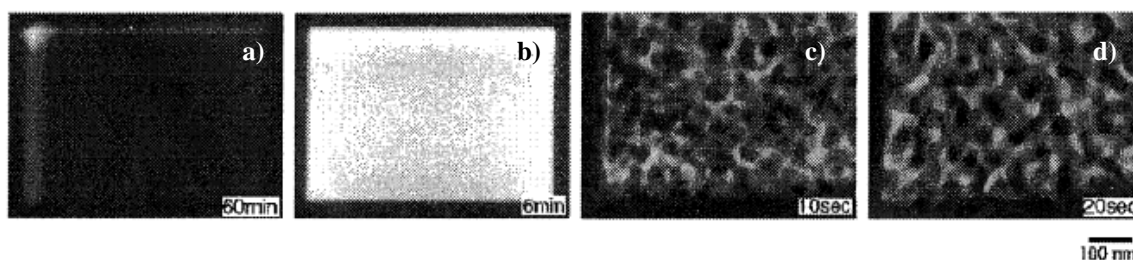


Fig. 52. The morphology of deposits from  $Ni(C_5H_5)_2$  was found to depend on the ratio between  $P_{\text{partial}}/P_{\text{equilibrium}}$ . The ratio’s  $P_{\text{partial}}/P_{\text{equilibrium}}$  are (a)  $1.7 \times 10^{-4}$ , (b)  $6.5 \times 10^{-4}$ , (c)  $1.8 \times 10^1$  and (d)  $9.6 \times 10^2$  [81].

### VIII.E. Conclusions

From the few systematic studies that have been performed, it becomes clear that electron-induced decomposition is a complex process. It is consistently reported that the deposit composition is not directly dependent on the stoichiometric composition of the precursor. For five purely organic precursors, the composition is constantly  $C_9H_2O_1$ . Most of the carbon is  $sp^2$  bonded, a small fraction is  $sp^3$  bonded. For four Cu precursors, the Cu content is 10-20% and a similar metal content is found for three gold precursors. Two Rh precursors, one having  $PF_3$ -ligands and the other  $CO_2$ -ligands, show similar decomposition paths. The elements at the core of the precursors (P and C, respectively) are present in relatively high concentrations. For all precursors, it is consistently reported that elements such as F, N and Cl are removed almost completely from the deposit. Further evidence of the complexity of the dissociation process comes from studies on the proximity effects and the deposition on insulators. The composition of parasitic deposits and dendritic deposits can be very different from the primary deposits.

For the Cu precursors, it is concluded that, rather than the stoichiometric composition, it is the thermodynamic stability of the precursor and the electron/precursor flux ratio that determines the final composition. For other precursors, this link is not so easy to see. For instance, the electron induced decomposition paths of the Rh precursors are very different from decomposition paths expected from calculations or thermal decomposition.

The influence of reactive gases is far from consistent. Adding H<sub>2</sub>O to Me<sub>3</sub>PtCp did not influence the deposit composition. Adding H<sub>2</sub> to WCl<sub>6</sub> or O<sub>2</sub> to Pt(PF<sub>3</sub>)<sub>4</sub> gave only a minor increase in metal content. The only cases where a significant effect was reported were for Me<sub>2</sub>-Au-hfac mixed with O<sub>2</sub> and Me<sub>2</sub>-Au-acac mixed with H<sub>2</sub>O. The former gave an increase in Au content from a few to twenty percent, the latter resulted in a Au core surrounded by an a-C shell.

A model has been developed to determine the distribution of gas molecules on a substrate for a nozzle geometry and results are consistent with experimental results. Higher precursor pressures lead to higher growth rates and in some cases a pressure threshold for EBID growth is reported.

## **IX. Conclusions**

In this review, the consistency of experimental results with each other and with existing models has been discussed. Most of the observed effects can be explained with available models. The lateral growth of deposits as function of the accumulated charge is characterized by a rapid increase followed by saturation. Deposits as small as 1.0 nm can be obtained by stopping the growth in the stage of rapid increase. At these small scales, the counting statistics of precursor molecules become visible as variations of the mass of the deposits. The vertical growth rate depends on the growth regime. In the electron-limited regime, the deposit height is proportional to the current density. In the precursor-limited regime, the deposit height depends on the gas flux. The substrate mainly affects the deposit dimensions, by the BSE and SE yields and the spatial extent of the electron scattering in the bulk.

Electron beam induced heating (EBIH) can play a significant role in EBID. Whether EBIH occurs, depends on the current density, the PE energy, the thermal conductivity of the deposit and the extent to which the electron scattering is confined to the deposit. The temperature rise as result of EBIH in specific cases is estimated to be about 50° C. Apart from reducing the vertical growth rate, EBIH can induce a change from electron- to precursor-limited growth. Additionally, it can lead to a change in the dissociation mechanism (see below). Similar effects are observed in experiments where the sample is heated during deposition. If the temperature reached during an experiment is in the order of the precursor thermal decomposition temperature, dissociation can be thermally-induced parallel to electron-induced. This has been observed for a number of metal-organic precursors. The result is a deposit with a (relatively) high purity, high density and high conductivity. This is the reason why high current densities are beneficial for the deposit properties; (1) a higher degree of electron-induced fragmentation is obtained and (2) EBIH occurs. The lateral growth rate is only affected if the temperature leads to a change of growth regime.

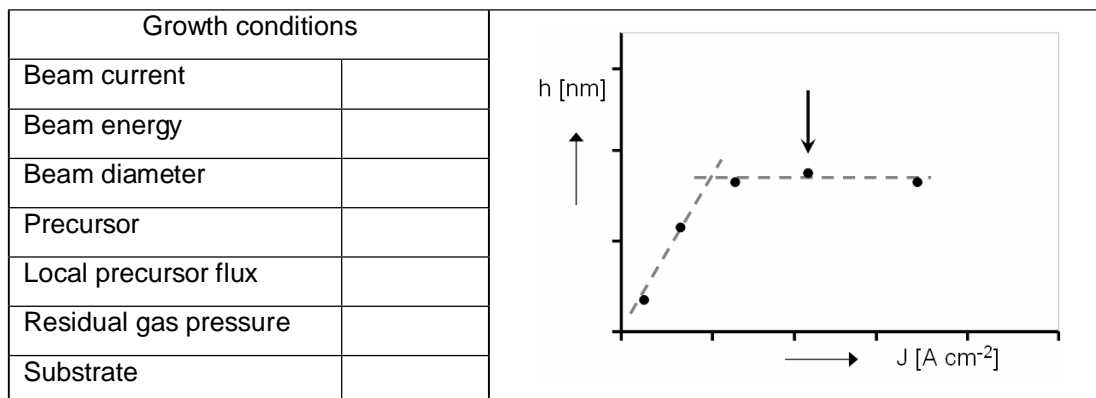
Studies of the influence of the PE energy on the vertical growth, composition, morphology and conductivity gave contradictory results. These contradictions could be explained to a large extent with a combination of the growth model and EBID, but this approach leaves some results unexplained. The scan pattern and scan strategy will mainly influence the deposit properties or the growth rate in the case that a change from the electron-limited to the precursor-limited regime (or vice versa) is induced. For instance, short dwell times and long loop times are beneficial for obtaining a high growth rate. On the other hand, long dwell times and short loop times are beneficial for obtaining a high-conductivity deposit. Post-deposition irradiation induces growth of metal crystals in metal-containing deposits and increases the conductivity. Post-deposition annealing can improve the metal content for metal containing deposits, although the treatment generally does not completely remove carbon.

Regarding the precursor chemistry, it is consistently reported that the deposit composition is not directly dependent on the stoichiometric composition of the precursor. For Cu precursors, it is concluded the thermodynamic stability of the precursor and the electron/precursor flux ratio are the main determining factors for the deposit composition. For other precursors, the electron-induced decomposition paths can be very different from those expected from calculations or thermal decomposition. It is consistently reported that elements such as F, N and Cl easily desorb during EBID. The influence of reactive gases is far from consistent. In a few cases the metal content significantly improves, in other cases a minor or even no change is observed.

From this review, it becomes clear that several major issues remain. A problem that is encountered when interpreting all the results from literature is the lack of information on the precise experimental conditions. Especially the local gas flux is often not mentioned, while this is important for getting an estimate of the regime in which growth occurred. To be helpful for the understanding of EBID, each report should at least mention the precursor, the local precursor flux (in units that allow a calculation of the number of molecules arriving at the irradiated spot per area per time unit), residual gas pressure, beam current, beam diameter, acceleration voltage and substrate. Ideally, articles are accompanied by a measurement of the deposit height as function of the current density (or deposited volume as function of the beam current) to demonstrate the growth regime in which the experiment of interest took place. Table IV shows an example of a checklist that can be used.

Secondly, the limited understanding of electron-induced precursor dissociation is an important issue. The situation in this review is perhaps typical: only about 10% of the pages are dedicated to the precursor chemistry. The precursor chemistry is one of the key factors determining the purity of the deposits and it is exactly the purity of the deposits that is the main limiting factor for a wider application of EBID. Now that elaborate continuum models and Monte Carlo simulations are being developed and a deeper understanding of the interplay between physical mechanisms (such as electron scattering, EBID and the growth regimes) emerges, it is time to develop a better understanding of the precursor chemistry.

*Table IV. Checklist that would ideally be included in every article reporting on EBID experiments. The essential experimental details are given, together with a measurement of the deposit height as function of the current density (or deposited volume as function of the beam current) to demonstrate the growth regime in which the experiment of interest (indicated with an arrow in the plot) took place.*



It was mentioned that the inconsistencies observed for variations of the PE energy cannot be fully explained. This may be related to the fact that the cross sections for dissociation are unknown. In several cases, a correlation between the vertical growth rate and the SE yield is observed (for variations of the PE energy, the slope dependent proximity effect and the deposition on a tilted sample). This correlation suggests that the contribution of the SE's is dominant over the contribution of direct dissociation by the PE's, but it is not hard evidence. Hard evidence will be difficult to obtain, since cross sections for SE generation and dissociative ionization of molecules in the gas phase show a similar dependency on the PE energy. If there is a significant contribution of the PE's to the growth, this is expected to occur only in the area irradiated by the PE's. Perhaps the only way to get an indication of the contribution of the PE's, is to model the growth of a tip for different PE energies. A comparison between the apex shapes from the model and from real experiments may give insight in the relative contributions of SE's and PE's.

To advance the understanding of EBID in a structural manner, Koops proposed the development of a standardized experiment [194]. In this experiment, deposition is performed under standard conditions with a standard precursor, which gives a common reference frame for future experiments. If inconsistencies still occur, they can be traced more easily to a specific difference between the experiments, thereby leading to a better understanding of the process. Finally, the development of EBID into a viable nanofabrication technique would benefit greatly from a 'diamond', a process that yields a deposit with properties that are widely applicable [194].

---

### 3. Experimental details

#### Contents

I. Precursor .....	74
II. Sample preparation .....	74
III. Experimental setup .....	75
IV. Pattern definition .....	75
IV.A. <i>ESVision</i> .....	75
IV.B. <i>Jscript</i> .....	76
IV.C. <i>National Instruments card</i> .....	76
V. ADF signal recording .....	77
V.A. <i>JScript</i> .....	77
V.B. <i>Picoscope and National Instruments card</i> .....	77

## I. Precursor

The precursors used for deposition experiments described in this thesis were  $W(CO)_6$  and contamination. All experiments with  $W(CO)_6$  were performed at the Center for Solid State Science at Arizona State University, where it was stored in a glass flask at room temperature. The same supply was used for all experiments.  $W(CO)_6$  was chosen because it is stable, commercially available, not very toxic, easy to handle and well known in literature. For contamination experiments, no special effort was made to increase or remove the amount of contamination on the sample.

## II. Sample preparation

Substrates used for deposition experiments were  $Si_3N_4$  membranes, amorphous carbon (a-C) membranes, quantifoils, BN crystals and graphite flakes. The  $Si_3N_4$  membranes were obtained from different sources (commercial products, fabricated at Philips in Eindhoven or fabricated at Dimes in Delft). It was found that the precise stoichiometry of the  $Si_3N_4$  can vary per manufacturer and the growth behavior of deposits on such membranes was sometimes found to be unpredictable and difficult to interpret. It is tentatively suggested that charging plays a significant role during deposition (see also Chapter 9).

Amorphous carbon (a-C) membranes were bought from a commercial supplier [195]. The thickness was 10 nm and the membranes were mounted on copper grids. The BN crystals were obtained from a commercial supplier.

For the preparation of electron transparent graphite flakes, it was found that ultrasonic exfoliation yielded the best results. Highly oriented pyrolytic graphite particles were dispersed in toluene (purity >99.999%) and put in a 600 W ultrasonic bath. After ultrasonic exfoliation for about 45 minutes, a few drops of the dispersion were placed onto a holey carbon TEM membrane using a pipette. This method does not yield freestanding sheets of graphite larger than about a few hundred nanometers, but the method is free of materials that are known to cause contamination. It was found for instance that exfoliation using adhesive tape gave very high levels of contamination in the electron microscope. Thin areas of graphite on the edges of the flakes provide very low contrast in the STEM, which makes them in principle very well suited for the study of the deposition behavior. Unfortunately, the graphite was not found to be homogeneous. Fig. 1a shows an ADF STEM image of typical graphite particle. The bright area in the top left is a (relatively) thick part of the graphite, the dark area in the bottom right is vacuum and in between is a thin area of graphite. On this thin part, there are brighter and darker areas. There was no precursor gas present during the imaging. Fig. 1b shows a bright field TEM image of a similar (though not identical) area. The darker area in the top left of the image is caused by a thicker part of the graphite particle and the vacuum is shown in the bottom right. The area in between is thin graphite. A blow-up of the boxed area shows lattice fringes (Fig. 1c) and the Fourier transform of this area shows the hexagonal symmetry typical of graphite (Fig. 1d). It is tentatively suggested that the brighter areas in Fig. 1a and the areas with noncrystalline contrast are fragments of graphite sheets remaining from the exfoliation process. These randomly distributed fragments make the graphite surface nonuniform and

give rise to very irregular deposit growth (see also Chapter 9). Therefore we chose to deposit on amorphous carbon samples instead.

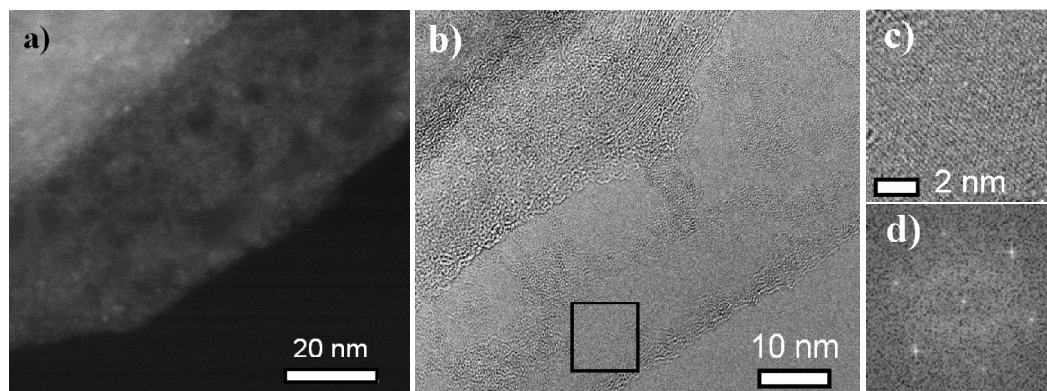


Fig. 1. (a) ADF STEM image of a thin part of a graphite particle. (b) Bright field TEM image of the thinnest part of a similar graphite crystal. (c) Blow-up of boxed area in (b), which shows lattice fringes. (d) Fourier transform of (c), showing hexagonal symmetry.

### III. Experimental setup

All experiments with  $W(CO)_6$  were performed on the Tecnai F20 environmental scanning transmission electron microscope (STEM) at the Center for Solid State Science at Arizona State University (see Fig. 2a). This 200keV microscope is equipped with a field-emission electron source and was operated in STEM mode with a nominal beam spot size of 0.3 nm with a current of approximately 3 - 30 pA. An electron energy loss spectrometer (EELS) is fitted for compositional analysis.

The environmental is designed to allow imaging at pressures of up to 10 Torr in the cell. Differential pumping is made possible by special apertures located in the upper and lower objective pole piece bores (first and second level pumping in Fig. 2b). The region above the condenser aperture and the viewing chamber (third level pumping) are evacuated by separate pumping systems. The pressure in the gas inlet is measured outside the microscope column. The column can be isolated from the gas handling system in order to switch between high vacuum TEM and ETEM modes.

The imaging performance in STEM mode is slightly limited by the differential pumping apertures (see Fig. 2b), causing the maximum collection angle of elastically scattered primary electrons to be only about 50 mrad. For high angle annular dark field imaging (or Z-contrast imaging), usually angles larger than about 50 mrad are used.

Experiments with contamination were performed on a standard FEI Tecnai F20 STEM at the Delft University of Technology and on a FEI Nova NanoSEM at Leiden University.

### IV. Pattern definition

#### IV.A. ESVision

On the Tecnai STEMs, the interface giving access to the scan coils is the program ESVision. The program is designed for STEM imaging and compositional analysis. It has the option to draw lines and arrays on the screen, which are translated by the program into beam

coordinates. For arrays, this works well for dwell times per position of more than  $\sim 0.5$  second. Shorter dwell times can be entered in the program, but the actual dwell times remain about a second.

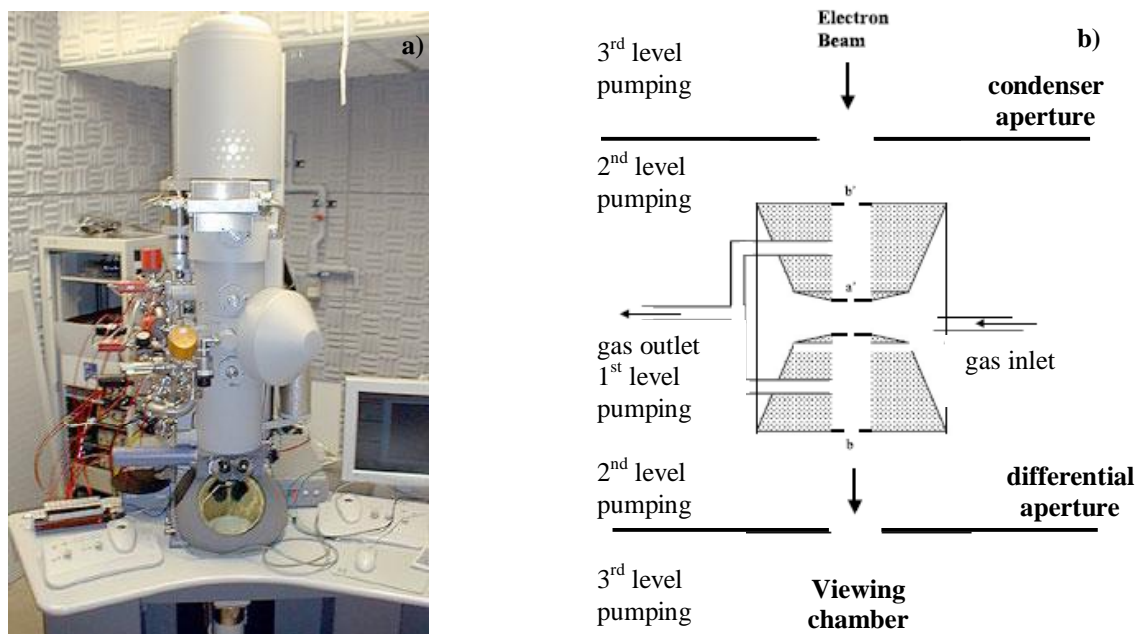


Fig. 2. (a) Tecnai F20 environmental scanning transmission electron microscope. (b) Schematic drawing of the environmental cell with the differential pumping apertures.

#### IV.B. Jscript

ESVision has the option to run scripts written in the Jscript language. With these scripts, the scan signals can be accessed either through the BeamControl command (to position the beam) or through the ScanningServer command (to position the beam and to collect data from a specified detector). The program is pixel-oriented. The size of the area that can be scanned depends on the magnification, the minimum frame size is 16x16 pixels. Positions are always given in relative coordinates: (0,0) for the center position, (1,1) for the top left position and (-1,-1) for the bottom right position (slightly counter intuitively). These coordinates are translated into scan signals ranging between +6.4 and -6.4 V which are the input for the current sources of the deflectors. The minimum dwell time is in the range of  $\mu\text{s}$  per pixel for the BeamControl and 0.001 s for the ScanningServer. Jscripts is a high-level interpreted language. This, together with the fact that the scripts are run on a Microsoft Windows platform designed for multitasking, makes iterating procedures slower than the dwell times suggest. Iteration times shorter than 40 ms cannot be achieved.

#### IV.C. National Instruments card

In the standard situation, the control PC is directly connected to the STEM cabinet. The output of the control PC (ranging from +6.4 to -6.4 V) is connected to connector X4 on the SID/SIM image distribution board in the STEM cabinet. This is represented with the solid

lines in the schematic drawing in Fig. 3. The details can be found in the documentation Tecnai Electronics Vol. 2 Part 3, page 4.1-66, Fig. 4-8.

For the experiments described in Chapter 8, shorter iteration times were required than could be obtained with standard configuration of the control PC and JScript. To go to shorter iteration times, a National Instruments card (NI USB 6259) in combination with an adding amplifier is used. The output from the control pc is disconnected from X4 and reconnected to one input of the adding amplifier. The output of the NI card is connected to the other input of the adding amplifier. The output of the adding amplifier is connected to X4 on the SID/SIM image distribution board. This is represented with the dashed lines in Fig. 3. The electron beam can now be controlled with both the control pc and the NI card. This modification needs to be done with great care, since the electronics is easily damaged.

The maximum scan rate that can be achieved is limited by the hardware of the microscope. It was found that for dwell times per pixel  $< 10 \mu\text{s}$  the pattern was not defined correctly anymore.

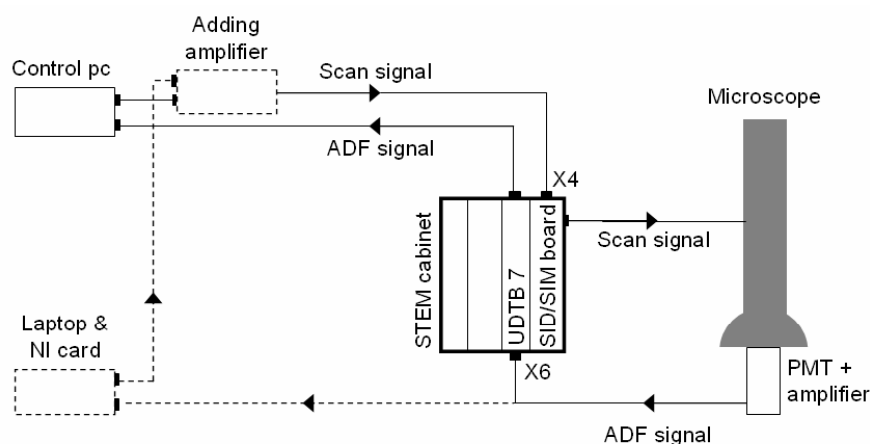


Fig. 3.3. Schematic drawing of the setup. The control pc (left) controls the microscope (right) through the STEM cabinet (middle). The normal configuration is shown with the solid lines. In the modified situation (dashed lines), the microscope can be controlled with a second computer as well.

## V. ADF signal recording

### V.A. JScript

The Jscripts that can be run on the ESVision program allow for recording the ADF signal. In the scripts, signals must be linked to a display window before they can be read and saved to a text file. In order to record the ADF signal during deposition, irradiation and reading data from the display window were iterated. Minimum iteration times were in the order of 40 ms.

### V.B. Picoscope and National Instruments card

On the E-STEM at ASU, the ADF electrons are focused on a photo-multiplier-tube (PMT). After being amplified, the ADF signal is connected with a BNC cable to connector X6 on the UDTB7 board in the STEM cabinet. This cable is represented with the solid line in the

schematic drawing in Fig. 3. The details can be found in the documentation Electronics Vol. 1, Fig. 16-28 (5). The output is in Volts.

From this connector, the ADF signal can be co-supplied to a data logger. Data loggers used were a USB Picoscope from Pico Technology and a National Instruments card (NI USB 6259). The minimum sampling time for the NI card was 1  $\mu$ s for recording data. If for future experiments a scan strategy is desired where the dwell times are dependent on the ADF signal, iteration times would be in the order of ms for this particular NI card due to the (relatively) slow communication over the USB connection.

#### 4. Approaching the resolution limit of nanometer scale electron beam induced deposition

*W.F. van Dorp*<sup>a)</sup>, *B. van Someren*<sup>a)</sup>, *C.W. Hagen*<sup>a)</sup>, *P. Kruit*<sup>a)</sup>, *P.A. Crozier*<sup>b)</sup>

<sup>a)</sup> Delft University of Technology, Faculty of Applied Sciences, Lorentzweg 1, 2628 CJ Delft, The Netherlands

<sup>b)</sup> Center for Solid State Science, Arizona State University, Tempe, Arizona 85287

Nano Letters **5**, 1303 (2005)

##### **Abstract**

We report the writing of very high resolution tungsten containing dots in regular arrays by electron beam induced deposition (EBID). The size averaged over 100 dots was 1.0 nm at FWHM. Because of the statistical spread in the dot size, large and small dots are present in the arrays with the smallest having a diameter of only 0.7 nm at FWHM. To-date these are the smallest features fabricated by EBID. We have also fabricated lines with the smallest having a width at FWHM of 1.9 nm and a spacing of 3.2 nm.

## Introduction

Electron beam-induced deposition (EBID) is a process in which an electron beam is focused on a substrate surface onto which precursor gas molecules are adsorbed. Due to inelastic collisions of the incoming (primary) electrons, secondary electrons (SE's) are generated in the substrate, some of which have sufficient energy to be re-emitted from the surface. Their energies are close to where the precursor dissociation cross section has a peak (typically 20-50 eV); therefore, the SEs are most likely to dissociate the precursor molecules in or close to the irradiated area. Nonvolatile products of this process adhere to the substrate and as a result, a deposit grows in the irradiated area. The composition of the deposit depends on the type of precursor.

Resist based electron beam lithography can currently achieve a resolution of about 10 nm [196]. EBID can go beyond that resolution, because modern electron microscopes are capable of bringing the electron beam diameter down to tenths of a nanometer. EBID allows the fabrication of structures for nanoscale research and perhaps the technique is suitable to continue Moore's law [197] into the sub 10 nm regime. Although the resolution of scanning probe lithography techniques is unsurpassable, they have the inherent problem of being limited in speed. EBID has a better prospect regarding speed even though it also has its limitations, but apart from that, it is interesting to determine the ultimate resolution limit of the technique. We have built a Monte Carlo simulation to study the influence of the substrate-electron beam interaction on the resolution of EBID [61]. The model predicted that a small electron beam in combination with a short illumination time would allow the writing of sub-10 nm structures. This was demonstrated successfully in a scanning transmission electron microscope (STEM) using contamination as precursor [4]. Although sub-10 nanometer structures have since been deposited using a scanning electron microscope (SEM) [84], the very small electron beams achievable in (S)TEMs have recently been used to synthesize sub-5 nm structures from a variety of precursors [83, 85]. The smallest nanodot of which an image was published, was a single dot of about 1.5 nm deposited from  $W(CO)_6$ , the diameter being estimated from a slightly overfocused high resolution TEM image [85]. This result was established in an ultrahigh vacuum TEM, using a very low precursor pressure of  $2 \times 10^{-6}$  Pa ( $1.5 \times 10^{-8}$  Torr) and a 1-nm-diameter beam. Sub-10 nm lines containing metal have been written by Jiang *et al.* [81] and Shimojo *et al.* [198]. However, at present there remain many questions about the ultimate experimental limits that can be achieved in nanostructures fabricated using EBID. Here we perform experiments that explore the resolution limits of EBID for fabrication of a variety of nanostructures. We demonstrate the capabilities of EBID as a resistless high-resolution patterning technique and show that this approach can be used to synthesize structures as small as 1.0 nm.

## Experimental

Nanolithography and characterization were conducted in a Tecnai environmental TEM, allowing the entire growth process to be observed and controlled *in situ* and in real time. This 200keV microscope is equipped with a field-emission electron source and was operated in STEM mode with a nominal beam spot size of 0.3 nm with a current of approximately 40 pA. The microscope is fitted with an environmental cell allowing gas pressures of up to 8 Torr in

the sample chamber during observation. The precursor used for deposition was  $W(CO)_6$ , and typical pressures were in the range of  $1 \times 10^{-3}$  Torr. The substrate consisted of a 30-nm-thick  $Si_3N_4$  membrane. To reduce the effect of hydrocarbon contamination, the substrate was plasma cleaned for about 3 hours in an  $Ar/O_2$ -mixture and then inserted in the microscope. Further substrate cleaning was performed in situ by heating to about  $200^\circ C$  in a stream of 5%  $H_2$  and 95%  $Ar$  for about 45 minutes. During experiments, the substrate was kept at a temperature of  $107^\circ C$ . The spectrum imaging software present on the Tecnai microscope was used to control the electron beam location during patterning. The program allowed the deposition of dots at designated locations, but full control of the beam was not possible. The scanning of continuous lines was not possible and instead, deposited lines were written with overlapping dots. Typical deposition times were on the order of 50 – 100 ms.

Most of the imaging was performed with the annular dark field (ADF) signal. This image has a strong Z-contrast component and interpretation and feature size measurements are relatively straightforward compared to phase-contrast TEM. This allows the detection of very small features (single atoms in the case of heavy elements on thin parts of the specimen), and for thin films, the image contrast is linear with mass or thickness. Since the definition of size becomes important when discussing the limits of resolution, we consequently consider the full width at half maximum (FWHM) measured in the ADF images.

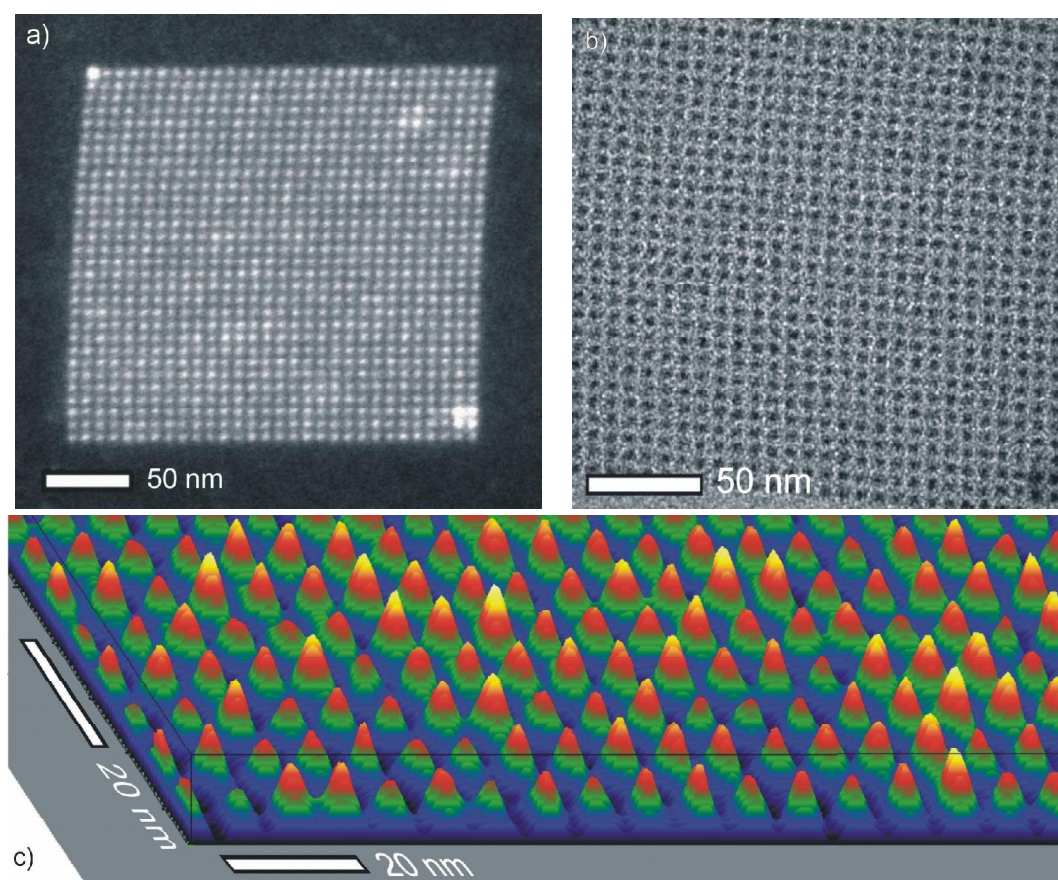


*Fig. 1. (a) ADF-image of an array of dots deposited from  $W(CO)_6$ . (b) TEM image of the same array at best focus to show the dots. (c) 3D intensity plot of a part of the ADF image.*

## Results

Fig. 1a shows a  $30 \times 30$  dot array. The dots are precisely placed on the intended grid, although the array is not square because of sample drift during the serial deposition process. The average dot size taken over 30 dots is 4.0 nm at FWHM. Fig. 1b shows a TEM image of a part of the array, taken at best focus to show the dots. A 3D intensity plot of the ADF image is shown in Fig. 1c, with arbitrary units along the z-axis.

Fig. 2 is a typical energy-loss spectrum recorded from a larger dot and shows a strong W signal confirming that W is the dominant species in the deposition. The small carbon signal present in the spectrum may be residual carbon species from the original carbonyl molecule.

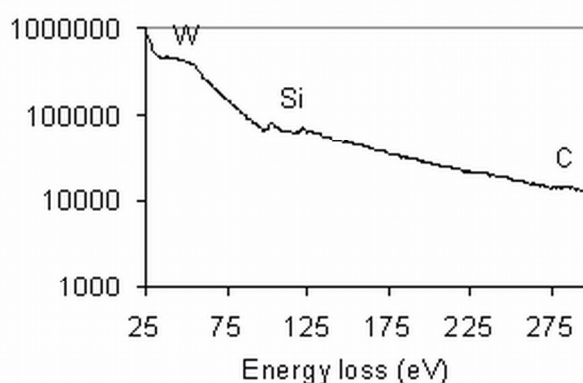
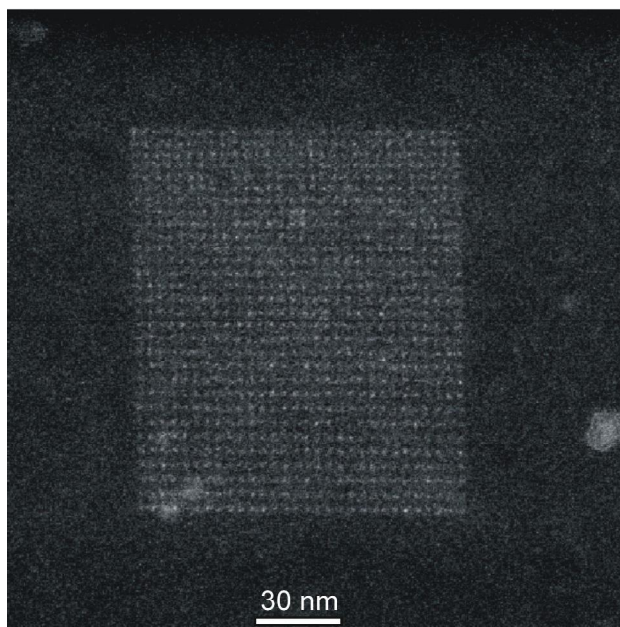


Fig. 2. Energy-loss spectrum from deposited dot showing the presence of W. The spectrum shows a W  $N_{67} O_{23}$ -edge at 40-50 eV, a Si L-edge at 100 eV (from underlying  $Si_3N_4$  substrate) and a C  $-K$ -edge at 284 eV.

A  $30 \times 30$  dot array with smaller dots and a spacing of 4.0 nm has been fabricated (Fig. 3). There is drift, making the array rectangular and slightly skewed, and the dots do not lie exactly on the intended pattern grid. There is also a spread in the dot size as can be seen in the ADF image from the varying brightness between individual dots.

The small spacing of the dots makes the measurement of the average dot size difficult; therefore, we fabricated another set with larger spacing. The  $10 \times 10$  array in Fig. 4a was fabricated under the same conditions as the array in Fig. 3, except for a larger spacing of 12.9 nm. To measure the dot size, we have averaged over the 100 dots of Fig. 4a by fitting a trapezoidal grid to the positions of the dots. For each grid point, a box was taken centered around the grid point and the sum of all boxes is shown in Fig. 4c. This procedure gives some widening of the average dot size because of the arbitrary placement of the dots. In Fig. 4d, we plot the intensity  $I(r)$  in Fig. 4c as the cross section through the dot, obtained by averaging in many different directions through the dot.  $N(r)$  is the intensity in a ring of radius  $(r, r+dr)$ .  $N_{tot}(r)$  is the integral function of  $N(r)$ , showing the total deposited W within a circle of radius  $r$ . The plot of  $I(r)$  shows a FWHM of 1.0 nm. This average dot diameter is precisely defined and to our knowledge represents a new world record for EBID. Because of the spread in the dot size, smaller diameters than the average are found, of course, the smallest of which is only 0.7 nm in diameter (FWHM), indicated by the arrow in Fig. 4b.



*Fig. 3. ADF-image of a  $30 \times 30$  array of dots, spaced at 4.0 nm. A spread in dot size can be seen from the varying brightness between individual dots.*

Both the variation in dot size and dot position (the arbitrary placement of the dots around the intended grid points) highlight the random nature of the deposition process at the nanometer and subnanometer length scales. Taking the volume of a single tungsten atom of  $0.0158 \text{ nm}^3$  and assuming the dots are half-spheres consisting of pure W and having a base diameter of 1.4 nm, the average number of atoms per dot is about 45. The spread in number of atoms is on the order of 6 or 7 (the square root of 45). Even when the dots would contain no W at all but would consist of pure carbon the average number of atoms per dot would be 96, with a statistical spread of about 10. This variation is much larger than the expected variation in the number of electrons involved in the writing of the dot (approximately  $3000/10^7$  electrons) and thus dominates the statistics. Of course, other mechanisms may also contribute to the observed spread, such as surface inhomogeneity, surface diffusion, or autocatalytic effects of the decomposition.

When discussing Moore's law, it is customary to define the resolution in terms of half pitch: the width of parallel lines separated by spacings equal to the line width. The most advanced integrated circuits are now written with 65 nm half pitch. In Fig. 5, ADF images of lines and spaces are shown, together with accompanying line scans integrated over 15 nm. Each individual line is written from top to bottom and the series of lines are written from left to right. The lines in Fig. 5a consist of 50 dots each along a 64 nm line, having a line width of 3.2 nm and a spacing of 19.5 nm. The lines in Fig. 5c consist of 25 dots each along a 39 nm line, having a line width of 1.9 nm and a spacing of 6.5 nm. The lines in Fig. 5e are written under the same conditions as the lines in Fig. 5c, except for a smaller spacing of 3.2 nm that corresponds to a half width of only 1.6 nm.

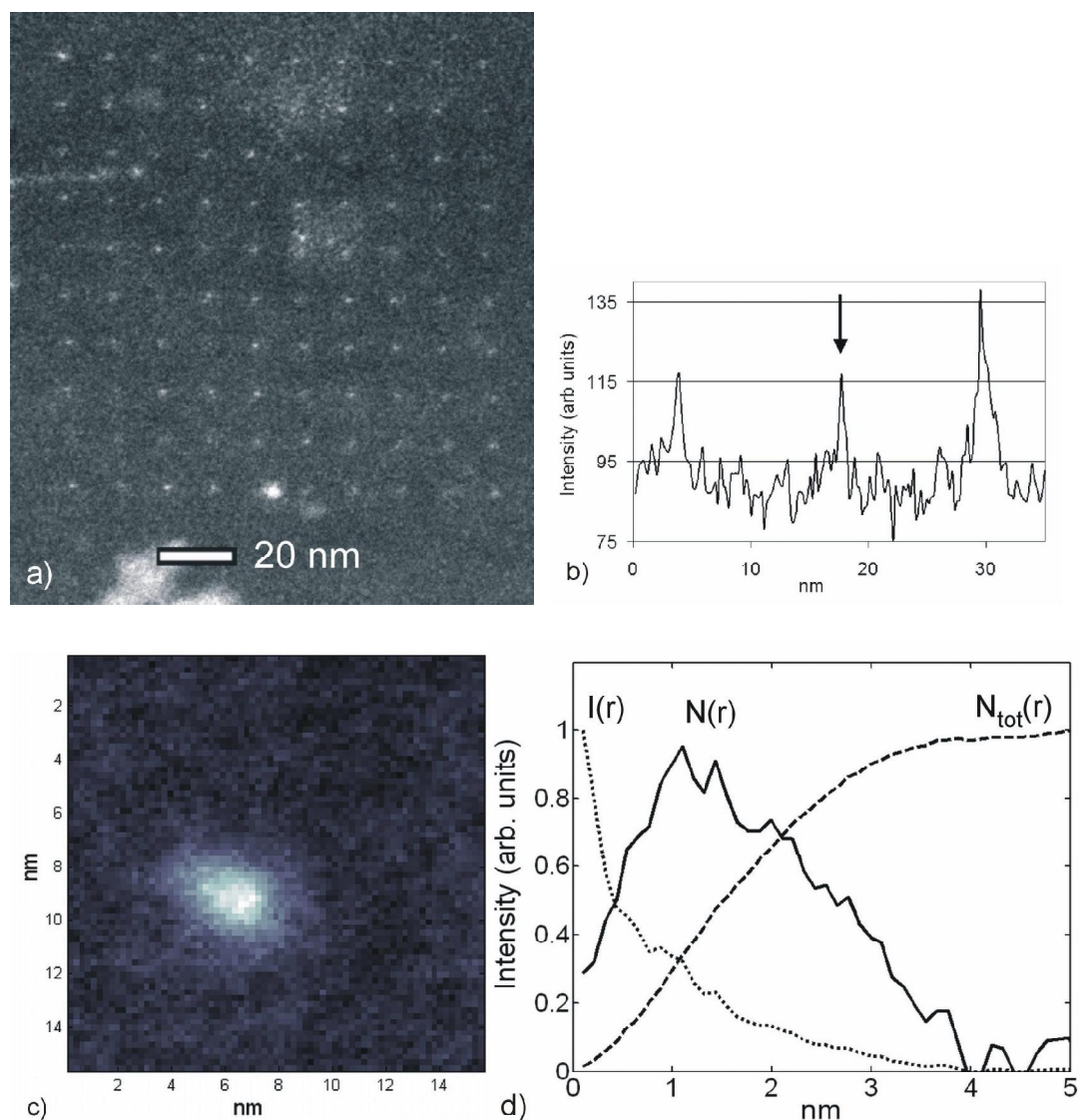
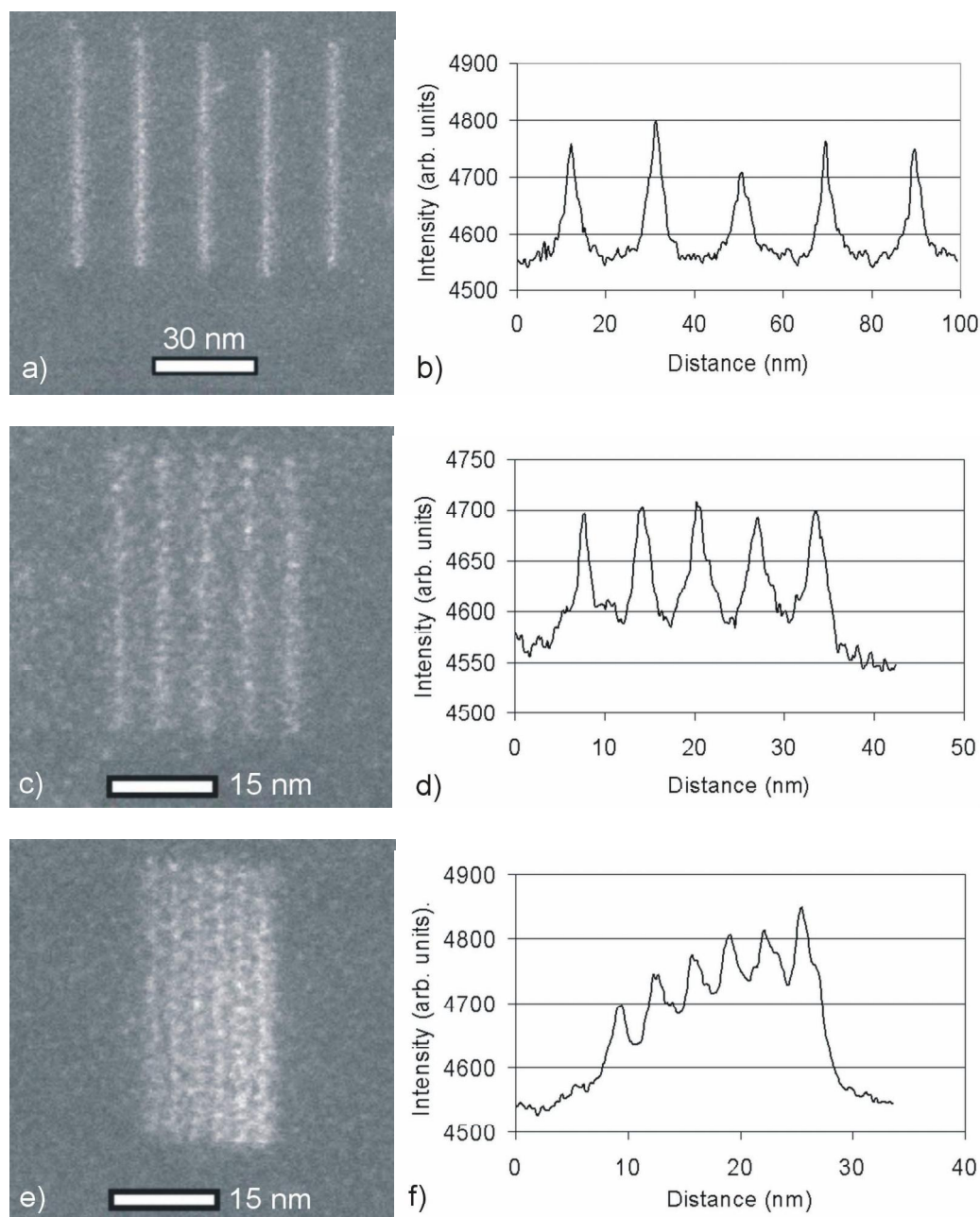


Fig. 4. (a) ADF-image of a  $10 \times 10$  array of dots deposited from  $W(CO)_6$ , with an average diameter of 1.0 nm. The array is slightly skewed due to drift. A spread in dot size can be seen as a variation in brightness. (b) Line scan from a part of the array in (a). The smallest dot (at position (2,8) counting from left to right, top to bottom) is 0.7 nm in diameter at FWHM and is indicated by the arrow. (c) Averaged profile of the 100 dots in (a). (d).  $I(r)$  shows the intensity in (c) as a cross section that is averaged over many directions through the dot. The diameter at FWHM is 1.0 nm.  $N(r)$  is the intensity in a ring of radius ( $r, r+dr$ ),  $N_{tot}(r)$  is the integral function of  $N(r)$ .

The line scan in Fig. 5d shows that the line bases in Fig. 5c overlap because of the nonlocal emission of secondary electrons from the sample surface. On more closely spaced lines, the intensity of the line base increases with each line drawn as shown in Fig. 5e and 5f. This is caused by the steady increase in secondary electron emission from the base as new lines are deposited. While the first line is deposited on a flat and clean surface, the second line is deposited on the already existing base of the first line. Secondary electron generation will be enhanced due to the fact that W is already present on the irradiated area, a heavier element

than Si or N. Secondly, when writing the second line, the surface is no longer perpendicular to the electron beam because of the presence of the base of the first line. The angle of incidence of the beam has changed and this allows more SE's to escape from the surface and dissociate more precursor species. This process is repeated for the following four lines and results in increasing line height from left to right. Hence, the profile of the two closely spaced lines is not a linear sum of two individual lines (as is the case for the lines in Fig. 5d) but rather consists of closely spaced lines superimposed on an increasing ramp.



*Fig. 5. ADF images of lines and spaces. Line widths for (a) and (c) are 3.2 and 1.9 nm, respectively. Spacings for (a), (c) and (e) are 19.5, 6.5 and 3.2 nm, respectively. Fig. 5 (b, d, f) Line scans from (a), (c) (d) respectively, integrated over a length of 15 nm.*

### **Conclusion**

In conclusion, we have written dots with an average FWHM of 1.0 nm that are the smallest structures made to date with the EBID approach. Under similar conditions, dots were written in an array with a spacing of 4.0 nm. The statistical spread in dot size and location due to the shot noise effect becomes evident and is significant at this high-resolution writing. Also, we have written continuous lines with a FWHM of 1.9 nm, with the smallest spacing being only 3.2 nm. These experiments demonstrate that EBID is a promising technique for high resolution resistless lithography, and that the STEM is a suitable instrument for achieving the sub-5 nm regime.

### **Acknowledgement**

We gratefully acknowledge the use of the facilities in the Center for Solid State Science at Arizona State University.

---

## 5. Statistical Variation Analysis of Sub-5 Nanometer Sized Electron Beam Induced Deposits

*W.F. van Dorp*<sup>a)</sup>, *B. van Someren*<sup>a)</sup>, *C.W. Hagen*<sup>a)</sup>, *P. Kruit*<sup>a)</sup>, *P.A. Crozier*<sup>b)</sup>

<sup>a)</sup> Delft University of Technology, Faculty of Applied Sciences, Lorentzweg 1, 2628 CJ Delft, The Netherlands

<sup>b)</sup> Center for Solid State Science, Arizona State University, Tempe, Arizona 85287

Journal of Vacuum Science and Technology B **24**, 618 (2006)

### Abstract

We report on the statistical analysis of the variations in the size and position of sub-5 nm tungsten containing dots in regular arrays deposited by electron-beam-induced deposition. Full widths at half maximum of the dots are 4.2 and 2.0 nm in average. It can be observed in the recorded annular dark field images that there is a variation in intensity for these dots. We have analyzed these variations and it is found that the relative standard deviation for the mass per dot is 0.092 for the 4.2 nm dots and 0.26 for the 2.0 nm dots. Comparing this to a relative standard deviation in the estimated number of precursor molecules that are pinned down per dot of 0.041 for the 4.2 nm dots and 0.11 for the 2.0 nm dots, it appears that the dot-to-dot variation in mass for both dot sizes compares reasonably well with the values expected from Poisson statistics on the number of molecules per dot. It can be concluded that at these dimensions, the statistics on the number of pinned precursor molecules dominates the control of feature sizes.

## Introduction

Electron-beam-induced deposition (EBID) is a process in which structures of arbitrary shape and size can be made, ranging from micrometer size down to nanometer size. In EBID, precursor molecules that are adsorbed from the gas phase onto a substrate are dissociated by an irradiating electron beam. Some fragments of the molecule bind to the substrate at the location of dissociation to form the deposit while other fragments remain volatile and are pumped away. The scan pattern of the beam determines the shape of the deposit. Recently, the search for the resolution limit of this technique has gained increasing attention. Sub-5 nm resolution was achieved in a scanning electron microscope [84] and even smaller deposits were fabricated in a scanning transmission electron microscope (STEM) [81, 4, 83, 85]. The smallest dots written so far are 1.0 nm full width half maximum (FWHM) in average [86]. The development of the dot diameter as function of the exposure time is sketched qualitatively in Fig. 1. The nucleation stage (0-A) is followed by an intermediate stage of fast growth (A-B) and eventually a stage in which the diameter saturates. The exact temporal behaviour of the deposit growth depends on many parameters, such as the precursor flux, beam current, precursor type, chemical state of the surface, chemical state of fragments of dissociated precursor molecules, substrate temperature and possibly many more. In this paper, we focus on the initial growth just after the nucleation stage. We have deposited arrays of tungsten containing dots on amorphous carbon membranes in a STEM. Careful inspection of the arrays of the smallest dots shows a variation in the size of the dots, even when the dots are grown under identical circumstances. This variation limits the control over dot size and linewidth variation. It possibly reveals a severe limit to the control in nanofabrication using electron beams at sub-5 nm resolution in general.

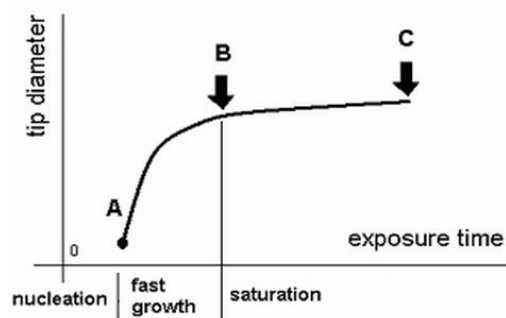


*Fig. 1. The development of the tip diameter as function of the exposure time. The nucleation stage (0-A) is followed by an intermediate stage of fast growth (A-B) and eventually a stage in which the diameter saturates.*

It is interesting to determine whether the observed fluctuations quantitatively compare to expected values. The number of primary electrons involved in the deposition of each dot is in the order of  $100 \times 10^6$ . Since the dots will consist of fewer and fewer molecules with decreasing dot size, the number of molecules per dot instead of the number of electrons is expected to dominate the statistics. As the number of molecules is a discrete quantity, one might expect the dot-to-dot variation to follow Poisson statistics. In this paper we describe

preliminary experiments to investigate if the dot-to-dot variation in the early stages of growth in EBID is related to the square root of the average mass of the dots.

### Experimental

Arrays of dots were written and measured in a Tecnai F20 environmental STEM, allowing the entire growth process to be observed and controlled *in situ* and in real time. This 200keV microscope is equipped with a field-emission electron source and was operated in STEM mode with a nominal beam spot size of 0.3 nm with a current of approximately 40 pA. The microscope is fitted with an environmental cell allowing gas pressures of up to 8 Torr in the sample chamber during observation. The precursor used for deposition was  $W(CO)_6$  and typical pressures were in the range of  $1 \times 10^{-3}$  Torr. The substrate consisted of a 10 nm thick amorphous carbon (a-C) membrane. To reduce the effect of hydrocarbon contamination, the substrate was put under a heat lamp for about 1 hour and then inserted in the microscope using a plasma-cleaned holder. Further substrate cleaning was performed *in situ* by heating to about 250°C in a stream of 5%  $H_2$  and 95% Ar for about 45 minutes. During experiments, the substrate was kept at a temperature of 148 °C. Control of the electron beam during patterning was performed both with the EELS analysis software and scripting software present on the Tecnai microscope. In contrast to the scripting software, the EELS analysis software did not allow a very precise control over the dwell time. Typical deposition times were on the order of 1 s.

Imaging was performed in annular dark field (ADF) mode. With the thin substrates and small dots, we assume that the intensity of the ADF image scales linearly with the mass of each dot.

### Analysis method

Due to specimen drift during deposition, the arrays of dots are not entirely square. In the image analysis, we first correct for the drift by fitting a trapezium shaped grid to the positions of the dots. From the ADF images we calculated an average dot by summing over the grey values of a box around each of the gridpoints of the trapezium shaped grid. The grid shape and position are optimized through finding the minimum width of the average dot by adjusting the cornerpoints of the trapezium grid.

After the grid optimization, the integrated intensity of each dot is calculated by finding, in an iterative procedure, the  $x$ - and  $y$ -position of the centre of gravity (COG) of each dot. An example of the tracing of the COG is shown in Fig. 2. The image shows 4 dots out of an array of 100, with the trapezium-grid overlaid in white. The sequence of black marks shows the iterative tracing of the COG. Next, two boxes are overlaid, centered around the dot's COG. Box 1 containing  $n_1$  pixels is large enough to overlap the area covered by the dot including its tails, box 2 containing  $n_2$  pixels is slightly larger than box 1. Then, the sums  $I_1$  and  $I_2$  of all intensity values of, respectively, box 1 and box 2 are calculated. The average background intensity value per pixel  $I_{BG}$  is calculated by:

$$I_{BG} = (I_2 - I_1) / (n_2 - n_1) \quad (1)$$

The total image intensity arising from the deposited material  $I_D$  is calculated by:

$$I_D = I_I - (I_{BG} n_I) \quad (2)$$

The procedure of overlaying the boxes, calculating the sums of intensities and dot intensity with background correction is performed for all dots in the array. For each array, the average  $\mu(I_D)$  and standard deviation  $\sigma(I_D)$  of the measured  $I_D$  are calculated for the analyzed images. The measured relative variation in intensity over the dots is expressed as  $[\sigma(I_D) / \mu(I_D)]$ .

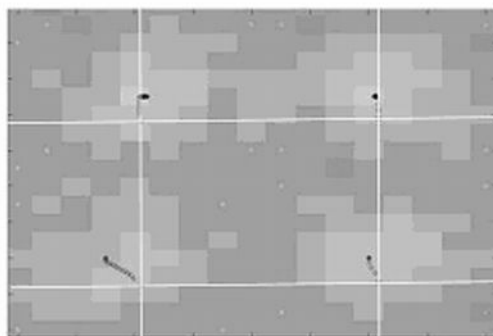


*Fig. 2. An example of the tracing of the COG is shown in Fig. 2. The image shows 4 dots out of a 100 dot array, with the trapezium grid overlaid in white. The sequence of black marks shows the iterative tracing of the COG.*

### **Number of pinned molecules per nm<sup>3</sup>**

The measured relative variation is compared to the expected relative variation due to Poisson statistics. The statistics that are observed in the deposition process will be determined by the number of  $W(CO)_6$  molecules that are pinned on the substrate and it is this number we need to estimate. The expected variation is expressed as  $(\sqrt{N}/N)$ , with  $N$  being the average number of  $W(CO)_6$  molecules per dot that were pinned down in order to create the deposit. To calculate  $N$ , we need to make an estimate of the volume and the composition of the dots. Together with a known value for the density of the dots, this yields a preliminary approximation of the average number of precursor molecules that are pinned down per dot.

The volume of the dots can be derived from the shape of the dots and making an estimate of the height. The dot shape is found by taking the sum of all boxes from the image analysis procedure. The resulting average intensity profile reveals that the dots have a Gaussian shape (see Fig. 3). With an iterative procedure, a two dimensional Gauss shape is fitted to this profile:

$$Z(X,Y) = \exp [-0.5 * (X/S_x)^2 - 0.5 * (Y/S_y)^2] \quad (3)$$

with  $S_x$  and  $S_y$  being the standard deviation in x- and y-direction, respectively. The volume  $V$  under a surface beneath a two-dimensional (2D) Gauss shape is calculated by:

$$V = 2\pi S_x S_y h \quad (4)$$

with  $h$  being the height of the Gauss. The height of the dots will be estimated from images of the tilted specimen.

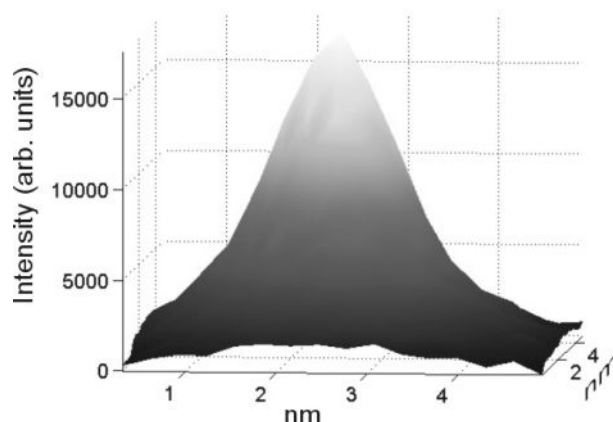


Fig. 3. Averaged intensity profile of the 2.0 nm FWHM dots.

Although it has been confirmed that dots deposited under nearly identical conditions contain tungsten [86], the exact composition of the deposits in the arrays is unknown. We use two ways to approximate the composition and in the end, we will evaluate the results with respect to the fluctuations we have found. Upon irradiation, the  $W(CO)_6$  molecule will be dissociated and pinned down on the substrate. The decomposition of precursor molecules is not very bond-specific and the decomposition will not be complete in the very first growth stages of the deposit. We can therefore assume that the deposition product in the dots is  $W(CO)_3$ , which is initially the most stable reaction product of the electron induced decomposition of  $W(CO)_6$  [199]. Alternatively, we can take the results from Koops *et al.* [29]. They have measured a composition typically of 55% W, 30% C and 15% O for deposits grown in an SEM from  $W(CO)_6$ , although it is not mentioned what the deposition parameters were exactly. However, this deposit is of micrometer scale and the growth stage is far beyond the very first instance as in our case. The original  $W(CO)_6$  molecules will have decomposed far more and will have reached a thermodynamically more stable situation. Still, in our calculations, we regard this deposit as consisting of ‘molecules’ of approximately  $W_1C_{0.5}O_{0.25}$ , since we are concerned with the number of  $W(CO)_6$  molecules we pin down and a  $W(CO)_6$  molecule contains 1 tungsten atom.

The last parameter required to calculate the average number of molecules per dot is the density of the deposit. This value is known from experiments with an atomic force microscopy setup, where the deposit mass is obtained from resonance measurements. An EBID deposit is grown on a cantilever and the cantilever’s resonance frequency is measured. Next, the deposit is mechanically removed and the resonance frequency is measured again. Finally, the deposit density is calculated by measuring the volume of the removed part of the deposit from SEM images. This measurement has been performed with a beam current of 100 pA for  $Co_2(CO)_8$ , which has a bulk density of  $1.87 \text{ g/cm}^3$  and a deposit density of  $4.21 \text{ g/cm}^3$  [70]. The density of a deposit from  $W(CO)_6$  (bulk density =  $2.65 \text{ g/cm}^3$ ) is estimated by assuming that the ratio of deposit density to bulk density is similar for  $W(CO)_6$ , leading to a deposit density for  $W(CO)_6$  of  $5.97 \text{ g/cm}^3$ .

The number of molecules that have been pinned down per dot  $N$  (deposits on both top and bottom side of the membrane) then follows from:

$$N = 2 (2\pi S_x S_y h) [(\rho N_A) / M] \quad (5)$$

with  $M$  being the molecular weight of the pinned down molecules,  $\rho$  the density of the deposit and  $N_A$  Avogadro's number.

### Results and discussion

Two different arrays of dots have been deposited. The arrays were analyzed with the method described above. In Fig. 4a, the array consists of 4.2 nm dots (FWHM), spaced at about 22 nm. In Fig. 4b, the array consists of 2.0 nm dots (FWHM), spaced at 13 nm. Fig. 4b shows most clearly that there is a variation in intensity over the dots. Additionally, a close observation will reveal a spread in position around the intended position on the array grid.

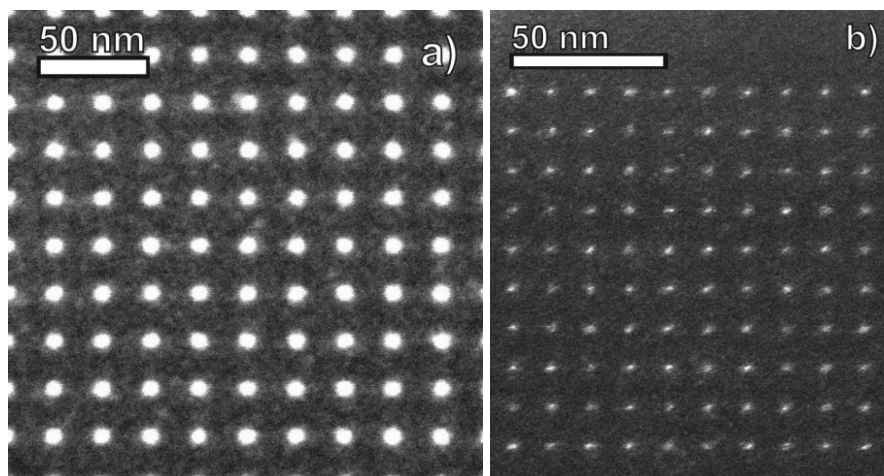


Fig. 4. Two ADF-images of dot arrays. (a) Array with 4.2 nm FWHM dots, spaced at 22 nm. (b) Array of 2.0 nm dots (FWHM), spaced at 13 nm.

The result of the analysis for the arrays in Fig. 4 with respect to the variation in integrated intensity is shown in Fig. 5 and Table I. Fig. 5 shows the distribution of  $I_D$  for the array of 4.2 nm FWHM dots. The distribution is bell shaped, which is in accordance with expectations. The values of  $[\sigma(I_D)/\mu(I_D)]$  for both arrays are given in Table I and it is shown that the measured relative dot-to-dot variation  $[\sigma(I_D)/\mu(I_D)]$  is larger for the 2.0 nm dots than for the 4.2 nm dots. This trend is consistent with Poisson statistics and it demonstrates that statistical fluctuations in number of molecules and in the positioning accuracy start playing a role when depositing nanometer-sized structures. It is a first indication of an effect that is important to nanofabrication using electron beams since it may prove to be a limitation in fabrication control at the sub-5 nm scale.

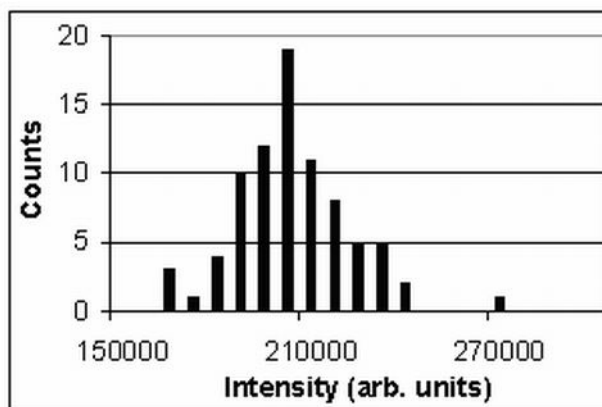


Fig. 5. Distribution of  $I_D$  for 4.2 nm dots. A similar distribution is found for the 2.0 nm dots.

Table I. Comparison of the found mass distributions with estimated values. From the average dot size we calculate the average number of molecules  $N$  per dot and the expected relative variation  $\sqrt{N}/N$  in number of molecules. The measured values are  $[\sigma(I_D)/\mu(I_D)]$ .

Average dot size (FWHM)	measured $\sigma(I_D)/\mu(I_D)$	Estimated $N$ and extremes	Estimated $\sqrt{N}/N$ and extremes
4.2 nm	0.092	598 ( $299 \leq N \leq 1555$ )	0.041 ( $0.058 \leq \sqrt{N}/N \leq 0.025$ )
2.0 nm	0.26	78 ( $39 \leq N \leq 202$ )	0.099 ( $0.16 \leq \sqrt{N}/N \leq 0.070$ )

To compare the experimental values to fluctuations expected from Poisson theory, we calculate the volume. The result from the described Gauss fit is that  $S_x = 1.79$  nm and  $S_y = 1.99$  nm for the 4.2 nm dots and  $S_x = 0.87$  nm and  $S_y = 1.07$  nm for the 2.0 nm dots. Dot heights can be estimated from the tilted view, the sample was tilted to 27 (Fig. 6a) and 20 degrees (Fig. 6b). As the projected width of the dots in tilted view does not change significantly with respect to the projected width in perpendicular view, it can be deduced that the dots are not very high. We assume a height  $h$  of 1.0 nm and 0.5 nm for the 4.2 nm and 2.0 nm dots, respectively. These values lead to a volume of  $22.3 \text{ nm}^3$  and  $2.9 \text{ nm}^3$  for the 4.2 nm and 2.0 nm dots, respectively.

The results of the previously described calculation of the average number of pinned down molecules per dot are added to the experimental values in Table I. The best estimates for the average number of molecules per dot and  $(\sqrt{N}/N)$  are given for the 4.2 nm dots and 2.0 nm dots, being respectively 1.0 nm and 0.5 nm high and consisting of  $\text{W}(\text{CO})_3$ . Together with this, the estimated extremes are given, calculated by taking margins of a factor of two larger and smaller for the height of the dots and taking the two mentioned compositions.

The measured values for  $[\sigma(I_D)/\mu(I_D)]$  are of the same order of magnitude as the expected  $(\sqrt{N}/N)$ , but do not fall within the estimated extremes. This may be due to an overestimation of the density of the deposit, since the decomposition process in the SEM will be more complete during the density measurement than during the nanodot fabrication in STEM. The ratio between the measured value and the value for the best estimate is constant for both arrays, which would indicate a systematical error such as for instance the overestimation of the density of the deposit.

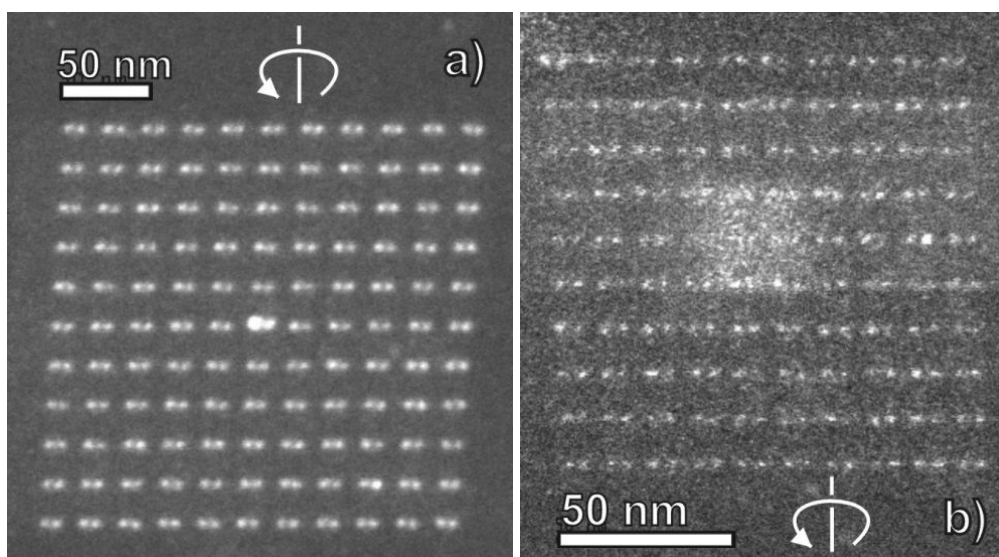


Fig. 6. Tilted images. (a) The 4.2 nm FWHM dots tilted to 20°. (b) The 2.0 nm FWHM dots tilted to 27°. The tilt axis is indicated. The brighter dot or region in the center of the array comes from the focussing of the electron beam during the experiments.

### Conclusion

We have deposited arrays of nanodots with average sizes of 4.2 and 2.0 nm in diameter (at FWHM). It can be observed that there is a variation in intensity for these dots. The number of primary electrons involved in the deposition of each dot is in the order of  $100 \times 10^6$ . Since the dots consist of numbers of molecules many orders of magnitudes less than that, this indicates that at these dimensions, the statistics on the number of molecules dominates the control of feature sizes. This may pose a severe limitation to sub-5 nm fabrication with electron beams. We have analyzed the variations and it can be concluded that the dot-to-dot variation in mass for both dot sizes has the same order of magnitude as the values expected from Poisson statistics on the number of precursor molecules that are pinned down per dot if it is assumed that the precursor decomposition process is incomplete in the very first growth stages.

### Acknowledgement

We gratefully acknowledge the use of the facilities in the Center for Solid State Science at Arizona State University.

## 6. Solutions to a proximity effect in high resolution electron beam induced deposition

*W.F. van Dorp*<sup>a)</sup>, *S. Lazar*<sup>b)</sup>, *C.W. Hagen*<sup>a)</sup>, *P. Kruit*<sup>a)</sup>

<sup>a)</sup> Delft University of Technology, Faculty of Applied Sciences, Lorentzweg 1, 2628 CJ Delft, the Netherlands

<sup>b)</sup> Delft University of Technology, National Center for High Resolution Electron Microscopy, Delft, 2628 AL, the Netherlands

Journal of Vacuum Science and Technology B **25**, 1603 (2007)

### **Abstract**

A new type of proximity effect in electron beam induced deposition (EBID) is presented. Proximity effects are well known in resist based electron beam lithography (EBL), where they presents themselves as an extra and unintentional exposure of the resist layer surrounding the irradiated areas. Several types of proximity effects have already been reported for EBID, which are of a different nature. We report a proximity effect where the amount of deposited mass increases with each new line that is deposited. This effect occurs when parallel lines are deposited at a spacing close to the width of the lines. The increase in deposition rate was found to be dependent on the angle between the irradiated target and the incident electron beam. Results from a simulation based on this model qualitatively show the same trend. A succesful strategy for reducing the effect is presented.

## Introduction

Electron beam induced deposition (EBID) is a good candidate for the fabrication of structures with sizes smaller than 20 nm. In the process, molecules adsorbed on a substrate are dissociated under the influence of a focused electron beam. Nonvolatile fragments of the precursor molecules stick to the substrate and form a deposit, while the volatile fragments are pumped away by the vacuum system.

Proximity effects are well known in resist based electron beam lithography (EBL). It is usually caused by backscattered electrons and presents itself as an extra and unintentional exposure of the resist layer surrounding the irradiated areas. Several types of proximity effects have already been reported for EBID, where matters are more complicated due to the fact that the irradiated targets are growing and therefore change in shape. An effect similar to that in EBL was reported by Lau *et al.* [12]. Around the base of a grown tip of a few micrometers high, extra material is deposited within the range of backscattered electrons (Fig. 1a). In the same article, they report the widening of already grown tips as result of the deposition of new tips in the close vicinity (Fig. 1b). When depositing a square array of tips with a spacing of 1  $\mu\text{m}$ , the earlier grown tips become wider as result of the deposition of later grown tips (the growth sequence was top to bottom and left to right). Their explanation for the widening is that “the backscattered electrons and other secondary electrons now emerge from the base of the column.”

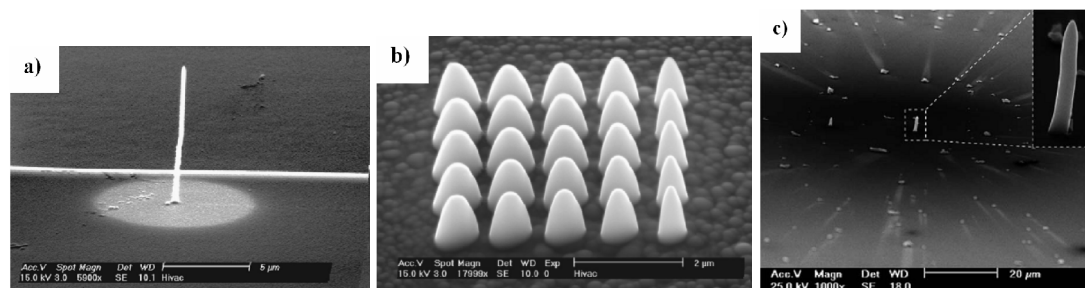


Fig. 1. Several types of proximity effect reported for EBID. (a) Deposition caused by backscattered electrons around the base of a grown tip. (b) Tips grown in the sequence top to bottom and left to right. The authors explain the widening of already grown tips by “the backscattered electrons and other secondary electrons now emerging from the base of the column.” Fig. (a) and (b) reused with permission from [12]. Copyright 2002, AVS The Science & Technology Society. (c) Deposition by electrons scattered from the tip, having lost 4 keV of their initial 25 keV (estimated). Reprinted from [69]. Copyright (2006), with permission from Elsevier.

Widening of EBID structures as result of the deposition of a neighboring structure was also reported by Martin *et al.* [137] and Aristov *et al.* [138]. They have observed that self-standing rods can become thicker as result of the deposition of new rods in the vicinity. Since the rods are self-standing, backscattered electrons cannot play a significant role and Aristov *et al.* concluded that the deposition was “likely to be induced by the secondary electrons emitted” during the deposition of the neighboring structure. A closely related proximity effect was

observed by Bret *et al.* [69] in the scanning electron microscope (Fig. 1c), Gopal *et al.* [114] with time-of-flight secondary-ion-mass-spectroscopy and Zhang *et al.* [135] in the transmission electron microscope. Similar to the experiments by Lau *et al.*, tips of some micrometers length were grown and additional deposition was found in the area surrounding the tip. However, this area could be as large as 50 or 60  $\mu\text{m}$  in diameter and was clearly larger than the backscattered electron range. In the model proposed by Bret *et al.*, the additional deposition is caused by (relatively) high energy electrons. These electrons are scattered radially from the growing tip and have not yet interacted with the substrate. In their experiments, the energy loss of the scattered electrons was estimated to be 4 keV (using a continuous slowing down approximation) for an incident electron energy of 25 keV.

But proximity effects do not only cause additional deposition in the vicinity of the irradiated area, deformation has also been reported. Mitsuishi *et al.* [141] have observed a change in shape of self standing rods as result of the growth of a new rod next to it. Based on experiments on insulating and conducting substrates, they attributed the effect to the charging of the already existing and the newly grown structures.

In contrast to the type of proximity effects mentioned above, which affect already deposited structures, this article deals with an effect that affects the new structure that is being written. This was first observed by Van Dorp *et al.* [86] with the deposition of lines from  $\text{W}(\text{CO})_6$ . When writing parallel lines at a spacing close to the width of the lines, the amount of deposited mass increased with each new line that was deposited (Fig 2). In the dark field image in Fig. 2, this appears as an increase in intensity. The lines were written from top to bottom, from left to right.

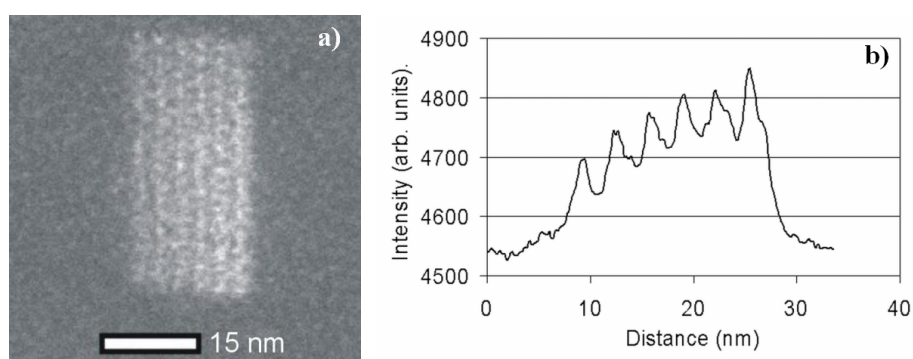


Fig. 2. First observation of the proximity effect. (a) The amount of deposited mass increases with each new line that is deposited. In the dark field image this appears as an increase in intensity. The lines were written from top to bottom, from left to right. (b) A horizontal line scan shows the increase in intensity. Fig. (a) and (b) reprinted with permission from [86]. Copyright (2005) American Chemical Society.

If EBID is to be used as a lithography technique, this type of proximity effect needs to be understood, characterized and, if possible, controlled.

### Experimental setup

Fabrication was done in a scanning transmission microscope (STEM) and a scanning electron microscope (SEM), both equipped with a Schottky source. The STEM was operated at 200 keV, with a beam diameter of 0.3 nm. Imaging was performed with the high angle annular dark field (HAADF) detector for the experiments in the STEM. The beam was controlled with the scripting software available on the machines. The SEM was operated at 15 keV, with a beam current of 11 pA and a beam diameter (according to specifications) of 1.4 nm. Imaging was performed with a transmission detector (TD) and the through-the-lens secondary electron (SE) detector. The beam was controlled with the standard pattern generation software available on the machine.

Deposition was done on thin carbon foils, with a thickness of 10 to 20 nm. The intensity in HAADF and TD images is assumed to be approximately linearly dependent on the deposited mass for the foils and low  $Z$  deposit (carbon). The precursor used for fabrication was the contamination present on the samples. No special effort was made to increase or remove the amount of contamination.

### Results

The experiment in the STEM was the following. The contamination lines that have been deposited, using a digital scan system for patterning, consisted of 20 pixels at very small spacing. The dwell time per pixel was 0.3 seconds, leading to lines having a full width at half maximum of 12.5 nm. When 15 of these lines are written parallel at a spacing of 7.6 nm, it can clearly be observed that the proximity effect leads to nonlinear deposition, as is shown in the HAADF image in Fig 3a. The scan sequence was from bottom to top, from left to right. The nonlinear increase in intensity (and amount of deposited mass) can be observed both in horizontal (left to right) and in vertical (bottom to top) direction.

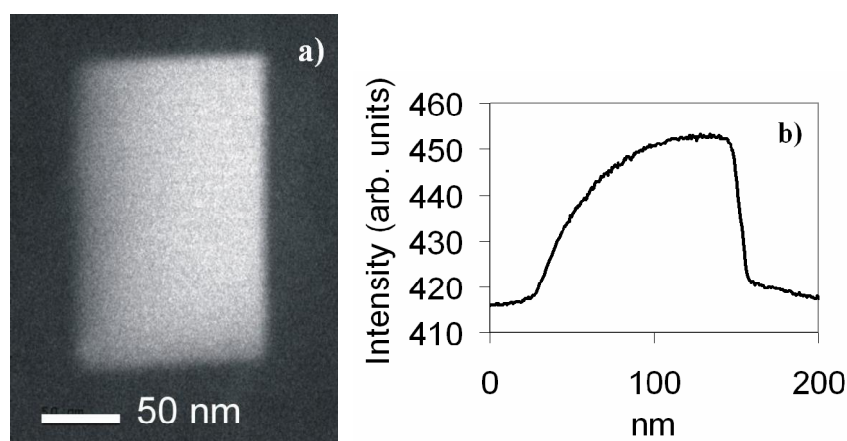


Fig. 3. (a) HAADF image of 15 lines having a width of 12.5 nm, deposited at a spacing of 7.6 nm. (b) Horizontal line scan, integrated over 150 nm, showing the nonlinear growth.

This experiment was repeated in the SEM. Again using a digital scan system, 500 nm long lines were scanned with an overlap of 50% between adjacent pixels. The maximum dwell time per pixel for the pattern generator software on the SEM is 4 ms per pixel, so in order to

have lines of sufficient height, each line was exposed 4 times by the electron beam, before moving on to write the next line. The resulting lines have a width of 21.8 nm (FWHM). The lines were written from bottom to top, left to right. Fig. 4a-d show the images of 14 lines written at spacings of 25, 20, 15 and 10 nm recorded with the TD, with the corresponding line scans (integrated over a width of 180 nm) in Figs. 4e-h, respectively. The proximity effect is clearly visible.

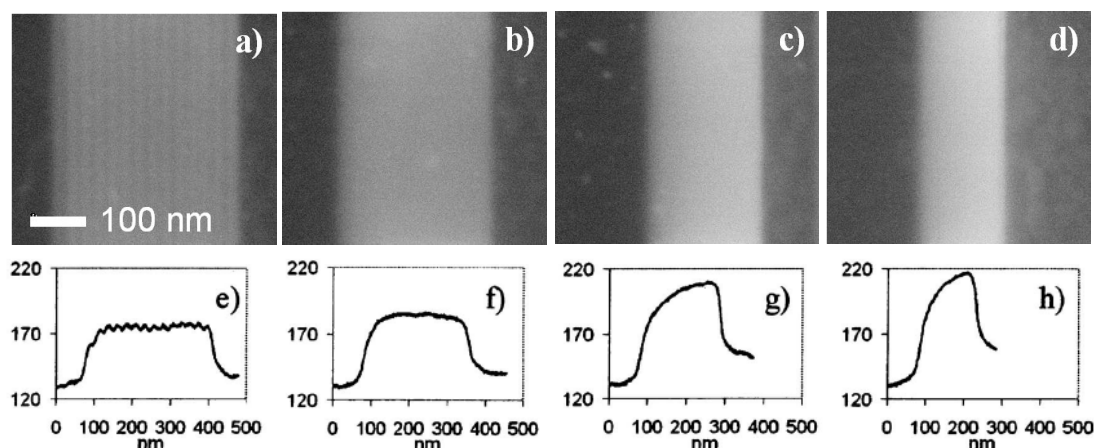


Fig. 4. TD images of 14 lines deposited at a spacing of (a) 25 nm, (b) 20 nm, (c) 15 nm, (d) 10 nm with the corresponding line scans (integrated over a width of 180 nm) in (e), (f), (g) and (h), respectively. On the vertical axis is the intensity in arbitrary units.

## Discussion

There may be several explanations for the observed proximity effect. First of all, the effect can be precursor specific. It has been proposed by many authors in the past that secondary electrons (SE's) play an important role in the deposition process and it is known that heavy elements generate more SE's than light elements. The EBID lines deposited from  $W(CO)_6$  in Fig. 3a contain W. The presence of W in the lines that are already deposited can for instance increase the emission of SE's and thereby lead to more deposition. However, the experiments described above show that the proximity effect is independent of the precursor that is used, since it also occurs with contamination.

Another explanation can be simply that the lines overlap. It is conceivable that a linear addition of several Gaussian-shaped lines at a small spacing could lead to the observed increase in deposited mass. We have simulated the profile of a structure created in the absence of nonlinear effects. In Fig. 5a, a profile of a line as deposited in the SEM is shown. The line profile from Fig. 5a has been repeated 14 times at a spacing of 10 and 25 nm and intensities have been added linearly. The result is shown in Fig 5b for 10 nm spacing and 25 nm spacing. Although the total intensity is higher for the 10 nm spaced lines than for the 25 nm spaced lines, the nonlinear effect is absent. The fact that the lines overlap is therefore not sufficient to explain the proximity effect.

As mentioned, the SE's possibly play an important role in the deposition process. It is known that SE emission is dependent on the angle between target and electron beam [52, 75]. If the angle between target and electron beam is decreased from normal incidence, the SE

emission increases. If the SE's are important for the deposition process, the deposition rate will also increase when the angle between target and incident beam becomes smaller than  $90^\circ$ .

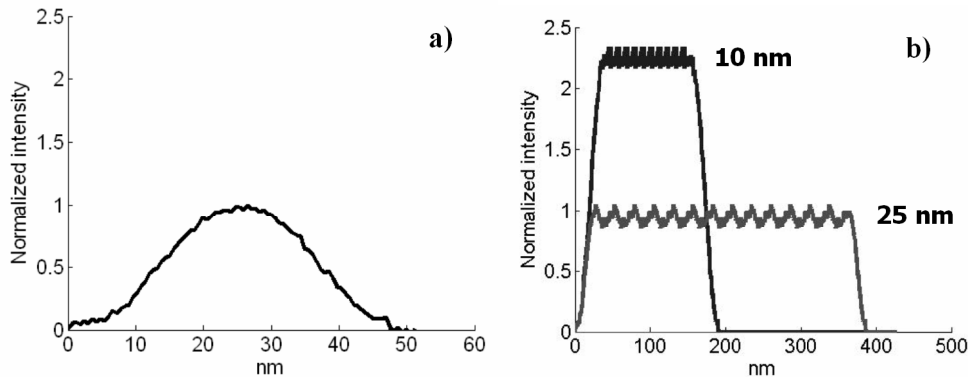


Fig 5. (a) Intensity profile of a single line as deposited in the SEM. (b) The simulated intensity profile of 14 lines spaced at 10 nm and 25 nm, where intensities have been added linearly. Nonlinear effects are absent.

In Fig. 6, the points of incidence on an intensity profile of a typical contamination line of the primary electron beam are plotted for the line spacings of Fig. 4. There is a similar trend between the magnitude of the proximity effect and the slope of the line at the point where the next line is deposited. The proximity effect is absent when the spacing is 25 nm and the angle between beam and target surface is  $90^\circ$ . The effect becomes noticeable for spacings of 15 and 10 nm, when the spacing is smaller than the line width and when the angle is smaller than  $90^\circ$ . Hence, we propose as model for the proximity effect that the deposition rate depends on the angle between the irradiated target and the incident electron beam.

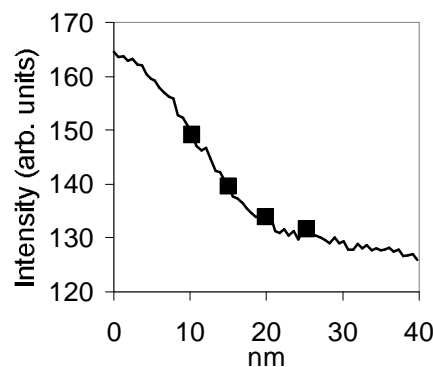


Fig 6. Cross section of a single line, written in the scanning electron microscope. The squares indicate the positions where subsequent lines are to be written.

This model was tested in the SEM, where the transmitted electrons and the secondary electrons emitted from the structure can be collected simultaneously. Fig. 7a-d shows the same structures as in Fig. 4a-d, but now imaged with the SE detector. The line scans integrated over 300 nm are superimposed on the images and show that SE emission comes mainly from the edges of the structure. Furthermore, the right edges of the structures have a

higher SE emission than the left edges, especially for the structures with a spacing of 15 and 10 nm. This demonstrates that the magnitude of the SE emission from right edges of the structures correspond well with the magnitude of the proximity effect.

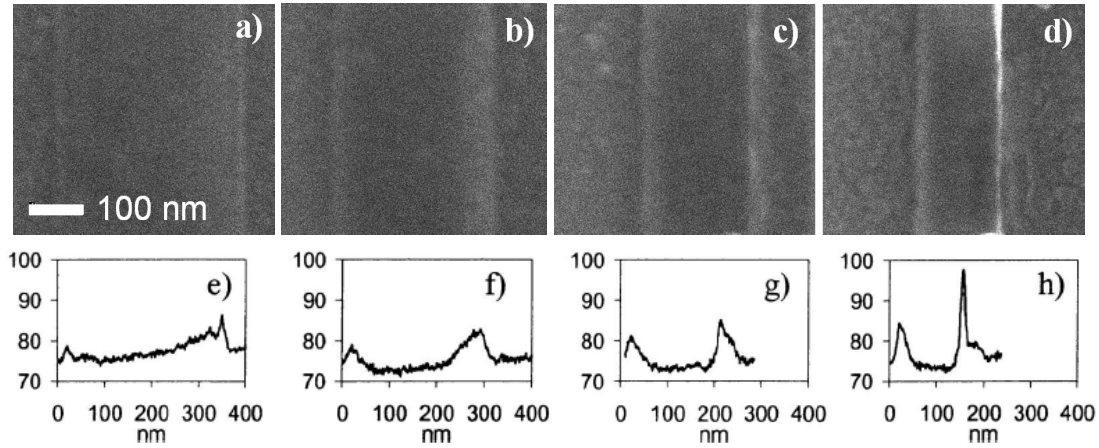


Fig. 7. SE images of 14 lines deposited at a spacing of (a) 25 nm, (b) 20 nm, (c) 15 nm, (d) 10 nm, with the corresponding line scans integrated over a width of 300 nm in (e), (f), (g) and (h), respectively. The increased SE emission at the right edge of the deposited structures for the smaller spacings is clearly visible.

We have simulated the dependence of the growth rate as a function of the angle of the irradiated surface with the electron beam. The simulated EBID line is assumed to have a Gaussian cross section:

$$F_{(x)} = H_n \exp \left( -\frac{1}{2} \left[ \frac{(X - X_0)}{S_x} \right]^2 \right) \quad (1)$$

with

$$H_n = H_0 / \sin(\alpha_x). \quad (2)$$

$H_n$  is the height of the  $n^{\text{th}}$  line,  $X_0$  is the  $x$ -position of the center of the line and  $S_x$  is the line width.  $H_0$  is the initial height of the line and  $\alpha$  is the angle between the surface that is being irradiated by the electron beam and the electron beam. Equation 2 reflects the angular dependence of the SE yield. When the first position is irradiated (circle in Fig. 8a), the substrate is flat and angle  $\alpha_x$  is  $90^\circ$ . This results in  $H_1 = H_0$  (line in Fig. 8a). For the position of the next line (circle in Fig. 8b), the angle  $\alpha_x$  has become smaller than  $90^\circ$  and  $H_2 > H_0$ . The second curve with  $H_2$  is added linearly to the previous line with  $H_1$ , resulting in the solid curve in Fig. 8b.

This process is continued for lines 3 to 14 and for various spacings. For  $S_x = 22$  and  $H_0 = 10$ , the resulting structure profiles are shown in Fig. 8c for the spacings of Fig. 3. The factor determining the magnitude of the proximity effect is  $1/\sin(\alpha_x)$  and this factor is shown in Fig 8d for the structures shown in Fig. 8c.

The qualitative agreement between the experimental results (Fig. 4 and 7) and the simulation (Fig. 8c and d) shows that the angular dependence of the SE yield might well give

rise to this proximity effect. Quantitatively, the simulation is not entirely accurate. The intensity of the curve for 10 nm spacing (relative to the intensities for other spacings) is lower in the experiment than in the simulation, which can be explained by the fact that the dark field signal in the SEM is not entirely linear anymore for the thickest part of the structure.

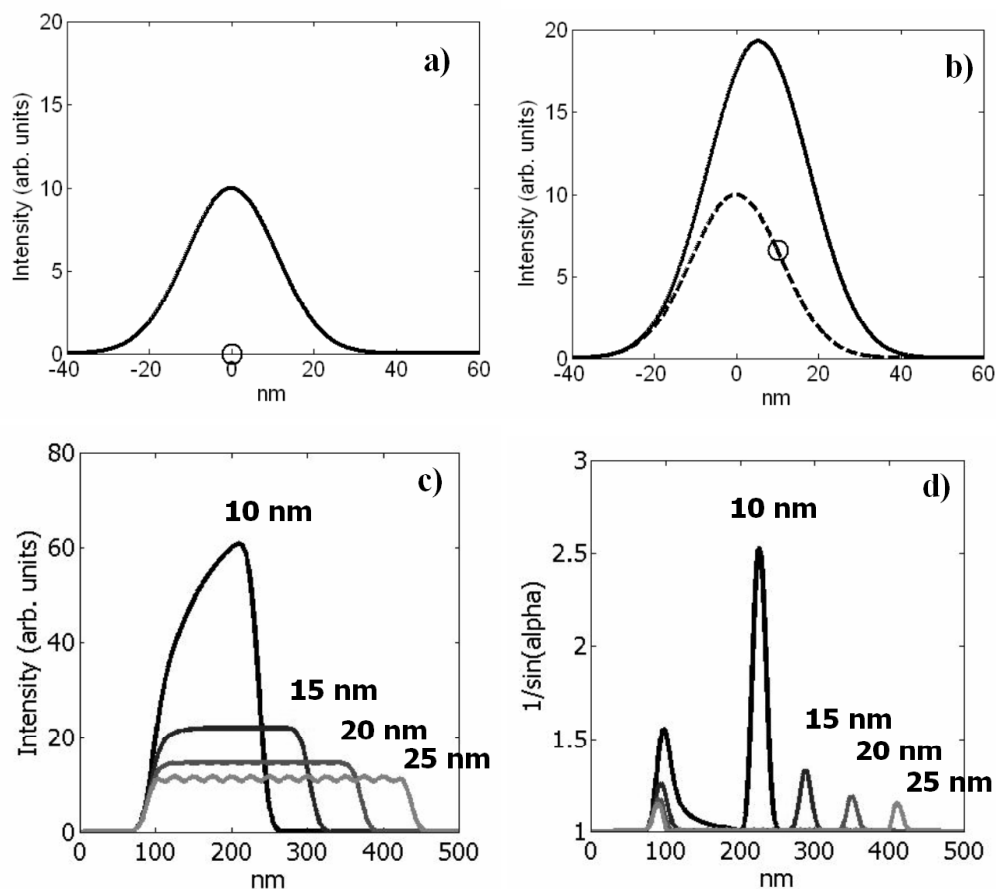
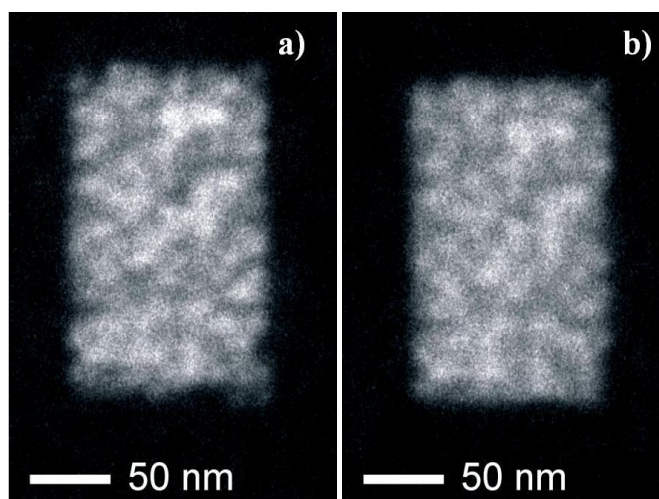


Fig. 8. Results from the simulation of the proximity effect, in which the magnitude of the proximity effect is proportional to  $1/\sin(\alpha_x)$ , where  $\alpha$  is the angle between the irradiated surface and the electron beam. (a) Initial situation where deposition occurs on a flat substrate and  $\alpha_x$  is  $90^\circ$ . (b) For the next line, deposition occurs on the slope of the already existing line (dashed curve) and  $\alpha_x < 90^\circ$ . The solid curve is the linear sum of the two lines. (c) Result for 14 lines at 10, 15, 20 and 25 nm spacing. (d) The factor  $1/\sin(\alpha_x)$  for the different spacings.

It needs to be remarked that, although the angular dependence of the SE yield and the proximity effect show a similar trend, these experiments do not give a direct evidence that the deposition is caused merely by the SE's. One can for instance argue that the adsorbed precursor molecules form a layer covering the substrate. The length of the trajectory that the incident (primary) electrons travel through that layer increases with  $1/\sin(\alpha_x)$ , which is the same relationship we have used for the angular dependence of the SE yield.

If EBID is to be used as a lithography technique, this proximity effect will have to be reduced. One solution might be to write the pattern in a random sequence. We repeated the pattern of Fig. 3, but now the pixels were scanned in a random sequence. The dark field image

in Fig. 9a shows that the proximity effect has not disappeared, but merely has spread over the entire structure. A random pattern appears and when the same random pixel sequence is scanned again at a different position on the substrate, the same pattern is reproduced (see Fig. 9b). This indicates that the morphology of the structure originates from the scan sequence and not from the substrate. Although this scan method makes the proximity effect less pronounced, it is not completely suppressed and therefore not ideal.



*Fig 9. (a) Same beam positions as used for Fig 3, but now scanned in a random sequence. (b) A deposit created by using the identical beam position sequence as in a) but at a different position on the substrate yields an identical mass distribution. This indicates that the deposit morphology originates from the writing sequence and not from the substrate.*

Another scan strategy to reduce the proximity effect is scanning the pattern in several passes. This can for instance be done by irradiating line 1-14 in sequence, before irradiating line 1 again. If each line receives only 1 pass instead of 4 passes before the next line is scanned, the material will be more homogeneously distributed across the total structure. The angle between irradiated surface and electron beam will remain small and the proximity effect will not develop, or only to a limited extent. We have tested this scan strategy by repeating the scan pattern of the lines in Fig. 4d with a spacing of 10 nm, but now with four passes of 14 lines instead of 14 four-pass lines. The total electron dose has remained unchanged. The TD image, SE image and the corresponding line scans (integrated over a width of 300 nm) are shown in Fig. 10a, b and c, resp. The proximity effect is absent and the SE emission from the right hand side of the structure is nearly equal to the SE emission from the left hand side. This indicates that the angle between irradiated surface and electron beam has indeed remained small and that this scan strategy is successful in reducing the proximity effect.

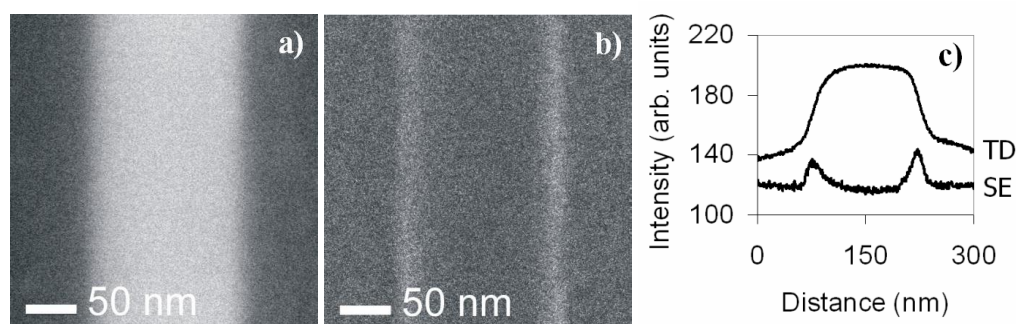


Fig 10. (a) TD image of 14 lines written in four passes. (b) SE image of the same structure. (c) The line scans, integrated over a width of 300 nm, show that the proximity effect is absent and that the SE emission is nearly identical on both sides of the structure.

A final strategy to prevent the proximity effect could be to correct with the electron dose. If the modeling of the proximity effect is quantitatively sufficiently accurate, the parts of the pattern that are written later in the scan sequence can receive a lower electron dose so that a smaller amount of material is deposited there. We have not tested this particular strategy.

## Conclusions

A new type of proximity effect in electron beam induced deposition (EBID) is presented. This effect occurs when parallel lines are deposited at a spacing close to the width of the lines. The amount of deposited mass increases with each new line that is deposited. The increase in deposition rate was found to be dependent on the angle between the irradiated target and the incident electron beam. If the angle is decreased from normal incidence, the deposition rate increases. This decrease in angle occurs when the spacing becomes close to the width of the lines. Every new line is then deposited on the slope of an already existing line. Results from a simulation based on this model qualitatively show the same trend. A successful scan strategy for reducing the proximity effect was found.

## Acknowledgement

We would like to thank Marcel Hesselberth and Erwin Heeres of the section of Condensed Matter Physics at Leiden University for the use of their facilities.

## 7. *In situ* monitoring and control of material growth for high resolution electron beam induced deposition

W.F. van Dorp <sup>a)</sup>, C.W. Hagen <sup>a)</sup>, P.A. Crozier <sup>b)</sup>, P. Kruit <sup>a)</sup>

<sup>a)</sup> Delft University of Technology, Faculty of Applied Sciences, Lorentzweg 1, 2628 CJ Delft, the Netherlands

<sup>b)</sup> Center for Solid State Science, Arizona State University, Tempe, Arizona 85287

Journal of Vacuum Science and Technology B, **25**, 2210 (2007)

### Abstract

During electron beam induced deposition (EBID) on electron transparent membranes, the transmitted annular dark field (ADF) signal can be monitored. A method was developed to use the ADF signal to obtain insight into the growth process and to control the mass of individual nanometer-sized deposits. Arbitrary 2D patterns can be defined. The smallest sampling time of the ADF signal monitoring is presently about 40 ms. For arrays of dots that were deposited, the growth of each individual dot was monitored. It is observed that the growth is different for each dot, although the average deposit growth rate is linear with the dwell time. Apart from monitoring the ADF signal during the growth, the amount of deposited mass can be controlled for individual deposits by terminating the growth process when the ADF signal exceeds a threshold value. The dynamic ADF feedback control was applied to reduce variations in deposit mass. This attempt did not succeed, but the method was successfully applied to prevent the occurrence of a proximity effect. When the electron beam irradiates the side of an already existing structure, the amount of deposited material is higher than if the electron beam irradiates an area that is under normal incidence. With the dynamic ADF feedback control, this effect can be compensated *in situ* and the amount of deposited material that is probed by the beam is constant regardless of the local growth rate.

The mass deposition resolution of the feedback system is estimated by assuming a volume and a density of the deposits. It is estimated that the ultimate mass resolution is a single molecule.

## Introduction

Focused electron beam induced processing (FEBIP) is a technique that allows the direct patterning of substrates. In a high vacuum chamber, an electron beam is focused on a surface. A precursor gas is introduced into the vacuum chamber and the precursor molecules adsorb on the substrate. Under the influence of the electron beam, the precursor molecules are dissociated. If the components of the precursor molecules that remain after the dissociation react with the substrate and form volatile species, the substrate is etched (in the case of electron beam induced etching, EBIE). If the components stick to the surface and form a deposit, one speaks of electron beam induced deposition (EBID). Since this beam induced reaction only occurs at or around the irradiated area and electron beams can be made as small as 0.1 nm, this technique is very well suited for sub-10 nm patterning.

The fabrication of <10 nm sized EBID structures has been demonstrated in scanning transmission electron microscopes (STEMs) and scanning electron microscopes (SEMs) with various materials [121, 84, 81, 83, 86]. In the very early stages of EBID growth, precise control over the growth process is not straightforward, because nonlinear effects can occur. It has for instance been shown before that the initial growth stage in EBID is a statistical process [200, 87]. When arrays are deposited with a constant dwell time, a distribution of deposited masses is found. Another nonlinear process observed is a proximity effect reported by Hiroshima and Komuro [75] and Van Dorp *et al.* [139]. It was found that the EBID growth rate depends on the angle between the electron beam and the irradiated area. The growth rate increases if the angle  $\alpha$  between the e-beam and the irradiated area decreases from normal incidence, even if all other parameters such as irradiation time, beam current or precursor flux are kept constant. The angle  $\alpha$  between e-beam and irradiated area is off-normal for instance when the beam is focused on the side of an already existing deposit. Hiroshima and Komuro observed this effect when starting the deposition of a new segment of an EBID wire, as shown in the AFM image in Fig. 1a and in the schematic picture in Fig. 1b. At the start of each new segment, the electron beam partially irradiates the side of the existing segment, and as a result the deposit height is larger due to the local increase in deposition rate. The writing direction is indicated with the arrow. Van Dorp *et al.* observed an increase in deposition rate when a line was deposited parallel to and partially on the side of an already existing line. The increase of the amount of deposited material presents itself as an increase in intensity in the annular dark field image (ADF) obtained in the STEM in Fig. 1c. The situation is schematically presented in Fig. 1d. In the ADF image, the intensity is assumed to be proportional to the amount of deposited mass. The writing direction was from top to bottom, from left to right. With every new line that is written, the image intensity and the amount of deposited material increases.

If EBID is used as a sub-10 nm lithography technique, these nonlinear effects are unwanted and it is important to control the amount of deposited material accurately. We present a method to monitor and control the growth process *in situ* for deposition on electron transparent substrates.

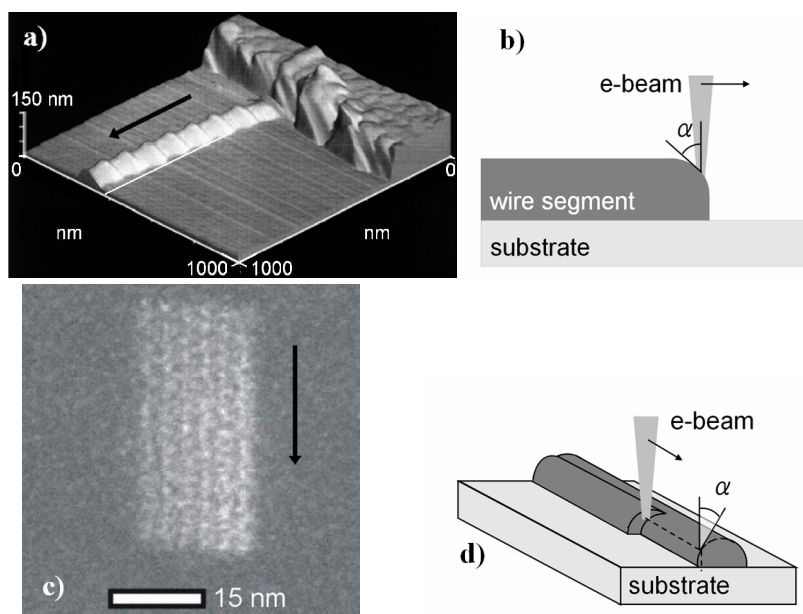


*Fig. 1. (a) AFM-image of an EBID wire. The wire was deposited in segments of 80 nm long. At the start of each segment, more material was deposited as result of the proximity effect. Reused with permission from Ref. 70. Copyright 1998, Institute of Physics Limited. (b) Schematic diagram. (c) A series of parallel lines, written from top to bottom, from left to right. With every new line that is written, more material is being deposited. Reprinted with permission from Ref. 86. Copyright 2005, American Chemical Society. (d) Schematic diagram.*

### Experimental setup

Deposition was done on thin carbon foils, with a thickness of 10 to 20 nm. Experiments were performed in a Tecnai F20 environmental STEM. This microscope is fitted with an environmental cell allowing gas pressures of up to 8 Torr in the sample chamber during observation and deposition. The microscope is equipped with a Schottky source and is operated at 200 keV with a nominal beam spot size of 0.3 nm and a beam current of approximately 40 pA. The precursor was  $W(CO)_6$ .

Imaging and dynamic growth control were performed with the annular dark field (ADF) signal for all experiments. This signal has a strong Z-contrast component and the signal strength is assumed to be linearly dependent on deposited mass (assuming a constant deposit composition). The patterning and dynamic growth control were performed with the scripting software available on the microscope.

The developed script allows the definition of arbitrary 2D patterns and actively monitors the amount of deposited material. For each beam position that is defined in the pattern, the corresponding position on the sample is irradiated for 10 ms after which the ADF signal value is read and saved in a file. The average time required for reading and saving the ADF signal value is about 30 ms. This alternating sequence of exposure, reading and saving is continued until a preset ADF signal value is reached.

## Results

Fig. 2a shows part of an array of small dots grown with the dynamic growth control. The array was  $9 \times 9$  in size and the average size of the dots was 2.2 nm. The growth curves of some of the dots in this array are shown in Fig. 2b. The preset ADF threshold is indicated with the dashed line and the script terminates the growth after the first measured value above the preset threshold. It can be observed that the growth process is different for each dot. This is the result of the nonlinear, statistical nature of the initial stages of the EBID growth as mentioned in the introduction. The second growth curve is shown in more detail in Fig 2c. The dynamic growth control leads to a distribution of dwell times (Fig. 2d).

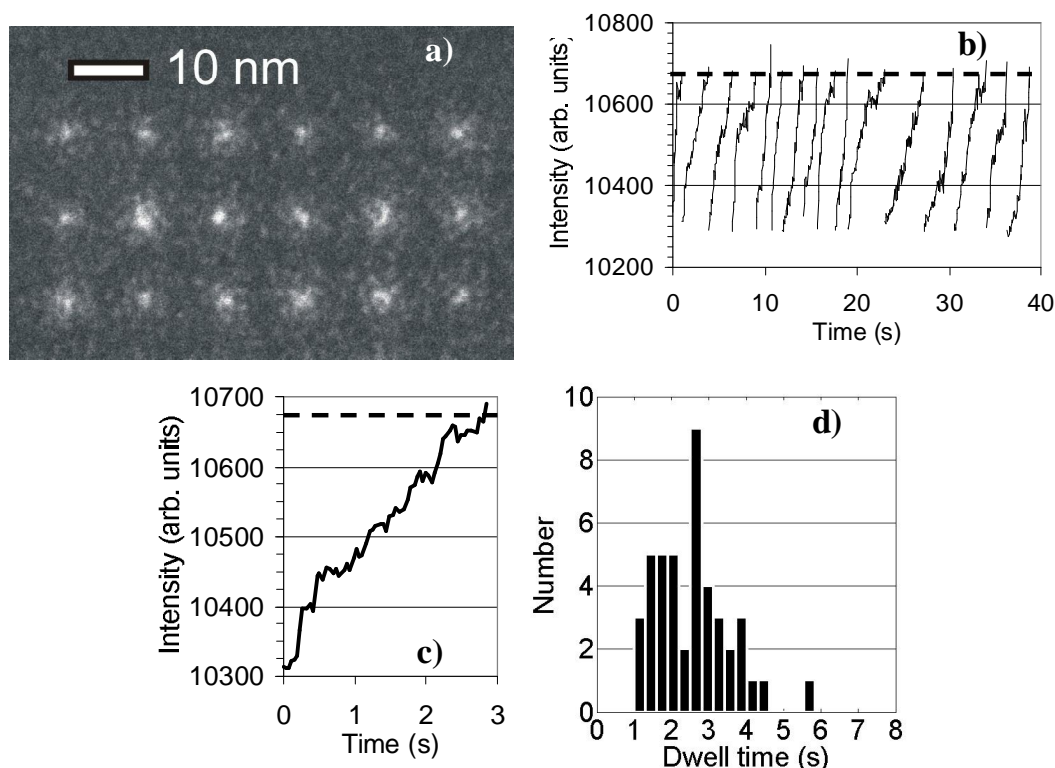


Fig. 2. (a) Dots in an array, written with dynamic ADF feedback control. (b) Growth curves for dots from the array. (c) Blow-up of the second curve from (b). (d) Histogram of the dwell times resulting from the dynamic growth control.

But despite our attempt to keep the amount of deposited mass constant, it is clear from Fig. 2a that the amount of deposited mass is not constant. Apart from measuring the development of the ADF signal *in situ*, it is also possible to calculate *ex situ* the total integrated intensity  $I_{\text{dot}}$  for each dot in the image. The distribution of  $I_{\text{dot}}$  for all dots in the array is shown in Fig. 3a. The fact that the distribution of deposited masses still has a significant width means that the dynamic feedback control did not work properly. We speculate that this is caused by the fact that the dot does not grow symmetrically around the irradiated spot. Only the part of the deposit that sits inside the primary electron beam is probed (see Fig. 3b). The part of the deposit outside the primary beam does not generate dark field electrons and does not contribute to the ADF signal. Since the electron beam has a diameter of about 0.3 nm and the

dots have an average diameter of 1.9 nm, this means that a significant amount of the material is deposited outside the beam, and not inside.

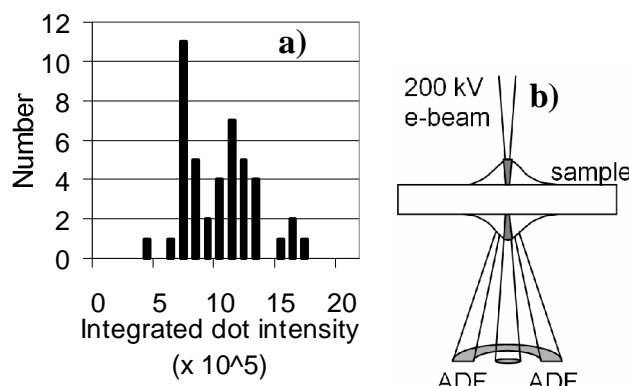


Fig. 3. (a) Histogram of the integrated dot intensities  $I_{dot}$  from the array in Fig. 2a. (b) Schematic drawing of the area from which the ADF signal originates. The growing dot is only partially probed by the electron beam.

It is observed that, although the growth curves and  $I_{dot}$  may vary from dot to dot, the overall growth process is linear. When  $I_{dot}$  is averaged per array and is plotted for various dwell times, the deposited mass increases linearly with the dwell time [87].

The other nonlinear effect described in the introduction is the proximity effect, an example of which is shown in Fig. 4a. The line was defined by 400 pixels over 160 nm with a constant dwell time per pixel. The height of the line is not constant as a result of the proximity effect. This is even more apparent in Fig. 4b where the sample was tilted over 20 degrees (tilt direction indicated). Since the substrate is transparent to electrons, a deposit grows both on the entrance and on the exit surface.

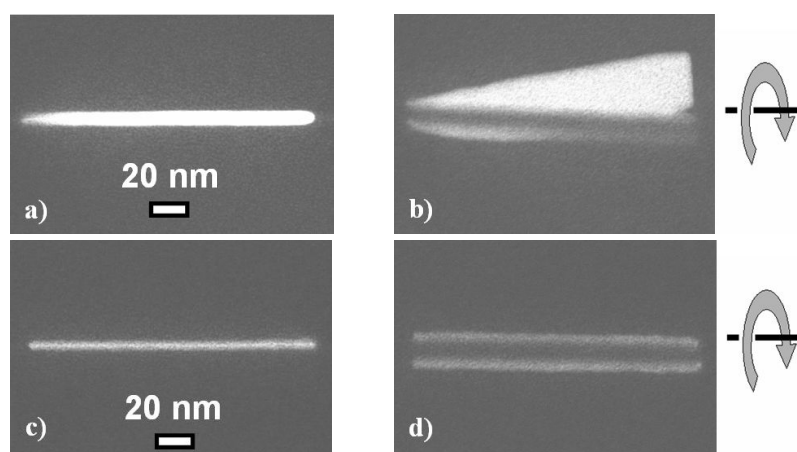


Fig. 4. (a) A line deposited with a constant dwell time per pixel, defined by 400 pixels over 160 nm. (b) The same line as in (a), but now tilted over  $20^\circ$  (tilt direction indicated). It is observed that the height of the line is not constant. Since the substrate is transparent to electrons, a deposit grows both on the entrance and on the exit surface. (c) The same pattern, but now written with the dynamic dwell time control. (d) The height of the deposited line is much more constant (tilt angle  $20^\circ$ ).

In [139] we demonstrated that this proximity effect can be prevented by writing patterns in multiple exposure passes or by random writing strategies. Here we demonstrate the proximity effect correction by making use of the ADF signal monitoring and control. When the same pattern is written with the dynamical ADF signal compensation, the height of the line becomes constant, as is observed in the untilted (Fig. 4c) and tilted views (Fig. 4d, tilt angle 20 degrees).

In Fig. 5 it becomes clear how the *in situ* monitoring and control of the dark field signal helps to prevent the proximity effect. The line in Fig. 5a was again defined by 400 pixels over a length of 160 nm and the threshold was set at an ADF intensity of 10750. In Fig. 5b, the ADF signal is plotted as function of time. It can be observed that the ADF signal from the second pixel onwards starts at a higher value than the ADF signal from the first pixel. This is because only the first position in the pattern is on the flat substrate and every following position is (partially) on the structure that was already deposited.

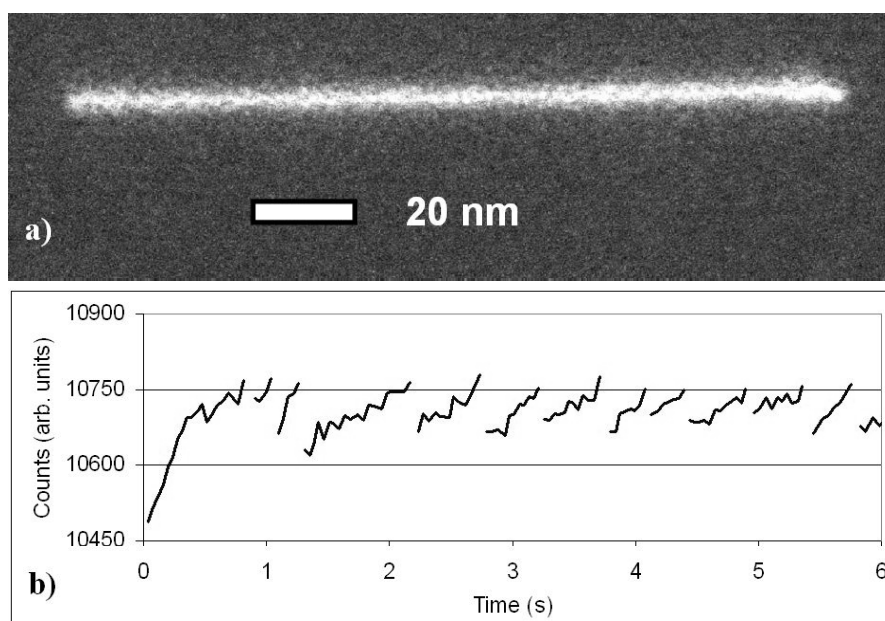


Fig. 5. (a) A line that was deposited while the growth process was controlled *in situ*. The line was defined by 400 points over 160 nm length. (b) The first seconds of the recorded ADF signal.

How well can this dynamic ADF feedback control be done? Can one control the deposition down to the level of a single molecule? To answer that question we have to estimate the mass deposition resolution of the feedback system. The average profile of a dot approaches the shape of a Gaussian. The volume beneath a 3D Gauss shape can be calculated using:

$$V = 0.36 \pi d_{\text{FWHM}}^2 h. \quad (1)$$

with  $d_{\text{FWHM}}$  the full width of the dot at half maximum and  $h$  the dot height. From tilt experiments, we have observed that the height of dots in their early growth stage (such as discussed here) is close to the width. So if we assume that a deposit with a  $d_{\text{FWHM}}$  of 2.1 nm has a height  $h$  of 2.0 nm ( $1.5 < h < 2.5$  nm), the volume  $V$  becomes  $9.6 \text{ nm}^3$  ( $7.2 < V < 12.0 \text{ nm}^3$ ).

We can get a reasonable estimate of the density from measurements by Utke *et al.* They have found a deposit density of  $4.21 \text{ g/cm}^3$  for  $\text{Co}_2(\text{CO})_8$ , compared to a bulk density of  $1.87 \text{ g/cm}^3$  [70]. The density of a deposit from  $\text{W}(\text{CO})_6$  is estimated by assuming that the ratio of deposit to bulk density is similar for  $\text{W}(\text{CO})_6$ . With a bulk density of  $2.65 \text{ g/cm}^3$ , this gives us a deposit density for  $\text{W}(\text{CO})_6$  of  $5.97 \text{ g/cm}^3$ . We assume that the decomposition of the precursor molecule is not complete during the early stages of the growth and the deposit consists of  $\text{W}(\text{CO})_3$  molecules. The number of molecules that have been pinned down per dot  $N$  (deposits on both top and bottom side of the membrane) then follows from:

$$N = 2 V [ (\rho N_A) / M ] \quad (2)$$

with  $M$  being the molecular weight of the pinned down molecules,  $\rho$  the density of the deposit and  $N_A$  Avogadro's number. This gives us a number of molecules of  $2.6 \times 10^2$  ( $1.9 \times 10^2 < N < 3.1 \times 10^2$ ) per deposit that has a diameter of 2.1 nm. The intensity in the ADF images is assumed to be linearly dependent on the amount of deposited mass. With the calculated  $I_{\text{dot}}$  for a 2.1 nm dot, this gives an intensity per molecule  $I_{\text{molecule}}$  of  $1.6 \times 10^2$  ( $2.1 \times 10^2 < I_{\text{molecule}} < 1.3 \times 10^2$ ). From the data shown in Fig. 5b, it can be calculated that the standard deviation of the noise on the ADF signal is 17 counts. This means that the mass deposition resolution that can be ultimately achieved with this technique is a single molecule.

It is observed that the estimated  $I_{\text{molecule}}$  of  $1.6 \times 10^2$  is large compared to the increase in the ADF signal shown in Fig. 2c and 5b. If a precursor molecule would be deposited directly in the primary electron beam, this would give rise to a significant step in the growth curve. The largest measured step sizes in the growth curves are in the order of 80. Although the measured values do not fall within the estimated extremes, the estimated  $I_{\text{molecule}}$  is still reasonable taking into account that the actual height and composition of the dots are unknown.

When the dynamic ADF feedback control is applied for the writing of lines, it is effective in reducing the proximity effect for two reasons. First of all, the ADF noise level is below the mass deposition resolution. Second of all, the electron beam probes the relevant part of the line. The proximity effect is dependent on the angle between the area that is irradiated and the focused electron beam. This area is exactly the area that is probed for the dynamic ADF feedback control. This explains that the proximity effect is well controlled. However, when the dynamic ADF feedback control is applied for the writing of dots, the method turns out to be ineffective: there still remains a distribution of deposited masses. This indicates that the variation in masses of the dots is not determined by the mass resolution of the dynamic ADF feedback control, but the physical processes that occur in the initial stages of the growth. We suggest that in the initial growth stages a significant part of the dot grows nonsymmetrically outside the area exposed by the electron beam. This can for instance be the result of diffusion of dissociated molecules, local fluctuations in the substrate or of secondary electron scattering in the substrate.

Although the *in situ* monitoring method described here is limited to electron transparent substrates, it offers valuable insight into the growth process of individual nanometer-sized deposits. Similar *in situ* monitoring methods may be applied to nontransparent substrates. Bret

*et al.* have for instance measured the sample current in the SEM [101] during EBID growth, and x-rays and the secondary electron signal are possibly suitable as well.

### **Conclusions**

During electron beam induced deposition (EBID) on electron transparent membranes, the transmitted annular dark field (ADF) signal can be monitored. A method was developed to use the ADF signal to obtain insight into the growth process and to control the mass of individual nanometer-sized deposits. Arbitrary 2D patterns can be defined. The smallest sampling time of the ADF signal monitoring is presently about 40 ms. For arrays of dots that were deposited, the growth of each individual dot was monitored. It is observed that the growth is different for each dot, although the average deposit growth rate is linear with the dwell time. Apart from monitoring the ADF signal during the growth, the amount of deposited mass can be controlled for individual deposits by terminating the growth process when the ADF signal exceeds a threshold value. The dynamic ADF feedback control was applied to reduce variations in deposit mass. This attempt did not succeed, but the method was successfully applied to prevent the occurrence of a proximity effect. When the electron beam irradiates the side of an already existing structure, the amount of deposited material is higher than if the electron beam irradiates an area that is under normal incidence. With the dynamic ADF feedback control, this effect can be compensated *in situ* and the amount of deposited material that is probed by the beam is constant regardless of the local growth rate.

The mass resolution of the feedback system is estimated by assuming a volume and a density of the deposits. It is estimated that the mass resolution is a single molecule.

### **Acknowledgement**

The authors gratefully acknowledge the use of the facilities in the Center for Solid State Science at Arizona State University.

## 8. Growth behavior near the ultimate resolution of nanometer-scale focused electron beam-induced deposition

*W.F. van Dorp*<sup>a)</sup>, *C.W. Hagen*<sup>a)</sup>, *P.A. Crozier*<sup>b)</sup>, *P. Kruit*<sup>a)</sup>

<sup>a)</sup> Delft University of Technology, Faculty of Applied Sciences, Lorentzweg 1, 2628 CJ Delft, the Netherlands

<sup>b)</sup> Center for Solid State Science, Arizona State University, Tempe, Arizona 85287

### Abstract

The nucleation stage of electron beam induced deposition (EBID) has been studied by depositing arrays of dots from  $W(CO)_6$ . Measurements of the annular dark field (ADF) signal during the growth and post-deposition ADF image processing were combined with atomic force microscope measurements. The smallest average dot diameter measured is 0.72 nm for the full width at half maximum and 1.0 nm for the diameter containing 50% of the deposit volume. The average growth rate after 1.0 s of deposition time was 2.9 nm<sup>3</sup>/s. The development of a deposit as a function of time is found to be different for each dot, despite identical growth conditions. The center of mass of each dot is not exactly on the position irradiated by the e-beam but instead the deposit nucleates on a random spot close to the irradiated spot. Not only the first nucleus is deposited on a random position; later on in the process, material can still be deposited on random positions around the irradiated spot. As a result of this, the shape of the dots is nonsymmetric. The growth rate is not constant during deposition (varying between -3.3 and 15 nm<sup>3</sup>/s) and the final deposit volume varies from dot to dot. The distributions of deposit volumes found in the experiments were compared to Poisson distributions. This comparison allowed an estimation of  $\lambda$ , the expected number of discrete events during a specific interval. It was estimated that after 1.0 s of deposition time, the average deposition rate was 5.5  $\lambda$ /s, with a volume of 0.4 nm<sup>3</sup>/ $\lambda$  and a deposition efficiency of  $3.7 \times 10^6$  electron/ $\lambda$ . The volume of 0.4 nm<sup>3</sup>/ $\lambda$  is within a factor of 2 of the volume of a  $W(CO)_6$  molecule in the solid phase. Despite the efforts made, it was not possible to detect the deposition of single molecules or clusters of a constant size in the recorded ADF signal.

## Introduction

Developing techniques for the controlled fabrication of nanostructures is a topic of intense research and is critical to exploit the full potential of nanotechnology. Focused electron beam induced processing (FEBIP) can be used to define and precisely position arbitrary shaped patterns onto substrates. Precursor molecules, introduced into a vacuum chamber, adsorb on the substrate and are irradiated by a focused electron beam. Under the influence of the e-beam, the adsorbed molecules are dissociated into fragments. If these fragments react with the substrate and form volatile species, the substrate is etched (in the case of electron beam induced etching, EBIE). If the fragments stick to the surface and form a deposit, one speaks of electron beam induced deposition (EBID). Since the fragmentation only occurs in or very close to the irradiated area and electron beams can be made as small as 0.1 nm, EBID is very well suited for sub-10 nm patterning. This has been demonstrated with deposits having widths of 8 nm [80, 81], 5 nm [82], 4 nm [83], 3.5 nm [84], 1.5 nm [85] and even 1.0 nm [86]. The patterning capabilities are demonstrated with a world map that includes topographical information (see Fig. 1). The color indicates that the Himalayas, the Rocky Mountains and the Andes are higher than the rest of the world. Honduras is 7.5 nm wide.

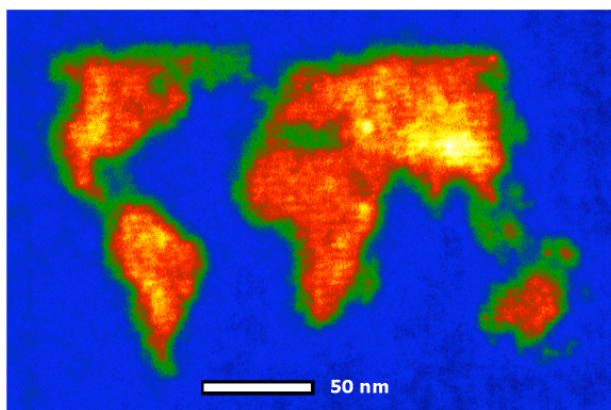


*Fig. 1. World map created with EBID. The false colors indicate that the Himalayas, the Rocky Mountains and the Andes are higher than the rest of the world.*

It has already been shown that for sub-5 nm deposits, the amount of deposited material is not constant, but fluctuates (even for identical fabrication conditions) [86]. Indications were found that the number of molecules dominates the statistics rather than the number of electrons required for the dissociation [200]. In this article, the nucleation stage of sub-10 nm EBID growth is explored. To perform this study, measurements of the annular dark field (ADF) signal during the growth and post-deposition ADF image processing were combined with atomic force microscope measurements.

## Experimental

EBID was performed in an environmental Tecnai F20 scanning transmission electron microscope (STEM), allowing the entire growth process to be observed and controlled in situ and in real time. The microscope is equipped with a field-emission electron source and was operated at 200keV with a nominal beam spot size of 0.3-0.4 nm. The precursor used for

deposition was  $W(CO)_6$  and typical pressures were in the range of  $1 \times 10^{-3}$  Torr. Substrates were 10 nm thick amorphous carbon and 50 nm thick  $Si_3N_4$  membranes. During experiments, the substrate was kept at a temperature of 150 °C.

Imaging was performed with the annular dark field (ADF) signal. For thin films, the ADF image intensity is linear with mass or thickness and is given in counts (arbitrary units). All depositions were done on an area that was not previously exposed to electrons.

Arrays of dots were deposited with two different scan routines. Suppose for instance that EBID was performed on three positions on the substrate, positions I, II and III (marked with “+” in Fig. 2a and 3a). In scan routine A (Fig. 2a), the positions were irradiated sequentially with the beam in stationary position for a specific dwell time (for instance 1000 ms).

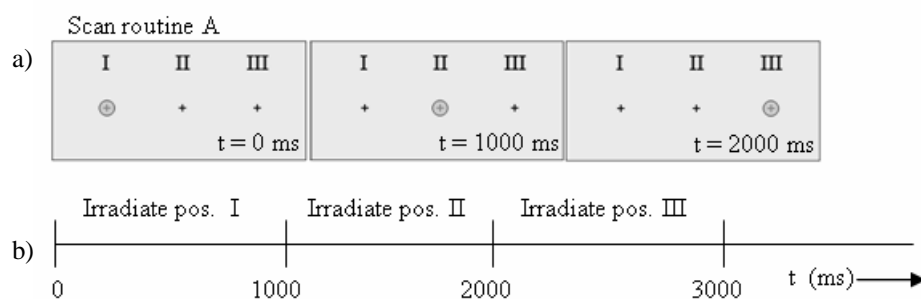


Fig. 2. (a) Schematic drawing of scan routine A. The  $e$ -beam is focused onto position I and kept stationary during the dwell time (1000 ms). Sequentially, position II and position III are irradiated. (b) Corresponding time line.

In scan routine B, the beam was scanned over position I (see Fig. 3a). The scan area was  $2 \times 2$  nm in size, divided into  $5 \times 5$  pixels and the dwell time  $t_{dwell, scanning}$  was 10  $\mu$ s per pixel. The time required for 1 frame,  $t_{frame}$ , was therefore 0.25 ms. During the scan, the ADF signal was collected and the intensity  $I_{scan}$  (integrated over the  $5 \times 5$  pixels) was saved to file. Next, position I was irradiated by keeping the beam stationary in the center of the  $2 \times 2$  nm<sup>2</sup> square. The irradiation time  $t_{irradiate}$  was chosen such that  $t_{irradiate} = 10 \times t_{frame}$ , so  $t_{irradiate}$  was 2.5 ms. This scan sequence (scanning, saving and irradiating) was repeated for a number of iterations (100, 200 or 400), after which the procedure was repeated for position II and III.

Both scan routines were performed with a constant dwell time (routine A) or a constant number of iterations (routine B) per array. At the end of the routines, the beam was blanked. During the writing of the arrays, the environmental cell was flooded with precursor gas. ADF images of the completed arrays were not taken until the precursor gas was pumped out (unless mentioned otherwise).

Dedicated hard- and software was developed to use scan routine B on the environmental STEM. Scan signals were generated with a National Instruments (NI) card and added with an adding amplifier to the scan signals of the standard microscope control. The maximum scan rate that could be achieved was limited by the hardware of the microscope. It was found that for dwell times per pixel  $< 10$   $\mu$ s the pattern was not defined correctly anymore.

The ADF signal was recorded using the same NI card. The minimum sampling time for the NI card was 1  $\mu$ s. This means that for a  $t_{dwell, scanning}$  of 10  $\mu$ s per pixel, the ADF signal was integrated over 10 samples.

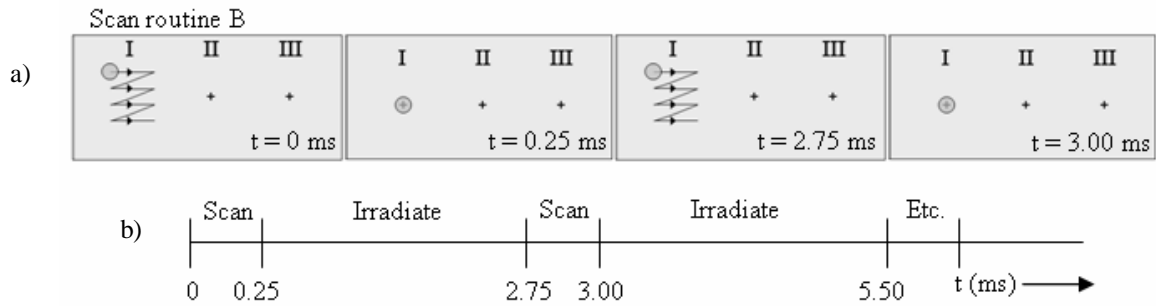


Fig. 3. (a) Schematic drawing of scan routine B. Firstly, the beam is scanned over position I, during which the ADF signal is collected. Next, the beam is kept stationary on position I for a given dwell time. This scan sequence of scanning (and collecting the ADF signal) and irradiating is repeated on position I for a number of iterations, after which the entire procedure is repeated for position II and III. (b) Corresponding time line (not to scale).

### Image analysis

In order to collect data from the EBID experiments, a technique to analyse the ADF images of the deposited arrays was developed. This technique is used to determine the diameter of the deposits and to determine the integrated intensity of each deposit,  $I_{dot}$ . In each array ( $11 \times 11$  or  $7 \times 7$ ), the dots were intended to be deposited on a square grid. However, the arrays are distorted because of drift of the specimen during deposition. To correct for this, a trapezium-shaped grid is overlaid on the ADF image, such that the points of the grid coincide as best as possible with the dot positions in the array.

For measurements of the deposit diameters, a box is overlaid on each point of the trapezium-shaped grid, centered around the grid point. Each box is  $n \times n$  pixels and is now a sub-image, containing the ADF image of a single dot. All boxes (i.e. all sub-images of the single dots) are added linearly, which yields an average ADF image (of  $n \times n$  pixels) of the dots in the array. In this averaged sub-image, the center of gravity of the dot is determined, which is used to measure the average diameter.

For the measurement of  $I_{dot}$ , two boxes are overlaid on each point of the trapezium-shaped grid, centered around the grid point. Box 1 contains  $N_1$  pixels and is large enough to overlap the area covered by the dot including its tails. Box 2 contains  $N_2$  pixels and is slightly larger than box 1. Then, the sums  $\Sigma I_1$  and  $\Sigma I_2$  of all intensity values of respectively box 1 and box 2 are calculated. The average background intensity value per pixel  $I_{BG}$  is calculated by:

$$I_{BG} = (\Sigma I_2 - \Sigma I_1) / (N_2 - N_1) \quad (1)$$

The integrated intensity arising from the deposited material  $I_{dot}$  on a particular grid point is calculated by:

$$I_{dot} = \Sigma I_i - (I_{BG} * N_i) \quad (2)$$

The procedure of overlaying the boxes and calculating  $I_{dot}$  is performed for all dots in the array. Since the pixel intensity in ADF images is proportional to the thickness of the probed area,  $I_{dot}$  (in arbitrary units) is proportional to the volume of the deposit.

### Results and discussion

Arrays with dwell times of 0.25, 0.125, 0.06 and 0.03 s have been deposited on a 10 nm thick amorphous carbon substrate with scan routine A. ADF images were recorded with the precursor gas present. The results are shown in Fig. 4. There are a number of observations to make on arrays obtained with scan routine A concerning (1) the average amount of deposited material, (2) the diameter of the dots, (3) the shape of the dots and (4) the positions of the dots with respect to the intended grid position. Starting with the amount of deposited material, it is observed that the amount of deposited material increases with increasing dwell time. This is visible in the ADF images as an increase in dot intensity.  $I_{dot}$  was determined for the arrays in Fig. 4 and is found to increase linearly with dwell time (see Fig. 5a).

Of the arrays shown in Fig. 4, the averaged sub-images have been taken and are shown in Fig. 5b-e.

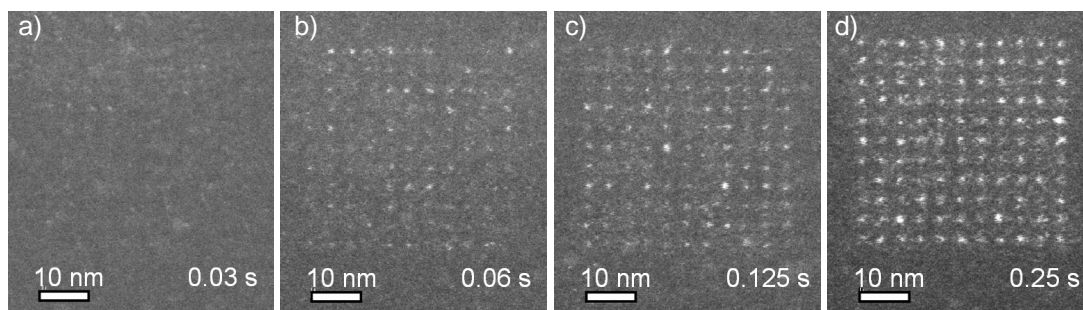


Fig. 4. Four  $11 \times 11$  arrays deposited with scan routine A, using different dwell times. As the dwell time increases, the amount of deposited material also increases (visible as an increase in dot intensity).

From these averaged sub-images, the dot diameter  $d_{dot}$  is determined. Fig. 5a shows the full width at half maximum (FWHM) and the FW50% (the diameter in which 50% of the dot volume is contained). It is observed that  $d_{dot}$  (FWHM) decreases from 0.90 nm to 0.83 nm for dwell times of 0.25 and 0.03 s, respectively. The smallest diameter measured is 0.72 nm for the FWHM and 1.0 nm for the FW50%. The outlier for the smallest dwell time (shown in grey) is the result of the difficulty in determining the center of gravity in the averaged sub-images. The noise level in the sub-images becomes significant because so little material was deposited (see Fig. 5a).

An average diameter of 1.0 nm for the smallest FW50% is the smallest that has been achieved until now. It is also close to the value that was predicted by a Monte Carlo simulation. In [201], results are described from a simulation of the scattering of 200 keV

primary electrons in a flat, 10 nm thick Cu sample. It turns out that, for a 0.2 nm diameter electron beam, 50% of the secondary electrons are emitted from an area of 0.86 nm in diameter. Although a different substrate was used in the experiment, it shows that the smallest average diameter in the experiment is very close to the ultimate EBID resolution.

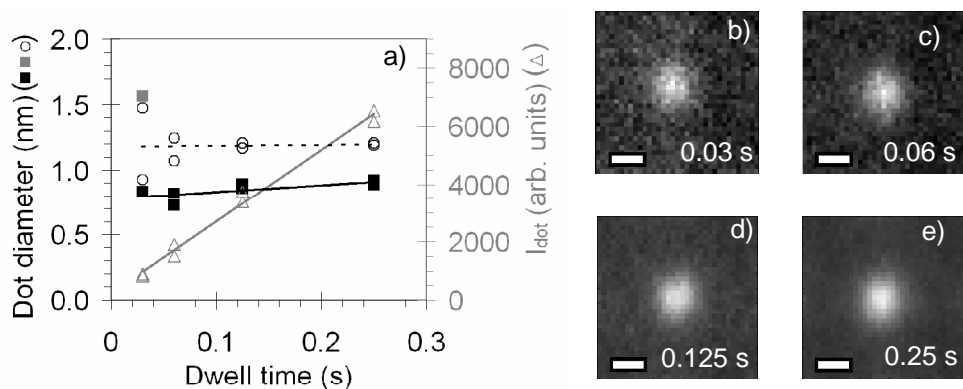


Fig. 5. (a) A plot of  $I_{dot}$  ( $\Delta$ ), the FWHM ( $\blacksquare$ ) and FW50% ( $\circ$ ) as function of the dwell time. The grey point is considered an outlier and is not used to fit the trendline for the FWHM. (b) – (e) The average sub-images of the dots. The scale bars indicate 1 nm.

The limit in spatial resolution for the *average* deposit may have been nearly reached, *individual* deposits can still be smaller than 0.86 nm. The smallest conceivable individual deposit is a single molecule. The factor currently limiting the *average* deposit diameter is the positioning precision, because the center of mass of each dot is not exactly on the intended position in the array. This can be due to several effects. First of all, the area from which secondary electrons are emitted from the substrate is larger than the diameter of a single molecule. Secondly, it is possible that molecules diffuse between the moment that it is dissociated and the moment it is actually pinned down. The result of these two effects is that the deposit nucleates on a random spot close to the irradiated spot. Fig. 6 shows a schematic drawing of three irradiated positions on the substrate (I, II and III).

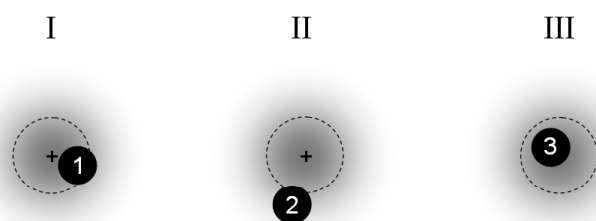


Fig. 6. Schematic drawing of three irradiated positions on the substrate (I, II and III). The electron beam irradiates the substrate at “+”, around which secondary electrons are emitted (shown in grey). The deposit nucleates on a random position in an area around “+”. The average distance between the intended position in the array and the center of mass of the dot is indicated with the dashed circle in Fig. 6 and is 0.23 nm for the dots in Fig. 4.

Supposing that the electron beam irradiates the substrate at “+”, secondary electrons are emitted from the area around it (shown in grey). The deposit does not necessarily nucleate on “+”, but can for instance nucleate on position 1, 2 and 3. Although the *individual* deposits may be single molecules in each case, the *average* diameter will be larger. Finally, other factors contributing to the *average* diameter are specimen drift and (possibly) small vibrations in the electron beam during writing and imaging of the deposit. The average distance between the intended position in the array and the center of mass of the dot is indicated with the dashed circle in Fig. 6 and is 0.23 nm for the dots in Fig. 4.

It appears that not only the first nucleus is deposited on a random position. Later on in the process, material can still be deposited on random positions around the irradiated spot. This becomes evident from the ADF images in Fig. 7. Dots are shown for 3 different dwell times. The deposition conditions were similar (though not identical) to the conditions used to create the arrays in Fig. 4. Per dwell time, the dots were taken from the same array, so the deposition conditions were identical. The white squares indicate  $5 \times 5$  nm. It is clearly observed that the dots are nonsymmetric and all different from each other. The nonsymmetry of the dots implies that the definition of the size of an individual deposit becomes difficult.

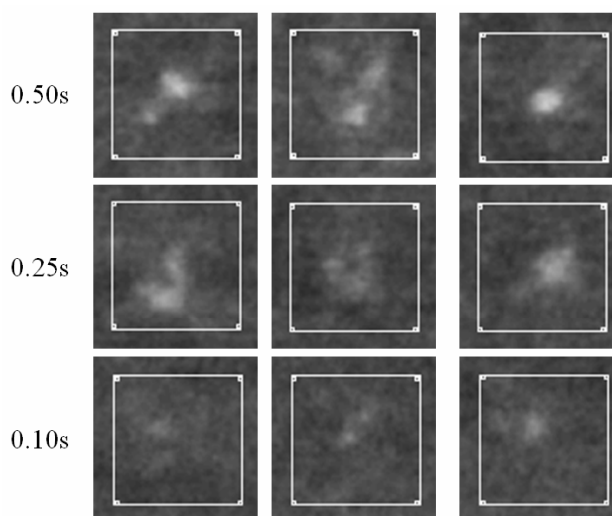


Fig. 7. Close-up of some of the dots. The white squares indicate  $5 \times 5$  nm. Many of the dots are nonsymmetric. The time on the left is the dwell time.

The results discussed until now are based solely on arrays deposited with scan routine A. It has been reported earlier that *in situ* measurements of the ADF signal give valuable insight into the growth process and can even allow control over the deposition of lines [202]. It was estimated that the sensitivity was a single molecule. An attempt was made to use this *in situ* measurement of the ADF signal to control variations in the mass of dots, but this was not successful. The explanation given was that “a significant part of the dot grows nonsymmetrically outside the area exposed by the electron beam”.

To be able to probe the entire dot and detect the deposition of single molecules, scan routine B was developed. Typical developments of  $I_{scan}$  as function of time are shown in Fig. 8a-e. The raw data is presented in grey, the averaged data (moving average over 35 datapoints) is

presented in black. Fig. 8a shows a measurement of the noise, recorded by executing scan routine B in the absence of precursor gas. The standard deviation of  $I_{scan}$  for this measurement is 4.1 mV. Fig. 8b-e are measurements with precursor gas. Fig. 8f is the average curve for 147 deposits, which shows that the average increase in  $I_{scan}$  is about 17 mV. This means that the strong increase observed in Fig. 8c and e are outliers and not typical of the deposition process. It is observed that the growth rate is not constant during the deposition. During the periods indicated with A, C and E the ADF signal stays roughly constant for as much as tenths of seconds. There are gentle (C and F) and stronger (D) increases even decreases (G) of the ADF signal. Occasionally, sharp changes in the signal are observed. Examples of these sharp changes are indicated with black lines in Fig. 8d and e. The values are averages over the width of the lines.

The average growth curve in Fig. 8f makes clear that the growth in the very early stage is not linear (assuming that the composition remains constant). A similar nonlinearity was observed by Guise *et al.* [159]. It is tentatively suggested that this is due to the change in target surface during the first stages of growth. As the deposit grows, the surface onto which precursor molecules adsorb changes from substrate to deposit. The resulting change in residence time of precursor molecules and/or SE yield can lead to lower growth rates later on.

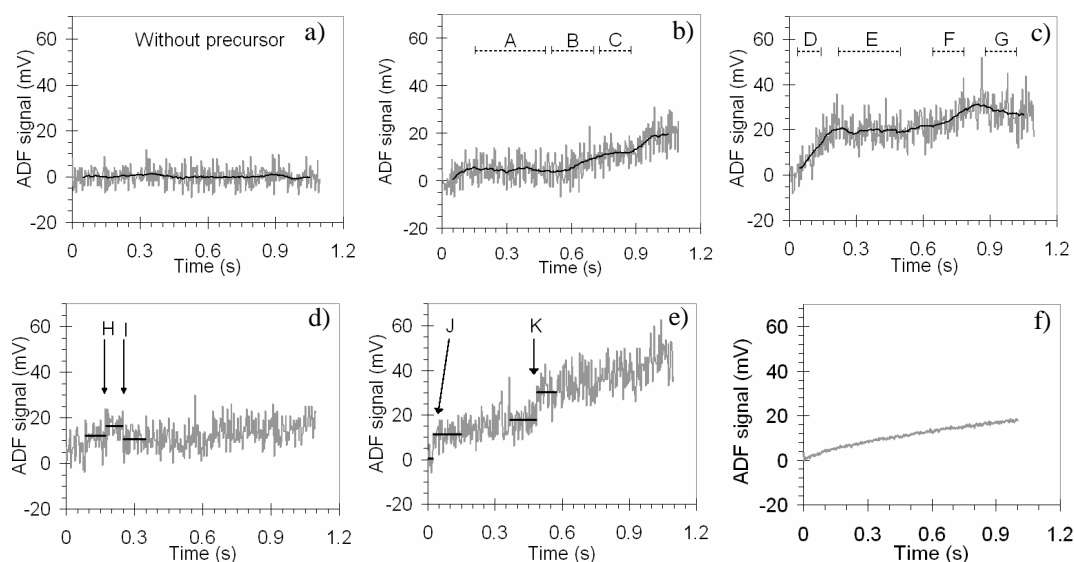


*Fig. 8. (a) Scan routine B executed without precursor gas present. No deposition is observed, which allows the determination of the noise level. (b, c, d, e) Scan routine B executed with precursor gas present. Curves shown in grey are raw data, curves shown in black are averaged data. Averaging for (b, c) was over 35 data points, averaging for (d, e) was over the width of the indicated lines. Indicated are periods of no significant growth (A, C, E), increases (C, D, F), a decrease (I) and sudden jumps (H, J, K). (f) Data averaged over 147 growth curves.*

What are the sharp changes observed in Fig. 8d and e? Are they the deposition of single molecules? If so, what do the more gentle changes in Fig. 8b and c mean? To answer these questions, it is important to characterize the deposits in more detail. In the first place, this is

done by determining the height of the deposits by AFM. Secondly, the variations in deposit mass are analysed. In Fig. 4, it is observed that the dot intensity (i.e. the deposited mass) is not constant over the array. There is a variation in intensity, even though the deposition conditions were identical for each dot in the array. A better understanding of these variations may be helpful for interpreting the growth curves in Fig. 8.

To be able to probe the dots with an AFM, dots were deposited on a 50 nm thick  $\text{Si}_3\text{N}_4$  membrane with a beam current of 36 pA. The results are shown in Fig. 9. The insets in (a), (b) and (c) show a schematic representation of the orientation of the sample with respect to the electron beam or the AFM tip. In the transmission microscope, the recorded images give a projection of the sample. Assuming that the composition of the deposit is constant, the highest point of the deposit is represented by the highest intensity of the deposit,  $I_{max}$ . Since EBID is performed on an electron transparent membrane, a deposit grows on the entrance as well as on the exit side, so  $I_{max}$  is the sum of the intensity of the deposit on the entrance and exit side:

$$I_{max} = I_{max, entrance} + I_{max, exit} \quad (3)$$

A dot array was deposited (Fig. 9a). With the AFM, only the part of the dot on the exit side of the membrane was probed (see Fig. 9b). This gives the height of the highest part of the deposit,  $h_{max, exit}$ . To have a measure for  $I_{max, exit}$ , the membrane was tilted to  $15^\circ$  (see Fig. 9c). From these tilted ADF images, the integrated intensities  $\Sigma I_{dot, entrance}$  and  $\Sigma I_{dot, exit}$  are determined. It is assumed that the growth rates at the entrance and exit side are identical for these small deposits. In other words, it is assumed that:

$$I_{max, exit} = I_{max} * [ \Sigma I_{dot, exit} / (\Sigma I_{dot, entrance} + \Sigma I_{dot, exit}) ] \quad (4)$$

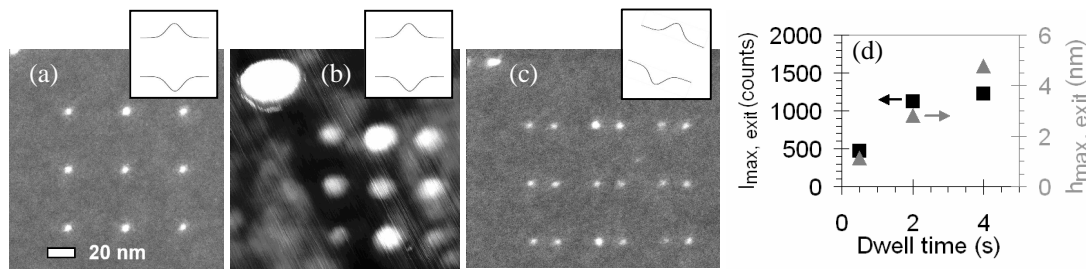


Fig. 9. (a) ADF image of dots written with a beam current of 36 pA and a dwell time of 2 s per dot (perpendicular). (b) AFM image of the exit side of the array in (a). (c) ADF image of the array in (a), but now tilted to  $15^\circ$ . (d)  $I_{max, exit}$  and  $h_{max, exit}$  plotted as function of the dwell time. The insets in (a, b, c) show a schematic representation of the orientation of the sample with respect to the electron beam or the AFM tip.

Both  $I_{max, exit}$  and  $h_{max, exit}$  are averaged per array. Fig. 9d shows these average values for 3 different dwell times. It is observed that  $h_{max, exit}$  is linearly proportional to  $I_{max, exit}$  for dwell times of 0.5 and 2.0 s. For the array deposited with 4.0 s, this is not the case anymore. We suspect that at a dwell time of 4.0 s, the growth rate at the entrance and exit sides are no

longer identical, because the deposit at the entrance side has become too thick. This means that relationship (4) is not valid for this array.

Assuming a constant composition, the ADF intensity is proportional to the deposit height, so the AFM measurements can be used to scale ADF intensities (in arbitrary units) to height (in nm). Based on the values of  $h_{max, exit}$  and  $I_{max, exit}$  for the 0.5 and 2.0 s arrays, the scaling factor  $C_{36 pA}$  is  $2.5 \times 10^{-3}$  nm/count.

Fig. 10a shows an ADF image of a deposit written on a 10 nm thick amorphous carbon substrate with a beam current of 3.2 pA. It is assumed that the ADF current decreases proportionally to the beam current. Taking into account a difference in magnification, the intensity conversion factor  $C_{3.2 pA}$  is  $1.4 \times 10^{-2}$  nm/count. In Fig. 10b, the same ADF image is shown, but now in 3D representation with the z-axis in nm. The line profile of the dot in Fig. 10a is shown in Fig. 10c. The horizontal and vertical axis are shown with identical scaling to demonstrate the relative dimensions.

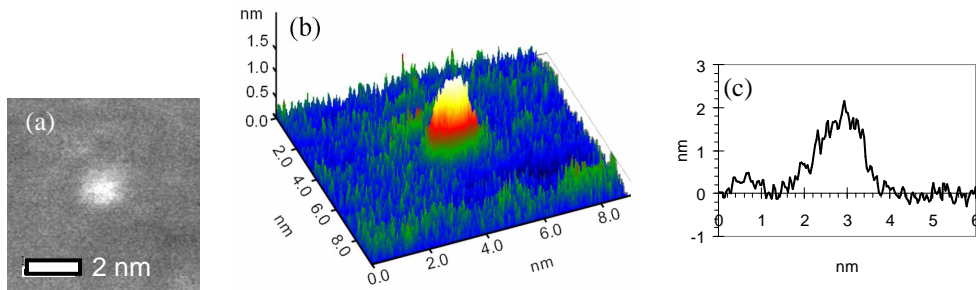


Fig. 10. (a) ADF image. (b) Same ADF image, but now in 3D representation with scaling of the z-axis in nm. (c) Height profile of the dot in (a). The horizontal and vertical axis are shown with identical scaling to demonstrate the relative dimensions.

With the AFM measurements, the intensity variations such as observed in Fig. 4 can be expressed in terms of variations in deposited volume. This has been done for arrays of dots deposited on a 10 nm thick amorphous carbon substrate, with dwell times of 1.00, 0.50, 0.25 and 0.10 s and a beam current of 3.2 pA. For each position in the array  $I_{dot}$  has been determined. For each dwell time, three  $7 \times 7$  arrays have been deposited, which gives 147 measurements of  $I_{dot}$  per dwell time.  $I_{dot}$  is proportional to the volume of the deposit (in arbitrary units) and can be scaled to  $V_{dot}$  (in  $\text{nm}^3$ ) using  $C_{3.2 pA}$  (in nm) and the area per pixel in the ADF images (in  $\text{nm}^2$ ). Please note that  $V_{dot}$  is the sum of the volume of the deposits on the entrance and the exit side of the membrane.

The values for  $V_{dot}$  were binned and are shown in the histogram in Fig. 11a. The number of occurrences  $N_V$  have been normalized to the total number of measurements per dwell time (147). So for instance, if a  $V_{dot}$  of  $1.4 \text{ nm}^3$  occurred 28 times in the 0.25 s arrays, this gives an  $N_V$  of  $28/147 = 0.2$  in Fig. 11a. It is observed that, as the dwell time increases, the average amount of deposited material also increases. The negative values are the result of noise in the ADF images. At the smallest dwell times, there are many positions in the array where there is very little or even no deposit and the background correction applied in equation (2) can give rise to negative values for  $I_{dot}$  (and hence negative values for  $V_{dot}$ ).

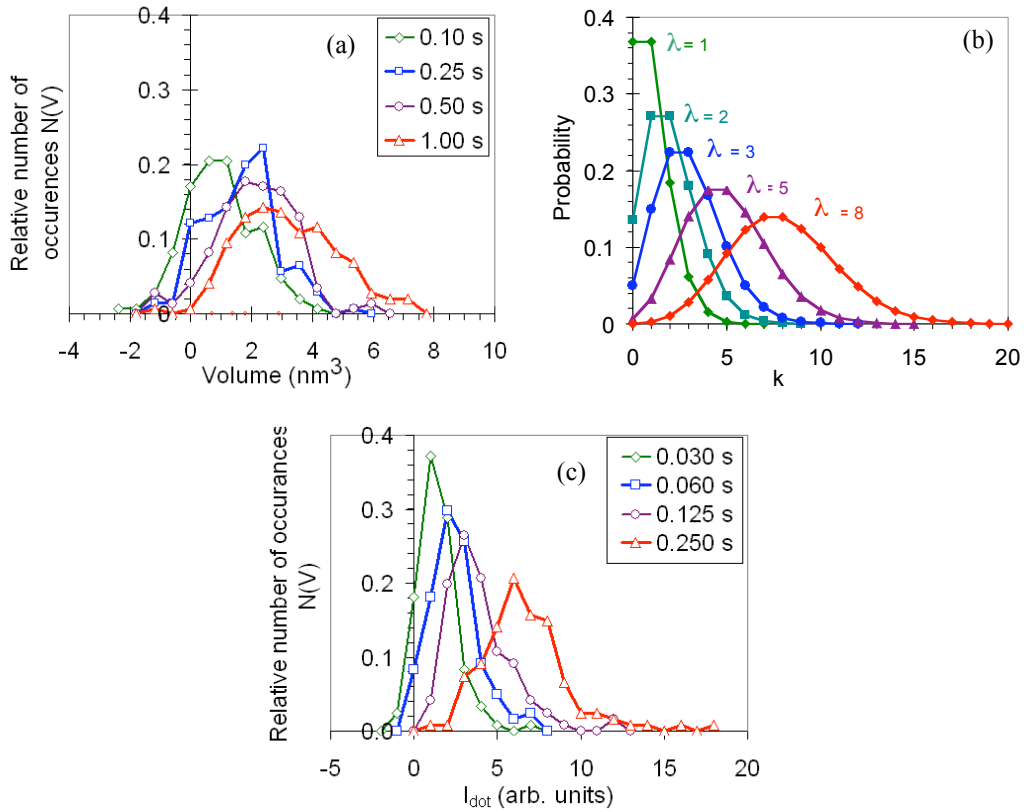


Fig. 11. (a) The relative frequency with which dot volumes occur in arrays deposited with dwell times of 0.10, 0.25, 0.50 and 1.00 s. (b) Poisson statistics for expectation values  $\lambda$  of 1, 2, 3, 5 and 8 (lines are drawn to guide the eye and do not indicate continuity). (c) The relative frequency with which  $I_{\text{dot}}$  occurs in the arrays in Fig. 4.

The growth of a deposit consists of a series of dissociation events. If these dissociation events do not influence each other and occur at a known average rate, the volume distributions can be modeled with Poisson distributions. A Poisson distribution expresses the probability  $P_{(k)}$  that a particular event occurs  $k$  times for a given expected number of discrete events ( $\lambda$ ) during an interval of known length. Poisson distributions are calculated with:

$$P_{(k)} = (\lambda^k e^{-\lambda}) / k! \quad (3)$$

In the experiments described here,  $k$  represents the number of discrete units that have been deposited, or the amount of material that was deposited ( $V_{\text{dot}}$  in Fig. 11a). The probability  $P_{(k)}$  corresponds to the relative number of times  $N_V$  that a particular number of units or a particular volume is found. Parameter  $\lambda$  then represents the average number of dissociation events for a given dwell time. The values of  $P_{(k)}$  have been calculated for  $\lambda = 1, 2, 3, 5$  and 8 and are shown in Fig. 11b. It is observed that the shapes of the distributions in Fig. 11a and Fig. 11b are similar, with the exception of the values for 0.10s dwell time in Fig. 11a. This is probably due to the noise in the ADF images and in the image processing. The shape of these distributions is reproducible, as becomes clear from the histogram of values for  $I_{\text{dot}}$  in Fig.

11c. These values were calculated from the arrays in Fig. 4 and, although  $I_{dot}$  was not calibrated with the AFM measurement, the trend is clearly similar to that in Fig. 11b.

By fitting the Poisson distributions to the volume distributions, an estimate can be made of  $\lambda$  for each dwell time used in the experiments. This estimate is based on the assumption that every deposited molecule is visible in the ADF image. In Fig. 12a, an example of a fit is shown. Two fit parameters were used:  $\lambda$  and the linear scaling factor  $f$ . The factor  $f$  merely served to scale values of  $k$  to the volumes found in the experiment. Values for  $P_{(k)}$  were not scaled.

In Fig. 12b the data from the different sources are shown as function of time. The averages for  $V_{dot}$  ( $\blacktriangle$ ) are calculated from the distributions in Fig. 11a. The fitted  $\lambda$  ( $\blacksquare$ ) and the average values for  $I_{scan}$  (same data as in Fig. 8f) are shown in grey. From Fig. 12b, it is calculated that after 1.0 s deposition time the average  $V_{dot}$  is  $2.9 \text{ nm}^3$ , the scaling factor for  $I_{scan}$  is  $6.1 \text{ mV/nm}^3$ , the average dissociation rate  $R_{diss}$  is  $5.5 \lambda/\text{s}$  and the average volume per  $\lambda$  ( $V_\lambda$ ) is  $0.4 \text{ nm}^3$ . From the beam current of  $3.2 \text{ pA}$  it is calculated that the dissociation efficiency is  $3.7 \times 10^6 \text{ electrons}/\lambda$ .

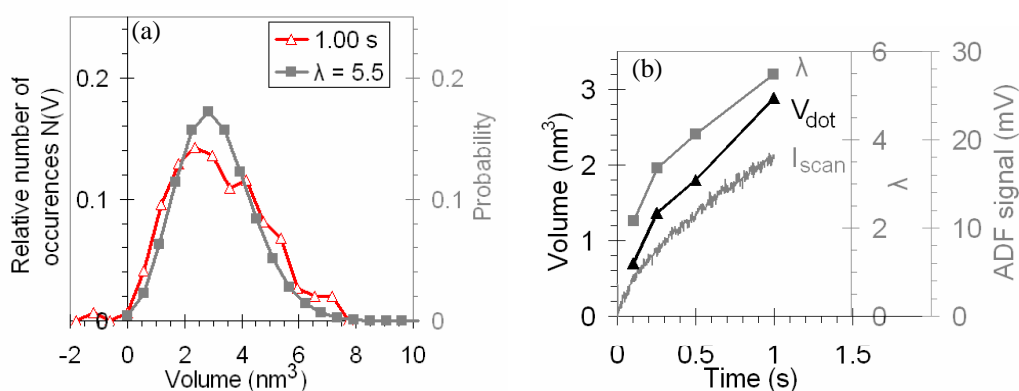


Fig. 12. (a) A fit of a Poisson distribution to the volume distribution of arrays with 1.00 s dwell time. (b) The average values for  $V_{dot}$  and the fitted values for  $\lambda$  as function of the dwell time. The average dissociation rate after 1 s was  $5.5 \lambda/\text{s}$ , the average volume of material that is deposited per  $\lambda$  is  $0.4 \text{ nm}^3$ .

The question remains what  $\lambda$  is.  $V_\lambda$  is within a factor of 2 of the volume of a  $\text{W}(\text{CO})_6$  molecule, which is  $0.22 \text{ nm}^3$  (calculated from the density in the solid phase,  $2.65 \text{ g/cm}^3$ ). If  $\lambda$  represents one  $\text{W}(\text{CO})_x$  molecule, the fact that  $V_\lambda$  is so large could indicate that the fragmentation of the precursor molecules is far from complete and that most of the CO groups are still in the deposit. It can also mean that  $V_\lambda$  is overestimated. If the ADF signal is not sensitive enough to detect single  $\text{W}(\text{CO})_x$  molecules, the fit procedure for  $\lambda$  (as shown in Fig. 12b) underestimates the number of molecules per dwell time, leading to an overestimation of  $V_\lambda$ . It is also possible that  $\lambda$  represents a cluster of several molecules. It is not straightforward to suggest a measurement that allows a discrimination between the two options.

In Fig. 13, the information from the different analysis methods is put together. Fig. 13a shows three growth curves (on the left vertical axis  $\text{nm}^3$ , on the right vertical axis  $\lambda$ ). In Fig.

13b, the ADF images of the corresponding dots are shown. The size of the area that was scanned during scan routine B ( $2 \times 2$  nm) is indicated with the white squares overlaid on the ADF images. As a comparison to scan routine B, Fig. 13c shows an ADF image acquired after scan routine A for dots written with comparable dwell times under identical conditions.

Similar to the growth curves in Fig. 8, levels are observed in Fig. 13a where the ADF signal is (roughly) constant. If these levels were separated by a constant step size, it would suggest that the deposition of a constant volume (either single molecules or clusters of molecules) is detected. However, a detailed analysis of the data shows that the step sizes between the levels are randomly distributed. A constant step size is not detected.

This means that the sharp changes in  $I_{scan}$  observed earlier in Fig. 8d and e are part of a random distribution. The magnitude of the changes is  $0.9 \text{ nm}^3$  (H),  $-1.0 \text{ nm}^3$  (I),  $2.0 \text{ nm}^3$  (J) and  $2.0 \text{ nm}^3$  (K). These values are significantly larger than  $V_\lambda$  and it is tentatively suggested that these sharp changes are clusters of molecules that move into or out of the scanned area by adsorption, desorption or diffusion during the deposition process.

The growth rate in Fig. 8 varies between  $-3.3$  and  $15 \text{ nm}^3/\text{s}$ .

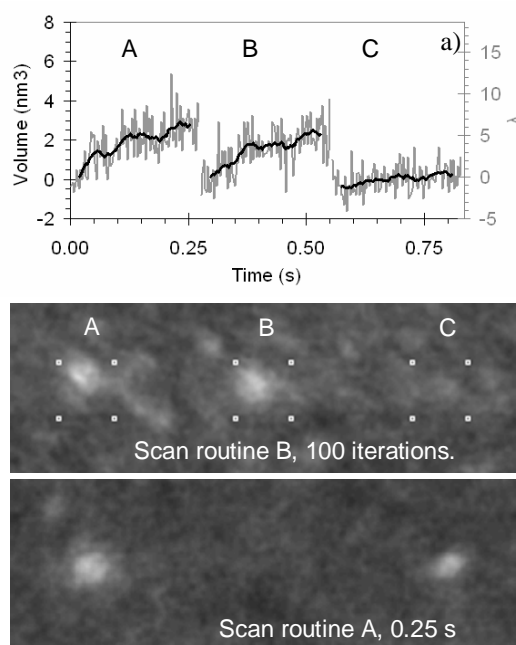


Fig. 13. (a)  $I_{scan}$  as function of time for 3 positions. (b) An ADF image of the dots corresponding to the growth curves in (a). (c) An ADF image of dots written with scan routine A, deposited with a comparable dwell time and under identical conditions as the dots in (b).

The fact that steps of a constant size were not detected in the development of  $I_{scan}$  as function of time, can be due to several (parallel) effects. First of all, it is possible that the noise level is too high. The noise level is  $4.1 \text{ mV}$  (equivalent to  $0.7 \text{ nm}^3$ ) and this could prevent the visibility of steps of  $0.4 \text{ nm}^3$ . But even in the moving averaged curves (black lines in Fig. 13), where the noise level is much lower, steps of a constant height are not observed.

It is also possible that the contribution of the parasitic deposition during the scanning was too large; The background intensity in Fig. 13b is considerably higher than in Fig. 13c, which is due to deposition during  $t_{frame}$ . If we assume that the deposition process is discrete and (on average) linear in time, there are two periods in each iteration of scan routine B where dissociation can occur: during  $t_{frame}$  and during  $t_{irradiate}$ . If molecules are dissociated during  $t_{irradiate}$ , they would be fully probed during  $t_{frame}$ , which means a complete step would appear in the ADF signal. If molecules are dissociated during  $t_{frame}$ , it is possible that this happens when the molecule is only partially and not completely under the beam. In that case, it would be probed partially and give a partial step in the ADF signal. It is conceivable that the partial steps occurring during  $t_{frame}$  smear out the complete steps during  $t_{irradiate}$ . However, since  $t_{irradiate} = 10 \times t_{frame}$ , this is not expected.

Another possibility is that the precursor molecule does not dissociate into fragments of a constant composition. Measurements of the composition with electron energy loss spectrometry have shown that the deposited material is not pure W. Rather, the deposits consist of fragmented  $W(CO)_x$  molecules, where  $x$  can vary (theoretically speaking) from 5 to 0. The composition is important for the ADF intensity, because it scales with approximately  $Z^{1.6}$  to  $Z^{1.9}$  [203]. For  $x = 5$ ,  $Z_{CO_5} = (6 + 8) \times 5 = 70$ , which is of the same order of magnitude as  $Z_W$  (74). This means that the  $Z$  of a dissociated molecule can vary nearly continuously from 74 ( $Z_W$ ) to 144 ( $Z_{W(CO)_5}$ ), smearing out (possible) steps in the ADF signal.

Related to this is the possibility that the contamination level was too high during the experiment. The environmental cell in the microscope was cleaned before the experiment, but the gas supply system or the precursor reservoir may have contained other species in addition to  $W(CO)_6$ . This may have reduced the partial pressure of  $W(CO)_6$  and the partial contribution to the deposition process.

Furthermore, if the deposit does not grow entirely inside the scanned area, it will not be probed entirely during  $t_{frame}$ . It is possible that due to specimen drift or perhaps the diffusion of dissociated molecules, a  $2 \times 2$  nm box was not large enough to probe the entire deposit.

Finally, it is possible that the ADF sensitivity is not enough to detect single molecules. However, with the measured volumes and deposit sizes, it is unlikely that the sensitivity is more than one order of magnitude less than single molecules. In conclusion, there are three likely causes for the absence of steps of a constant size in the growth curves: the  $W(CO)_6$  molecules do not dissociate into fragments of a constant composition, the contamination level was too high and the deposits were not probed entirely.

## Conclusions

The nucleation stage of EBID has been studied for deposits from  $W(CO)_6$ . Measurements of the ADF signal during the growth and post-deposition ADF image processing were combined with atomic force microscope measurements. The smallest average diameter measured is 0.72 nm for the FWHM and 1.0 nm for the FW50%. The average growth rate after 0.1 s of deposition time was 2.9 nm<sup>3</sup>/s. The development of a deposit as function of time is found to be different for each dot, despite identical growth conditions. The center of mass of each dot is not exactly on the position irradiated by the e-beam, instead the deposit nucleates on a

random spot close to the irradiated spot. Not only the first nucleus is deposited on a random position. Later on in the process, material can still be deposited on random positions around the irradiated spot. As a results of this, the shape of the dots is nonsymmetric. The growth rate is not constant during deposition (varying between -3.3 and 15 nm<sup>3</sup>/s) and the final deposited volume varies from dot to dot. The volume distributions found in the experiments were compared to Poisson distributions. This comparison allowed an estimation of  $\lambda$ , the expected number of discrete events during a specific interval. It was estimated that after 1.0 s of deposition time, the average deposition rate was 5.5  $\lambda$ /s, with a volume of 0.4 nm<sup>3</sup>/ $\lambda$  and a deposition efficiency of  $3.7 \times 10^6$  electrons/ $\lambda$ . The volume of 0.4 nm<sup>3</sup> is within a factor of 2 of the volume of a W(CO)<sub>6</sub> molecule in the solid phase. Despite the low growth rate, it was not possible to detect the deposition of single molecules or clusters as discrete steps in the recorded ADF signal.

### **Acknowledgement**

We would like to thank Jacques Nonhebel and Frans Berwald for developing the hardware and software for scan routine B and gratefully acknowledge the use of the facilities in the Center for Solid State Science at Arizona State University.



---

## 9. Remaining issues

### Contents

I. Si <sub>3</sub> N <sub>4</sub> as substrate .....	130
II. Graphite as a substrate .....	131
III. Resolution dependence on pressure and/or temperature.....	133
IV. Entrance/exit growth .....	134

In this chapter, results are discussed that have been obtained during the research for this thesis, but from which conclusions cannot be drawn unambiguously. If explanations are suggested, this is done so tentatively.

### I. $\text{Si}_3\text{N}_4$ as substrate

Since  $\text{Si}_3\text{N}_4$  membranes can be fabricated with various thicknesses in a controlled fashion and are chemically stable, it was assumed they would be useful substrates for EBID experiments. Growth of  $\text{W}(\text{CO})_6$  dots on these membranes was found to be very irregular. Scan routine A as described in Chapter 8 was used to deposit the dots. The growth rates were found to vary from position to position and the variations were much larger than expected on the basis of Poisson statistics as described earlier. As shown in Fig. 1a, some dots are even branched. The inset shows a blow-up of the dot, tilted to 20 degrees. The  $\text{Si}_3\text{N}_4$  membrane was 10 nm thick, it was kept at 100 °C, the dwell time was 8 s per dot, the beam current was approximately 40 pA and the precursor pressure was  $2.5 \times 10^{-3}$  Torr.

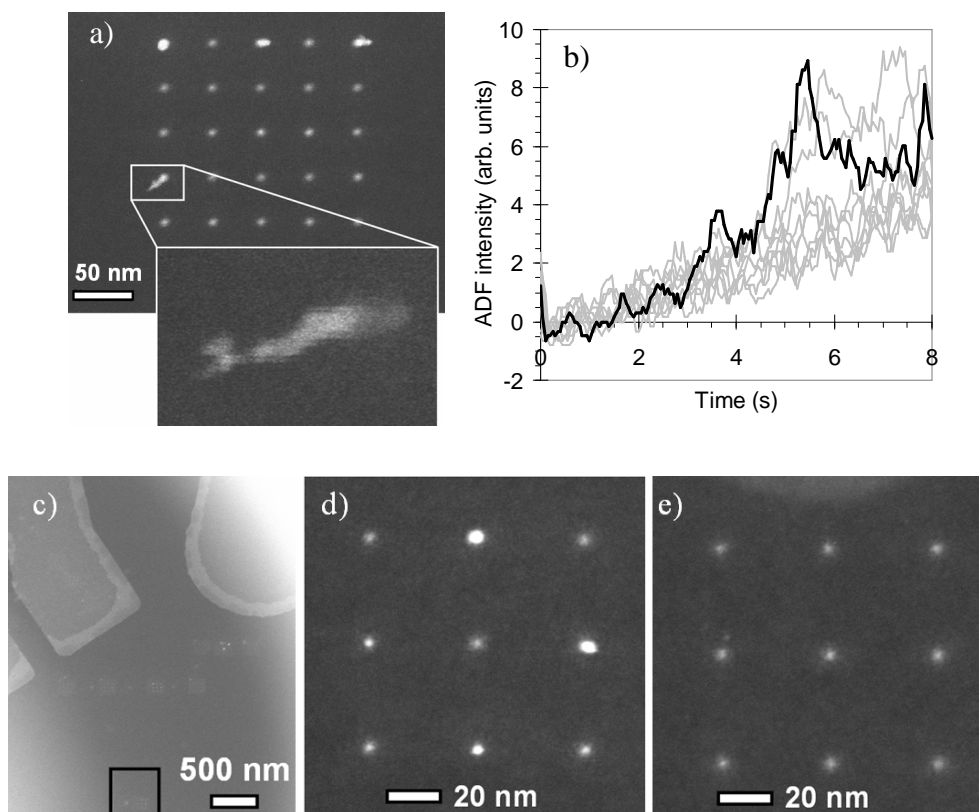


Fig. 1. (a) Array of dots on a 10 nm  $\text{Si}_3\text{N}_4$  membrane. Irregular growth with (sometimes) branched deposits is observed. The dwell time per dot was 8 s. The inset shows a blow-up of a branched dot, viewed under  $20^\circ$  of tilt. (b) The ADF signal as function of time for the dots in (a). The black curve is the ADF signal for the dot in the inset in (a). (c) STEM image of a patterned  $\text{Si}_3\text{N}_4$  with conducting lines fabricated by EBL. (d) Array of dots with irregular growth, deposited on the location indicated with a box in (c). (e) Array of dots with more regular growth, deposited close to a conducting electrode.

Fig. 1b shows the ADF signal that was monitored with a Picoscope during the growth of the dots in Fig. 1a. The growth curve of the dot in the inset is shown in black. It is observed that the bright dots initially have a growth rate similar to the average growth rate before they ‘spark’. The time it takes before dots ‘spark’ can vary from fractions of a second to seconds.

The branching of the dot is similar to the nanodendritic growth observed for deposition on  $\text{Al}_2\text{O}_3$  [174]. The nanodendritic growth was explained by charging of the substrate and field-induced diffusion of the precursor. It is tentatively suggested that the same mechanism occurred on the  $\text{Si}_3\text{N}_4$  membrane. Consistent with this hypothesis is an experiment where deposition was performed as function of distance from 10 nm thick conducting Ti/Ni lines (deposited by EBL). These lines are shown in the STEM image in Fig. 1c in the top left and right. Far from the conducting lines, in the area indicated with a box in Fig. 1c, growth was irregular (Fig. 1d). Close to the conducting lines, growth was much more regular (Fig. 1e, at the top edge the finger-shaped electrode is vaguely visible).

## II. Graphite as a substrate

The graphite substrate was prepared as described in Chapter 3. The deposition of dots from  $\text{W}(\text{CO})_6$  gave very irregular growth, but different from the Poisson statistics or the growth on the  $\text{Si}_3\text{N}_4$ . In Fig. 2 a STEM image of a deposited array is shown. The dark area in the upper left is vacuum, the bright area in the bottom right is the amorphous carbon support and in the upper right deposition due to the focusing of the beam is visible. Deposition was performed with a dwell time of 0.8 s per dot, a beam current of approx. 40 pA, a substrate temperature of 150 °C and a precursor pressure of  $3.8 \times 10^{-3}$  Torr. The intensity of the dots seems to depend on the intensity of the background. If the area on the graphite is brighter, the amount of deposited material is larger. On the dark areas of the graphite, hardly any deposit is visible. It is tentatively suggested that the bright areas are fragments of graphite layers.

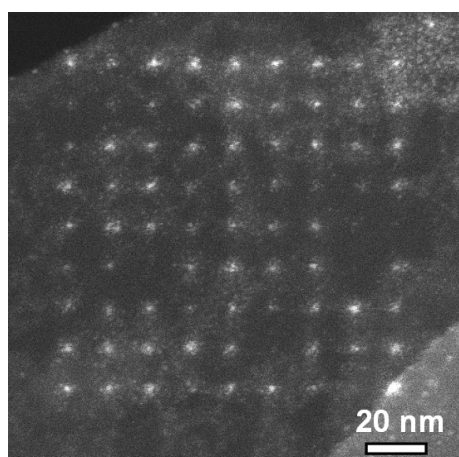
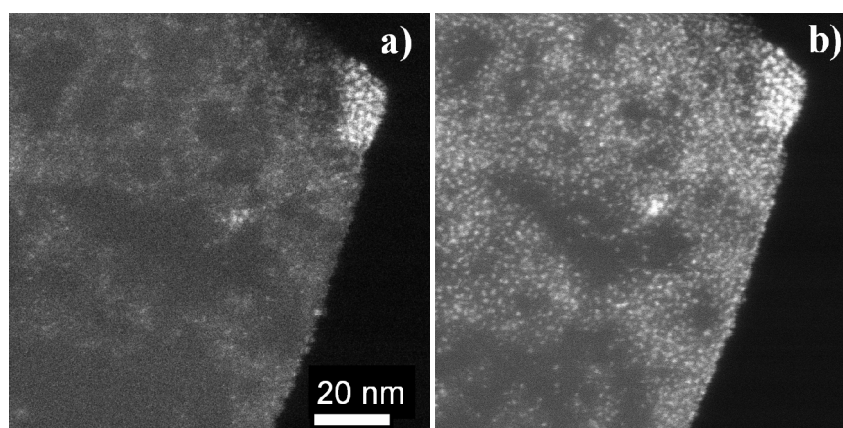


Fig. 2. A STEM image of a deposited array is shown. The dark area in the upper left is vacuum, the bright area in the bottom right is the amorphous carbon support and in the upper right deposition due to the focusing of the beam is visible. The growth rate seems to correlate with the intensity of the background.

One can think of several mechanisms explaining the difference in growth rate. There may be a difference in adsorption behavior of the precursor molecules between the bright and dark areas on the graphite substrate, causing the residence time of precursor molecules to be longer on the bright areas than on the dark areas. The effect is that either the probability of dissociation by an incident electron is much higher or that the dissociated molecule desorbs less easily directly after interaction with the incident electron. Another mechanism is that the dark areas are so thin that the SE yield is dependent on the thickness of the substrate. If the bright areas are thicker, the secondary electron yield on the brighter areas will be larger than on the dark areas. Finally, the bright areas may be less flat, leading to a larger SE yield than the dark areas. As a result of these (possibly parallel) effects, more material is being deposited on the bright areas.

To get more evidence of the influence of the nonuniformities of the graphite, we imaged a piece of graphite in the presence of the precursor. We scanned an area of  $2048 \times 2048$  pixels over  $110 \times 110$  nm with a dwell time per pixel of  $10 \mu\text{s}$  and recorded the ADF signal. After every complete scan, the image was saved. As the electron beam scanned over the substrate, precursor molecules were dissociated. Fig. 3a shows the situation after the first complete scan. The regions of higher and lower contrast can be clearly distinguished. The bright spot in the center of the image comes from an erroneous pause of the e-beam in spot mode for approximately a second and the bright area in the upper right corner of the image comes from focusing the e-beam. Fig. 3b shows the same area on the substrate, but now after 3 additional scans. As result of the irradiation with the electron beam, tungsten containing material was deposited and the average intensity on the substrate has increased. The increase is not uniform though, because the low contrast areas on the substrate can still be recognized. Deposition occurred preferentially on the areas where there already was material deposited earlier. This is an indication that the adsorption on the clean (i.e. dark) areas is lower than on the brighter areas.



*Fig. 3. (a) Initial condition of a graphite substrate, imaged in the presence of  $\text{W}(\text{CO})_6$ . The dark and uniform areas can clearly be distinguished from the brighter and more irregular areas. (b) Substrate after 4x imaging in the presence of  $\text{W}(\text{CO})_6$ . It is observed that deposition occurs preferentially at the brighter, nonuniform areas.*

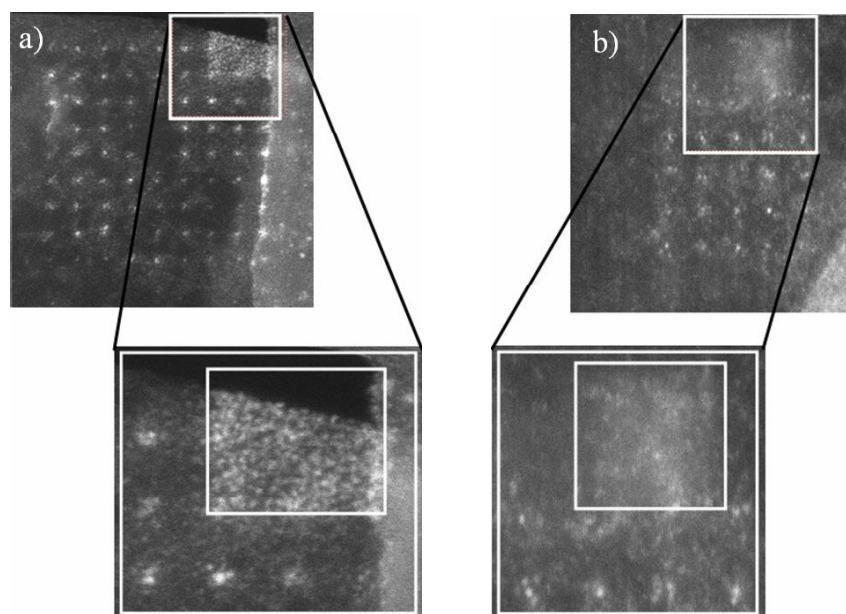


Fig. 4. (a) Effect of focussing the electron beam in the presence of  $W(CO)_6$ . A deposit with a grainy appearance is observed. (b) When focussing in the presence of contamination, only a brighter area is observed, without any significant morphology.

During deposition on the graphite it is also observed that the morphology of deposits is different for  $W(CO)_6$  than for contamination. When focussing the electron beam in the presence of  $W(CO)_6$ , a deposit was obtained with a grainy appearance. This is shown in Fig. 4a. When focussing without the presence of  $W(CO)_6$  but in the presence of contamination (allowed into the microscope by accident), an area of higher intensity without any morphology was observed.

### III. Resolution dependence on pressure and/or temperature

At some point during experiments, it was observed that deposits appeared blurry (see Fig. 5a), not as sharp and small as usual. The substrate used was an a-C membrane, 10-20 nm thick, the beam current was approx. 40 pA.

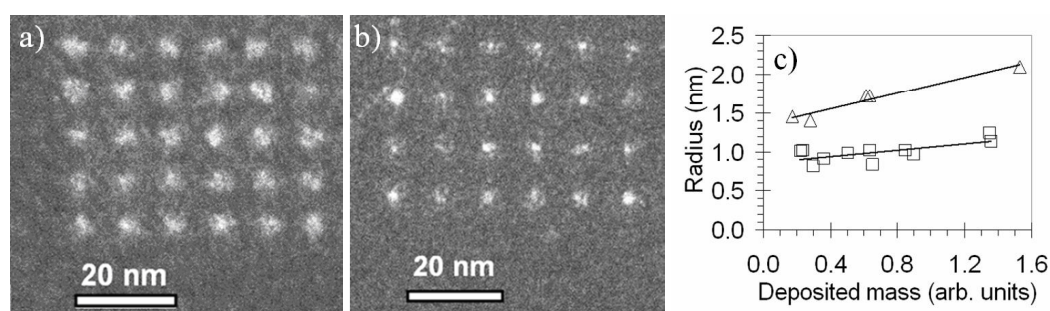


Fig. 5. (a) Blurry dots, deposited from  $W(CO)_6$  on a-C at a temperature of  $149\text{ }^\circ\text{C}$  and a pressure of  $4.7 \times 10^{-3}\text{ Torr}$ . (b) Sharper dots, deposited at  $120\text{ }^\circ\text{C}$  and  $7.4 \times 10^{-3}\text{ Torr}$ . (c) Deposit radius as function of the deposited mass (open triangles for the regime in (a), open squares for the regime in (b)). The lines are drawn to guide the eye.

It was found that smaller and sharper dots could be obtained by decreasing the temperature from 149 °C to 120 °C and increasing the pressure from  $4.7 \times 10^{-3}$  Torr to  $7.4 \times 10^{-3}$  Torr (see Fig. 5b). The average deposited mass per dot in Fig. 5a and 5b is identical. Fig. 5c shows a plot of the diameters as function of the deposited mass per dot, for high temperature and low pressure (open triangles) and low temperature and high pressure (open squares). The changes in temperature and pressure were 30 °C and a factor of 2, respectively, while the radius changed by roughly a factor of 1.5. The simultaneous variation of temperature and pressure prohibits definite conclusions.

#### **IV. Entrance/exit growth**

When dots are deposited on an electron transparent membrane, a deposit grows on the entrance and on the exit side of the substrate. In [204], dots were grown on 100 nm thick a-C from  $W(CO)_6$  at 200 kV. It is reported that during the first stages of growth, the deposit on the exit side grows faster than on the entrance side (see Fig. 6a). We have observed that this is not always the case. Values (the percentage of the deposits that has the brightest part at the entrance side) are shown Fig. 6b for a-C (■) and  $Si_3N_4$  (▲). Fig. 6c and d show examples of ADF images of tilted arrays of dots on  $Si_3N_4$  and a-C, respectively. Please note that the dots were defined using the method as described in paragraph 3.4.1, so the shortest dwell times presented here may not have been the actual dwell times. Preferential growth on the exit side was observed for 30 nm thick  $Si_3N_4$ , but not for 10 nm thick a-C. It was stated in [204] that “the preferential growth of the downside part ... implies that the forward electrons are more effective than the back-emerging electrons in EBID.” The results here indicate that this is not true and/or that other (possibly parallel) mechanisms are playing a role.

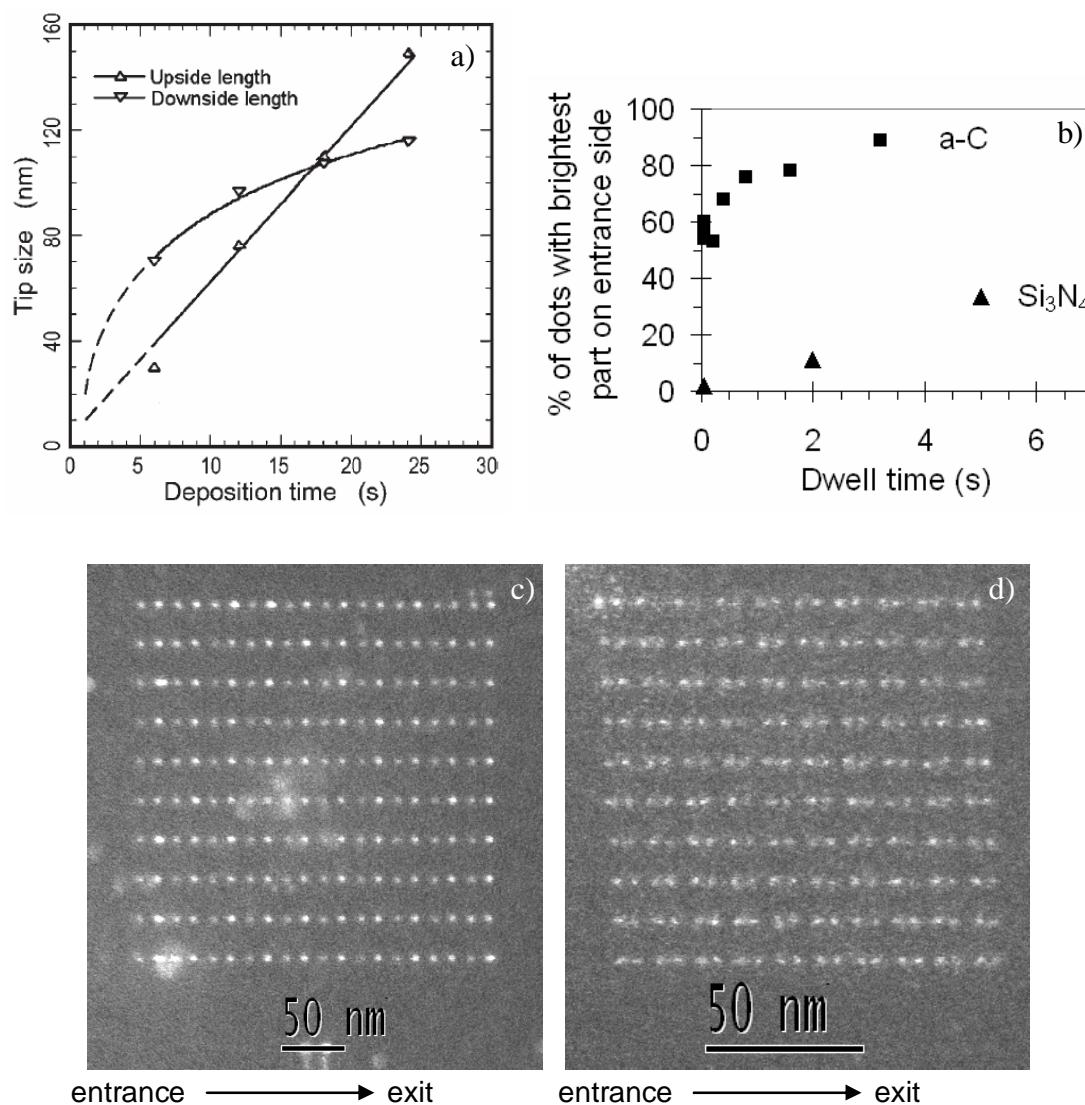


Fig. 6. (a) The length of the deposit on the entrance and exit side as function of dwell time. W was deposited from  $W(CO)_6$  on a 100 nm thick a-C membrane at 200 kV. From [202]. (b) Percentage of the dots with the brightest part on the entrance side plotted as function of dwell time for 10 nm thick a-C (■) and 30 nm thick  $Si_3N_4$  (▲). Results from work in this thesis. (c) An array on  $Si_3N_4$ , dwell time 0.05 s. (d) An array on a-C, dwell time 0.4 s. The entrance and exit sides of the membranes are indicated.



---

## 10. Conclusions and outlook

### Contents

I. Conclusions.....	138
II. Outlook.....	139
<i>II.A. Applications</i> .....	139
<i>II.B. Resolution in SEM</i> .....	139
<i>II.C. Precursor dissociation chemistry</i> .....	140
<i>II.D. Improvement of the resolution</i> .....	140

## I. Conclusions

This research work has focused on studying the growth behavior of electron beam induced deposition (EBID) near its ultimate resolution.

An extensive critical review of the literature on EBID from the past 70-odd years makes clear that the majority of the experimental results can be explained using a model for electron scattering in a solid, knowledge of growth regimes and a model for electron beam induced heating. This indicates that most of the physical processes are well understood. However, there is still room for improvement. The models do not allow for precise quantitative predictions yet, for instance. Another issue is the effect of the electron energy on the deposit properties. The cross sections for inelastic scattering, elastic scattering and dissociation are not well known, which makes it difficult to explain results from experiments where the primary electron energy was varied. In several cases, a correlation between the vertical growth rate and the SE yield was found. This correlation suggests that the contribution of the SE's is dominant over the contribution of direct dissociation by the PE's, but conclusive evidence for this hypothesis has not been found. An issue that complicates interpretation of results from literature is the lack of information on experimental details. Often, important parameters (such as the local precursor pressure) are not reported. Finally, the process of electron-induced precursor dissociation is not well understood. The dissociation mechanism is one of the key factors determining the purity of the deposits and a better understanding of this process is vital to develop EBID to its full potential.

The study of sub-10 nm EBID started with the fabrication of dots with an average full width at half maximum (FWHM) of 1.0 nm and lines with a FWHM of 1.9 nm. Deposits of these sizes are so small, that the statistics on the number of molecules per deposit determine the feature sizes. The variations in deposited mass were analysed and were of the same order of magnitude as variations expected from Poisson statistics. A proximity effect was studied, where the deposition rate was found to be dependent on the angle between the irradiated target and the incident electron beam. A scan strategy for reducing this effect was proposed and tested.

To obtain more insight into and control over the growth process, a technique was developed to monitor the transmitted annular dark field (ADF) signal during growth. An attempt was made to use this technique to reduce variations in deposit mass for nanometer-sized deposits. This attempt did not succeed yet, but the method was successfully applied to prevent the occurrence of the proximity effect.

In the final experiments, the resolution of EBID was brought very close to its ultimate limit. The smallest values for the diameter of dots was 0.72 for the FWHM and 1.0 nm for the diameter in which 50% of the deposit volume is contained. A detailed study confirmed that growth in the early stage is dominated by random processes. This means that, despite identical growth conditions, the growth is different for each deposit. For instance, deposits do not nucleate exactly on the irradiated spot, but on random positions tenths of nanometers around it. As a result of this, the deposits grow nonsymmetrically around the electron beam. During the deposition, the growth rate is not constant and this causes the final deposited mass to vary from dot to dot. AFM measurements allowed quantification of the deposited volume. By

fitting Poisson distributions to the volume distributions found in the experiments, an estimate was made of  $\lambda$ , the expected number of discrete events during a dwell time. This yielded a value of  $0.4 \text{ nm}^3/\lambda$ , which is within only a factor of 2 of the volume of a  $\text{W}(\text{CO})_6$  precursor molecule in the solid phase.

## II. Outlook

### II.A. Applications

The experiments described in this work show the capability of EBID as an ultra-high lithography technique. Resist-based electron beam lithography was the main technique that gave access to the  $\sim 10$  to  $200 \text{ nm}$  regime. Similarly, EBID gives access to the  $\sim 1$ - $20 \text{ nm}$  regime (see Fig. 1) and has the potential to become just as important.

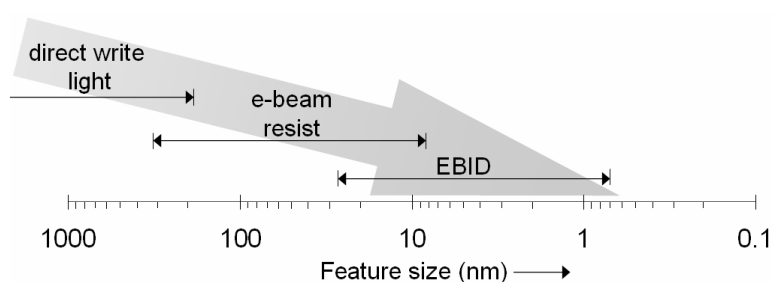


Fig. 1. Three lithography techniques and the regimes to which they give access.

Sub-10 nm EBID will be applied mainly for the fabrication of devices research or for very specialistic applications. A current application of high resolution EBID is mask repair. EBID (as well as EBIE) is used to add or remove features from photolithography masks used for the transfer of patterns in IC fabrication. EBID is currently tested to be used for the fabrication of single electron tunneling devices. For this application, the deposit serves as a negative mask against dry etching.

If the current limitations are solved, future applications can be more diverse. For instance, EBID can be used for the fabrication of sub-10 nm details on imprint masks or to create quantum dots. One can also envision the deposition of single molecules or nanometer-sized dots in microreactors to act as a binding site for bioactive complexes or as catalyst particles to locally enhance reactions. In the far future, it might even be possible to create new phases of material by combining atoms of different elements.

### II.B. Resolution in SEM

To make sub-10 nm EBID easier to perform, the resolution needs to be demonstrated in the SEM. State of the art SEMs can focus electron beams down to less than a nanometer, approaching the capability of STEMs, so in principle a similar spatial resolution should be possible. SEMs are easier to operate, there is more room for large samples and detectors and even transmission detectors can be used.

### *II.C. Precursor dissociation chemistry*

A key issue in developing EBID to its full potential is a better understanding of the precursor dissociation mechanism. The main limiting factor is the impurity and the low conductivity of deposits. A better understanding can be obtained by studying the fundamental electron-molecule interactions, using techniques such as X-ray photoelectron spectroscopy, temperature programmed desorption, angle-resolved detection of electron-stimulated ion desorption and infrared spectroscopy. Another option is a systematic approach, where the composition and morphology of deposits is studied for different, yet closely related precursors. The effect of variation in (for instance) temperature, accumulated charge or beam current can reveal valuable information about the dissociation mechanism. Such studies have already been performed for carbon, Rh and Cu precursors.

Control over the deposit composition can perhaps be obtained by introducing reactive species. This has already been tried with molecular species such as O<sub>2</sub> or H<sub>2</sub>O, with varying degrees of success. Atomic species, such as atomic hydrogen, possibly yield better results because of the higher reactivity.

### *II.D. Improvement of the resolution*

If a further improvement of the resolution is to be pursued, the next big step is the one by one deposition of single molecules. An electron beam smaller than 0.2 nm may give a slight improvement in resolution, but significant progress requires a systematic approach. The feedback system which uses the ADF signal is suitable for terminating the growth process. Key issue in this approach is to improve the signal to noise (S/N) ratio of the ADF signal. Increasing sampling or scan rates does not help, because they have already reached their practical limit. At the sample rate and the beam current used in this study (1 MS/s and 3.2 pA, resp.), there were only ~20 electrons per sample. And at scan rates above 100 kHz, the microscope does not define the pattern accurately anymore. The best strategy is most likely to go to a precursor limited regime. The precursor flux determines the growth rate and the beam current can be increased to improve the S/N ratio. Unfortunately, it was not tested in this work what the regime was at the pressure of 10<sup>-3</sup> Torr (electron- or precursor-limited). If it was precursor-limited, a precursor pressure to 10<sup>-5</sup> Torr and background pressure of 10<sup>-6</sup> Torr should decrease the growth rate by a factor of 100. This should be sufficient to observe and control the deposition of single precursor molecules and such pressures should be feasible for the setup described in Chapter 3, after some modifications.

However, a low growth rate alone is not enough. To use the ADF signal for the detection of single molecules, it helps to have a signal that is easy to interpret, for instance a high signal on a low background. Preferably, one uses a precursor that dissociates more cleanly into a high-Z deposit than W(CO)<sub>6</sub> and a substrate that has a low and very uniform background. Graphite may be a good candidate as a substrate, if it can be made uniform enough. The preparation method tried in this research (ultrasonic exfoliation as described in Chapter 3) was not adequate.

## 11. References

---

- 1 Lorusso GF, Goethals AM, Jonckheere R, Hermans J, Ronse K, Meyers AM, Kim I, Niroomand A, Iwamoto F, Ritter D, *EUV lithography at IMEC*, Presented at EIPBN 2007
- 2 Grigorescu A, Van der Krogt M, Hagen CW, Kruit P, *Influence of the development process on ultimate resolution Electron Beam Lithography using ultra-thin HSQ resist layers*, *J Vac Sci Technol B* **25**, 1998 (2007)
- 3 Eigler DM, Schweitzer EK, *Positioning single atoms with a scanning tunnelling microscope*, *Nature* **344**, 524 (1990)
- 4 Silvis-Cividjian N, Hagen CW, Kruit P, Van der Stam MAJ, Groen HB, *Direct fabrication of nanowires in an electron microscope*, *Appl Phys Lett* **82**, 3514 (2003)
- 5 Steward RL, *Insulating films under electron and ion bombardment*, *Phys Rev* **45**, 488 (1934)
- 6 Christy RW, *Formation of thin polymer films by electron bombardment*, *J Appl Phys* **31**, 1680 (1960)
- 7 Baker AG, Morris WC, *Deposition of metallic films by electron impact decomposition of organometallic vapors*, *Rev Sci Instrum* **32**, 458 (1961)
- 8 Hübner B, Koops HWP, *Tips for scanning tunneling microscopy produced by EBID*, *Ultramicroscopy* **42-44**, 1519 (1992)
- 9 Schoessler C, Koops HWP, *Nanostructured integrated electron source*, *J Vac Sci Technol B* **16**, 862 (1998)
- 10 Utke I, Hoffmann P, Berger R, Scandella L, *High-resolution magnetic Co supertips grown by a focused electron beam*, *Appl Phys Lett* **80**, 4792 (2002)
- 11 Utke I, Bret T, Laub D, Buffat Ph, Scandella L, Hoffmann P, *Thermal effects during focused electron beam induced deposition of nanocomposite magnetic-cobalt-containing tips*, *Microelectron Eng* **73-74**, 553 (2004)
- 12 Lau YM, Chee PC, Thong JTL, Ng V, *Properties and applications of cobalt-based material produced by electron-beam-induced deposition*, *J Vac Sci Technol A* **20**, 1295 (2002)
- 13 Schiffmann KI, *Investigation of fabrication parameters for the electron-beam-induced deposition of contamination tips used in atomic force microscopy*, *Nanotechnology* **4**, 163 (1993)
- 14 Wendel M, Lorenz H, Kotthaus JP, *Sharpened electron beam deposited tips for high resolution atomic force microscope lithography and imaging*, *Appl Phys Lett* **67**, 3732 (1995)
- 15 Schössler C, Urban J, Koops HWP, *Conductive supertips for scanning probe applications*, *J Vac Sci Technol B* **15**, 1535 (1997)
- 16 Edinger K, Gotszalk T, Rangelow IW, *Novel high resolution thermal probe*, *J Vac Sci Technol B* **19**, 2856 (2001)

- 
- 17 Kindt JH, Fantner GE, Thompson JB, Hansma PK, *Automated wafer-scale fabrication of electron beam deposited tips for atomic force microscopes using pattern recognition*, *Nanotechnology* **15**, 1131 (2004)
  - 18 Bøggild P, Hansen TM, Kuhn O, Grey F, Junno T, Montelius L, *Scanning nanoscale multiprobes for conductivity measurements*, *Rev Sci Instrum* **71**, 2781 (2000)
  - 19 Mølhave K, Nørgaard Madsen D, Rasmussen AM, Carlsson A, Appel CC, Brorson M, Jacobsen CJH, Bøggild P, *Solid Gold Nanostructures Fabricated by Electron Beam Deposition*, *Nano Lett* **3**, 1499 (2003)
  - 20 Ding W, Dikin DA, Chen X, Piner RD, Ruoff RS, Zussman E, Wang X, Li X, *Mechanics of hydrogenated amorphous carbon deposits from electron-beam-induced deposition of a paraffin precursor*, *J Appl Phys* **98**, 14905 (2005)
  - 21 Yu MF, Lourie O, Dyer MJ, Moloni K, Kelly TF, Ruoff RS, *Strength and Breaking Mechanism of Multiwalled Carbon Nanotubes Under Tensile Load*, *Science* **287**, 637 (2000)
  - 22 Fukuda T, Arai F, Dong L, Nakajima M, *Nanolaboratory - a prototype nanomanufacturing system*, *Fifth World Congress on Intelligent Control and Automation* **701**, 2698 (2004)
  - 23 Brintlinger T, Fuhrer MS, Melngailis J, Utke I, Bret T, Perentes A, Hoffmann P, Aboudira M, Doppelt P, *Electrodes for carbon nanotube devices by focused electron beam induced deposition of gold*, *J Vac Sci Technol B* **23**, 3174 (2005)
  - 24 Banhart F, *The Formation of a Connection between Carbon Nanotubes in an Electron Beam*, *Nano Lett* **1**, 329 (2001)
  - 25 Li PG, Jin AZ, Tang WH, *Pt/Ga/C and PVC composite nanowires fabricated by focused ion and electron beam induced deposition*, *Physica Status Solidi A* **203**, 282 (2006)
  - 26 Croitoru MD, Bertsche G, Kern DR, Burkhardt C, Bauerdick S, Şahakalkan S, Roth S, *Visualization and in situ contacting of carbon nanotubes in a scanning electron microscope*, *J Vac Sci Technol B* **23**, 2789 (2005)
  - 27 Tsukatani Y, Yamasaki N, Murakami K, Wakaya F, Takai M, *Transport properties of Pt nanowires fabricated by beam-induced deposition*, *Jpn J Appl Phys* **44**, 5683 (2005)
  - 28 Rotkina L, Lin JF, Bird JP, *Nonlinear current-voltage characteristics of Pt nanowires and nanowire transistors fabricated by electron-beam deposition*, *Appl Phys Lett* **83**, 4426 (2003)
  - 29 Koops HWP, Weiel R, Kern DP, Baum TH, *High-resolution electron-beam induced deposition*, *J Vac Sci Technol B* **6**, 477 (1988)
  - 30 Edinger K, Becht H, Bühr J, Boegli V, Budach M, Hofmann T, Koops HWP, Kuschnerus P, Oster J, Spies P, Weyrauch B, *Electron-beam-based photomask repair* *J Vac Sci Technol B* **22**, 2902 (2004)
  - 31 Liang T, Freundberg E, Lieberman B, Stivers A, *Advanced photolithographic mask repair using electron beams*, *J Vac Sci Technol B* **23**, 3101 (2005)

- 
- 32 Murakami K, Takai M, *Characteristics of nano electron source fabricated using beam assisted process*, J Vac Sci Technol B **22**, 1266 (2004)
- 33 Weber M, Rudolph M, Kretz J, Koops HWP, *Electron-beam induced deposition for fabrication of vacuum field emitter devices*, J Vac Sci Technol B **13**, 461 (1995)
- 34 Edgcombe CJ, Valdre U, *Experimental and computational study of field emission characteristics from amorphous carbon single nanotips grown by carbon contamination - I. Experiments and computation*, Philos Mag B **82**, 987 (2002)
- 35 Boero G, Utke I, Bret T, Quack N, Todorova M, Mouaziz S, Keijk P, Brugger J, Popovic RS, Hoffmann P, *Submicrometer Hall devices fabricated by focused electron-beam-induced deposition*, Appl Phys Lett **86**, 42503 (2005)
- 36 Umbach CP, Washburn S, Webb RA, Koch R, Bucci M, Broers AN, Laibowitz RB, *Observation of  $h/e$  Aharonov-Bohm Interference Effects in Sub-Micron Diameter, Normal Metal Rings*, J Vac Sci Technol B **4**, 383 (1986)
- 37 Bøggild P, Hansen TM, Tanasa C, Grey F, *Fabrication and actuation of customized nanotweezers with a 25 nm gap*, Nanotechnology **12**, 331 (2001)
- 38 Ooi T, Matsumoto K, Nakao M, Otsubo M, Shirakata S, Tanaka S, Hatamura Y, *3D nano wire-frame for handling and observing a single DNA fiber*, Proc IEEE Micro Electro Mechanical Systems (MEMS) 580 (2000)
- 39 Perentes A, Bachmann A, Leutenegger M, Utke I, Sandu C, Hoffmann P, *Focused electron beam induced deposition of a periodic transparent nano-optic pattern*, Microelectron Eng **73-74**, 412 (2004)
- 40 Koops HWP, Hoinkis OE, Honsberg MEW, Schmidt R, Blum B, Boettger G, Kuligk A, Liguda C, Eich M, *Two-dimensional photonic crystals produced by additive nanolithography with electron beam-induced deposition acts as filters in the infrared*, Microelectron Eng **57-58**, 995 (2001)
- 41 Koops HWP, Munro E, Rouse J, Kretz J, Rudolph M, Weber M, Dahm G, *Miniature low voltage beam systems producable by combined lithographies*, Nucl Instrum Methods Phys Res A **363**, 1 (1995)
- 42 Miura N, Ishii H, *Electron beam induced deposition of carbonaceous microstructures using SEM*, Appl Surf Sci **113-114**, 269 (1997)
- 43 Mukawa T, Okada S, Kobayashi R, Fujita J, Ishida M, Ichihashi T, Ochiai Y, Kaito T, Matsui S, *Position-Controlled Carbon Fiber Growth Catalyzed Using Electron Beam-Induced Chemical Vapor Deposition Ferrocene Nanopillars*, Jpn J Appl Phys **44**, 5639 (2005)
- 44 Randolph SJ, Fowlkes JD, Rack PD, *Effects of heat generation during electron-beam-induced deposition of nanostructures*, J Appl Phys **97**, 124312 (2005)
- 45 Silvis-Cividjian N, Hagen CW, *Electron-Beam-Induced Nanometer-Scale Deposition*, Advances in Imaging and Electron Physics **143** (2006)
- 46 Randolph SJ, Fowlkes JD, Rack PD, *Focused, nanoscale electron-beam-induced deposition and etching*, Crit Rev Solid State Mater Sci **31**, 55 (2006)

- 
- 47 Koshikawa T, Shimizu R, *A Monte Carlo calculation of low-energy secondary electron emission from metals*, Journal of Physics D **7**, 1303 (1974)
- 48 Kotera M, *A Monte Carlo simulation of primary and secondary electron trajectories in a specimen*, J Appl Phys **65**, 3991 (1989)
- 49 Joy DC, *Monte Carlo Modeling for Electron Microscopy and Microanalysis*, Oxford University Press, New York Oxford (1995), and references therein.
- 50 Hagen CW, Silvis-Cividjian N, Kruit P, *Resolution limit for electron beam induced deposition on thick substrates*, Scanning **27**, 90 (2005)
- 51 Egerton RF, Wang F, Crozier PA, *Beam-induced damage to thin specimens in an intense electron probe*, Microsc Microanal **12**, 1 (2006)
- 52 Reimer L, *Scanning electron microscopy*, Springer-Verlag, Berlin, page 5 (1998).
- 53 Silvis-Cividjian N, *Electron Beam Induced Nanometer Scale Deposition*, PhD thesis, Delft University Press (2002)
- 54 Rowntree P, Parenteau L, Sanche L, *Anion yields produced by low-energy electron impact on condensed hydrocarbon films*, J Phys Chem **95**, 4902 (1991)
- 55 Hirsh EH, *Image formation by electron bombardment of metal targets*, Brit J Appl Phys **11**, 547 (1960)
- 56 Mezhenny S, Lyubinetsky I, Choyke WJ, Yates JT, *Electron stimulated decomposition of adsorbed hexafluoroacetylacetonate, Cu(I) vinyltrimethylsilane, Cu(I)(hfac)(vtms)*, J Appl Phys **85**, 3368 (1999)
- 57 George PM, Beauchamp JL, *Deposition of metal films by the controlled decomposition of organometallic compounds on surfaces*, Thin Solid Films **67**, L25 (1980)
- 58 Rowntree P, *Chemical processes of electron beam induced deposition*, oral presentation at the First International EBID Workshop in Delft, 2006
- 59 Henderson MA, Ramsier RD, Yates JT, *Low-energy electron induced decomposition of Fe(CO)<sub>5</sub> adsorbed on Ag(111)*, Surf Sci **259** 173 (1991)
- 60 Tian C, Vidal CR, *Cross sections of the electron impact dissociative ionization of CO, CH<sub>4</sub> and C<sub>2</sub>H<sub>2</sub>*, J Phys B **31**, 895 (1998)
- 61 Silvis-Cividjian N, Hagen CW, Leunissen LHA, Kruit P, *The role of secondary electrons in electron-beam-induced-deposition spatial resolution*, Microelectron Eng **61-62**, 693 (2002)
- 62 Fowlkes JD, Randolph SJ, Rack PD, *Growth and simulation of high-aspect ratio nanopillars by primary and secondary electron-induced deposition*, J Vac Sci Technol B **23**, 2825 (2005)
- 63 Mitsuishi K, Liu ZQ, Shimojo M, Han M, Furuya K, *Dynamic profile calculation of deposition resolution by high-energy electrons in electron-beam-induced deposition*, Ultramicroscopy **103**, 17 (2005)
- 64 Scheuer V, Koops HWP, Tschudi T, *Electron beam decomposition of carbonyls on silicon*, Microelectron Eng **5**, 423 (1986)

- 
- 65 Wang S, Sun YM, Wang Q, White JM, *Electron-beam induced initial growth of platinum films using Pt(PF<sub>3</sub>)<sub>4</sub>*, J Vac Sci Technol B **22**, 1803 (2004)
- 66 Ichihashi T, Matsui S, *In situ observation on electron beam induced chemical vapor deposition by transmission electron microscopy*, J Vac Sci Technol B **6**, 1869 (1988)
- 67 Li W, Joy DC, *Study of temperature influence on electron beam induced deposition*, J Vac Sci Technol A **24**, 431 (2006)
- 68 Folch A, Servat J, *High-vacuum versus "environmental" electron beam deposition*, J Vac Sci Technol B **14**, 2609 (1996),
- 69 Bret T, Utke I, Hoffmann P, Aboudira M, Doppelt P, *Electron range effects in focused electron beam induced deposition of 3D nanostructures*, Microelectron Eng **83**, 1482 (2006)
- 70 Utke I, Friedli V, Michler J, Bret T, Multone X, Hoffmann P, *Density determination of focused-electron-beam-induced deposits with simple cantilever-based method*, Appl Phys Lett **88**, 031906 (2006)
- 71 Koops HWP, Kretz J, Rudolph M, *Constructive three-dimensional lithography with EBID of quantum effect devices*, J Vac Sci Technol B **11**, 2386 (1993)
- 72 Kohlmann-von Platen KT, Chlebek J, Weiss M, Reimer K, *Resolution limits in electron-beam induced tungsten deposition*, J Vac Sci Technol B **11**, 2219 (1993)
- 73 Liu ZQ, Mitsuishi K, Furuya K, *The growth behavior of self-standing tungsten tips fabricated by electron-beam-induced deposition using 200 keV electrons*, J Appl Phys **96**, 3983 (2004)
- 74 Hübner U, Plontke R, Blume M, Reinhardt A, Koops HWP, *On-line nanolithography using electron beam-induced deposition technique*, Microelectron Eng **57-58**, 953 (2001)
- 75 Hiroshima H, Komuro M, *Fabrication of conductive wires by electron-beam-induced deposition*, Nanotechnology **9**, 108 (1998)
- 76 Hoyle P, Cleaver J, Ahmed H, *Electron beam induced deposition from W(CO)<sub>6</sub> at 2 to 20KeV and its applications*, J Vac Sci Technol B **14**, 662 (1996)
- 77 Shimojo M, Zhang W, Takeguchi M, Tanaka M, Mitsuishi K, Furuya K, *Nanodot and nanorod formation in electron-beam-induced deposition using iron carbonyl*, Jpn J Appl Phys **44**, 5651 (2005)
- 78 Beaulieu D, Ding Y, Wang ZL, Lakey WJ, *Influence of process variables on electron beam chemical vapor deposition of platinum*, J Vac Sci Technol B **23**, 2151 (2005)
- 79 Liu ZQ, Mitsuishi K, Furuya K, *The growth behavior of self-standing tungsten tips fabricated by electron-beam-induced deposition using 200 keV electrons*, J Appl Phys **96**, 3983 (2004)
- 80 Broers AN, Molzen WW, Cuomo JJ, Wittels ND, *Electron-beam fabrication of 80-A metal structures*, Appl Phys Lett **29**, 596 (1976)
- 81 Jiang H, Borca CN, Xu B, Robertson BW, *Fabrication of 2-and 3-dimensional nanostructures*, Int J Mod Phys B **15**, 3207 (2001)

- 
- 82 Fujita J, Ishida M, Ichihashi T, Ochiai Y, Kaito T, Matsui S, *Carbon nanopillar laterally grown with electron beam-induced chemical vapor deposition*, J Vac Sci Technol B **21**, 2990 (2003)
- 83 Crozier PA, Tolle J, Kouvetakis J, Ritter C, *Synthesis of uniform GaN quantum dot arrays via electron nanolithography of D<sub>2</sub>GaN<sub>3</sub>*, Appl Phys Lett **84**, 3441 (2004)
- 84 Guise O, Ahner J, Yates J, Levy J, *Formation and thermal stability of sub-10-nm carbon templates on Si(100)*, Appl Phys Lett **85**, 2352 (2004)
- 85 Tanaka M, Shimojo M, Han M, Mistuishi K, Furuya K, *Ultimate sized nano-dots formed by electron beam-induced deposition using an ultrahigh vacuum transmission electron microscope*, Surf Interface Anal **37**, 261 (2005)
- 86 Van Dorp WF, Van Someren B, Hagen CW, Kruit P, Crozier PA, *Approaching the resolution limit of nanometer-scale electron beam-induced deposition*, Nano Lett **5**, 1303 (2005)
- 87 Van Dorp WF, Van Someren B, Hagen CW, Crozier PA, Kruit P, *One nanometer structure fabrication using electron beam induced deposition*, Microelectron Eng **83**, 1468 (2006)
- 88 Koops HWP, Kretz J, Rudolph M, Weber M, Dahm G, Lee KL, *Characterization and Application of Materials Grown by Electron-Beam-Induced Deposition*, Jpn J Appl Phys **33**, 7099 (1994)
- 89 Koops HWP, Kaya A, Weber M, *Fabrication and characterization of platinum nanocrystalline material grown by electron-beam induced deposition*, J Vac Sci Technol B **13**, 2400 (1995)
- 90 Weber M, Koops HWP, *New compound quantum dots materials produced by EBID* J Vac Sci Technol B **13**, 1364 (1995)
- 91 Bret T, *Physico-chemical study of the focused electron beam induced deposition process*, PhD thesis, Lausanne, EPFL (2005)
- Utke I, Michler J, Gasser P, Santschi C, Laub D, Cantoni M, Buffat PA, Jiao C, Hoffmann P, *Cross section investigations of compositions and sub-structures of tips obtained by focused electron beam induced deposition*, Adv Eng Mat **7**, 323 (2005)
- 93 Kunz RR, Mayer TM, *Electron-beam induced surface nucleation and low-temperature decomposition of metal-carbonyls*, J Vac Sci Technol B **6**, 1557 1988
- 94 Utke I, Hoffmann P, Dwir B, Leifer K, Kapon E, Doppelt P, *Focused electron beam induced deposition of gold*, J Vac Sci Technol B **18**, 3168 (2000)
- 95 Bruk MA, Zhikharev EN, Grigor'ev EI, Spirin AV, Kal'nov VA, Kardash IE, *Focused electron beam-induced deposition of iron- and carbon-containing nanostructures from triiron dodecacarbonyl vapor*, High Energy Chemistry **39**, 65 (2005)
- 96 Schöblier C, Kaya A, Kretz J, Koops HWP, *Electrical, and field emission properties of nanocrystalline materials fabricated by electron-beam induced deposition*, Microelectron Eng **30**, 471 (1996)
- 97 Komuro M, Hiroshima H, *Fabrication and properties of dot array using electron-beam-induced deposition*, Microelectron Eng **35**, 273 (1997)

- 
- 98 Seiler H, *Secondary electron emission in the scanning electron microscope*, J Appl Phys **54**, R1 (1983)
- 99 Völkel B, Gölzhäuser A, Müller HU, David C, Grunze M, *Influence of secondary electrons in proximal probe lithography*, J Vac Sci Technol B **15**, 2877 (1997)
- 100 Lipp *et al.*, Bauerdick *et al.*, Beaulieu *et al.*, Croitoru *et al.* and Kohlmann *et al.* report a change in beam current when changing the PE energy. Hoyle *et al.*, Kohlmann *et al.*, Randolph *et al.*, Schiffmann *et al.* and Miura *et al.* have performed their experiments at a constant beam current, but reported a change in the beam diameter when varying the PE energy.
- 101 Bret T, Utke I, Bachmann A, Hoffmann P, *In situ control of the focused-electron-beam-induced deposition process*, Appl Phys Lett **83**, 4005 (2003)
- 102 Wang S, Sun YM, White JM, *Electron induced deposition and in situ etching of CrOxCl<sub>y</sub> films*, Appl Surf Sci **249**, 110 (2005)
- 103 Lipp S, Frey L, Lehrer C, Demm E, Pauthner S, Ryssel H, *A comparison of focused ion beam and electron beam induced deposition processes*, Microelectron Reliab **36**, 1779 (1996)
- 104 Bauerdick S, Burkhardt C, Rudolf R, Barth W, Bucher V, Nisch W, *In-situ monitoring of electron beam induced deposition by atomic force microscopy in a scanning electron microscope*, Microelectron Eng **67-68**, 963 (2003)
- 105 Takai M, Jarupoonphol W, Ochiai C, Yavas O, Park YK, *Processing of vacuum microelectronic devices by focused ion and electron beams*, Appl Phys A-Mater **76**, 1007 (2003)
- 106 Hoyle P, Cleaver J, Ahmed H, *Ultralow-energy focused electron beam induced deposition*, Appl Phys Lett **64**, 1448 (1994)
- 107 Kunze D, Peters O, Sauerbrey G, *Polymerization absorbiertes Kohlenwasserstoffe bei Elektronenbeschuss*, Z Angew Phys **22**, 69 (1967)
- 108 Lee KL, Hatzakis M, *Direct electron-beam patterning for nanolithography*, J Vac Sci Technol B **7**, 1941 (1989)
- 109 Fischer M, Wanzenboeck HD, Gottsbachner J, Mueller S, Brezna W, Schramboeck M, Bertagnolli E, *Direct-write deposition with a focused electron beam*, Microelectron Eng **83**, 784 (2006)
- 110 Miura N, Ishii H, Yamada A, Konagai M, *Application of carbonaceous material for fabrication of nano-wires with a scanning electron microscopy*, Jpn J Appl Phys **35**, L1089 (1996)
- 111 Bell DA, Falconer JL, Lü Z, McConica CM, *Electron beam-induced deposition of tungsten*, J Vac Sci Technol B **12**, 2976 (1994)
- 112 Cicoira F, Hoffmann P, Olsson COA, Xanthopoulos N, Mathieu HJ, Doppelt P, *Auger electron spectroscopy analysis of high metal content micro-structures grown by electron beam induced deposition*, Appl Surf Sci **242**, 107 (2005)
- 113 Kohlmann-von Platen KT, Buchman, *Electron beam induced tungsten deposition: growth rate enhancement and applications*, J Vac Sci Technol B **10**, 2690 (1992)

- 
- 114 Gopal V, Stach EA, Radmilovic VR, Mowat IA, *Metal delocalization and surface decoration in direct-write nanolithography by electron beam induced deposition*, Appl Phys Lett **85**, 49 (2004)
- 115 Fourie J, *The controlling parameter in contamination of specimens in electron microscopes*, Optik **44**, 111 (1975)
- 116 Reimer L, Wächter M, *Contribution to the contamination problem in TEM*, Ultramicroscopy **3**, 169 (1978)
- 117 Utke I, Friedli V, Michler J, *Resolution and growth regimes in focused ion and electron beam induced processing*, Presented at EIPBN 2007
- 118 Smith DA, Fowlkes JD, Rack PD, *A nanoscale three-dimensional Monte Carlo simulation of electron-beam-induced deposition with gas dynamics*, Nanotechnology **18**, 65308 (2007)
- 119 Amman M, Sleight J, Lombardi D, Welsler R, Deshpande M, *Atomic force microscopy study of electron beam written contamination structures*, J Vac Sci Technol B **14**, 54 (1996)
- 120 Utke I, Luisier A, Hoffmann P, Laub D, Buffat PA, *Focused-electron-beam-induced deposition of freestanding three-dimensional nanostructures of pure coalesced copper crystals*, Appl Phys Lett **81**, 3245 (2002)
- 121 Liu ZQ, Mitsuishi K, Furuya K, *Three-dimensional nanofabrication by electron-beam-induced deposition using 200-keV electrons in scanning transmission electron microscope*, Appl Phys A-Mater **80**, 1437 (2005)
- Cicoira F, Leifer K, Hoffmann P, Utke I, Dwir B, Laub D, Buffat PA, Kapon E, Doppelt P, *Electron beam induced deposition of rhodium from the precursor  $[RhCl(PF_3)_2]_2$ : morphology, structure and chemical composition*, J Cryst Growth **265**, 619 (2004)
- 123 Lipp S, Frey L, Lehrer C, Frank B, Demm E, Pauthner S, Ryssel H, *Tetramethoxysilane as a precursor for focused ion beam and electron beam assisted insulator ( $SiO_x$ ) deposition*, J Vac Sci Technol B **14**, 3920 (1996)
- 124 Sanchez EJ, Krug II JT, Xie XS, *Ion and electron beam assisted growth of nanometric  $Si_mO_n$  structures for near field microscopy*, Rev Sci Instrum **73**, 3901 (2002)
- 125 Hoyle P, Ogasawara M, Cleaver J, *Electrical resistance of electron beam induced deposits from tungsten hexacarbonyl*, Appl Phys Lett **62**, 3043 (1993)
- 126 Utke T, Dwir B, Leifer K, Cicoira F, Doppelt P, Hoffmann P, Kapon E, *Electron beam induced deposition of metallic tips and wires for microelectronics applications*, Microelectron Eng **53**, 261 (2000)
- 127 Mølhave K, Nørgaard Madsen D, Dohn, S, Bøggild P, *Constructing, connecting and soldering nanostructures by environmental electron beam deposition*, Nanotechnology **15**, 1047 (2004)
- 128 Okada S, Mukawa T, Kobayashi R, Fujita J, Ishida M, Ichihashi T, Ochiai Y, Kaito T, Matsui S, *Growth manner and mechanical characteristics of amorphous carbon*

- 
- nanopillars grown by electron-beam-induced chemical vapor deposition*, Jpn J Appl Phys **44**, 5646 (2005)
- 129 Luisier A, Utke I, Bret T, Cicoira F, Hauert R, Rhee S-W, Doppelt P, Hoffmann P, *Comparative study of Cu precursors for 3D focused electron beam induced deposition*, J Electrochem Soc **151**, C535 (2004)
- 130 Bret T, Utke I, Gaillard C, Hoffmann P, *Periodic structure formation by focused electron-beam-induced deposition*, J Vac Sci Technol B **22**, 2504 (2004)
- 131 Igaki JY, Kanda K, Haruyama Y, Ishida M, Ochiai Y, Fujita J, Kaito T, Matsui S, *Comparison of FIB-CVD and EB-CVD growth characteristics*, Microelectron Eng **83**, 1225 (2006)
- 132 Liu ZQ, Mitsuishi K, Furuya K, *Features of self-supporting tungsten nanowire deposited with high-energy electrons*, J Appl Phys **96**, 619 (2004)
- 133 Han M, Mitsuishi K, Shimojo M, Furuya K, *Nanostructure characterization of tungsten-containing nanorods deposited by electron-beam-induced chemical vapour decomposition*, Philos Mag A **84**, 1281 (2004)
- 134 Bret T, Utke I, Hoffmann P, *Influence of the beam scan direction during Focused Electron Beam deposition of 3D nanostructures*, Microelectron Eng **78-79**, 307 (2005)
- 135 Zhang W, Shimojo M, Takeguchi M, Che RC, Furuya K, *Generation mechanism and in situ growth behavior of alpha-iron nanocrystals by electron beam induced deposition*, Adv Eng Mat **8**, 711 (2006)
- 136 Gopal V, Radmilovic VR, Daraio C, Jin S, Yang P, Stach EA, *Rapid prototyping of site-specific nanocontacts by electron and ion beam assisted direct-write nanolithography*, Nano Lett **4**, 2059 (2004)
- 137 Martin JP, Speidel R, *Herstellung freitragender Mikrogitter in REM*, Optik **1**, 13 (1972)
- 138 Aristov V, Kislov N, Khodos I, *Direct electron-beam-induced formation of nanometer scale carbon structures in STEM. The growth of rods outside the substrate*, Microsc Microanal Microstruct **3**, 313 (1992)
- 139 Van Dorp WF, Lazar S, Hagen CW, Kruit P, *Solutions to proximity effect in high resolution electron beam induced deposition*, J Vac Sci Technol B **25**, 1603 (2007)
- 140 Aristov VV, Kasumov AY, Kislov NA, Kononenko OV, Matveev VN, *A new approach to fabrication of nanostructures*, Nanotechnology **6**, 35 (1995)
- 141 Mitsuishi K, Shimojo M, Takeguchi M, Tanaka M, Furuya K, *Proximity effect in Electron-Beam-Induced Deposition*, Jpn J Appl Phys **45**, 5517 (2006)
- 142 Zhang W, Shimojo M, Takeguchi M, Furuya K, *Electron beam-induced formation of nanosized alpha-Fe crystals*, J Mater Sci **41**, 2577 (2006)
- 143 Zaera, F, *Kinetic Study of the Chemical Vapor Deposition of Iron Films Using Iron Pentacarbonyl*, Langmuir **7**, 1188 (1991)
- 144 Kunz RR, Mayer TM, *Catalytic growth rate enhancement of electron beam deposited iron films*, Appl Phys Lett **50**, 962 (1987)

- 
- 145 Ketharanathan S, Sharma R, Drucker J, *Nanoscale electron stimulated chemical vapor deposition of Au in an environmental transmission electron microscope*, J Vac Sci Technol B **23**, 2403 (2005)
- 146 West GA, Beeson KW, *Chemical vapor deposition of cobalt silicide*, Appl Phys Lett **53**, 740 (1988)
- 147 Takahashi T, Arakawa Y, Nishioka M, Ikoma T, *MOCVD selective growth of GaAs:C wire and dot structures by electron beam irradiation*, J Cryst Growth **124**, 213 (1992)
- 148 Matsui S, Mori K, *New selective deposition technology by electron beam induced surface reaction*, J Vac Sci Technol B **4**, 299 (1986)
- 149 Ishibashi A, Funato K, Mori Y, *Electron-beam-induced resist and aluminium formation*, J Vac Sci Technol B **9**, 169 (1991)
- 150 Tanaka M, Chu F, Shimojo M, Takeguchi M, Mitsuishi K, Furuya K, *Formation of iron silicide nano-islands on Si substrates by metal organic chemical vapor deposition under electron beams*, J Mater Sci **41**, 2667 (2006)
- 151 Tanaka M, Han M, Takeguchi M, Chu F, Shimojo M, Mitsuishi K, Furuya K, *Morphology of iron silicide nanorods formed by electron-beam-induced deposition using ultrahigh-vacuum transmission electron microscope*, Jpn J Appl Phys **44**, 5635 (2005)
- 152 Ochiai Y, Fujita J, Matsui S, *Electron-beam-induced deposition of copper compound with low resistivity*, J Vac Sci Technol B **14**, 3887 (1996)
- 153 Koops HWP, Schössler C, Kaya A, Weber M, *Conductive dots, wires, and supertips for field electron emitters produced by electron-beam induced deposition on samples having increased temperature*, J Vac Sci Technol B **14**, 4105 (1996)
- 154 Yavas O, Ochiai C, Takai M, Park YK, Lehrer C, Lipp S, Frey L, Ryssel h, Hosono A, Okuda S, *Field emitter array fabricated using focused ion and electron beam induced reaction*, J Vac Sci Technol B **18**, 976 (2000)
- 155 Frabboni S, Gazzadi GC, Spessot A, *Transmission electron microscopy characterization and sculpting of sub-1 nm Si-O-C freestanding nanowires grown by electron beam induced deposition*, Appl Phys Lett, **89**, 13108 (2006)
- 156 Takeguchi M, Shimojo M, Furuya K, *Fabrication of magnetic nanostructures using electron beam induced chemical vapour deposition*, Nanotechnology **16**, 1321 (2005)
- 157 Takeguchi M, Shimojo M, Furuya K, *Fabrication of alpha-iron and iron carbide nanostructures by electron-beam induced chemical vapor deposition and postdeposition heat treatment*, Jpn J Appl Phys **44**, 5631 (2005)
- 158 Shimojo M, Takeguchi M, Tanaka M, Mitsuishi K, Furuya K, *Electron beam-induced deposition using iron carbonyl and the effects of heat treatment on nanostructure*, Appl Phys A Mater **79**, 1869 (2004)
- 159 Guise O, Marbach H, Levy J, Ahner J, Yates JT, *Electron-beam-induced deposition of carbon films on Si(100) using chemisorbed ethylene as a precursor molecule*, Surf Sci **571**, 128 (2004)

- 
- 160 Kislov NA, Khodos II, Ivanov ED, Barthel J, *Electron-beam-induced fabrication of metal-containing nanostructures*, Scanning **18**, 114 (1996)
- 161 Ichihashi T, Fujita J, Ishida M, Ochiai Y, *In situ Observation of Carbon-Nanopillar Tubulization Caused by Liquidlike Iron Particles*, Phys Rev Lett **92**, 215702 (2004)
- 162 Jin CH, Wang JY, Chen Q, Peng L-M, *In situ fabrication and graphitization of amorphous carbon nanowires and their electrical properties*, J Phys Chem B **110**, 5423 (2006)
- 163 Crozier PA, private communication
- 164 Steward, RL, *Insulating films under electron and ion bombardment*, Phys Rev **45**, 488 (1934)
- 165 Komuro M, Hiroshima H, Takechi A, *Miniature tunnel junction by electron-beam-induced deposition*, Nanotechnology **9**, 104 (1998)
- 166 Murakami K, Yamasaki N, Abo S, Wakaya F, Takai M, *Effect of thermal annealing on emission characteristics of nanoelectron source fabricated using beam-assisted process*, J Vac Sci Technol B **23**, 759 (2005)
- 167 Utke I, Cicoira F, Jaenchen G, and Hoffmann P, Scandella L, Dwir B, Kapon E, Laub D, Buffat Ph, Xanthopoulos N, Mathieu HJ, *Focused electron beam induced deposition of high resolution magnetic scanning probe tips*, Mat Res Soc Symp Proc Boston **706**, 307 (2002)
- 168 Matsui S, Toshinari I, *Electron beam induced selective etching and deposition technology*, J Vac Sci Technol B **7**, 1182 (1989)
- 169 Joy DC, *A database of electron-solid interactions*, <http://web.utk.edu/~srcutk/html/interact.htm>
- 170 Ueda K, Yoshimura M, *Fabrication of nanofigures by focused electron beam-induced deposition*, Thin Solid Films **464-465**, 331 (2004)
- 171 Mitsuishi K, Shimojo M, Han M, Furuya K, *Electron-beam-induced deposition using a subnanometer-sized probe of high-energy electrons*, Appl Phys Lett **83**, 2064 (2003)
- 172 Liu ZQ, Mitsuishi K, Furuya K, *A dynamic Monte Carlo study of the in situ growth of a substance deposited using electron-beam-induced deposition*, Nanotechnology **17**, 3832 (2006)
- 173 Hagen CW, Silvis-Cividjian N, Kruit P, *Resolution limit for electron beam induced deposition on thick substrates*, Scanning **27**, 90 (2005)
- 174 Song M, Mitsuishi K, Tanaka M, Takeguchi M, Shimojo M, Furuya K, *Fabrication of self-standing nanowires, nanodendrites, and nanofractal-like trees on insulator substrates with an electron-beam-induced deposition*, Appl Phys A **80**, 1431 (2005)
- 175 Song MH, Mitsuishi K, Furuya K, *Crystallization under 1 MeV electron beam irradiation of nanometer-sized W-dendrites fabricated on alumina substrates with electron-beam-induced deposition*, Mat Sci Forum **475-479**, 4035 (2005)
- 176 Xie GQ, Song MH, Mitsuishi K, Furuya K, *Characterization of nanometer-sized Pt-dendrite structures fabricated on insulator Al<sub>2</sub>O<sub>3</sub> substrate by electron-beam-induced deposition*, J Mater Sci **41**, 2567 (2006)

- 
- 177 Xie G, Song M, Furuya K, *Fabrication and characterization of Au-nanoparticle/W-nanodendrite structures on Al<sub>2</sub>O<sub>3</sub> substrate*, J Mater Sci **41**, 4537 (2006)
- 178 Banhart F, *Laplacian growth of amorphous carbon filaments in a non-diffusion-limited experiment*, Phys Rev E **52**, 5156 (1995)
- 179 Wang HZ, Liu XH, Yang XJ, Wang X, *Intergrowth of a carbon layer and fractal-like trees on 3Y-TZP in TEM observations*, Mater Sci Eng A **311**, 180 (2001)
- 180 Hagen CW, Van Dorp WF, Crozier PA, *The nucleation stage in electron beam induced deposition*, Proceedings of EMAG '07, Institute of Physics Conference Series, accepted (2007)
- 181 Hoffmann P, *Precursors for focused electron beam induced deposition*, oral presentation at the First International EBID Workshop in Delft, 2006
- 182 Bell DA, McConica CM, Falconer JL, Lü Z, *Corrosion of Reactor Wall Surfaces by WF(6)*, J Electrochem Soc **141**, 2884 (1994)
- 183 Hoffmann P and Crozier PA, private communication.
- 184 Shimojo M, Bysakh S, Mitsuishi K, Tanaka M, Song M, Furuya K, *Selective growth and characterization of nanostructures with transmission electron microscopes*, Appl Surf Sci **241**, 56 (2005)
- 185 Bret T, Mauron S, Utke I, Hoffmann P, *Characterization of focused electron beam induced carbon deposits from organic precursors*, Microelectron Eng **78-79**, 300 (2005)
- 186 Seuret P, Cicoira F, Ohta T, Doppelt P, Weber J, Wesolowski TA, *An experimental and theoretical study of [RhCl(PF<sub>3</sub>)(2)](2) fragmentation*, Phys Chem Chem Phys **5**, 268 (2003)
- 187 Doppelt P, Weigel V, Guinot P, *Mineral Precursor for Chemical Vapor-Deposition of Rh Metallic-Films*, Mat Sci Eng B **17**, 143 (1993)
- 188 Ivanova AR, Nuesca G, Chen X, Goldberg C, Kaloyeros AE, Arkles B, Sullivan JJ, *The Effects of Processing Parameters in the Chemical Vapor Deposition of Cobalt from Cobalt Tricarbonyl Nitrosyl*, J Electrochem Soc **146**, 2139 (1999)
- 189 Hoshino M, Kasai K, Komeno J, *Surface Morphology and Line Fill Properties of Gold Grown by Organometallic Chemical Vapor Deposition*, Jpn J Appl Phys **31**, 4403 (1992)
- 190 Folch A, Tejada J, Peters CH, Wrighton MS, *Electron beam deposition of gold nanostructures in a reactive environment*, Appl Phys Lett **66**, 2080 (1995)
- 191 Tseng AA, *Nanofabrication: Fundamentals and Applications*, World Scientific Publishing Co., Singapore, (2007)
- 192 Kohlmann KT, Buchmann LM, Brünger WH, *Repair of open stencil masks for ion projection lithography by e-beam induced metal deposition*, Microelectron Eng **17**, 427 (1992)
- 193 Utke I, Friedli V, Amorosi S, Michler J, Hoffmann P, *Measurement and simulation of impinging precursor molecule distribution in focused particle beam deposition/etch systems*, Microelectron Eng **83**, 1499 (2006)

- 
- 194 Koops HWP, *A story about the past and the present of electron beam induced deposition*, oral presentation at the First International EBID Workshop in Delft, 2006
- 195 ACF Metals, 2239 E. Kleindale Road, Tuscon, Arizona 85719
- 196 Word MJ, Adesida I, Berger PR, *Nanometer-period gratings in hydrogen silsesquioxane fabricated by electron beam lithography*, *J Vac Sci Technol B* **21**, L12 (2003)
- 197 Moore GE, *Cramming more components onto integrated circuits*, *Electronics* **38**, 114 (1965)
- 198 Shimojo M, Mitsuishi K, Tameike A, Furuya K, *Electron induced nanodeposition of tungsten using field emission scanning and transmission electron microscopes*, *J Vac Sci Technol B* **22**, 742 (2004)
- 199 Winters RE, Kiser RW, *Mass Spectrometric Studies of Chromium, Molybdenum, and Tungsten Hexacarbonyls*, *Inorg Chem* **4**, 157 (1964)
- Van Dorp WF, Van Someren B, Hagen CW, Kruit P, Crozier PA, *Statistical variation analysis of sub-5-nm-sized electron-beam-induced deposits*, *J Vac Sci Technol B* **24**, 618 (2006)
- 201 Hagen CW, Silvis-Cividjian N, Kruit P, *Resolution limit for electron beam induced deposition on thick substrates*, *Scanning* **27** 90 (2005)
- 202 Van Dorp WF, Hagen CW, Crozier PA, Kruit P, *In situ monitoring and control of material growth for high resolution electron beam induced deposition*, *J Vac Sci Technol B* **25**, 2210 (2007)
- 203 Hartel P, Rose H, Dinges C, *Conditions and reasons for incoherent imaging in STEM*, *Ultramicroscopy* **63**, 93 (1996)
- 204 Liu ZQ, Mitsuishi K, Furuya K, *Modeling the Process of Electron-Beam-Induced Deposition by Dynamic Monte Carlo Simulation*, *J J Appl Phys* **44**, 5659 (2005)

## References

---

**Appendices****Contents**

<i>I. Precursor names</i> .....	156
<i>II. Symbols used in Chapter 2</i> .....	158
<i>III. Abbreviations</i> .....	159

## I. Precursor names

Material	Precursor	Full name
Al	TMA	Tri-methyl-aluminium
Au	AuCl(PF <sub>3</sub> ) <sub>3</sub>	Chloro(trifluorophosphine) gold
Au	AuCl <sub>3</sub>	Gold trichloride
Au	Me <sub>2</sub> -Au-acac	Dimethyl acetylacetonate gold
Au	Me <sub>2</sub> -Au-tfac	Dimethyl-trifluoro-acetylacetonate gold
Au	Me <sub>2</sub> -Au-hfac	Dimethyl-hexafluoro-acetylacetonate gold
C	C <sub>6</sub> H <sub>5</sub> CHCH <sub>2</sub>	Styrene
C	CH <sub>2</sub> CHCOOH	Acrylic acid
C	CH <sub>3</sub> CH <sub>2</sub> COOH	Propionic acid
C	HCOOH	Formic acid
C	CH <sub>3</sub> COOH	Acetic acid
C	CH <sub>3</sub> C <sub>10</sub> H <sub>8</sub>	Alkylnaphtalene
Co	Co <sub>2</sub> CO <sub>8</sub>	Dicobalt octacarbonyl
Co	[Co(CO <sub>3</sub> )NO],	Cobalt tricarbonyl nitrosyl
Cu	Cu(hfac) <sub>2</sub>	Bis-hexafluoro-acetylacetonate copper
Cu	hfac-Cu-VTMS	Hexafluoro-acetylacetonate copper vinyl-trimethyl-silane
Cu	hfac-Cu-DMB	Hexafluoro-acetylacetonate copper dimethyl-butene
Cu	hfac-Cu-MHY	Hexafluoro-acetylacetonate copper dimethyl-1-hexen-3-yne
Cr	CrO <sub>2</sub> Cl <sub>2</sub>	Chromyl chloride
Cr	Cr(CO) <sub>6</sub>	Chromium hexacarbonyl
Fe	Fe(CO) <sub>5</sub>	Iron pentacarbonyl
Fe	Fe <sub>3</sub> (CO) <sub>12</sub>	Tri-iron dodecacarbonyl
GaAs	TMG and AsH <sub>3</sub>	Tri-methyl-gallium and arsine
GaN	D <sub>2</sub> GaN <sub>3</sub>	Perdeuterated gallium azide
Ir	[IrCl(PF <sub>3</sub> ) <sub>2</sub> ] <sub>2</sub>	Di-μ-chloro-tetrakis trifluorophosphine di-iridium
Mo	Mo(CO) <sub>6</sub>	Molybdenum hexacarbonyl
Ni	Ni(C <sub>5</sub> H <sub>5</sub> ) <sub>2</sub>	Nickelocene
Os	Os <sub>3</sub> (CO) <sub>12</sub>	Tri-osmium dodecacarbonyl
Pt	CpPtMe <sub>3</sub>	Trimethyl-platinum-cyclopentadienyl
Pt	MeCpPtMe <sub>3</sub>	Trimethyl-platinum-methylcyclopentadienyl
Pt	Pt(PF <sub>3</sub> ) <sub>4</sub>	Tetrakis trifluorophosphine platinum
Re	Re <sub>2</sub> (CO) <sub>10</sub>	Dirhenium decacarbonyl
Rh	[RhCl(PF <sub>3</sub> ) <sub>2</sub> ] <sub>2</sub>	Di-μ-chloro-tetrakis trifluorophosphine dirhodium
Rh	[RhCl(CO) <sub>2</sub> ] <sub>2</sub>	Tetracarbonyl di-η-chloro dirhodium
Ru	Ru <sub>3</sub> (CO) <sub>12</sub>	Triruthenium dodecacarbonyl
Si	SiH <sub>2</sub> Cl <sub>2</sub>	Dichlorosilane

*I. Precursor names (continued)*

Material	Precursor	Full name
SiO <sub>x</sub>	TEOS	Tetra-ethoxy-silane
SiO <sub>x</sub>	TMOS	Tetramethyl ortho-silicate
W	W(CO) <sub>6</sub>	Tungsten hexacarbonyl
W	WF <sub>6</sub>	Tungsten hexafluoride
W	WCl <sub>6</sub>	Tungsten hexachloride

## II. Symbols used in Chapter 2

Symbol	Unit	Meaning
$A_{beam}$	[cm <sup>2</sup> ]	Area of the electron beam
$A_{deposit}$	[cm <sup>2</sup> ]	Area of the deposit
$d_{beam}$	[cm]	Diameter of the electron beam
$d_{deposit}$	[cm]	Diameter of the deposit
$E_{des}$	[J]	Desorption energy
$F$	[cm <sup>-2</sup> s <sup>-1</sup> ]	Precursor gas flux
$g$	[-]	Sticking factor
$h$	[nm]	Deposit height
$I$	[electrons s <sup>-1</sup> ]	Current
$J$	[electrons s <sup>-1</sup> cm <sup>-2</sup> ]	Total current density
$J_{BSE}$	[electrons s <sup>-1</sup> cm <sup>-2</sup> ]	BSE current density
$J_{PE}$	[electrons s <sup>-1</sup> cm <sup>-2</sup> ]	PE current density
$J_{SE}$	[electrons s <sup>-1</sup> cm <sup>-2</sup> ]	SE current density
$k$	[m <sup>2</sup> kg s <sup>-2</sup> K <sup>-1</sup> ]	Boltzmann constant
$\nu$	[s <sup>-1</sup> ]	Vibrational frequency of an adsorbed molecule
$N$	[cm <sup>-2</sup> ]	Precursor molecule coverage
$N_0$	[cm <sup>-2</sup> ]	Available adsorption sites in a monolayer
$P_{partial}$	Pa	Precursor partial pressure
$P_{equilibrium}$	Pa	Precursor equilibrium pressure
$Q$	[C]	Accumulated charge
$R$	[cm/s]	Vertical growth rate
$\sigma_{(E)}$	[cm <sup>2</sup> ]	Cross section for dissociation
$\sigma$	[cm <sup>2</sup> ]	Integral value of $\sigma_{(E)}$
$t$	[s]	Time
$t_{dwell}$	[s]	Dwell time
$\tau$	[s]	Residence time
$T$	[K]	Temperature
$V_{deposit}$	[cm <sup>3</sup> ]	Volume of a deposit
$V_{molecule}$	[cm <sup>3</sup> ]	Volume of a deposited molecule

*III. Abbreviations*

Abbreviation	Short for
a-C	Amorphous carbon
BSE	Backscattered electron
DEA	Dissociative electron attachment
DD	Dipolar dissociation
DI	Dissociative ionization
EBIH	Electron beam induced heating
EBL	Electron beam lithography
EELS	Electron energy loss spectrometry
e.l.	Electron-limited
EBID	Focused electron beam induced deposition
EBIE	Electron beam induced etching
FEBIP	Focused electron beam induced processing
FSE	Forward scattered electron
PE	Primary electron
p.l.	Precursor-limited
SE	Secondary electron
SEM	Scanning electron microscope
STEM	Scanning transmission electron microscope
SQUID	Superconducting quantum interference devices
TEM	Transmission electron microscope
UHV	Ultra-high vacuum
UV	Ultraviolet

## Curriculum Vitae

Willem Frederik van Dorp  
born on June 26<sup>th</sup> 1976 in Opperdoes, the Netherlands

- 1988 - 1993 Hoger Algemeen Voorgezet Onderwijs at the Ulenhof College in Doetinchem
- 1993 - 1995 Voorbereidend Wetenschappelijk Onderwijs at the Ulenhof College in Doetinchem
- 1995 - 1999 Chemical Technology at the Hogeschool Enschede in Enschede
- 1999 - 2003 Materials Science and Technology at the Delft University of Technology in Delft
- 2003 - 2007 PhD student at the Delft University of Technology, faculty of Applied Sciences, Charged Particle Optics Group in Delft

## Bibliography

1. W.F. van Dorp, B. van Someren, C.W. Hagen, P. Kruit, P.A Crozier  
*Approaching the ultimate resolution of electron beam induced deposition*  
Nano Letters **5**, 1303 (2005)
2. W.F. van Dorp, B. van Someren, C.W. Hagen, P. Kruit, P.A. Crozier  
*Diffraction patterns of artificial two-dimensional crystals synthesized in situ in an environmental scanning transmission electron microscope*  
Journal of Microscopy Oxford **221**, 159 (2006)
3. W.F. van Dorp, B. van Someren, C.W. Hagen, P. Kruit, P.A. Crozier  
*Statistical variation analysis of sub-5-nm-sized electron-beam-induced deposits*  
Journal of Vacuum Science and Technology B **24**, 618 (2006)
4. W.F. van Dorp, C.W. Hagen, B. van Someren, P. Kruit, P.A. Crozier  
*One nanometer structure fabrication using electron beam induced deposition*  
Microelectronic Engineering **83**, 1468 (2006)
5. W.F. van Dorp, S. Lazar, C.W. Hagen, P. Kruit  
*Solutions to a proximity effect in high resolution electron beam induced deposition*  
Journal of Vacuum Science and Technology **25**, 1603 (2007)
6. W.F. van Dorp, C.W. Hagen, P.A. Crozier, P. Kruit  
*In situ monitoring and control of material growth for high resolution electron beam induced deposition*  
Journal of Vacuum Science and Technology **25**, 2210 (2007)
7. C.W. Hagen, W.F. van Dorp, P.A. Crozier  
*The nucleation stage in electron beam induced deposition*  
Proceedings of EMAG '07, Institute of Physics Conference Series, accepted (2007)
8. C.W. Hagen, W.F. van Dorp, P.A. Crozier, P. Kruit  
*Electronic pathways in nanostructure fabrication*  
Surface Science, accepted (2007)
9. W.F. van Dorp, C.W. Hagen  
*A critical literature review of focused electron beam induced deposition*  
Journal of Applied Physics, submitted (2007)
10. W.F. van Dorp, C.W. Hagen, P.A. Crozier, P. Kruit  
*Growth behavior near the ultimate resolution of nanometer-scale focused electron beam-induced deposition*  
Nanotechnology, submitted (2007)

## Acknowledgement

The success of a PhD project depends, amongst others, on the ability to recognize fields which are unexplored while at the same time the tools to explore them are within reach. Pieter Kruit and Kees Hagen spotted such a field and I am very grateful that they offered me the opportunity to explore it. I couldn't have wished for a job more suited.

Not in the least because I have noticed next to nothing from the notorious solitude in which some PhD-students find themselves. The Charged Particle Optics Group (CPO) is full of frightfully smart and supportive people. Pieter was very good at challenging me to go for the highest goal and giving some clues on how to get there. Kees was always there to help me, to read my writings and to cheer me up. His seemingly unlimited supply of optimism was very stimulating, for instance in those crucial moments when I was tired, moral was low, the stomach was empty and we were trying to find the door of a mysteriously hidden local restaurant in Sapporo. Coming from right across our coffee table in Delft, the sound of Jim uttering his frustrations with whatever it was (hehe!) will stick for a long time, I think. I liked how Bob explained the workings of all sorts of devices and how he never got tired of answering my many questions. Ad was always in for a good laugh and Jacques never ceased to amaze me: nearly every time I walked into his office, he had exactly the piece of information or equipment I was looking for. Regarding Carel and Jan, I don't know who comes up with the most unlikely stories, but both of them helped me a great deal. Just as much as Frans, who even was kind enough to answer questions he shouldn't be asked (hey, why doesn't my computer work?). I hope I didn't mess up Elly's and Margaret's administration too much by continually trying to arrange stuff myself. I enjoyed the company and help of Vladimir and all the PhD and graduate students in the group and hopefully Martin hasn't suffered too much from my inexperience at being an advisor.

And then there was the travelling. Conceptually speaking, the tools may have been within reach, but in practice it took quite a number of hours on the plane to actually fiddle with the buttons. For a home bird like me, there is always a bit of a threshold to get over when travelling is involved, but destinations such as Lausanne, Phoenix, Denver and Sapporo definitely were well worth the trouble.

A special word of thanks is reserved for Peter Crozier. His large experience as a microscopist and his continuous focus on progress and efficiency have contributed a lot to the success of this project. He's wonderful to work with (if you can stand being ridiculed every other sentence) and I've learned a great deal. My visits to Phoenix always consisted of a rather odd combination of activities. The one day, we would sit in the dark for hours on end, on our way to set new world records and meanwhile figuring out why the stupid microscope wasn't doing what it was supposed to do. The other day, we would do something as every-day as walking the dogs under a brilliant blue sky in a park somewhere in Phoenix or in the Superstition Mountains. But whatever the activity, we always had endless discussions about everything and what not. I loved it and I must say the viewpoint of a cynical Scotsman in the Arizona desert is very refreshing.

Which brings me to things bigger than my PhD project. Self-knowledge may seem simple and obvious for some, but for me it was quite challenging to obtain it. And although I don't see an end to this particular job yet, it already has made life a lot more enjoyable. Just like a PhD project, one doesn't do this alone. Family and friends were very supportive, but nobody has been more important for me in this respect than Mariëtte. Without her, life would certainly have been a lot less jolly. Good work, shmooops!

## Dankwoord

Het succes van een promotieonderzoek hangt, onder andere, af van het vermogen om gebieden te herkennen die onbekend zijn, terwijl de middelen om ze in kaart te brengen, binnen handbereik zijn. Pieter Kruit en Kees Hagen hebben zo'n veld gespot en ik ben er erg dankbaar voor dat ze mij de kans hebben geboden het te verkennen. Ik had het niet beter kunnen treffen.

Niet in het minst omdat ik hoegenaamd niets heb gemerkt van de beruchte eenzaamheid waar promovendi soms mee worstelen. Deeltjesoptica is een groep vol buitengewoon slimme en behulpzame mensen. Het lukte Pieter erg goed mij uit te dagen om voor het hoogste doel te gaan en wat suggesties te doen over hoe ik daar zou kunnen komen. Kees had altijd tijd om mij te helpen, om te lezen wat ik geschreven had en om mij op te beuren. Zijn schier onuitputtelijke optimisme was erg stimulerend, bijvoorbeeld op die cruciale momenten dat ik moe was, geen zin meer had, de maag leeg was en we op zoek waren naar de deur van een geheimzinnig verborgen lokaal restaurantje in Sapporo. Het geluid van Jim die vanaf de andere kant van de koffietafel in Delft zijn frustraties uitte over wat dan ook (hehe!), zal nog wel een poosje blijven hangen, denk ik. Ik vond het leuk hoe Bob de werking van van alles en nog wat kon uitleggen en hoe hij altijd bereid was mijn vragen te beantwoorden. Ad was altijd wel in voor een goede grap en Jacques hield nooit op mij te verbazen: elke keer als ik bij hem binnenliep, had hij telkens precies datgene waar ik naar op zoek was. Wat betreft Carel en Jan weet ik niet wie er de sterkste verhalen heeft, maar beiden hebben mij altijd goed geholpen. Net als Frans, die zelfs vragen beantwoordt die hem helemaal niet gesteld moeten worden (hee, waarom doet mijn computer het nou niet?). Ik hoop dat ik Elly's en Margarets administratie niet teveel overhoop het gegooid door steeds alles zelf te willen doen. Het was altijd erg gezellig met Vladimir en alle promovendi en studenten in onze groep en ik hoop dat Martin niet al te veel heeft geleden onder mijn gebrek aan ervaring als begeleider.

En dan was er al het reizen. Conceptueel gezien waren de middelen misschien binnen handbereik, in de praktijk waren er toch heel wat uurtjes in het vliegtuig voor nodig om met de knoppen te kunnen spelen. Een huismus zoals ik moet altijd even over een drempel heen als het om reizen gaat, maar bestemmingen zoals Lausanne, Phoenix, Denver en Sapporo waren zeer zeker de moeite waard.

Ik wil Peter Crozier in het bijzonder bedanken. Zijn grote ervaring als een microscopist en zijn onophoudelijke focus op voortgang en efficiëntie hebben veel bijgedragen aan het succes van dit project. Met hem samenwerken is heel leuk (als je er tegen kan om om de haverklap belachelijk gemaakt te worden) en ik heb veel geleerd. Mijn bezoeken aan Phoenix bestonden uit een nogal ongewone combinatie van activiteiten. De ene dag zaten we eindeloos in het donker, op weg naar nieuwe wereldrecords en ondertussen worstelend met die stomme microscoop die niet deed wat hij moest doen. De andere dag deden we zoiets alledaags als de honden uitlaten onder een knalblauwe lucht in een park ergens in Phoenix of in het Superstitiongebergte. Maar wat we ook deden, we hadden altijd eindeloze discussies over van alles en nog wat. Ik hield daar erg van en ik moet zeggen dat het gezichtspunt van een cynische Schot in de woestijn van Arizona erg verfrissend is.

Wat mij bij grotere dingen dan mijn promotieonderzoek brengt. Zelfkennis is voor sommigen misschien simpel en voor de hand liggend, voor mij was het nogal een uitdaging om die te krijgen. En hoewel ik het einde van die klus misschien nog niet helemaal zie, is het leven er al wel een stuk aangener door geworden. Net als een promotieonderzoek doet een mens dit niet alleen. Ik heb veel steun gehad van familie en vrienden, maar niemand is in dit opzicht belangrijker voor mij geweest dan Mariëtte. Zonder haar zou het leven een stuk minder vrolijk geweest zijn. Good work, shmooops!

